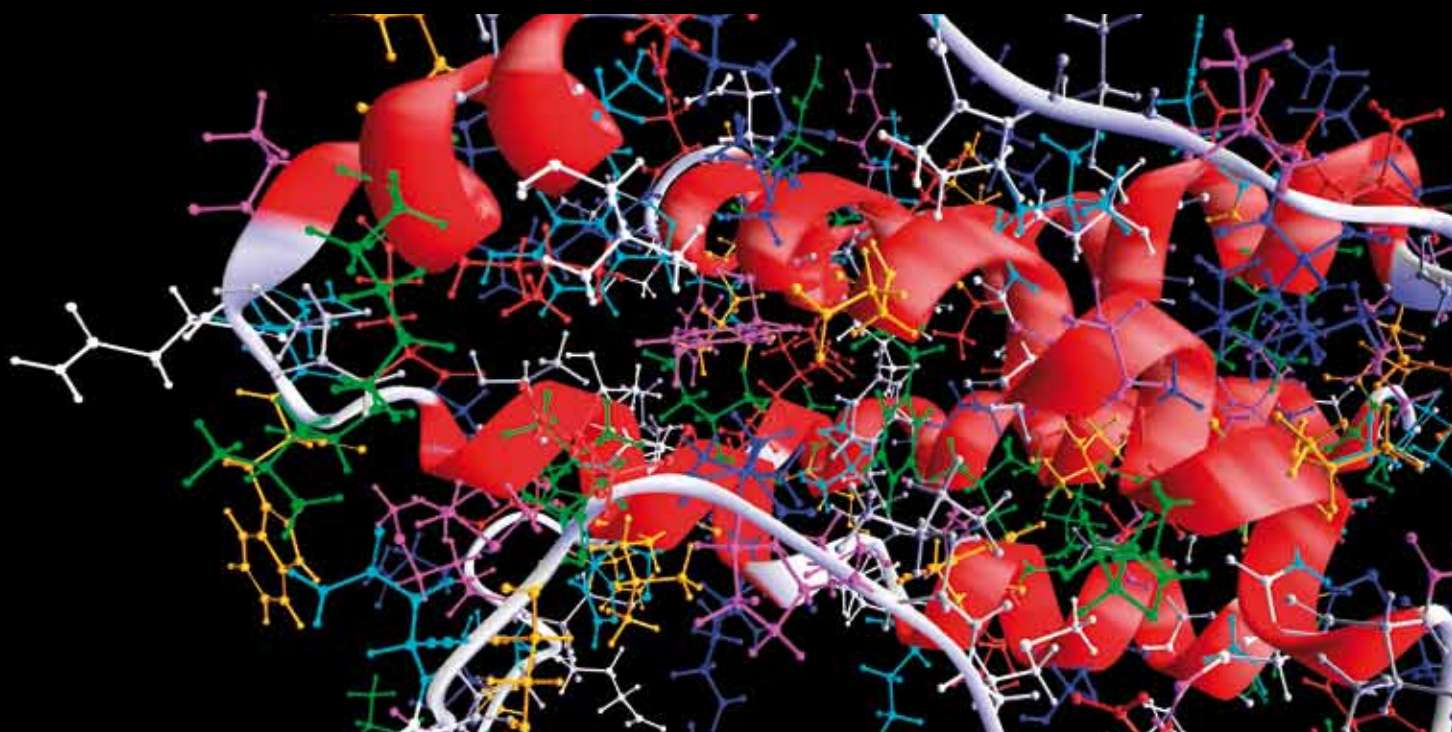


CARDIOVASCULAR SYSTEM MODELING

GUEST EDITORS: LING XIA, ALAN MURRAY, DINGCHANG ZHENG, FENG LIU, XUESONG YE,
AND GANGMIN NING





Cardiovascular System Modeling

Computational and Mathematical Methods in Medicine

Cardiovascular System Modeling

Guest Editors: Ling Xia, Alan Murray, Dingchang Zheng,
Feng Liu, Xuesong Ye, and Gangmin Ning



Copyright © 2012 Hindawi Publishing Corporation. All rights reserved.

This is a special issue published in “Computational and Mathematical Methods in Medicine.” All articles are open access articles distributed under the Creative Commons Attribution License, which permits unrestricted use, distribution, and reproduction in any medium, provided the original work is properly cited.

Editorial Board

Zvia Agur, Israel
Emil Alexov, USA
Gary C. An, USA
Georgios Archontis, Cyprus
Pascal Auffinger, France
Facundo Ballester, Spain
Dimos Baltas, Germany
Chris Bauch, Canada
Maxim Bazhenov, USA
Niko Beerenwinkel, Switzerland
Philip Biggin, UK
Michael Breakspear, Australia
Thierry Busso, France
Carlo Cattani, Italy
Bill Crum, UK
Timothy David, New Zealand
Gustavo Deco, Spain
Carmen Domene, UK
Wim Van Drongelen, USA
Frank Emmert-Streib, UK
Ricardo Femat, Mexico
Alfonso T. García-Sosa, Estonia
Kannan Gunasekaran, USA

Damien R. Hall, Japan
William F. Harris, South Africa
Vassily Hatzimanikatis, USA
Tasawar Hayat, Pakistan
Volkhard Helms, Germany
J.-H. S. Hofmeyr, South Africa
Seiya Imoto, Japan
Bleddyn Jones, UK
Lawrence A. Kelley, UK
Lev Klebanov, Czech Republic
Ina Koch, Germany
David Liley, Australia
Quan Long, UK
Yoram Louzoun, Israel
Jianpeng Ma, USA
C.-M. C. Ma, USA
Reinoud Maex, France
Francois Major, Canada
Simeone Marino, USA
Ali Masoudi-Nejad, Iran
Seth Michelson, USA
Michele Migliore, Italy
Karol Miller, Australia

Ernst Niebur, USA
Kazuhisa Nishizawa, Japan
Martin Nowak, USA
Markus Owen, UK
Hugo Palmans, UK
Lech S. Papiez, USA
Jean Pierre Rospars, France
David James Sherman, France
Sivabal Sivaloganathan, Canada
Elisabeth Tillier, Canada
Nestor V. Torres, Spain
Anna Tramontano, Italy
Nelson J. Trujillo-Barreto, Cuba
Kutlu O. Ulgen, Turkey
Nagarajan Vaidehi, USA
Edelmira Valero, Spain
Jinliang Wang, UK
Jacek Waniewski, Poland
Guang Wu, China
X. George Xu, USA
Henggui Zhang, UK

Contents

Cardiovascular System Modeling, Ling Xia, Alan Murray, Dingchang Zheng, Feng Liu, Xuesong Ye, and Gangmin Ning
Volume 2012, Article ID 583172, 2 pages

Discrete-State Stochastic Models of Calcium-Regulated Calcium Influx and Subspace Dynamics Are Not Well-Approximated by ODEs That Neglect Concentration Fluctuations, Seth H. Weinberg and Gregory D. Smith
Volume 2012, Article ID 897371, 17 pages

Simulation of Exercise-Induced Syncope in a Heart Model with Severe Aortic Valve Stenosis, Matjaž Sever, Samo Ribarič, and Marjan Kordaš
Volume 2012, Article ID 138401, 9 pages

Simulation of the Frank-Starling Law of the Heart, Samo Ribarič and Marjan Kordaš
Volume 2012, Article ID 267834, 12 pages

Simulations of Complex and Microscopic Models of Cardiac Electrophysiology Powered by Multi-GPU Platforms, Bruno Gouvêa de Barros, Rafael Sachetto Oliveira, Wagner Meira Jr., Marcelo Lobosco, and Rodrigo Weber dos Santos
Volume 2012, Article ID 824569, 13 pages

Coronary Artery Center-Line Extraction Using Second Order Local Features, Farsad Zamani Boroujeni, Rahmita Wirza O. K. Rahmat, Norwati Mustapha, Lilly Suriani Affendey, and Oteh Maskon
Volume 2012, Article ID 940981, 20 pages

A Hybrid Model of Maximum Margin Clustering Method and Support Vector Regression for Noninvasive Electrocardiographic Imaging, Mingfeng Jiang, Feng Liu, Yaming Wang, Guofa Shou, Wenqing Huang, and Huaxiong Zhang
Volume 2012, Article ID 436281, 9 pages

A Fully Coupled Model for Electromechanics of the Heart, Henian Xia, Kwai Wong, and Xiaopeng Zhao
Volume 2012, Article ID 927279, 10 pages

A Study of Mechanical Optimization Strategy for Cardiac Resynchronization Therapy Based on an Electromechanical Model, Jianhong Dou, Ling Xia, Dongdong Deng, Yunliang Zang, Guofa Shou, Cesar Bustos, Weifeng Tu, Feng Liu, and Stuart Crozier
Volume 2012, Article ID 948781, 13 pages

Fast Parameters Estimation in Medication Efficacy Assessment Model for Heart Failure Treatment, Yinzi Ren, Xiao Fu, Qing Pan, Chengyu Lin, Guiqiu Yang, Li Li, Shijin Gong, Guolong Cai, Jing Yan, and Gangmin Ning
Volume 2012, Article ID 608637, 9 pages

Simulation of Arrhythmogenic Effect of Rogue RyRs in Failing Heart by Using a Coupled Model,

Luyao Lu, Ling Xia, and Xiuwei Zhu

Volume 2012, Article ID 183978, 10 pages

Impact of Competitive Flow on Hemodynamics in Coronary Surgery: Numerical Study of ITA-LAD

Model, Jinli Ding, Youjun Liu, Feng Wang, and Fan Bai

Volume 2012, Article ID 356187, 7 pages

An Image-Based Model of the Whole Human Heart with Detailed Anatomical Structure and Fiber

Orientation, Dongdong Deng, Peifeng Jiao, Xuesong Ye, and Ling Xia

Volume 2012, Article ID 891070, 16 pages

Editorial

Cardiovascular System Modeling

Ling Xia,¹ Alan Murray,² Dingchang Zheng,² Feng Liu,³ Xuesong Ye,¹ and Gangmin Ning¹

¹ Department of Biomedical Engineering, Zhejiang University, Hangzhou 310027, China

² Cardiovascular Physics and Engineering Research Group, Institute of Cellular Medicine, Newcastle University, Freeman Hospital, Newcastle upon Tyne NE7 7DN, UK

³ School of Information Technology and Electrical Engineering, The University of Queensland, Brisbane, QLD 4072, Australia

Correspondence should be addressed to Ling Xia, xialing@zju.edu.cn

Received 29 November 2012; Accepted 29 November 2012

Copyright © 2012 Ling Xia et al. This is an open access article distributed under the Creative Commons Attribution License, which permits unrestricted use, distribution, and reproduction in any medium, provided the original work is properly cited.

Mathematical models and numerical simulations of the cardiovascular system are very useful for understanding the mechanisms influencing its function and its physiological and pathological processes. This modeling research increases the potential for developing new diagnostic and therapeutic cardiovascular techniques or devices and is also helpful for pharmacological research [1]. The recent development of computational methods to solve modeling difficulties in diverse disciplines such as systems biology and computer science led to the idea of compiling a special volume on the subject.

This special issue mainly focuses on computational and mathematical methods in cardiovascular system modeling. The research papers cover the topics of cellular or subcellular cardiac cell modeling, cardiovascular anatomical structure modeling, cardiac electrophysiology modeling and simulation, cardiac mechanics modeling and analysis, heart failure modeling and simulation, GPU-based cardiac computational technology, modeling and simulation of the vascular system and mechanics, and computational methods in cardiovascular imaging. In the following, we briefly summarize the twelve papers included in this issue.

Calcium dynamics is very important in cardiac cell modeling and is often modeled using deterministic ordinary differential equations (ODEs). However, is it appropriate to model the dynamics of the subspace calcium using deterministic ODEs? Do we require a stochastic description that accounts for the fundamentally discrete nature of the calcium-regulated calcium influx? To answer these questions, S. H. Weinberg and G. D. Smith constructed and analyzed a minimal Markov model of a calcium-regulated calcium channel and associated subspace and also compared the

expected steady-state subspace calcium concentration in the stochastic model (a result that accounts for the small subspace volume) with the corresponding deterministic ODE model (an approximation that assumes large system size).

L. Lu et al. developed a coupled calcium dynamics model by integrating the spatiotemporal Ca^{2+} reaction-diffusion system into the cellular electrophysiological model. Their model was applied to study the effect of rogue RyRs on Ca^{2+} cycling and membrane potential in failing heart. Their simulation showed that rogue RyR with tiny Ca^{2+} release flux is an important factor in triggering arrhythmia in failing cardiac cells and suggested that rogue RyRs could influence the initiation of Ca^{2+} release events (especially Ca^{2+} waves) and consequently delayed afterdepolarizations or triggered action potentials.

Modeling and simulation of the high complexity of the cardiac electrophysiological processes and the detailed microstructure of cardiac tissue face the challenges of the high computational cost. B. G. de Barros et al. developed a cardiac electrophysiological model using a very fine spatial discretization ($8\ \mu\text{m}$) and a complex cell model based on Markov chains for the characterization of ion channel's structure and dynamics. Multi-GPU platform was then used to compute parallelly. The execution time of the simulations was reduced from over 6 days (on a single processor) to 21 minutes (on a small 8-node cluster equipped with 16 GPUs, i.e., 2 GPUs per node).

D. Deng et al. developed a human heart model with detailed anatomical structure, conduction system, and experimentally measured fiber orientations. Such detailed anatomical heart model could be very useful for a better

understanding of the mechanisms influencing cardiovascular function and its physiological and pathological processes.

Electromechanical modeling of the heart is one of the hottest topics in cardiovascular system modeling. H. Xia et al. presented a fully coupled electromechanical model of a dog heart. This model integrated cardiac electrophysiology and cardiac mechanics through excitation-induced contraction and deformation-induced current. It provides a useful tool to understand cardiovascular dynamics. J. Dou et al. presented a mechanical optimization strategy for cardiac resynchronization therapy (CRT) based on an electromechanical heart model. This mechanical-based optimization approach, in combination with the electrical-based approach, provided a more reasonable method for optimization of lead positions and pacing delays of CRT.

M. Jiang et al. reported a new approach for solving the ECG inverse problem. The inverse problem was treated as a regression problem with multiinputs (body surface potentials (BSPs)) and multioutputs (transmembrane potentials (TMPs)) and was then solved by a maximum margin clustering-support vector regression method. Their new approach achieved a good performance in reconstructing TMPs from BSPs and could be useful for noninvasive electrocardiographic imaging [2].

In the area of cardiac mechanics and the vascular system, in order to simulate the Frank-Starling law of the heart, S. Ribarič and M. Kordaš developed a lumped parameter model with a vascular circuit based on a frog heart with one atrium and one ventricle. This model could be used to study the basic concept of cardiovascular physiology in a macroscopic manner, for example, the time course of atrial and ventricular pressure during systole and diastole, the rate of myocardial contraction and relaxation, and so on. A similar model was used by M. Sever et al. to simulate the exercise-induced syncope in patients with severe aortic valve stenosis, and the effects of controlled change in heart rate and the ventricular contractility or systemic vascular resistance on the cardiac hemodynamics were investigated.

F. Z. Boroujeni et al. presented an improved center-line tracing algorithm for automatic extraction of the coronary arterial tree based on the second-order local features. This algorithm avoided the limitations in handling highly curved segments and sudden changes of vessel diameter at the site of arterial lesions and thus could be more suitable for feature extraction and quantitative coronary analysis in real applications with inherently noisy data.

J. Ding et al. investigated the hemodynamic effect of competitive flow caused by different degrees of left anterior descending (LAD) artery stenosis in internal thoracic artery (ITA) bypass graft. An idealized ITA-LAD model was developed, and the simulation suggested that the coronary bypass graft surgery should preferentially be carried out when the LAD stenosis is higher than 75%. This study is useful for guiding the treatment of proximal LAD stenosis.

Y. Ren et al. presented a fast parameters estimation algorithm to construct a cardiovascular model for the evaluation of drugs used for the treatment of heart failure (HF). The model is able to predict hemodynamic conditions of HF patients undergoing treatment. Also, a novel comprehensive

index was produced to assess the outcome of HF treatment. This study offers a quantitative tool for having a patient-specific HF treatment plan and is useful in evaluating the dose effect of HF drugs.

In summary, the twelve research papers in the special issue summarize the most recent developments and ideas in the field of cardiovascular system modeling. They are worth reading by the researchers who are working in the cardiovascular modelling or related fields.

Ling Xia
Alan Murray
Dingchang Zheng
Feng Liu
Xuesong Ye
Gangmin Ning

References

- [1] D. Noble, "Computational models of the heart and their use in assessing the actions of drugs," *Journal of Pharmacological Sciences*, vol. 107, no. 2, pp. 107–117, 2008.
- [2] C. Ramanathan, R. N. Ghanem, P. Jia, K. Ryu, and Y. Rudy, "Noninvasive electrocardiographic imaging for cardiac electrophysiology and arrhythmia," *Nature Medicine*, vol. 10, no. 4, pp. 422–428, 2004.

Research Article

Discrete-State Stochastic Models of Calcium-Regulated Calcium Influx and Subspace Dynamics Are Not Well-Approximated by ODEs That Neglect Concentration Fluctuations

Seth H. Weinberg and Gregory D. Smith

Department of Applied Science, The College of William and Mary, Williamsburg, VA 23187, USA

Correspondence should be addressed to Gregory D. Smith, greg@as.wm.edu

Received 29 June 2012; Accepted 17 September 2012

Academic Editor: Ling Xia

Copyright © 2012 S. H. Weinberg and G. D. Smith. This is an open access article distributed under the Creative Commons Attribution License, which permits unrestricted use, distribution, and reproduction in any medium, provided the original work is properly cited.

Cardiac myocyte calcium signaling is often modeled using deterministic ordinary differential equations (ODEs) and mass-action kinetics. However, spatially restricted “domains” associated with calcium influx are small enough (e.g., 10^{-17} liters) that local signaling may involve 1–100 calcium ions. Is it appropriate to model the dynamics of subspace calcium using deterministic ODEs or, alternatively, do we require stochastic descriptions that account for the fundamentally discrete nature of these local calcium signals? To address this question, we constructed a minimal Markov model of a calcium-regulated calcium channel and associated subspace. We compared the expected value of fluctuating subspace calcium concentration (a result that accounts for the small subspace volume) with the corresponding deterministic model (an approximation that assumes large system size). When subspace calcium did not regulate calcium influx, the deterministic and stochastic descriptions agreed. However, when calcium binding altered channel activity in the model, the continuous deterministic description often deviated significantly from the discrete stochastic model, unless the subspace volume is unrealistically large and/or the kinetics of the calcium binding are sufficiently fast. This principle was also demonstrated using a physiologically realistic model of calmodulin regulation of L-type calcium channels introduced by Yue and coworkers.

1. Introduction

Concentration changes of physiological ions and other chemical species (such as kinases, phosphatases, and various modulators of cellular activity) influence and regulate cellular responses [1]. These dynamics are often modeled using systems of deterministic ordinary differential equations (ODEs) that assume chemical species concentrations are nonnegative real-valued quantities (i.e., the state-space is continuous). In such descriptions, the rate of change of the concentration of each species is usually specified under the assumption of mass-action kinetics, that is, the rate of a reaction is proportional to the product of reactant concentrations. However, under physiological conditions the concentrations of chemical species are often quite low and,

in some cases, restricted subspaces in which these species are contained are very small. For example, L-type calcium channels in cardiac myocytes are typically clustered in small “diadic subspaces” that have a volume of 10^{-17} liters, with approximately 20,000 diadic subspaces per cell [2, 3]. Resting calcium concentration in the diad is typically 0.1 micromolar, a value that corresponds to an average of 0.6 calcium ions per subspace [4]. Because only whole numbers of calcium ions can be present in a subspace at any given time, the question arises: *is it appropriate to use deterministic ODEs to model subspace calcium dynamics?*

Previous studies have compared discrete-state (stochastic) and continuous-state (deterministic) models in the analysis of biological and chemical systems, including models of biochemical networks, enzyme kinetics, and population

dynamics [5–21]. These studies have shown that in the “large-system limit” (i.e., a large “copy number” of each chemical species), the solution of discrete and continuous models are equivalent [12]. However, for a small system, concentration values obtained from a continuous deterministic model (an approximation that neglects concentration fluctuations) can significantly deviate from the expected value obtained from the discrete stochastic model. When chemical reactions are higher than first order, there is no guarantee that the deterministic mass-action formulation will agree with, or be a good approximation to, the expected value of species concentrations obtained from a chemical master equation that accounts for discrete system states and concentration fluctuations [5]. An excellent study by Goutsias discusses the relationship between the discrete and continuous formulations for general biochemical systems [22] (for theoretical context, see [23]).

Because of recent interest in the physiological relevance of spatially localized control of voltage- and calcium-regulated calcium influx and sarcoplasmic reticulum calcium release in cardiac myocytes [24–26], we sought to determine precisely when the conventional deterministic formulation of these processes are a valid approximation. When is it appropriate to model the dynamics of subspace calcium using deterministic ODEs? When does one require a stochastic description that accounts for the fundamentally discrete nature of calcium-regulated calcium influx?

To answer this question, we constructed and analyzed a minimal Markov model of a calcium-regulated calcium channel and associated subspace. We compared the expected steady-state subspace calcium concentration in this stochastic model (a result that accounts for the small subspace volume) with the result obtained using the corresponding deterministic ODE model (an approximation that assumes large system size). Section 2.1 introduces our model formulation and shows the agreement between deterministic and stochastic descriptions when subspace calcium does not regulate calcium influx. However, when calcium binding regulates channel activity (through either activation or inactivation), the deterministic and stochastic descriptions often disagree (Sections 2.2 and 2.3). In general, the effect of concentration fluctuations in a spatially restricted calcium domain with a calcium-regulated calcium influx pathway (e.g., a stochastically gating L-type calcium channel) is only well-approximated by the deterministic description when the subspace volume is sufficiently (unphysiologically) large or the kinetics of calcium binding to the calcium-regulated channel are sufficiently fast. This principle was also demonstrated using a physiologically realistic model of calmodulin regulation of L-type calcium channels produced by Yue and coworkers (Section 2.4).

2. Methods and Results

2.1. Calcium Influx and Subspace Calcium Concentration Fluctuations. We begin with the case of a single calcium channel that is associated with a spatially restricted subspace but not regulated by subspace calcium (Figure 1 and Section 2.1). The description of the model in the absence

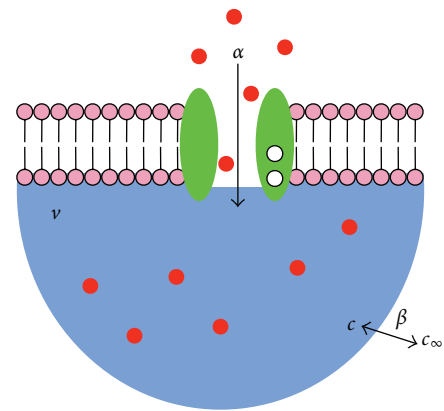


FIGURE 1: Diagram of the components and fluxes in a minimal subspace model. Calcium influx α (in units of $\mu\text{M}/\text{s}$) leads to increased calcium concentration c (units of μM) in a diadic subspace of volume v (liters). Subspace calcium moves to the bulk passively via diffusion at rate β (given by 0.01 ms^{-1}). Bulk calcium at the concentration $c_\infty = 0.1 \mu\text{M}$ returns to the subspace at the same rate. The equilibration time of subspace calcium is $\tau = 1/\beta = 100 \text{ ms}$ [27].

of calcium regulation simplifies the initial presentation of the model and allows us to illustrate general properties of subspace calcium concentration fluctuations. Subsequently, we present a more complete model formulation that includes calcium-regulated calcium influx (Figure 3 and Section 2.2). For simplicity, we neglect the presence of endogenous calcium binding proteins and assume a constant flux of calcium, denoted by α , into the subspace. The subspace calcium concentration is passively coupled with relaxation rate $\beta = 0.01 \text{ ms}^{-1}$ to the constant bulk concentration of $c_\infty = 0.1 \mu\text{M}$ [27]. These assumptions lead to the following deterministic model of subspace calcium dynamics:

$$\frac{dc}{dt} = \alpha - \beta c - c, \quad (1)$$

where the influx rate α has units of concentration per time (e.g., $\mu\text{M}/\text{ms}$) and the calcium concentration c is a continuous real-valued quantity.

2.1.1. Stochastic Model. In the corresponding stochastic description of calcium influx into a diadic subspace, the state variable is the number of calcium ions in the subspace (a discrete quantity that we will denote by $C = 0, 1, \dots$), where the caret ($\hat{}$) indicates that C is a dimensionless number of molecules rather than concentration, and the capitalization indicates a random variable. The fluctuating subspace calcium concentration (also a random variable, denoted by C) depends on both C and the subspace volume (v), that is,

$$C = \frac{C}{v}. \quad (2)$$

Using this relationship, it is straightforward to derive the transition rates between the discrete states of the stochastic

model that are consistent with (1). The resulting state-transition diagram for the stochastic model is

$$\begin{array}{c}
 \bar{\alpha} \\
 \beta \\
 \downarrow \\
 0 \xrightarrow{1} 1 \xrightarrow{2} \dots \xrightarrow{n-1} n-1 \xrightarrow{n} n \xrightarrow{n+1} n+1 \dots
 \end{array}
 \quad (3)$$

where the index that labels states, $n = 0, 1, \dots$, ranges over all possible numbers of calcium ions in the subspace and the constant $\bar{\alpha}$ is proportional to the subspace volume, that is,

$$\bar{\alpha} = \nu \alpha \beta c. \quad (4)$$

2.1.2. Master Equation and Steady-State Probability Distribution. If we write $p_n(t) = \Pr\{C(t) = n\}$, the equations for the dynamics of the probability of each state in (3), that is, the chemical master equation for the number of calcium ions in the subspace, is given by

$$\begin{aligned}
 \frac{dp_0}{dt} &= \bar{\alpha} p_0 - \beta p_1, \\
 \frac{dp_n}{dt} &= \bar{\alpha} n \beta p_{n-1} - \bar{\alpha} p_{n+1} - n \beta p_n, \quad n = 1, 2, \dots
 \end{aligned}
 \quad (5)$$

Note that the correspondence between the rate constants in the deterministic (1) and stochastic (3)–(5) models is established by substituting $c = c \nu$ in (1) to find the rate of change of the number of calcium ions in the deterministic model, that is,

$$\frac{dc}{dt} = \bar{\alpha} - \beta c. \quad (6)$$

This equation indicates that c increases at rate $\bar{\alpha}$ (due to influx and diffusion from the bulk), a value that is independent of the number of calcium ions in the subspace. At the same time, c decreases at rate βc , a value that is proportional to c because each ion has an opportunity to diffuse into the bulk. Consequently, the transition rates leading out of state $C = n$ in the stochastic model are given by $\bar{\alpha}$ for the $C = n$ to $n + 1$ transitions and βn for the $C = n$ to $n - 1$ transitions.

To find the steady-state probability distribution of C , we set the left hand sides of (5) to zero to obtain

$$n \beta p_n = \bar{\alpha} p_{n-1}, \quad n = 1, 2, \dots \quad (7)$$

from which it follows that p_n is a Poisson distribution with parameter $\lambda = \bar{\alpha} / \beta$, that is,

$$p_n = e^{-\lambda} \frac{\lambda^n}{n!}. \quad (8)$$

2.1.3. Analysis of Concentration Fluctuations. To see how the subspace calcium concentration fluctuations predicted by this minimal model depend on the parameters α, β, c , and ν , recall that the mean and variance of the Poisson distribution (8) is equal to the parameter λ and, consequently, the

steady-state expected number of calcium ions in the subspace is given by

$$E\{C\} = \sum_{n=0}^{\infty} n p_n = \lambda = \frac{\bar{\alpha}}{\beta} = \nu \frac{\alpha}{\beta} c = \nu c, \quad (9)$$

where the last equality defines c as follows:

$$c = \frac{\alpha}{\beta} c. \quad (10)$$

Using (9) and the fact that $C = C \nu$ implies $E\{C\} = E\{C\} \nu$, we can identify c as the expected subspace calcium concentration:

$$E\{C\} = c. \quad (11)$$

Similarly, the steady-state variance of the number of calcium ions in the subspace is

$$\text{Var}\{C\} = \sum_{n=0}^{\infty} n^2 p_n - \nu c^2, \quad (12)$$

and $\text{Var}\{C\} = \text{Var}\{C\} \nu^2$ implies that the variance of the subspace calcium concentration is

$$\text{Var}\{C\} = \frac{c}{\nu}. \quad (13)$$

Note that the coefficient of variation of C and C are identical and inversely proportional to subspace volume, that is, $\text{CV}\{C\} = \frac{\text{Var}\{C\}^{1/2}}{E\{C\}} = \frac{1}{\sqrt{\nu c}}$ and, similarly,

$$\text{CV}\{C\} = \frac{\sqrt{\text{Var}\{C\}}}{E\{C\}} = \frac{\sqrt{\text{Var}\{C\} \nu^2}}{E\{C\} \nu} = \frac{1}{\sqrt{\nu c}}. \quad (14)$$

This is a well-known principle from statistical physics: fluctuation amplitudes scale with the reciprocal of the square root of system size (the subspace volume ν).

Figure 2 illustrates fluctuation amplitudes in the minimal subspace model by plotting the steady-state probability distribution of C and C (left and right columns, resp.). In the first row, using subspace volume of $\nu = \nu_0 = 10^{17}$ liters and influx rate of $\alpha = 0.049 \mu\text{M}/\text{ms}$, the expected calcium concentration is $E\{C\} = c = \frac{\alpha}{\beta} c = 5 \mu\text{M}$, and the expected number of subspace calcium ions is $E\{C\} = \nu_0 c = 30$. In both cases the coefficient of variation is $1/\sqrt{30} = 0.18$ (the spread of the distributions as illustrated is due to the different x -axis scales). The following rows of Figure 2 show that in a subspace three or ten times larger ($\nu = 3\nu_0$ or $10\nu_0$), the coefficient of variation drops to 0.11 and 0.058, respectively, when the calcium influx rate is scaled to result in the same expected calcium concentration (c fixed, see (14)). As might be expected, concentration fluctuations in the stochastic model are more pronounced for small volumes and become negligible for large volumes, because $\text{CV}\{C\} = 1/\sqrt{\nu c} \rightarrow 0$ as $\nu \rightarrow \infty$ for fixed c .

Most importantly, the deterministic and stochastic descriptions of this minimal subspace model agree in the

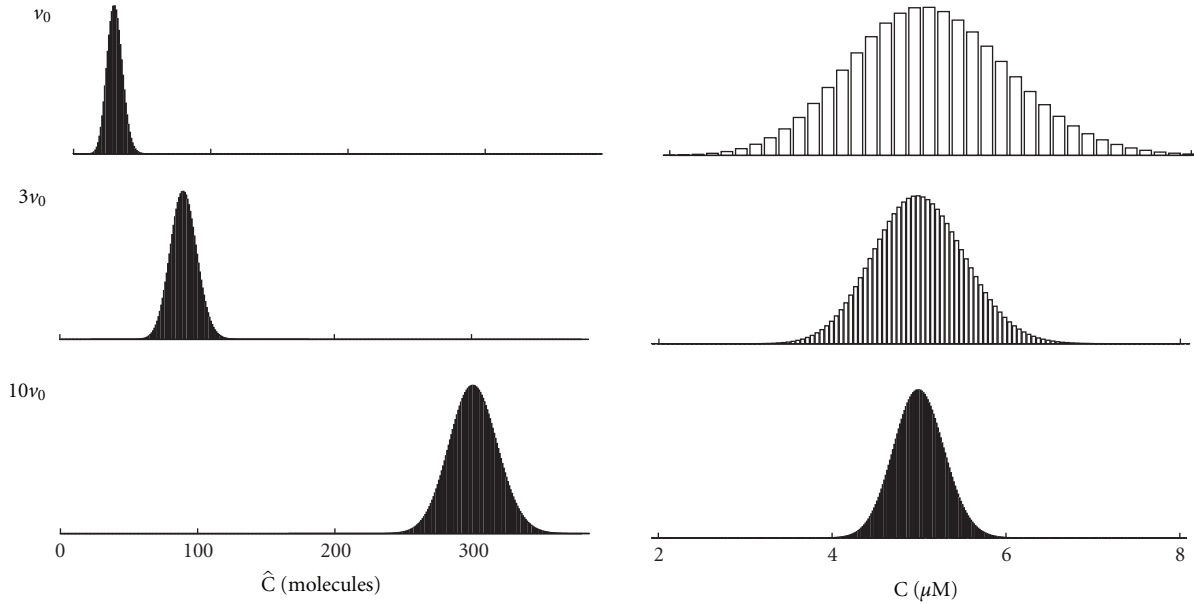


FIGURE 2: Steady-state probability distribution of the number of calcium ions (C , left column) and subspace calcium concentration (C , right column) for subspace volume of $v_0 = 10^{-17}$ liters and subspaces that are 3 and 10 times larger. Parameters: $\alpha = 0.049 \mu\text{M}/\text{ms}$, $\beta = 0.01 \text{ms}^{-1}$, $c = 0.1 \mu\text{M}$; the steady-state expected subspace calcium concentration is $E C = c = 5 \mu\text{M}$.

following sense: the expected value of the fluctuating calcium concentration in the stochastic model $E C = c = \frac{\alpha \beta}{\alpha + \beta}$ is equal to the steady-state of the deterministic ODE that neglects concentration fluctuations (found by setting the left hand side of (1) to zero). Readers familiar with fluctuations in biochemical models will understand that this agreement is a consequence of the fact that the minimal subspace model involves three elementary reactions, all of which are zeroth or first order (see arrows in Figure 1).

2.1.4. Moment Calculation. The numerical results presented above can be obtained analytically by considering the dynamics of the moments of the number of calcium ions in the subspace, defined as

$$\mu_q = \sum_{n=0}^{\infty} n^q p_n. \quad (15)$$

By conservation of probability, the zeroth moment $\mu_0 = 1$ and the first moment is the expected number of calcium ions in the subspace (9),

$$\mu_1 = E C. \quad (16)$$

The second moment μ_2 is related to the variance of the number of calcium ions via

$$\text{Var } C = \mu_2 - \mu_1^2. \quad (17)$$

By differentiating (15) with respect to time and substituting for the time derivatives using the master equation (5), it can

be shown that the zeroth moment is constant ($d\mu_0/dt = 0$) and, furthermore,

$$\frac{d\mu_1}{dt} = \bar{\alpha} - \beta\mu_1, \quad (18)$$

$$\frac{d\mu_2}{dt} = \bar{\alpha} - 2\bar{\alpha} - \beta\mu_1 - 2\beta\mu_2,$$

where we have used $\mu_0 = 1$. Setting the left hand sides of these equations to zero, we see that steady-state first and second moment are $\mu_1 = \bar{\alpha} / \beta$ and $\mu_2 = \bar{\alpha} / \beta + \bar{\alpha} / \beta^2$, consistent with (11) and (17).

2.2. Stochastic Subspace Model with Calcium Regulation.

This section augments the subspace model presented above to include calcium regulation of a calcium channel (see Figure 3). We assume that calcium binding instantaneously modifies the conductance of the channel, that is, the rate of calcium influx into the domain is α_0 when the channel is calcium-free and α_1 when the channel is calcium-bound. We further assume the channel has two binding sites for calcium and, for simplicity, approximate rapid sequential binding of calcium ions with instantaneous binding. Thus, the transitions between the two distinct states of the subspace (the so-called ‘‘stochastic functional unit’’ or ‘‘calcium release unit’’) occur at rates $k c^2$ and k , respectively, (Figure 3, curved arrows). Note that the rate constant k has units of ms^{-1} , $k c^2$ has units of $\mu\text{M}^{-2} \text{ms}^{-1}$, and the dissociation constant for calcium binding, denoted by κ , has units of μM and is given by $\kappa^2 = k / k$.

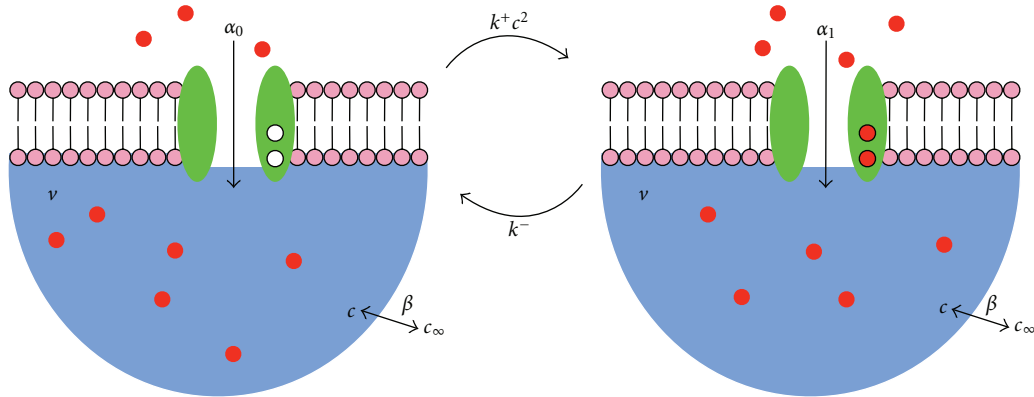


FIGURE 3: Diagram of the components and fluxes in a subspace model that includes calcium-regulated calcium influx. A single calcium channel (with two calcium binding sites) is associated with a subspace of volume v . The calcium influx rate is α_0 and α_1 when calcium is unbound and bound, respectively, and the transition rates between these states are $k^+ c^2$ and k^- , where c is the subspace calcium concentration. Subspace calcium is passively coupled at rate β to the bulk cytosol with constant concentration c_∞ .

2.2.1. *Stochastic Model.* Let us denote the states of the stochastic system by $(n, 0)$ and $(n, 1)$, where $n = 0, 1, \dots$, and the second element of the ordered pairs, either 0 or 1, indicates calcium-free and bound channel, respectively.

With a little thought we can sketch the following state-transition diagram for the stochastic subspace model with calcium influx,

$$\begin{array}{ccccccc}
 0, 0 & \xrightarrow{\bar{\alpha}_0} & 1, 0 & \xrightarrow{\bar{\alpha}_0} & 2, 0 & \xrightarrow{\bar{\alpha}_0} & 3, 0 & \xrightarrow{\bar{\alpha}_0} & 4, 0 \\
 & \searrow \beta & & \searrow 2\beta & & \searrow 3\beta & & \searrow 4\beta & \\
 & & & & \xrightarrow{2\bar{k}} & \xrightarrow{k} & \xrightarrow{6\bar{k}} & \xrightarrow{k} & \xrightarrow{12\bar{k}} & \xrightarrow{k} \\
 & & & & 0, 1 & & 1, 1 & & 2, 1 & \\
 & & & & & \searrow \beta & & \searrow 2\beta & & \\
 & & & & & & & & & &
 \end{array} \quad , \quad (19)$$

where $\bar{k} = k v^2$. The rate of calcium binding to the channel in the stochastic model is inversely proportional to the square of the volume, because of the concentration dependence of the association reaction ($k c^2 = k c^2 v^2$). The downward transitions between states $(n, 0)$ and $(n - 2, 1)$ include the combinatorial coefficient, $\binom{n}{2} = \frac{n(n-1)}{2}$, double the number of ways that two indistinguishable calcium ions can be chosen from the n ions in the subspace. This factor of two is required so that the microscopic propensity \bar{k} agrees with the macroscopic rate $k c^2$ for large n and v with $c = n/v$ fixed, that is,

$$\binom{n}{2} \bar{k} = \binom{n}{2} \frac{k}{v^2} = k c^2 \frac{c}{v}, \quad (20)$$

an expression that approaches $k c^2$ as $v \rightarrow \infty$ [28].

2.2.2. *Master Equation.* Let us write $p_n^0(t)$ to indicate the probability that at time t the channel is calcium-free and $C = n$. Similarly, $p_n^1(t)$ is the probability that $C = n$ and the channel is calcium bound. Reading off the transition rates from the state-transition diagram (19), we write the

following master equation for the calcium-regulated channel and subspace:

$$\begin{aligned}
 \frac{dp_n^0}{dt} &= \bar{\alpha}_0 p_{n-1}^0 - n\beta p_n^0 - \binom{n}{2} \bar{k} p_n^0 + \bar{\alpha}_1 p_{n-1}^1 + \binom{n-1}{2} \beta p_{n-1}^0 - k p_{n-2}^1, \\
 \frac{dp_n^1}{dt} &= \bar{\alpha}_1 p_{n-1}^1 - n\beta p_n^1 - k p_n^1 + \bar{\alpha}_0 p_{n-1}^0 + \binom{n-1}{2} \beta p_{n-1}^1 - \binom{n-2}{2} \bar{k} p_{n-2}^0.
 \end{aligned} \quad (21)$$

Similar to the approach described in the previous section, we define the moments of the number of calcium ions in the subspace *jointly distributed with the state of the channel*, as follows:

$$\mu_q^{0,1} = \sum_{n=0}^{\infty} n^q p_n^{0,1}, \quad (22)$$

where the superscript 0, 1 indicates either index occurring on both the left and right hand sides of the equality. Note

that the zeroth moments sum to unity by conservation of probability ($\mu_0^0 + \mu_0^1 = 1$). The expected number of calcium ions in the subspace *conditioned on the channel being calcium free or bound*, respectively, is given by

$$E^{0,1} C = \frac{\sum_{n=0}^{\infty} n p_n^{0,1}}{\sum_{n=0}^{\infty} p_n^{0,1}} = \frac{\mu_1^{0,1}}{\mu_0^{0,1}}. \quad (23)$$

Similarly the second moments $\mu_2^{0,1}$ are related to the conditional variances via

$$\text{Var}^{0,1} C = \frac{\mu_2^{0,1}}{\mu_0^{0,1}} - \left(\frac{\mu_1^{0,1}}{\mu_0^{0,1}} \right)^2. \quad (24)$$

2.2.3. Moment Calculation. By differentiating (22) with respect to time and substituting for the time derivatives using (21), it can be shown that the time-derivatives of the zeroth-moments, μ_0^0 and μ_0^1 —that is, the probability of the channel being in the calcium free or bound state—are given by

$$\frac{d\mu_0^0}{dt} = \bar{k} \mu_2^0 - \bar{k} \mu_1^0 - k \mu_0^1, \quad (25)$$

$$\frac{d\mu_0^1}{dt} = \bar{k} \mu_2^1 - \bar{k} \mu_1^1 - k \mu_0^0, \quad (26)$$

where we note that $d\mu_0^0/dt + d\mu_0^1/dt = 0$ and $\mu_0^0 + \mu_0^1 = 1$. In the same way, the equations for the first moments, μ_1^0 and μ_1^1 , are found to be

$$\frac{d\mu_1^0}{dt} = \bar{\alpha}_0 \mu_0^0 - \beta \mu_1^0 - \bar{k} \mu_3^0 - \bar{k} \mu_2^0 - k \mu_1^1 - 2k \mu_0^1, \quad (27)$$

$$\frac{d\mu_1^1}{dt} = \bar{\alpha}_1 \mu_0^1 - \beta \mu_1^1 - \bar{k} \mu_3^1 - 3\bar{k} \mu_2^1 - 2\bar{k} \mu_1^0 - k \mu_1^0.$$

Setting the left hand side of (25) to zero, we find that the steady-state probability of a calcium-bound channel is

$$\mu_0^1 = \frac{\mu_2^0 \mu_1^0}{\kappa^2 \nu^2} = \frac{E^0 C^2}{\kappa^2} \frac{E^0 C}{E^0 C + \nu}, \quad (28)$$

where in the second equality we have used $\mu_2^0 = \mu_0^0 E^0 C^2 / \mu_0^0 \nu^2 E^0 C^2$.

Note that as the volume increases ($\nu \rightarrow \infty$), $E^0 C / \nu$ becomes negligible compared to $E^0 C^2$, while $E^0 C^2 / \nu$ becomes negligible as the conditional variance goes to zero ($\text{Var}^{0,1} C \rightarrow 0$). Thus, in the large system limit, the probability that the channel is in the calcium-bound state is given by

$$\mu_0^1 = \frac{E^0 C}{\kappa^2} \frac{E^0 C}{E^0 C + \nu}. \quad (29)$$

In the case of a calcium-activated channel, μ_0^1 is the open probability.

2.2.4. Analysis of Concentration Fluctuations. The moment analysis in the previous section suggests that the expected calcium concentration in the subspace given by

$$E C = \mu_0^0 E^0 C + \mu_0^1 E^1 C \quad (30)$$

and the probability that a calcium-activated channel is open, $p_{\text{open}} = \mu_0^1$, may depend on the subspace volume. In order to analyze the effect of small system size and concentration fluctuations at steady-state, we integrated (21) and determined the probability distributions $p_n^{0,1}$ for various model parameters.

Figures 4(a) and 4(b) show the probability distribution for $\nu = \nu_0$ and $8\nu_0$ using a representative set of parameters (see caption). In these calculations, the channel is closed when calcium-free and open when calcium-bound, that is,

$$\bar{\alpha}_0 = \nu\beta c, \quad \nu\beta c = \nu\alpha + \beta c, \quad \bar{\alpha}_1 = \alpha. \quad (31)$$

For this reason, Figures 4(a) and 4(b) show a conditional expectation for the calcium concentration (vertical dotted lines) that is greater when the channel is calcium bound ($E^1 C = E^0 C$). Note that the eight-fold increase in system size leads to a significant increase in the channel open probability, that is, $p_{\text{open}} = \mu_0^1 = 0.23$ and 0.78 for $\nu = \nu_0$ and $8\nu_0$, respectively. Thus, the open probability of the channel is significantly influenced by the subspace volume, in spite of the fact that the calcium influx rate is scaled so that in the absence of calcium-regulation there is no effect of volume (α constant, as in Section 2.1). Comparison of Figures 4(a) and 4(b) also shows a qualitative change in the probability distribution of the subspace calcium concentration (unimodal when $\nu = \nu_0$, bimodal when $\nu = 8\nu_0$).

Figure 4(c) shows the expected calcium concentration $E C$ (30) and open probability ($p_{\text{open}} = \mu_0^1$) for the calcium-activated channel as a function of subspace volume ν and different rate constants for calcium binding k (fixed dissociation constant κ). Both $E C$ and p_{open} increase with subspace volume ν , that is, the restricted volume of a physiological subspace leads to an open probability and expected calcium concentration that is less than predicted in the corresponding (approximate) continuous description.

Both the open probability and expected calcium concentration asymptotically approach values in a range that are easily precalculated. For example, $E C$ and p_{open} must be greater than the values obtained by assuming channel gating is extremely slow, in which case $E C = c$ and $p_{\text{open}} = c^2 / \kappa^2 + c^2$, because the transition from the calcium-free to -bound channel usually occurs with a subspace that is equilibrated with bulk calcium. In addition, $E C$ and p_{open} are always less than the values obtained under the assumption of rapid channel binding, values given by simultaneous solution of $p_{\text{open}} = c^2 / \kappa^2 + c^2$ and $c / p_{\text{open}} = \alpha + \beta c$. These fast and slow system limits are indicated in Figure 4(c) by red and blue horizontal lines, respectively.

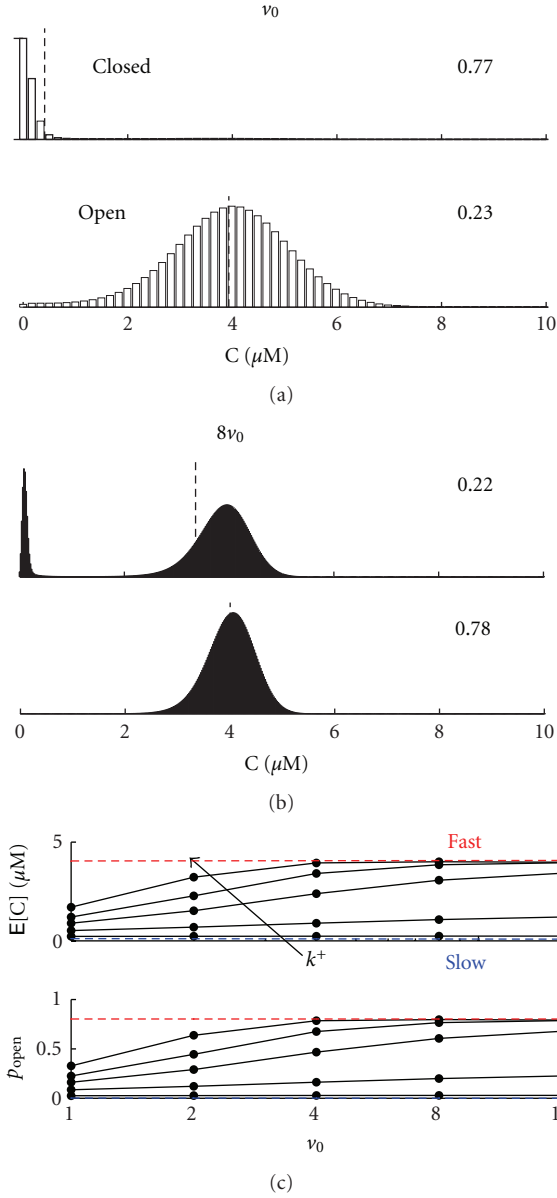


FIGURE 4: Subspace volume-dependence of calcium fluctuations and open probability of a calcium-activated channel. Steady-state probability distribution for $v = v_0$ (a) and $8v_0$ (b) for the calcium-activated channel ($\kappa = 2 \mu\text{M}$, $k = 0.05 \mu\text{M}^{-2} \text{ms}^{-1}$) [29, 30]. (c) Steady-state $E[C]$ and $P_{\text{open}} = \mu_0^1$ for integer multiples of the unitary volume v_0 and different rate constants for calcium binding k (0.005 to $0.15 \mu\text{M}^{-2} \text{ms}^{-1}$) with κ fixed.

In order to further characterize the effect of subspace volume on the calcium-regulated channel and subspace dynamics, we defined the small system deviation Δ as

$$\Delta = \frac{E[C]_{v_0} - E[C]_{\infty}}{E[C]_{\infty}}, \quad (32)$$

where $E[C]_{v_0}$ is calculated using a system volume of $v = v_0$ and $E[C]_{\infty}$ is the same quantity calculated in the large system size limit ($v \rightarrow \infty$, numerically estimated using $v = 10v_0$).

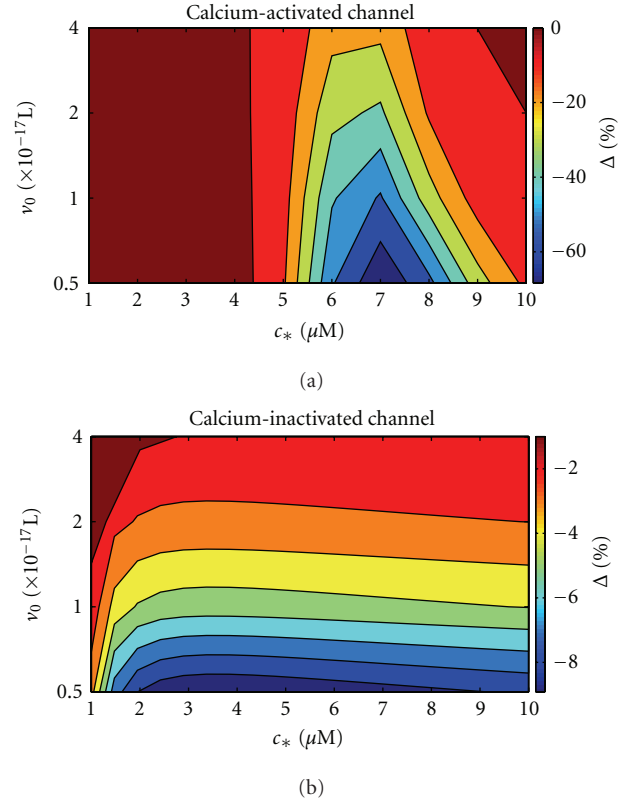


FIGURE 5: Percentage small system deviation (Δ , (32)) as a function of unitary subspace volume v_0 and influx parameter c for a single calcium-activated channel ($\kappa = 2 \mu\text{M}$, $k = 0.005 \mu\text{M}^{-2} \text{ms}^{-1}$) and calcium-inactivated channel ($\kappa = 0.63 \mu\text{M}$, $k = 0.05 \mu\text{M}^{-2} \text{ms}^{-1}$).

Figure 5 shows the small system deviation as a function of unitary subspace volume v_0 and influx parameter c for a calcium-activated channel. In all cases, Δ was negative, meaning that $E[C]$ for $v = v_0$ was suppressed below the large system size limit and increased with volume (cf. Figure 4(c)). For small c , Δ was near zero. For intermediate values of c (5–10 μM), the suppression was quite large ($\Delta \approx -60\%$). As v_0 increased, Δ becomes less negative and approaches zero. In general, as c increased above this range, the suppression ultimately becomes negligible.

For comparison, Figure 5(b) shows the small system deviation for a calcium-inactivated channel. In general, the magnitude of Δ for the calcium-inactivated channel was smaller than the calcium-activated channel. For small c (1–3 μM), the magnitude of Δ increased with c , while above this range Δ was essentially independent of c . As with the calcium-activated channel, the magnitude of Δ decreased and approached zero as v_0 increased.

2.3. Calcium Regulation of Multiple Channels. The previous section analyzed the effect of subspace volume when the influx pathway involves calcium regulation of a single channel. In this section, we assume that the total number of channels increases with subspace volume (see Figure 6). As before, we assume that calcium binding instantaneously

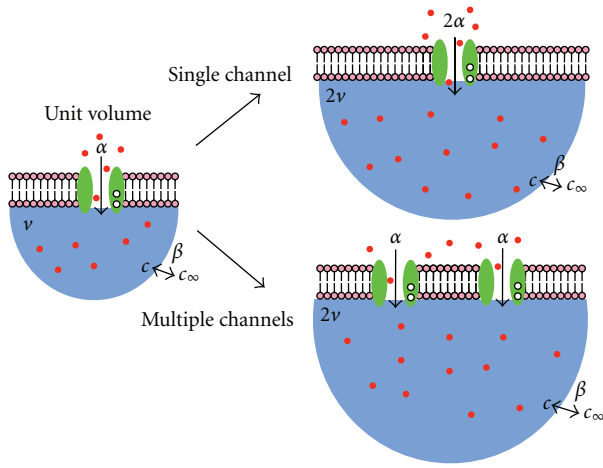


FIGURE 6: Illustration of two possible volume scalings. For the single channel volume scaling, calcium influx α increases proportional to the increase in v , but the single channel has only two conductance levels, α_0 and α_1 , depending on whether calcium is free or bound. In the alternative scaling, the number of channels increases in proportion to the volume v , and when there are many channels the calcium influx rate may take many values between α_0 and α_1 .

modifies the calcium channel conductance, that is, the rate of calcium influx into the domain is determined by α_0 when all channels are calcium-free and α_1 when all channels are calcium-bound.

2.3.1. Deterministic Model. Assuming as before that two free calcium ions C bind to channel B to form the complex C_2B , we can write the following kinetic scheme:



The deterministic ODE system that applies in the case of a large subspace volume is

$$\begin{aligned} \frac{dc}{dt} &= \alpha_0 \frac{b}{b_t} - \alpha_1 \frac{b_t - b}{b_t} - \beta c + c - k c^2 b + k b_t b, \\ \frac{db}{dt} &= k c^2 b - k b_t b, \end{aligned} \quad (34)$$

where we have written $c = C$ and $b = B$. Because the total (calcium-free plus-bound) concentration of channels, $b_t = B + C_2B$, is a constant determined by initial conditions, we have eliminated the equation for C_2B . At steady-state the channels will be in equilibrium with subspace calcium, that is, $b/b_t = \kappa^2 c^2 / c^2$. Thus, in the case of a calcium-activated channel $\alpha_0 = 0, \alpha_1 = 0$, the steady-state calcium concentration satisfies

$$0 = \alpha_1 \frac{c^2}{\kappa^2 c^2} - \beta c + c, \quad (35)$$

while in the case of a calcium-inactivated channel ($\alpha_0 = 0, \alpha_1 = 0$),

$$0 = \alpha_0 \frac{\kappa^2}{\kappa^2 c^2} - \beta c + c. \quad (36)$$

Figure 7 shows bifurcation diagrams for the steady-state calcium concentration in both cases. For the calcium-activated channel there is a range of κ that leads to bistability (Figure 7(a)), while no bistable regime exists for a calcium-inactivated channel (Figure 7(b)).

2.3.2. Stochastic Model. Following the notation developed in the previous section, we write $p_n^m = P(C=n, C_2B=m, t)$. $P(C=n, B=b_t-m)$ for $n=0, 1, \dots$, and $m=0, 1, \dots, b_t$ and, where b_t is the total number of channels (for integer ℓ , $b_t = \ell$ when $v = \ell v_0$). The state-transition diagram for the Markov process (not shown) is analogous to (19) but with $b_t = 1$ rows as opposed to two. The master equation for the dynamics of the calcium channel and subspace calcium concentration is

$$\begin{aligned} \frac{d p_n^m}{dt} &= \bar{\alpha}_m - n\beta - mk - n(n-1)b_t m \bar{k} p_n^m \\ \bar{\alpha}_m p_{n-1}^m &= (n-1)\beta p_n^{m-1} \\ m-1 &= k p_n^{m-1} \\ n-2 &= n-1 b_t m \bar{k} p_n^{m-1}, \end{aligned} \quad (37)$$

where $\bar{\alpha}_m = v \alpha_m - \beta c$ and

$$\alpha_m = \alpha_0 \frac{b_t - m}{b_t} + \alpha_1 \frac{m}{b_t}. \quad (38)$$

In (38), it is understood that terms in the master equation involving negative indices (i.e., n or $m = 0$) evaluate to zero.

2.3.3. Concentration Fluctuations. Figure 8(A) shows the steady-state probability distribution for $v = v_0, 2v_0$ and $4v_0$ for a calcium-activated channel with dissociation constant chosen so that the deterministic system is monostable ($\kappa = 0.45 \mu M$). For $v = v_0$, there is one channel and two channel states (closed and open). For the closed channel, the distribution of calcium concentration is Poisson-like with conditional mean near c , while for the open channel, the conditional mean is near c . For $v = 2v_0$ and $4v_0$, there are two or four channels and thus three or five system states, each corresponding to a particular number of free versus bound channels (38). While the conditional expectation of the calcium concentration is always between c and c , these distributions deviate from Poisson.

Figure 8(B)a shows $E[C]$ and p_{open} for subspace volumes v given by different discrete multiples of the unitary volume v_0 . Using parameters that lead to a monostable deterministic ODE system, we find, similar to the case of the single channel (Figure 4), a significant deviation between the

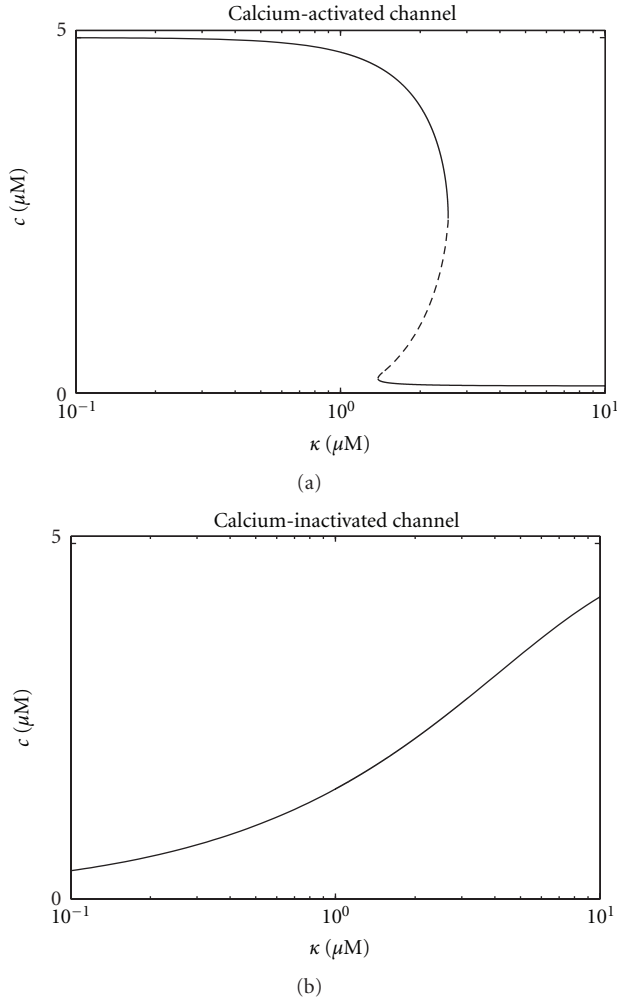


FIGURE 7: Bifurcation diagram showing the steady-state calcium concentration c as a function of dissociation constant κ in the deterministic ODE model for a subspace containing multiple calcium-activated (a) and calcium-inactivated (b) channels. Other parameters as in Figure 2.

expected calcium concentration and open probability for a small subspace as compared to the large system limit (35). As expected, both $E C$ and p_{open} approached the fast/large system limit as ν increased. This also occurs for fixed ν with increasing k , that is, the rate constant for calcium binding. For fixed κ , smaller values of k can cause Δ to approach 100%, that is, the small volume associated with a diadic subspace can almost completely suppress the open probability of a calcium-activated channel. When parameters are chosen so that the deterministic ODE system is bistable, the dependence of $E C$ and p_{open} is more complex (Figure 8(B)b). Interestingly, the small system deviation in this case is often a biphasic function of system volume.

Figure 9 shows analogous results for calcium-inactivated calcium influx. As with the calcium-activated channel, $E C$ and p_{open} were suppressed below the fast/large system limit (Figure 9(B)). Δ is often negative, but became negligible as

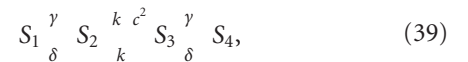
k increased. Similarly, as ν increased, both $E C$ and p_{open} approached the fast/large system limit.

Figure 10 summarizes the dependence of the small system deviation (Δ , (32)) on the unitary subspace volume (ν_0) and calcium influx parameter (c) for the scaling that involves multiple calcium-activated and -inactivated channels. In all cases, Δ was negative, meaning that $E C$ was suppressed compared with the large system values predicted by the deterministic ODE model. Up to 80% suppression was observed for the calcium-activated channel, but for the calcium-inactivated channel the maximum suppression was 20%. In both cases, the largest suppression (most negative Δ) occurs when p_{open} is small (i.e., small c for the calcium-activated channel and large c for the calcium-inactivated channel). In general, as the unitary volume ν_0 is increased, there is less suppression compared to the large system size limit.

2.4. The Effect of Domain Size in a Model of Calmodulin-Mediated Channel Regulation. In the previous sections, we demonstrated that the expected steady-state subspace concentration determined using a minimal model of a calcium-activated or -inactivated channel was volume-dependent and could greatly differ from the steady-state concentration computed from deterministic ODEs. In this section, we show similar results for a state-of-the-art model of calmodulin-mediated calcium regulation.

Both the N-lobe and C-lobe of calmodulin have two binding sites for calcium. Depending on the calcium channel type (L, N, or P/Q), calcium binding to the C-lobe has been shown to be responsible for either activation or inactivation of the channel, while N-lobe binding appears to be primarily responsible for channel inactivation [32]. Yue and colleagues demonstrated that the C-lobe responds primarily to the local subspace calcium concentration, while the N-lobe responds to the global or bulk concentration [31]. Tadross et al. developed a 4-state model for calmodulin regulation of the calcium channel (see Figure 11(A)) that includes states for the calmodulin regulator lobe (either the C-lobe or N-lobe) bound to a preassociation site that does not alter channel activity (state 1), unbound (state 2), bound to two calcium ions (state 3), or bound to two calcium ions and an effector site that does alter channel activity (state 4) [31]. Tadross et al. demonstrated that depending on the model parameters, in particular the ratio of the transition rates between states, the calmodulin regulation was sensitive to either local or global calcium levels.

Using this published model as a starting point, we formulated the corresponding discrete Markov model. The elementary reactions for calmodulin-mediated regulation of the channel are



where states S_1 and S_2 are calcium-free, states S_3 and S_4 are calcium-bound, and state S_4 determines the fraction of channels activated (or inactivated) by calmodulin. When it is assumed that a single calmodulin molecule is colocalized

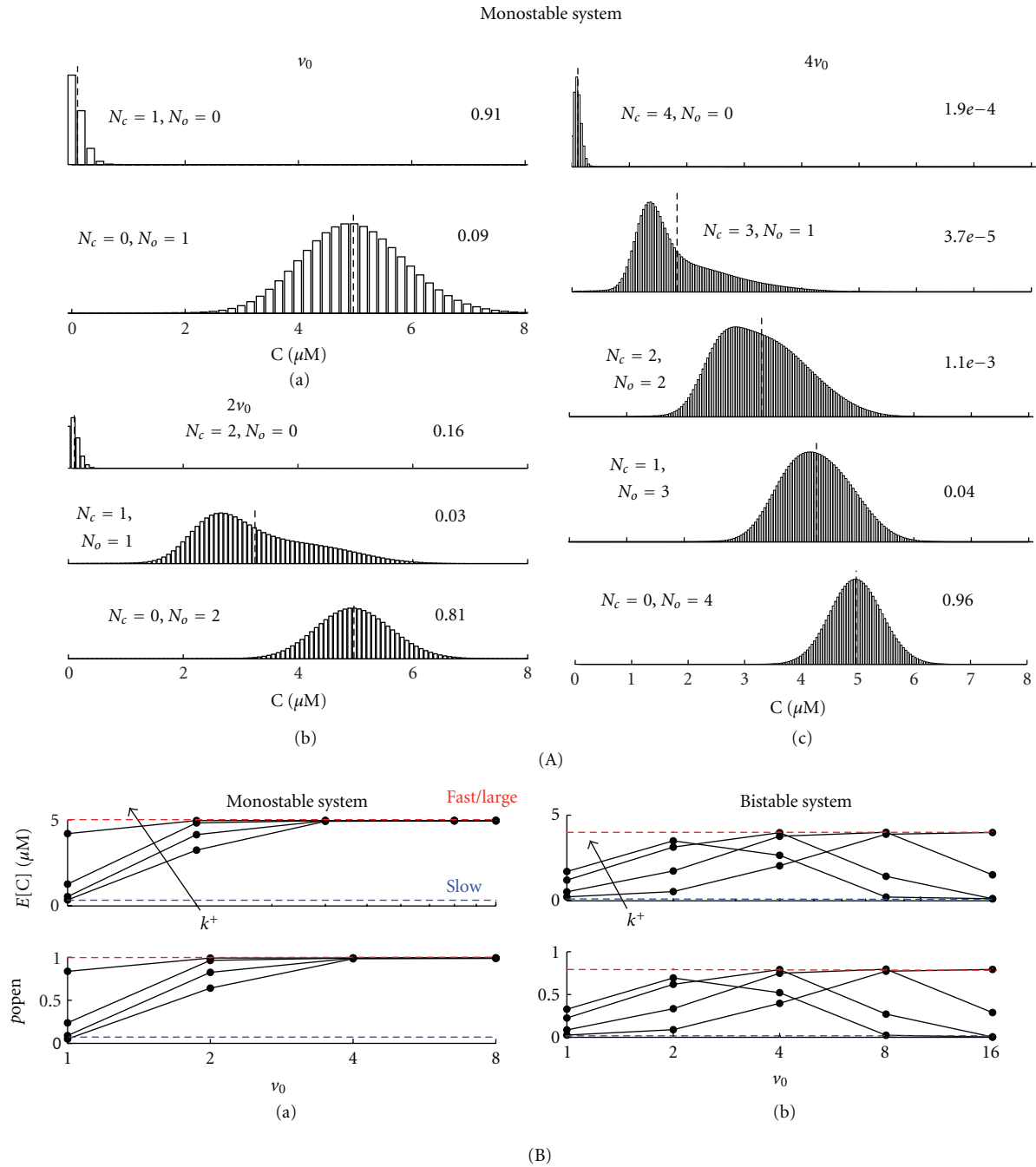


FIGURE 8: Subspace volume-dependence of concentration fluctuation and channel open probability for multiple calcium-activated channels. (A) Steady-state probability distribution for $\nu = \nu_0$ (a), $2\nu_0$ (b), and $4\nu_0$ (c) ($\kappa = 0.45 \mu\text{M}$, $k = 5 \cdot 10^{-4} \mu\text{M}^{-2} \text{ms}^{-1}$). For each panel, the dashed black line denotes the conditional expected concentration ($E^m C$). The steady-state probability distribution is shown for each possible number of closed (N_C) and open (N_O) channels. (B) (a) Steady-state $E[C]$ and p_{open} for the monostable system as a function of ν for rate constants of calcium binding ($k = 5 \cdot 10^5$ to $5 \cdot 10^3 \mu\text{M}^{-2} \text{ms}^{-1}$). The fast/large and slow system limits are shown in red and blue, respectively. (b) Steady-state $E[C]$ and p_{open} for the bistable system ($\kappa = 2 \mu\text{M}$) as a function of ν using $k = 0.005$ to $0.015 \mu\text{M}^{-2} \text{ms}^{-1}$. In the bistable system, the larger of the two stable equilibrium (large system limit) is shown in red. The smaller equilibrium is approximately equal to the slow system limit (shown in blue).

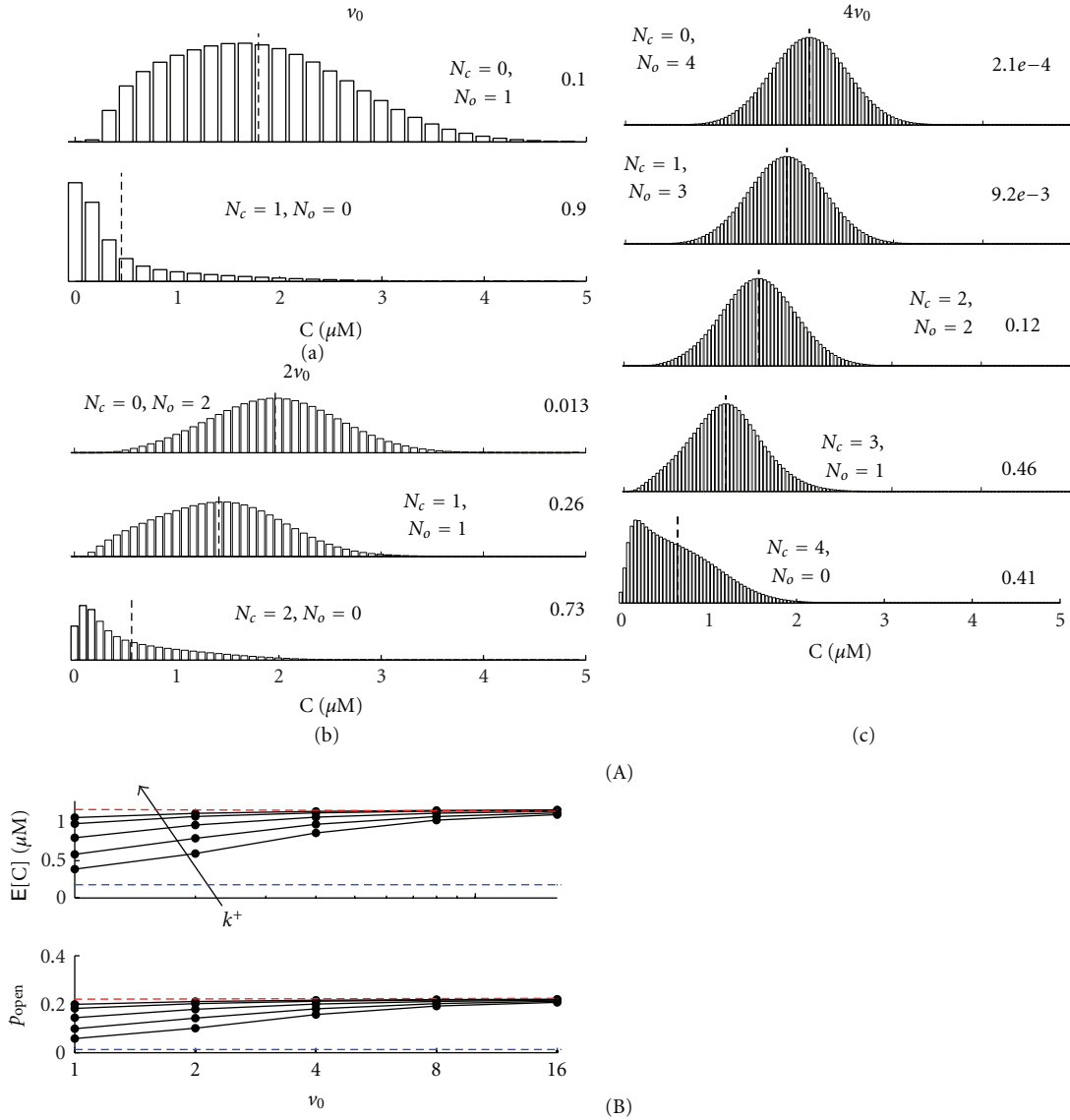


FIGURE 9: Subspace volume-dependence of concentration fluctuation and channel open probability for multiple calcium-inactivated channels. (A) Steady-state probability distribution for $\nu =$ (a) ν_0 , (b) $2\nu_0$, and (c) $4\nu_0$ ($\kappa = 0.63 \mu\text{M}$, $k = 0.005 \mu\text{M}^2 \text{ms}^{-1}$). (B) Steady-state $E[C]$ and p_{open} as a function of ν ($k = 0.0015$ to $0.15 \mu\text{M}^2 \text{ms}^{-1}$).

with the calcium channel (as in Section 2.2), the master equation takes the following form:

$$\begin{aligned}
 \frac{dp_n^1}{dt} &= \bar{\alpha}_0 n\beta - \gamma p_n^1 \\
 &+ \bar{\alpha}_0 p_{n-1}^1 - (n-1)\beta p_{n-1}^1 - \delta p_n^2, \\
 \frac{dp_n^2}{dt} &= \bar{\alpha}_0 n\beta - \delta n - (n-1)\bar{k} p_n^2 \\
 &+ \bar{\alpha}_0 p_{n-1}^2 - (n-1)\beta p_{n-1}^2 - \gamma p_n^1 - k p_{n-2}^3, \\
 \frac{dp_n^3}{dt} &= \bar{\alpha}_0 n\beta - \gamma k p_n^3 \\
 &+ \bar{\alpha}_0 p_{n-1}^3 - (n-1)\beta p_{n-1}^3 \\
 &+ \delta p_n^4 - (n-2)n - (n-1)\bar{k} p_{n-2}^2,
 \end{aligned}$$

$$\begin{aligned}
 \frac{dp_n^4}{dt} &= \bar{\alpha}_1 n\beta - \delta p_n^4 \\
 &+ \bar{\alpha}_1 p_{n-1}^4 - (n-1)\beta p_{n-1}^4 - \gamma p_n^3,
 \end{aligned} \tag{40}$$

where for a calmodulin-activated channel $\bar{\alpha}_0$ and $\bar{\alpha}_1$ are given by (31).

Figure 11(B) shows the steady-state probability distribution numerically calculated from these equations. Using a parameter set referred to as “slow CaM,” Tadross et al. showed that calmodulin was primarily sensitive to the local subspace calcium level (representing the C-lobe) when calcium binding to calmodulin was slow [31]. With “slow CaM” parameters, we found that calmodulin bound to the effector site (S_4) had the greatest steady-state probability. Because the

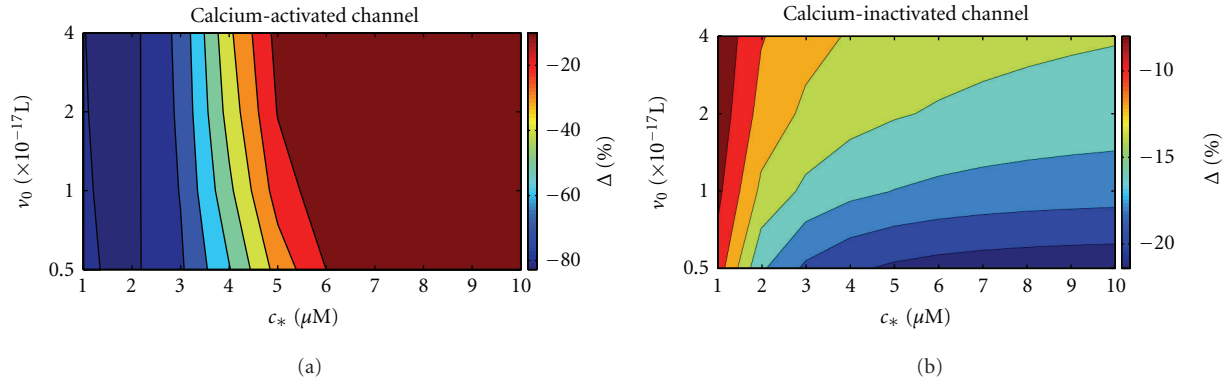


FIGURE 10: Percentage small system deviation (Δ) as a function of unitary subspace volume v_0 and influx parameter c for multiple (a) calcium-activated channels ($\kappa = 0.45 \mu\text{M}, k = 0.005 \mu\text{M}^{-2} \text{ms}^{-1}$) and (b) calcium-inactivated channels ($\kappa = 0.63 \mu\text{M}, k = 0.05 \mu\text{M}^{-2} \text{ms}^{-1}$).

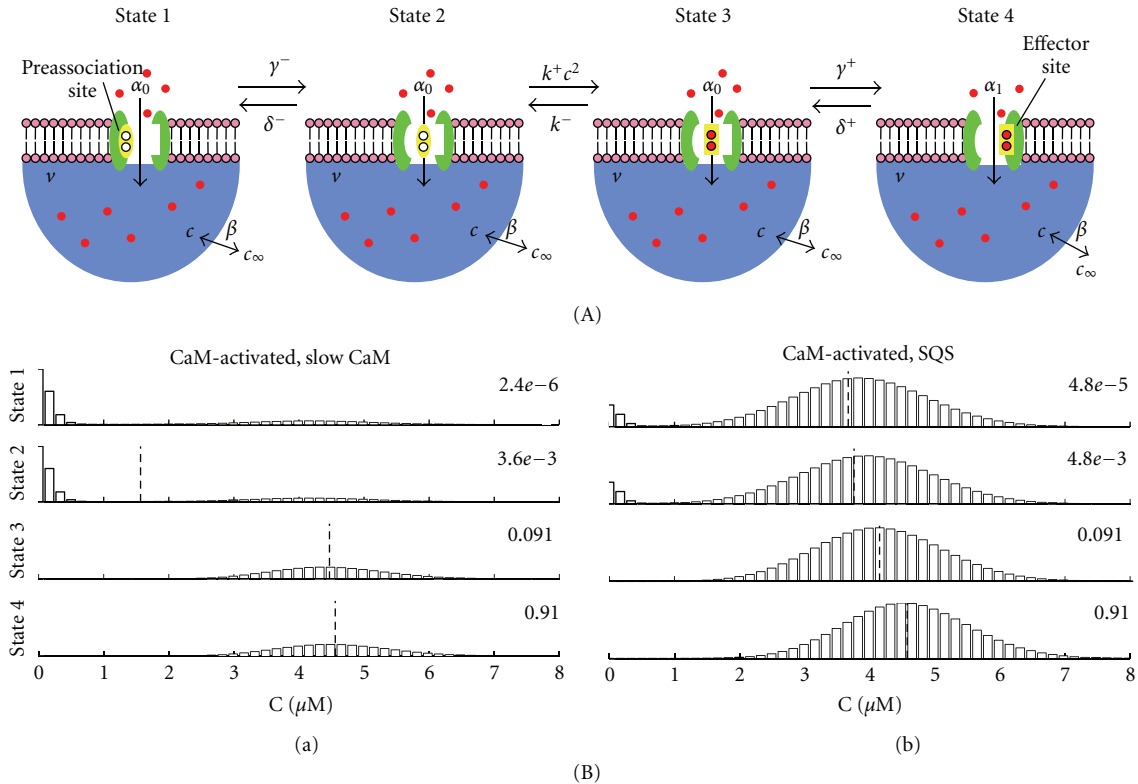


FIGURE 11: Calmodulin regulation of the calcium channel at steady-state. (A) State diagram of calmodulin regulation of a calcium channel (modified from [31]). (B) Steady-state probability distribution for the calmodulin-activated channel using (a) “slow CaM” and (b) “SQS” parameters [31].

calmodulin binding was slow, each conditional distribution had their respective largest peaks near the slow limit (c for states S_1 and S_2 , c for S_3 and S_4) (Figure 11(B)a). Using an alternate parameter set referred to as “SQS,” Tadross et al. showed that calmodulin was primarily sensitive to the global calcium level (representing the N-lobe), when calcium binding to calmodulin was fast. Similar to the slow CaM case, state S_4 had the greatest steady-state probability using the SQS parameters. Due to the fast binding kinetics, the

conditional distributions were more similar than in the slow CaM case (Figure 11(B)b). For both parameter sets, the calcium concentration distribution for the low occupancy states (S_1 and S_2) were bimodal, with peaks near c and c .

Figure 12 shows the small system size suppression Δ for both slow CaM and SQS parameter sets assuming a single calmodulin-regulated channel. As in our simplified model (Figure 5), Δ was quite large in magnitude for some conditions (up to 30% suppression). For the calmodulin-activated

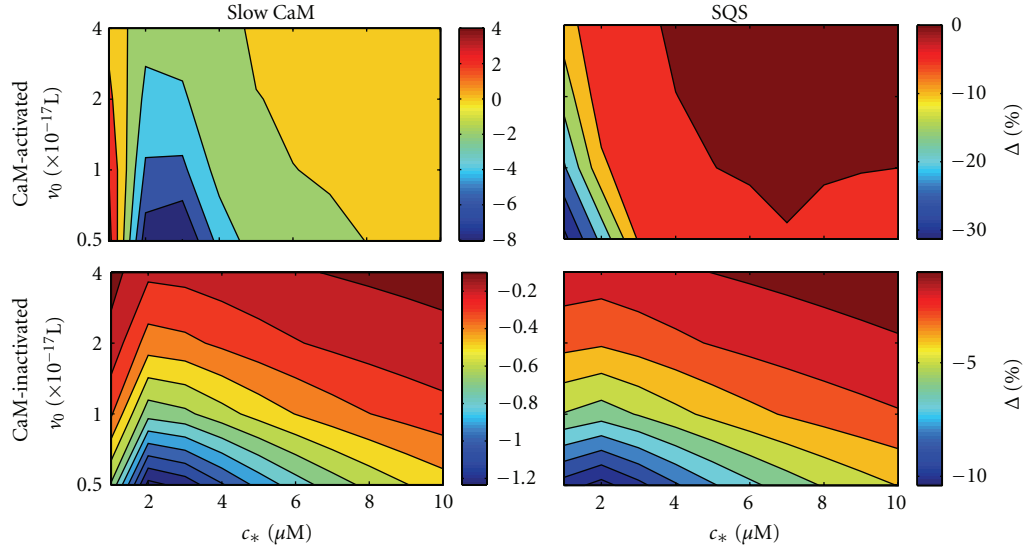


FIGURE 12: Small system deviation for a single calmodulin-activated and -inactivated channel using “slow CaM” and “SQS” parameters (see text).

channel, the dependence of Δ on v_0 and c was similar to our simplified model (cf. Figure 5(a)), decreasing in magnitude and approaching 0 as v_0 or c increased.

The parameter space for the calmodulin-inactivated channel differed somewhat from our simplified model (Figure 5(b)). For both the slow CaM and SQS parameters, Δ decreased as c or v_0 increased. Additionally, for both the calmodulin-activated and -inactivated channels, Δ had greater dependence on v_0 for the SQS parameters, which is consistent with calmodulin being more sensitive to the bulk concentration (since increasing v_0 greatly influences the number of ions entering from the bulk).

We also calculated the small system deviation Δ for the case of multiple calmodulin-regulated channels (Figure 13). For the calmodulin-activated channel, results were similar to our simplified model (Figure 10(a)), in particular Δ approached 0 as both c and v_0 increased. The magnitude of Δ was smaller for the SQS parameters compared with the slow CaM parameters, consistent with faster kinetics approaching the large system limit and calmodulin being less sensitive to the local calcium concentration. The parameter space for multiple calmodulin-inactivated channels also differed somewhat from our simplified model (Figure 10(b)). In general, the magnitude of Δ decreased as c increased. However, in contrast with the parameter space using SQS parameters, Δ was fairly insensitive to v_0 using slow CaM parameters, which is consistent with calmodulin being, in this case, less sensitive to the bulk calcium concentration.

3. Discussion

We developed a minimal model of a calcium-regulated channel in a small subspace and formulated a Markov model in which each possible discrete state is represented. For small subspace volumes, we found that the value predicted by a continuous-state, deterministic ODE model often deviated

from the expected steady-state calcium concentration in the discrete-state, stochastic model. We analyzed how this deviation depends on channel binding kinetics, subspace volume, and calcium influx rate. We demonstrated that the deterministic description also deviated from the stochastic model in a physiologically realistic model of calmodulin-mediated calcium channel regulation.

3.1. Physiological Implications. Many studies have modeled the influence of signaling proteins on intracellular and transmembrane ion channel/receptor kinetics, such as calcium/calmodulin-dependent kinase II phosphorylation [33] or beta-adrenergic signaling [34] in cardiac myocytes and glutamate receptor activation in neurons [35]. Many of these signaling interactions occur in small volumes (e.g., the cardiac dyad [4] and neuronal synapse [36]) and include binding interactions with species present in low concentration (calcium and glutamate, resp.). In cardiac myocytes, the local calcium concentration can greatly influence the whole cell response through calcium-induced calcium release, the sodium-calcium exchanger current (which can trigger activation of an action potential), and a host of intracellular signaling pathways [37]. We found that a stochastic model that accounts for the discrete nature of such interactions may deviate from the corresponding deterministic ODE model. Under certain conditions, the small system deviation is negligible, in particular for the case of a large calcium influx rate (Figure 10). During a cardiac action potential, many L-type calcium channels are synchronously opened, and thus the calcium concentration rapidly increases from the micro- to millimolar range. Similarly, following neuronal firing the glutamate concentration in the synaptic cleft can increase several orders of magnitude [35]. In these situations, the deviation of species concentrations from that suggested by deterministic ODE models may not be physiologically

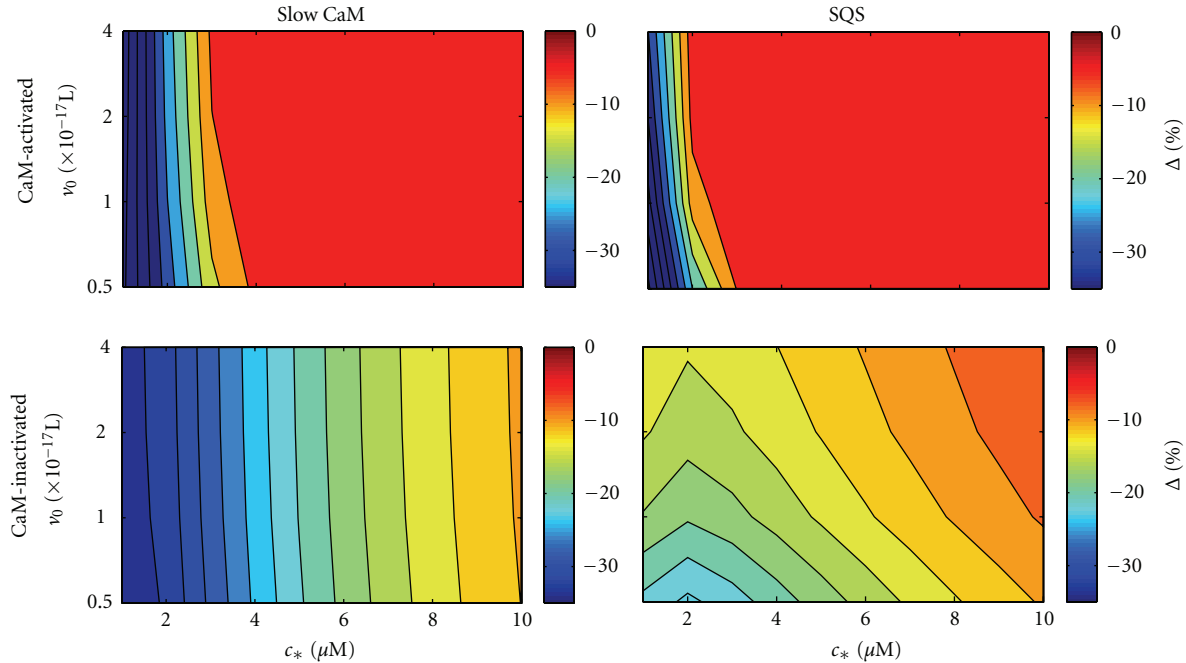


FIGURE 13: Small system deviation for multiple calmodulin-activated and -inactivated channels, using “slow CaM” and “SQS” parameters.

significant. However, during resting conditions, the deviation may be significant, and concentration fluctuations due to the small subspace volume could influence channel dynamics (Sections 2.2–2.4). It has been shown that stochastic openings in calcium release channels in the dyadic subspace of cardiac myocytes during diastole can lead to spontaneous calcium release and arrhythmias during heart failure [38]. Our findings demonstrate that a discrete model of the subspace concentration may be important in this physiological context, because it is likely that fluctuations due to the small number of calcium ions play a significant role in generating spontaneous calcium release events.

In addition to demonstrating that a discrete/stochastic model of calcium-regulated calcium influx often deviates from a continuous/deterministic description, we analyzed how subspace volume and concentration fluctuations influence channel dynamics. Because calmodulin effectively colocalizes with the L-type calcium channel [39], the results associated with the “single channel” volume scaling (Figure 5 and Section 2.2) are most relevant. Such colocalization is ubiquitous; many regulators have been shown to colocalize with channels or receptors, including phospholamban with calcium ATPase in the sarcoplasmic reticulum membrane [40], G-protein receptor kinases with G-protein receptors on the cell membrane [41], and Bax with voltage-dependent ion channels in the mitochondrial membrane [42]. Additionally, the volume of diadic subspaces can be greatly altered during pathophysiological conditions. For example, the L-type calcium channels and ryanodine receptors localization in the dyad is disrupted during heart failure and the subspace volume in which these channels reside is much greater in heart failure than during physiological conditions [43]. Our findings show that when a small number of molecules

are present in the subspace (small v_0 and c), subspace volume can greatly influence the steady-state properties of stochastically gating channels (Figures 10 and 13).

3.2. Relation to Prior Studies. Prior work by our lab has investigated calcium channel regulation through a host of various mechanisms. Groff and Smith investigated the influence of inactivation on calcium spark dynamics in a channel regulated by both calcium-activation and -inactivation [44]. Mazzag et al. demonstrated that residual calcium that accumulates in a subspace during channel openings can influence channel gating [27]. Perhaps more relevant to this study of how concentration fluctuations depend on the subspace volume and influence average rates of calcium binding, channel gating, and calcium influx, Smith and coworkers previously investigated how the number of subspace domains and the number of channels per subspace can influence cellular responses. Williams et al. demonstrated that a population of subspace domains can be represented by a probability density approach and can be utilized to simulate global calcium dynamics [45]. Hartman et al. utilized a model of a small number of coupled calcium activated channels to predict the global calcium release dynamics in response to pharmacological modification of single channel kinetics [46]. However, this study is the first to compare a model of calcium channel regulation accounting for the finite subspace volume (and using a discrete representation of the number of subspace calcium ions) with the corresponding ODE formulation that assumes a large system size (and uses a continuous representation of calcium concentration).

Only a few previous studies have utilized a discrete representation of calcium ions in the context of cardiac myocyte

subspace dynamics. Winslow and colleagues simulated the spatial location of discrete diffusing calcium ions, as well as the spatial structure and geometry of the L-type calcium channel and ryanodine receptor in the cardiac dyad [47]. They demonstrate that stochastic fluctuations produce variability in the L-type calcium channel-ryanodine receptor signaling interactions (specifically excitation-contraction coupling gain), but their analysis does not distinguish between the influence of fluctuations due to channel gating, calcium diffusion, and small calcium ion number. Similar to this study, von Wegner and Fink presented a stochastic model of the L-type calcium channel, incorporating calcium diffusion, buffering, and channel gating and conductance, and they demonstrated how calcium concentration fluctuations could influence downstream signalling pathways [48]. Our results are novel in their focus on the influence of subspace volume and the kinetics of calcium-regulation of an L-type channel. Most importantly, we provide a thorough analysis of the deviation of the approximate deterministic description from the full stochastic model and clarify the conditions leading to large versus small deviations.

Previous studies have modeled biochemical reaction networks using master equations and compared results with deterministic ODE models. McQuarrie demonstrated in 1963 that for first-order reactions, the expected steady-state concentrations derived from the chemical master equation and deterministic ODEs agree [5]. In Section 2.1, calcium influx from an unregulated channel is modeled using zeroth- and first-order reactions and, consequently, the stochastic and deterministic descriptions must agree. Our observation that concentration fluctuations increased as the subspace volume became smaller is consistent with well-understood principles of statistical physics and should come as no surprise [23].

Darvey et al. demonstrated for several generic second-order reactions, the expected concentration computed from the chemical master equation may deviate from the corresponding ODE model [20]. The deviation is typically negative (i.e., $\Delta < 0$), with greatest suppression when concentration fluctuations are large. Other recent studies have demonstrated that the concentrations of species in stochastic biochemical networks can deviate from deterministic ODE descriptions. In agreement with our findings, the deviation is often negative [18, 21, 28], although positive deviation was observed in some biochemical systems [12, 49]. Our findings are consistent with Darvey et al., in that Δ had the greatest magnitude when either the subspace volume or calcium influx rate was small (Figure 10) (both result in larger concentration fluctuations, see (14)).

We found that the small system size deviation was particularly complex in cases where the deterministic ODE, that is, the model appropriate for the large system size limit, is bistable (Figure 8). Lestas et al. recently investigated bistability/bimodality in a network of gene regulation and demonstrated that bistability in the deterministic ODE model did not imply bimodality in the discrete system and, conversely, bimodality in the discrete system did not imply bistability in the corresponding ODEs [50]. We obtained similar results, as bimodality in distribution was not present

in the bistable system for $\nu = \nu_0$ (Figure 4(a)) but was present for $\nu = 8\nu_0$ (Figure 4(b)). Conversely, for the calmodulin-regulated channel, bimodality was present in the distribution for the monostable system (Figure 11). Interestingly, for the bistable system, $E[C]$ computed from the discrete model need not be well approximated by either of the two stable equilibria in the deterministic model; rather, $E[C]$ is given by an intermediate value and can have a complex dependence of subspace volume (Figure 8(C)). But it is important to note that the small system size deviation does not require a bistable deterministic model. The deviation can be quite pronounced even in a monostable deterministic model (Figures 8(B), 9, and 10).

3.3. Limitations. The two-state kinetic models of the calcium channel introduced in Section 2.1 is minimal and should be interpreted as phenomenological (as opposed to statistical) model of single channel kinetics, that is, the topology and parameters of this model were not obtained by fitting to patch clamp recordings [51]. On the other hand, the kinetic model for regulation of the calcium channel presented in Section 2.4 is state-of-the-art. Both minimal and physiologically realistic channel models are affected by the decision to account for (or neglect) fluctuations in calcium concentration that result from the small number of ions in the subspace.

The most significant limitation in the model formulation is our neglect of spatial dynamics of calcium diffusion within the dyadic subspace and the details of the spatial arrangement of the ryanodine receptors [47, 52]. However, for the purposes of the present study, that is, investigation of the influence of concentration fluctuations on the regulation of calcium influx, a nonspatial Markov chain model that includes subspace volume as a model parameter and accounts for the finite number of calcium ions in the domain is sufficient.

Another limitation of the present work is that we focus on *stationary* statistics, for example, the expected value of the steady-state subspace calcium concentration, in our analysis of the deviation of continuous ODE description from the discrete stochastic formulation. Future studies could address how *transient* dynamics, for example, the cellular response to a depolarizing voltage step, excitation-contraction coupling gain, and so forth, are affected by calcium concentration fluctuations resulting from small subspace volume.

4. Conclusions

Our findings demonstrate the physiological relevance of concentration fluctuations in both minimal and realistic models of a calcium-regulated channels associated with subspaces of small volume. The take home message is: *concentration fluctuations do not “average out” in a manner that causes stochastic and deterministic descriptions of subspace dynamics to be equivalent.* Future studies will investigate how subspace calcium concentration fluctuations may influence global calcium dynamics and plasma membrane electrical activity in physiological and pathophysiological conditions.

Conflict of Interests

The authors do not have any conflict of interests.

Acknowledgments

The work was supported in part by National Science Foundation Grant DMS-1121606 and the Biomathematics Initiative at The College of William & Mary. The authors acknowledge stimulating discussions with graduate students Xiao Wang and Mary Mohr. This study was inspired by comments made at the 2012 UC Davis Cardiovascular Symposium.

References

- [1] T. J. Kamp and J. W. Hell, "Regulation of cardiac L-type calcium channels by protein kinase A and protein kinase C," *Circulation Research*, vol. 87, no. 12, pp. 1095–1102, 2000.
- [2] W. C. Rose, C. W. Balke, W. G. Wier, and E. Marban, "Macroscopic and unitary properties of physiological ion flux through L-type Ca²⁺ channels in guinea-pig heart cells," *Journal of Physiology*, vol. 456, pp. 267–284, 1992.
- [3] J. L. Greenstein and R. L. Winslow, "An integrative model of the cardiac ventricular myocyte incorporating local control of Ca²⁺ release," *Biophysical Journal*, vol. 83, no. 6, pp. 2918–2945, 2002.
- [4] V. Iyer, R. Mazhari, and R. L. Winslow, "A computational model of the human left-ventricular epicardial myocyte," *Biophysical Journal*, vol. 87, no. 3, pp. 1507–1525, 2004.
- [5] D. A. McQuarrie, "Kinetics of small systems. I," *The Journal of Chemical Physics*, vol. 38, pp. 433–436, 1963.
- [6] J. Liang and H. Qian, "Computational cellular dynamics based on the chemical master equation: a challenge for understanding complexity," *Journal of Computer Science and Technology*, vol. 25, no. 1, pp. 154–168, 2009.
- [7] H. Qian, "Nonlinear stochastic dynamics of mesoscopic homogeneous biochemical reaction systems—an analytical theory," *Nonlinearity*, vol. 24, no. 6, pp. R19–R49, 2011.
- [8] H. Qian and L. M. Bishop, "The chemical master equation approach to nonequilibrium Steady-state of open biochemical systems: linear single-molecule enzyme kinetics and nonlinear biochemical reaction networks," *International Journal of Molecular Sciences*, vol. 11, no. 9, pp. 3472–3500, 2010.
- [9] C. J. Gadgil, "Size-independent differences between the mean of discrete stochastic systems and the corresponding continuous deterministic systems," *Bulletin of Mathematical Biology*, vol. 71, no. 7, pp. 1599–1611, 2009.
- [10] E. Arslan and I. J. Laurenzi, "Kinetics of autocatalysis in small systems," *Journal of Chemical Physics*, vol. 128, no. 1, Article ID 015101, 2008.
- [11] D. J. Higham, "Modeling and simulating chemical reactions," *SIAM Review*, vol. 50, no. 2, pp. 347–368, 2008.
- [12] C. A. Gómez-Urbe and G. C. Verghese, "Mass fluctuation kinetics: capturing stochastic effects in systems of chemical reactions through coupled mean-variance computations," *Journal of Chemical Physics*, vol. 126, no. 2, Article ID 024109, 2007.
- [13] M. Calder, A. Duguid, S. Gilmore, and J. Hillston, "Stronger computational modelling of signalling pathways using both continuous and discrete-state methods," in *Computational Methods in Systems Biology*, vol. 4210 of *Lecture Notes in Computer Science*, pp. 63–77, 2006.
- [14] O. Wolkenhauer, M. Ullah, W. Kolch, and K. H. Cho, "Modeling and simulation of intracellular dynamics: choosing an appropriate framework," *IEEE Transactions on Nanobioscience*, vol. 3, no. 3, pp. 200–207, 2004.
- [15] T. E. Turner, S. Schnell, and K. Burrage, "Stochastic approaches for modelling in vivo reactions," *Computational Biology and Chemistry*, vol. 28, no. 3, pp. 165–178, 2004.
- [16] K. Vasudeva and U. S. Bhalla, "Adaptive stochastic-deterministic chemical kinetic simulations," *Bioinformatics*, vol. 20, no. 1, pp. 78–84, 2004.
- [17] H. Qian, S. Saffarian, and E. L. Elson, "Concentration fluctuations in a mesoscopic oscillating chemical reaction system," *Proceedings of the National Academy of Sciences of the United States of America*, vol. 99, no. 16, pp. 10376–10381, 2002.
- [18] I. J. Laurenzi, "An analytical solution of the stochastic master equation for reversible bimolecular reaction kinetics," *Journal of Chemical Physics*, vol. 113, no. 8, pp. 3315–3322, 2000.
- [19] H. Wang and Q. Li, "Master equation analysis of deterministic chemical chaos," *Journal of Chemical Physics*, vol. 108, no. 18, pp. 7555–7559, 1998.
- [20] I. G. Darvey, B. W. Ninham, and P. J. Staff, "Stochastic models for second-order chemical reaction kinetics. The equilibrium state," *The Journal of Chemical Physics*, vol. 45, no. 6, pp. 2145–2155, 1966.
- [21] Q. Zheng and J. Ross, "Comparison of deterministic and stochastic kinetics for nonlinear systems," *The Journal of Chemical Physics*, vol. 94, no. 5, pp. 3644–3648, 1991.
- [22] J. Goutsias, "Classical versus stochastic kinetics modeling of biochemical reaction systems," *Biophysical Journal*, vol. 92, no. 7, pp. 2350–2365, 2007.
- [23] J. E. Keizer, *Statistical Thermodynamics of Nonequilibrium Processes*, Springer, Berlin, Germany, 1987.
- [24] S. Wray and T. Burdya, "Sarcoplasmic reticulum function in smooth muscle," *Physiological Reviews*, vol. 90, no. 1, pp. 113–178, 2010.
- [25] R. L. Winslow and J. L. Greenstein, "Cardiac myocytes and local signaling in nano-domains," *Progress in Biophysics and Molecular Biology*, vol. 107, no. 1, pp. 48–59, 2011.
- [26] M. B. Cannell and C. H. T. Kong, "Local control in cardiac E-C coupling," *Journal of Molecular and Cellular Cardiology*, vol. 52, pp. 298–303, 2011.
- [27] B. Mazzag, C. J. Tiganelli, and G. D. Smith, "The effect of residual Ca²⁺ on the stochastic gating of Ca²⁺-regulated Ca²⁺ channel models," *Journal of Theoretical Biology*, vol. 235, no. 1, pp. 121–150, 2005.
- [28] J. Wu, B. Vidakovic, and E. O. Voit, "Constructing stochastic models from deterministic process equations by propensity adjustment," *BMC Systems Biology*, vol. 5, no. 187, pp. 1–21, 2011.
- [29] I. Györke and S. Györke, "Regulation of the cardiac ryanodine receptor channel by luminal Ca²⁺ involves luminal Ca²⁺ sensing sites," *Biophysical Journal*, vol. 75, no. 6, pp. 2801–2810, 1998.
- [30] M. A. Huertas and G. D. Smith, "The dynamics of luminal depletion and the stochastic gating of Ca²⁺-activated Ca²⁺ channels and release sites," *Journal of Theoretical Biology*, vol. 246, no. 2, pp. 332–354, 2007.
- [31] M. R. Tadross, I. E. Dick, and D. T. Yue, "Mechanism of local and global Ca²⁺ sensing by calmodulin in complex with a Ca²⁺ channel," *Cell*, vol. 133, no. 7, pp. 1228–1240, 2008.
- [32] H. Liang, C. D. DeMaria, M. G. Erickson, M. X. Mori, B. A. Alseikhan, and D. T. Yue, "Unified mechanisms of Ca²⁺ regulation across the Ca²⁺ channel family," *Neuron*, vol. 39, no. 6, pp. 951–960, 2003.

- [33] Y. L. Hashambhoy, J. L. Greenstein, and R. L. Winslow, "Role of CaMKII in RyR leak, EC coupling and action potential duration: a computational model," *Journal of Molecular and Cellular Cardiology*, vol. 49, no. 4, pp. 617–624, 2010.
- [34] J. Heijman, P. G. A. Volders, R. L. Westra, and Y. Rudy, "Local control of β -adrenergic stimulation: effects on ventricular myocyte electrophysiology and Ca²⁺-transient," *Journal of Molecular and Cellular Cardiology*, vol. 50, no. 5, pp. 863–871, 2011.
- [35] S. Pendyam, A. Mohan, P. W. Kalivas, and S. S. Nair, "Computational model of extracellular glutamate in the nucleus accumbens incorporates neuroadaptations by chronic cocaine," *Neuroscience*, vol. 158, no. 4, pp. 1266–1276, 2009.
- [36] D. A. Rusakov, M. Y. Min, G. G. Skibo, L. P. Savchenko, M. G. Stewart, and D. M. Kullmann, "Role of the synaptic microenvironment in functional modification of synaptic transmission," *Neurophysiology*, vol. 31, pp. 99–101, 1999.
- [37] D. M. Bers, "Cardiac excitation-contraction coupling," *Nature*, vol. 415, no. 6868, pp. 198–205, 2002.
- [38] W. Chen, G. Aistrup, J. Andrew Wasserstrom, and Y. Shiferaw, "A mathematical model of spontaneous calcium release in cardiac myocytes," *American Journal of Physiology*, vol. 300, no. 5, pp. H1794–H1805, 2011.
- [39] M. X. Mori, M. G. Erickson, and D. T. Yue, "Functional stoichiometry and local enrichment of calmodulin interacting with Ca²⁺ channels," *Science*, vol. 304, no. 5669, pp. 432–435, 2004.
- [40] D. L. Stenoien, T. V. Knyushko, M. P. Londono et al., "Cellular trafficking of phospholamban and formation of functional sarcoplasmic reticulum during myocyte differentiation," *American Journal of Physiology*, vol. 292, no. 6, pp. C2084–C2094, 2007.
- [41] J. Krupnick and J. Benovic, "The role of receptor kinases and arrestins in G protein-coupled receptor regulation," *Annual Review of Pharmacology and Toxicology*, vol. 39, Article ID 2890319, 1998.
- [42] M. Narita, S. Shimizu, T. Ito et al., "Bax interacts with the permeability transition pore to induce permeability transition and cytochrome c release in isolated mitochondria," *Proceedings of the National Academy of Sciences of the United States of America*, vol. 95, no. 25, pp. 14681–14686, 1998.
- [43] L. S. Song, E. A. Sobie, S. McCulle, W. J. Lederer, C. W. Balke, and H. Cheng, "Orphaned ryanodine receptors in the failing heart," *Proceedings of the National Academy of Sciences of the United States of America*, vol. 103, no. 11, pp. 4305–4310, 2006.
- [44] J. R. Groff and G. D. Smith, "Calcium-dependent inactivation and the dynamics of calcium puffs and sparks," *Journal of Theoretical Biology*, vol. 253, no. 3, pp. 483–499, 2008.
- [45] G. S. B. Williams, M. A. Huertas, E. A. Sobie, M. S. Jafri, and G. D. Smith, "A probability density approach to modeling local control of calcium-induced calcium release in cardiac myocytes," *Biophysical Journal*, vol. 92, no. 7, pp. 2311–2328, 2007.
- [46] J. M. Hartman, E. A. Sobie, and G. D. Smith, "Spontaneous Ca²⁺ sparks and Ca²⁺ homeostasis in a minimal model of permeabilized ventricular myocytes," *American Journal of Physiology*, vol. 299, no. 6, pp. H1996–H2008, 2010.
- [47] R. L. Winslow, A. Tanskanen, M. Chen, and J. L. Greenstein, "Multiscale modeling of calcium signaling in the cardiac dyad," *Annals of the New York Academy of Sciences*, vol. 1080, pp. 362–375, 2006.
- [48] F. Von Wegner and R. H. A. Fink, "Stochastic simulation of calcium microdomains in the vicinity of an L-type calcium channel," *European Biophysics Journal*, vol. 39, no. 7, pp. 1079–1088, 2010.
- [49] R. Grima, "Study of the accuracy of moment-closure approximations for stochastic chemical kinetics," *The Journal of Chemical Physics*, vol. 136, Article ID 154105, 2012.
- [50] I. Lestas, J. Paulsson, N. E. Ross, and G. Vinnicombe, "Noise in gene regulatory networks," *IEEE Transactions on Automatic Control*, vol. 53, pp. 189–200, 2008.
- [51] B. Sakmann and E. Neher, *Single-Channel Recording*, Springer, 2nd edition, 1995.
- [52] J. R. Groff and G. D. Smith, "Ryanodine receptor allosteric coupling and the dynamics of calcium sparks," *Biophysical Journal*, vol. 95, no. 1, pp. 135–154, 2008.

Research Article

Simulation of Exercise-Induced Syncope in a Heart Model with Severe Aortic Valve Stenosis

Matjaž Sever,¹ Samo Ribarič,² and Marjan Kordaš²

¹ Department of Hematology, Faculty of Medicine, University of Ljubljana, 1104 Ljubljana, Slovenia

² Institute of Pathophysiology, Faculty of Medicine, University of Ljubljana, 1104 Ljubljana, Slovenia

Correspondence should be addressed to Samo Ribarič, samo.ribaric@mf.uni-lj.si

Received 22 June 2012; Revised 8 October 2012; Accepted 15 October 2012

Academic Editor: Gangmin Ning

Copyright © 2012 Matjaž Sever et al. This is an open access article distributed under the Creative Commons Attribution License, which permits unrestricted use, distribution, and reproduction in any medium, provided the original work is properly cited.

Severe aortic valve stenosis (AVS) can cause an exercise-induced reflex syncope (RS). The precise mechanism of this syncope is not known. The changes in hemodynamics are variable, including arrhythmias and myocardial ischemia, and one of the few consistent changes is a sudden fall in systemic and pulmonary arterial pressures (suggesting a reduced vascular resistance) followed by a decline in heart rate. The contribution of the cardioinhibitory and vasodepressor components of the RS to hemodynamics was evaluated by a computer model. This lumped-parameter computer simulation was based on equivalent electronic circuits (EECs) that reflect the hemodynamic conditions of a heart with severe AVS and a concomitantly decreased contractility as a long-term detrimental consequence of compensatory left ventricular hypertrophy. In addition, the EECs model simulated the resetting of the sympathetic nervous tone in the heart and systemic circuit during exercise and exercise-induced syncope, the fluctuating intrathoracic pressure during respiration, and the passive relaxation of ventricle during diastole. The results of this simulation were consistent with the published case reports of exertional syncope in patients with AVS. The value of the EEC model is its ability to quantify the effect of a selective and gradable change in heart rate, ventricular contractility, or systemic vascular resistance on the hemodynamics during an exertional syncope in patients with severe AVS.

1. Introduction

Exertional syncope, a syncope present during increased heart workload due to increased muscle work, is an important complication of advanced aortic valve stenosis (AVS) [1]. The mechanism of syncope is complex, and several factors contribute to its development [2]. What is common to all forms is an acute and brief reduction of cerebral blood flow leading to a transient loss of consciousness and followed by a spontaneous and complete recovery. The standard classification of the etiology of syncope recognizes three broad categories of pathophysiological mechanisms: the reflex (neurally mediated) syncopes, the syncopes due to orthostatic hypotension, and the cardiac (cardiovascular) syncopes [2].

A consistent change in hemodynamics during exertional syncope is systemic hypotension, a reduction in both systolic

and diastolic blood pressure. Changes in heart rate are variable, ranging from insignificant to sinus bradycardia or even sinus node arrest [1–5]. Significantly, bradycardia does not occur simultaneously with a sudden fall of systemic arterial pressure but follows systemic and pulmonary hypotension [1, 3, 4]. Systemic hypotension during syncope can be the result of a reduced cardiac output, decreased peripheral resistance, or an inadequate venous return (e.g., due to venous pooling). Therefore, an exertional syncope in a patient with severe AVS can be either a reflex, a cardiac, or a combination of both. The reflex syncopes (RS) are a heterogeneous group of syncopes that attenuates the cardiovascular reflexes essential for the short-term control of adequate perfusion of vital organs. The effects of a RS are mediated by modulating the activity of the efferent sympathetic and parasympathetic pathways. When hypotension predominates, due to loss of vasoconstrictor tone, this

syncope is subclassified as a vasodepressor reflex syncope (VRS). A cardioinhibitory variant (CIRS) is present when bradycardia or asystole are the predominating clinical signs. Therefore, the clinical signs can reflect a cardioinhibitory, a vasodepressor, or a mixed variant of the RS [2].

The triggers for the reflex syncope are not completely understood [6–8]. Most of the evidence does not support the suggestion that vasodilatation and bradycardia are triggered by a paradoxical stimulation of the cardiac ventricular receptors [7, 9–12]. More likely, the precise trigger for the vasovagal syncope varies from patient to patient and depends on a complex interaction of neuronal inputs, autonomic output, humoral effects, and ischaemia [7].

Cardiac syncopes can be due to arrhythmias (drug induced, idiopathic, or associated with myocardial ischemia/infarction) or due to structural diseases of the heart or major blood vessels. The most common cause of a cardiac (cardiovascular) syncope is an arrhythmia, for example, a bradycardia or a tachycardia [2].

Patients with severe AVS are more prone to exertional syncope than healthy individuals. Firstly, severe AVS limits the ability of the cardiovascular system to maintain an adequate perfusion of the brain during increased muscle work. Secondly, these patients may have developed compensatory changes (myocardial fibrosis and impaired coronary vasodilator reserve) that increase the chances of left ventricular dysfunction with or without myocardial ischemia or arrhythmias (bradycardias or tachycardias) during increased muscle work. To summarise, exertional syncope in a patient with severe AVS is caused by different mechanisms [7] and concomitant AVS-related structural changes of the cardiovascular system [13] that prevent an optimal adjustment of stroke volume, heart rate, or peripheral resistance to provide adequate perfusion of the brain.

We studied the differential effects of arrhythmia (e.g., bradycardia) or reduced stroke volume (e.g., decreased inotropy due to myocardial ischemia) in the presence of syncope-related homeostasis failure of the cardiovascular system with venous pooling of blood and decreased peripheral resistance. The lumped-parameter computer model of this cardiovascular system was based on equivalent electronic circuits (EECs). For the presented study we upgraded an existing EEC model of the cardiovascular system with AVS [14–16]. The upgraded model, for simulating exertional syncope in a patient with AVS, includes

- (1) an improved subcircuit controlling ventricular contractility that gives an ejection fraction value of 70% for a normal heart;
- (2) a heart model with severe AVS, moderately decreased left ventricular contractility, and systolic insufficiency (as a complication of compensatory ventricular hypertrophy). The simulated left ventricle still has a preserved but limited capacity to respond to inotropic mechanisms, thus more closely resembling the clinical conditions of a patient with AVS that develops exertional syncope;

- (3) the ability to simulate different patterns of the RS during exercise by selectively activating or inactivating the vasodepressor reflex (loss of venoconstriction) or the cardioinhibitory reflex (reduced left ventricular contractility or reduced heart rate).

In addition, the results of the simulation were analyzed with the pressure-volume (P-V) loop diagrams of left ventricular work.

2. Methods

Analyses are performed by developing an equivalent electronic circuit (EEC) by using Electronics Workbench (EWB) Personal version 5.12 [14–16]. In this model of the cardiovascular system, venous tone, heart rate, and contractility of the right and left ventricle are modulated by a negative feedback mechanism.

Compared to the earlier EECs [14–16], the left ventricular circuit is slightly modified. The mitral and the aortic valves are simulated by diodes D1; therefore, in the left ventricle, there is no “reverse flow” (neither from aorta into the ventricle during diastole nor from the ventricle into the atrium during systole). The nominal gain is increased from 50 to 100, and in the left ventricle contractility modulation, the upper inotropic limit is increased up to 8 FGU (factor of gain units; 8 V; Figure 1).

Decreased left ventricle contractility is achieved by decreasing the nominal gain from 100 to about 20 (Figure 1). AVS is simulated by increasing output resistance of the ventricle (0.8 U) by inserting a 800 k Ω resistor in series to the output diode. Please note that the unit to measure the resistance to flow (U) is defined as 100 mm Hg/100 mL/s (For details please refer to [14–16]).

Results are shown graphically, as the time course of equivalent variables. Thus, electrical variables: voltage, current, resistance, capacitance, and charge, correspond to physiological variables: pressure, blood flow, resistance, capacitance, and volume (for details refer to [14–16]). The interdependence of pressure and volume of the left ventricle is shown by pressure-volume analysis (P-V loop diagrams) describing the left ventricle work load during one cardiac cycle. Acronyms of variables studied are listed in Table 1.

3. Results

In all simulations, the sequence of parameter change (in the five time sequence sections) is as follows:

- (1) 50 s–70.5 s: sedentary, normal (initial) conditions;
- (2) 70.5 s–110.5 s: development of decreased LV contractility in sedentary conditions;
- (3) 110.5 s–150.5 s: development of decreased LV contractility and severe AVS in sedentary conditions;
- (4) 150.5 s–240.5 s: decreased-LV contractility and AVS, and MAoP reset and peripheral resistance decreased by 50% during physical exercise;
- (5) 240.5 s–550 s: failure of homeostasis due to activation of the reflex syncope response during physical

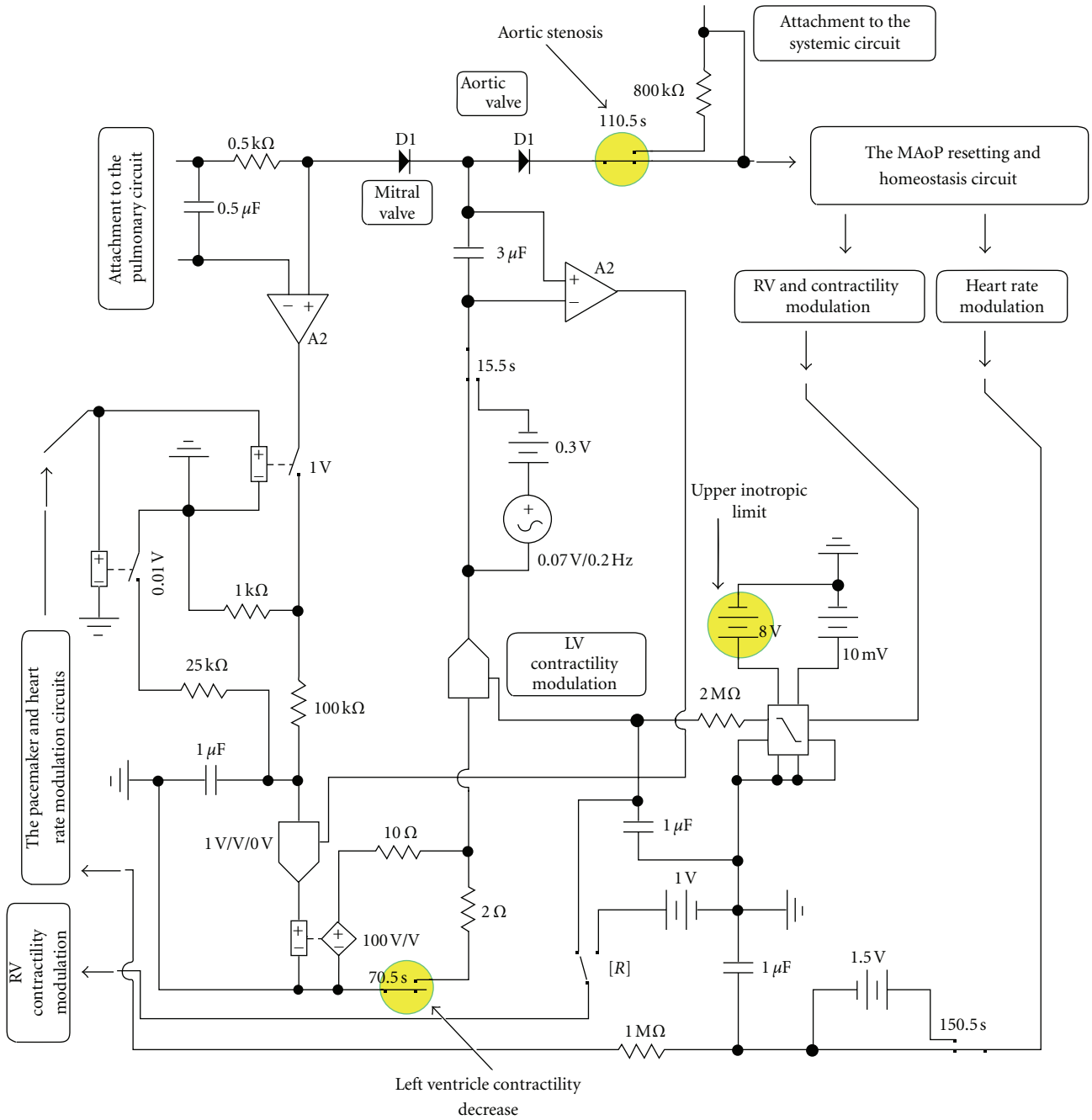


FIGURE 1: Equivalent circuit of the left ventricle. If left ventricular contractility is decreased (note the switch activated at 70.5 s), it is still acted upon by some residual inotropic influence. Note that its upper limit is determined by the battery in the voltage limiter. Aortic stenosis is simulated by introducing a series resistance $0.8 U$ (800 k Ω) at the output of the aortic valve.

exercise (during exertional syncope). This is achieved by differentially switching off the negative feedback circuits controlling heart frequency, left ventricular contractility, and venous tone. Figures 2 and 3 show hemodynamic changes after activation of a RS response with inhibition of left ventricular contractility and vasodilatation but no significant effect on heart frequency.

The time course of AoP, MAoP, CO, CVV, Sy, and LATP during simulation as described above is shown in Figure 2, top records. Note that, if a parameter is changed, a transient phenomenon shows up, but very soon a new steady state is established. Thus, after LV contractility is decreased, AoP, MAoP, and CO are transiently decreased and heart rate increased. However, due to the homeostatic negative feedback, Sy is increased, resulting also in venoconstriction

TABLE 1: Recorded variables (with corresponding units) and acronyms used in text and illustrations.

Variable	Acronym
Aortic pressure (mm Hg)	AoP
Cardiac output (mL/min)	CO
Contractible volume of veins (mL)	CVV
Ejection fraction of left ventricle	EF
End-diastolic pressure in left ventricle (mm Hg)	EDPLV
End-diastolic volume of left ventricle (mL)	EDVLV
End-systolic volume of left ventricle (mL)	ESVLV
Factor of gain (FGU)	FG
Intrathoracic pressure (mm Hg)	ITP
Left atrial pressure (mm Hg)	LAtP
Left ventricle	LV
Left ventricular pressure (mm Hg)	LVP
Left ventricular volume (mL)	LVV
Mean arterial pressure (mm Hg)	MAoP
Stroke volume of the left ventricle (mL)	SVLV
Sympathetic (inotropic) homeostatic contractility modulation	Sy

and decreased CVV. Therefore, LAtP is increased. Similar changes, also compensated by Sy, can be seen after aortic stenosis is induced. As expected, exercise (decreased peripheral resistance and MAoP reset) results in an increased Sy, and consequently, increased heart rate, CO, MAoP and systolic AoP.

Failure of homeostasis results in a dramatic change of almost all variables; their steady state is established at about 500 s of simulation time (Figure 2, bottom records). However, steady state levels of variables depend on the type of homeostasis failure. If heart rate is 120/min and Sy is 1 FGU, CO is almost equal to initial conditions despite hypotension and small pulse pressure (Figure 2(a)). A decrease in Sy results in a decreased CO as well as AoP and MAoP (Figure 2(b)). If heart rate is 45/min and Sy is 0.5 FGU, CO, AoP, and MAoP are extremely low (Figure 2(c)). However, if Sy is increased to 1.5 FGU, CO is almost equal to initial conditions, but MAoP is low and pulse pressure very large (Figure 2(d)).

The time course of AoP, MAoP, LVP, LAtP, and CO during one cardiac cycle and the corresponding P-V loop diagram, are shown in Figure 3, in four sections (columns; cf. Figure 3).

- (1) Normal, sedentary (initial) conditions (first column; time sequence 68.7 s–69.3 s): note that peak LVP is reached in less than 0.1 s, indicating a relatively high rate of LV contraction. SVLV is 87 mL, EF is 63%, and diastolic LVP is slightly negative. Accordingly, the P-V loop diagram shows relatively low ventricle volume and low ventricular diastolic pressure.

- (2) Decreased LV contractility in sedentary conditions (second column; time sequence 103.7 s–104.3 s): maximum LVP is almost normal, but peak LVP is reached in more than 0.1 s, indicating a relatively low rate of LV contraction. EDVLV and ESVLV are strongly increased, SVLV only slightly decreased, but EF strongly decreased to about 30%. Diastolic LVP is positive. Accordingly, the P-V loop diagram is shifted to the right, to an increased ventricular diastolic pressure and a relatively high ventricle volume.
- (3) Decreased LV contractility and AVS in sedentary conditions simulate the conditions of an AVS related systolic ventricular dysfunction (third column; time sequence 148.7 s–149.3 s): an aortic-ventricular pressure gradient (about 50 mm Hg) shows up. Maximum LVP is almost 170 mm Hg, but peak LVP is reached in more than 0.1 s, indicating a relatively low rate of LV contraction. EDVLV and ESVLV further increased, SVLV maintained, and EF strongly decreased to about 25%. The P-V loop diagram is shifted strongly to the right and upwards, to a relatively very high ventricle volume and systolic pressure.
- (4) Decreased LV contractility AVS and MAoP reset, and peripheral resistance decreased by 50% during physical exercise (fourth column; 233.7 s–234.3 s): the aortic-ventricular pressure gradient is increased to about 70 mm Hg. Maximum LVP is almost 190 mm Hg and peak LVP is reached in about 0.1 s, indicating an improved rate of LV contraction. EDVLV and ESVLV decreased, SVLV is about 107 mL, and EF 56%. Accordingly, the P-V loop diagram is shifted to the left and upwards, to a relatively low ventricle volume and high ventricle systolic pressure.

Various types of homeostasis failure are also shown in steady state (after about 540 s of simulation time) as the time course of AoP, MAoP, LVP, LAtP, and CO during systole and part of diastole (543.7 s–544.3 s). All data are shown in columns (a)–(d) (Figure 4, cf. also Figure 2), including the corresponding P-V loop diagrams. In these, for the sake of comparison, also the P-V loop diagram in exercise is shown (cf. Figure 3(d)). Note that the pressure gradient and its magnitude are dependent on Sy and on heart rate.

If heart rate is 120/min and Sy is 1 FGU (Figure 4(a)), the P-V loop diagram is depressed, shifted to the right, and becomes narrow. If in this condition Sy is decreased (0.5 FGU; Figure 4(b)), these changes are even more pronounced. They agree excellently with corresponding time course of various variables, showing decreased LVP, SVLV, and increased EDVLV.

If the heart rate is 45/min and the Sy is 0.5 FGU, the P-V loop diagram is shifted to extreme right, but maintains its width. EDVLV is strongly increased, increasing also SVLV. If in this condition the Sy is increased to 1.5 FGU, the P-V loop diagram is shifted to the left, increasing its width: EDVLV is decreased, but SVLV increased, as is also shown in the time course of ventricular volume and pressure.

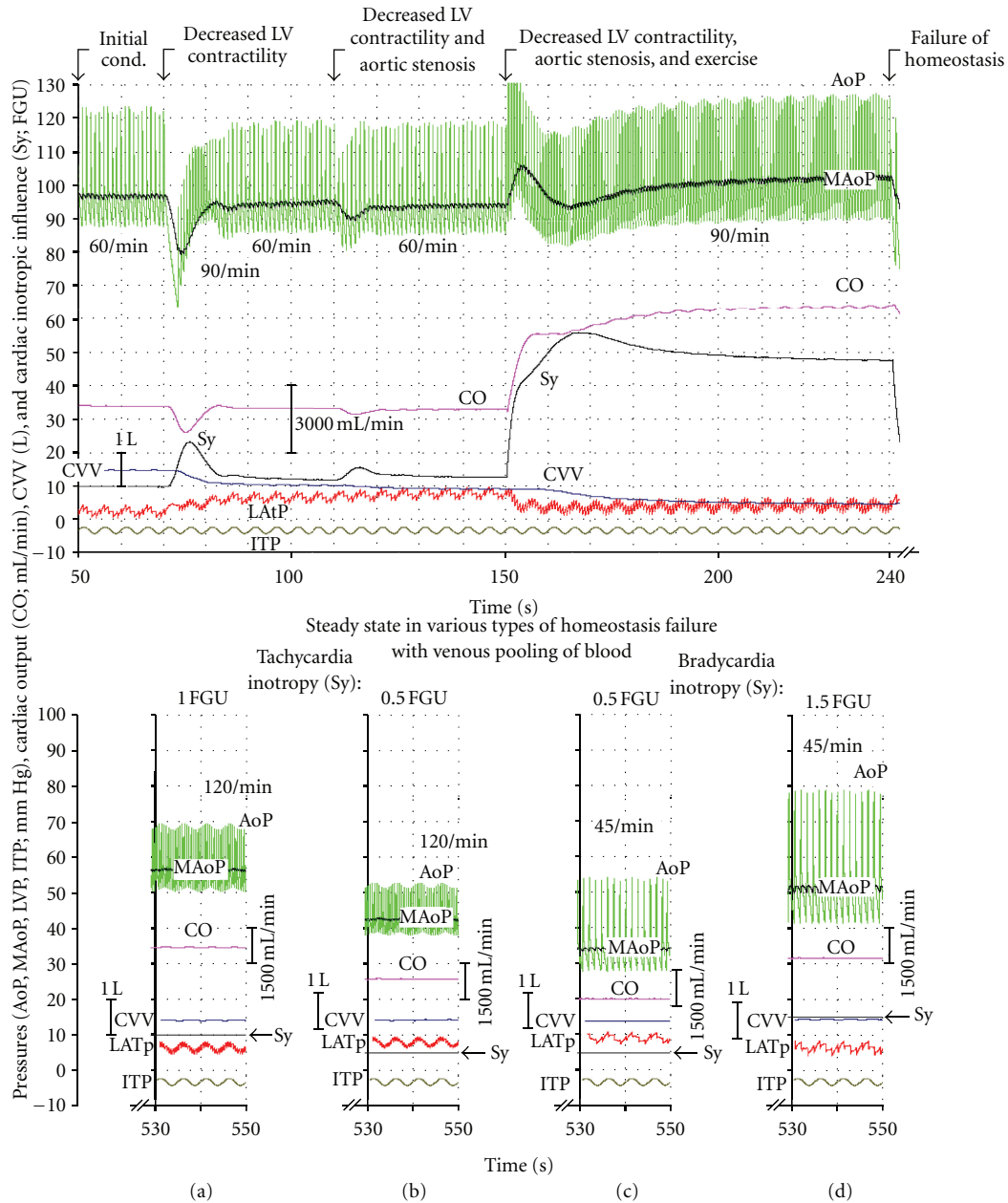


FIGURE 2: Top records. The time course of AoP, MAoP, CO, CVV, Sy, and LATp in initial conditions (50 s–70.5 s), after LV contractility is decreased (70.5 s–110.5 s), after aortic stenosis (110.5 s–150.5 s), after exercise (150.5 s–240.5 s), and after failure of homeostasis (240.5 s onwards). If a parameter is changed, due to the homeostatic negative feedback, a transient phenomenon shows up, but very soon a new steady state is established. As expected, exercise (decreased peripheral resistance and MAoP reset) results in an increased Sy, and consequently, increased heart rate, CO, MAoP, and systolic AoP. Steady state levels of variables, depending on the type of homeostasis failure, are shown in the bottom records in columns (a–d) (530 s–550 s of simulation time). Failure of homeostasis results in a dramatic change of almost all variables. Steady state levels of variables (interval 530 s–550 s of simulation time) depend on the type of homeostasis failure. At heart rate 120/min and Sy equal to 1 FGU, AoP is decreased and pulse pressure lowered (a). A decrease in Sy results in a further decrease of AoP and MAoP (b). At a heart rate of 45/min and a Sy equal to 0.5 FGU, the AoP and MAoP are extremely low (c). If the Sy is increased to 1.5 FGU, the MAoP is low and the pulse pressure very large (d).

4. Discussion

4.1. *General and Technical Comments.* Technical details important to be considered in simulations have already been discussed [14]. Note that gain in left ventricle circuit is increased from 50 to 100. Therefore, the left ventricle

contractility (and its ejection fraction) is improved. Therefore, blood volume is slightly smaller.

Compared to earlier AVS simulations [14], in the present EEC, the left ventricle contractility simulation is upgraded similarly as in [16]. Therefore, if LV basic contractility is decreased (Figure 1; nominally by about 80%), it can be,

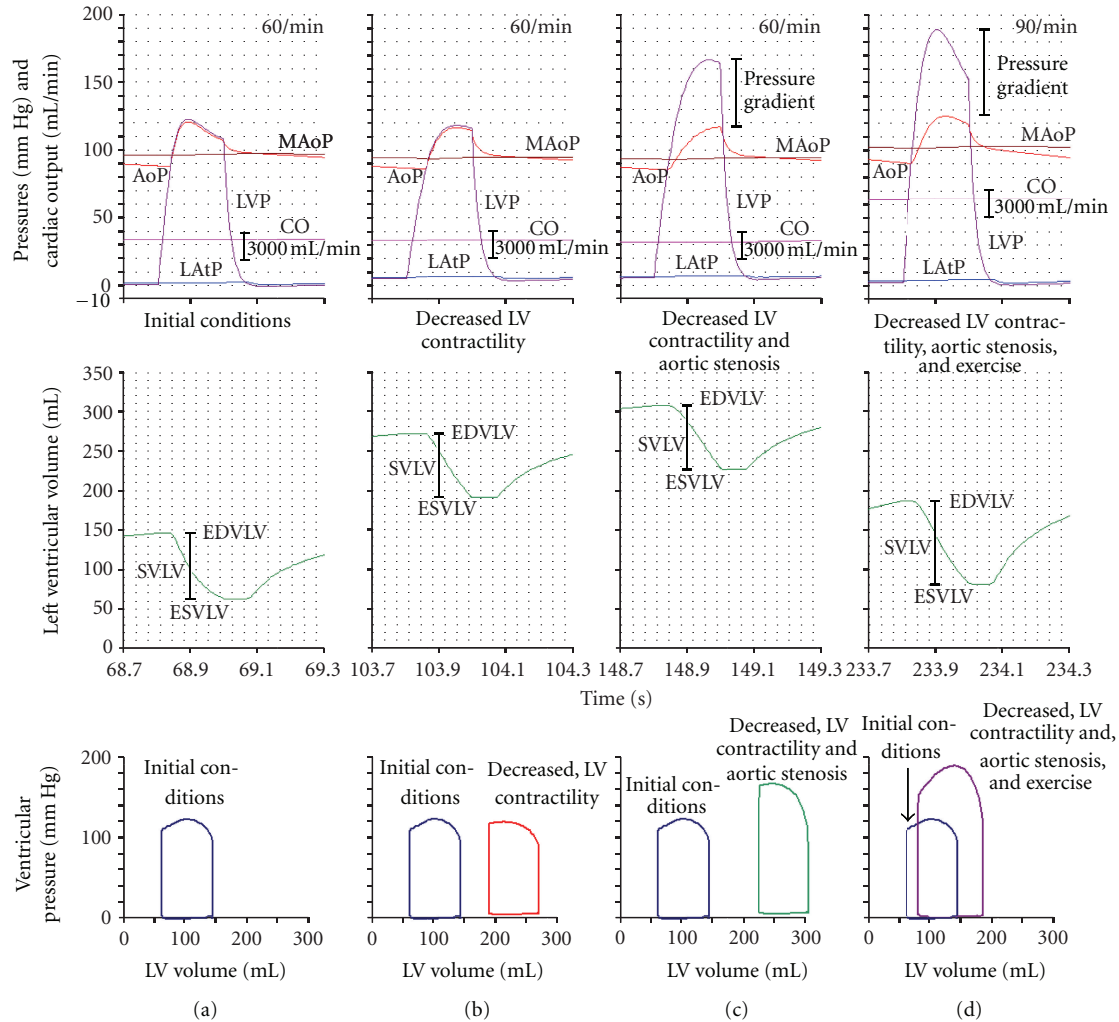


FIGURE 3: Data are arranged in four columns according to the simulation sequence described in Figure 2. In the upper parts of each column, there are time courses of various variables during systole and part of diastole (AoP, MAoP, LVP, LATP, CO, ventricular volume). Note that a decreased LV contractility results in a decreased rate of contraction of LV (b). After aortic stenosis, a ventriculoaortic pressure gradient appears (c). EDVLV is increased, but due to a negative feedback SVLV is almost normal. In exercise (d), the pressure gradient is further increased, but due to the negative feedback (S_y increased) the heart rate and CO are increased and the EDVLV decreased. These changes are in excellent agreement with corresponding P-V loop diagrams. Note that in decreased LV contractility, the P-V loop diagram is shifted to the right. In aortic stenosis (note the pressure gradient), due to the inotropic effect (increased S_y), the P-V loop diagram shows a large ventricular pressure. The full inotropic effect is shown in exercise, where the P-V loop diagram is shifted to the left.

to a limited degree, still acted upon through the inotropic mechanism of the negative (homeostatic) feedback.

It should be noted that at any heart rate, the duration of systole is constant, 0.2 s. Therefore, if heart rate is increased, only the duration of systole is decreased. Atria do not contract. It should also be noted that in the present circuit:

- (1) a flow-dependent decrease in pulmonary vascular resistance is not simulated;
- (2) the control of peripheral (arteriolar) resistance is not included into the negative feedback.

In principle, it would be possible to include both features. However, this would contribute considerably to the complexity of the circuitry, without contributing very much to the understanding of underlying physiological mechanisms.

Despite the model's deficiencies described above, the negative feedback (incorporating the control of venous volume, of contractility of RV and LV, and of heart rate) seems to be quite similar to that controlling the human cardiovascular system [17–19]. After a parameter in the circuit is changed (i.e., a disturbance introduced), the time course of many variables can be studied to demonstrate the relation—not only on a magnitude scale, but also on a time scale—between the disturbance and homeostatic response. The changing time course of left ventricle pressure also shows how total vascular impedance—affected by AVS and by peripheral vasodilatation—affects the process of left ventricle contraction.

By using the present model various physiological and clinical conditions have been simulated (effects of heart rate

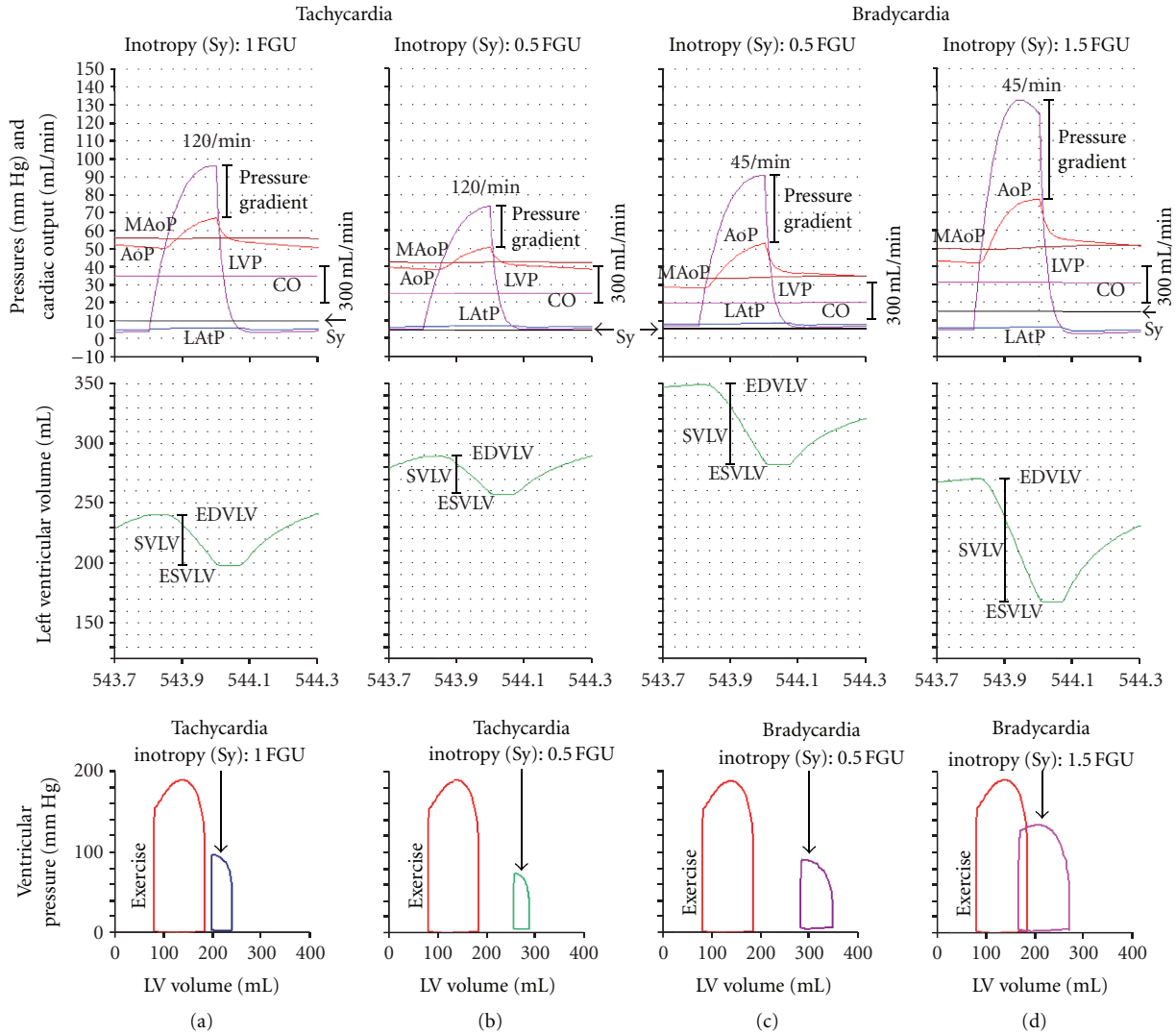


FIGURE 4: Data are arranged in four columns according to the type of homeostasis failure, after the steady state is established. The upper two sections of columns (a–d) present the time course of AoP, MAoP, LVP, LATP, ventricular volume, and CO during systole and part of diastole (543.7 s–544.3 s). Note that the pressure gradient and its magnitude are dependent on the Sy and on the heart rate. In the bottom of each column there are the corresponding P-V loop diagrams. In these, for the sake of comparison, also the P-V loop diagram in exercise is shown (cf. Figure 3(d)). If the heart rate is 120/min and the Sy is 1 FGU 4(a), the P-V loop diagram is depressed, shifted to the right, and narrowed. If in this condition Sy is decreased (0.5 FGU; 4(b)), these changes are even more pronounced. They agree excellently with the corresponding time course of various variables, showing the decreased LVP and SVLV and the increased EDVLV. If the heart rate is 45/min and the Sy is 0.5 FGU, the P-V loop diagram is shifted to extreme right, but maintains its width. EDVLV is strongly increased, increasing also SVLV. If in this condition the Sy is increased to 1.5 FGU, the P-V loop diagram is shifted to the left, increasing its width: the EDVLV is decreased, but the SVLV is increased, as is also shown in the time course of ventricular volume and pressure.

changes, volume loading, exercise, heart failure, AVS, mitral and aortic regurgitation). Our unpublished data also show that, by a suitable modification of the ventricle circuit, even the cardiac aneurysm can be simulated quite satisfactorily.

4.2. Comparison with Other Simulations. In the present EEC, blood inertia is not simulated; therefore, the aortic dirotic notch—as simulated in [20]—is absent. Changes effected by left ventricular failure were simulated by Kim et al. [20]. In their work, results were shown as a time course of left ventricular pressure and of left ventricular volume and also

as P-V loop diagrams. All data are, qualitatively, readily comparable to data obtained by the presented EEC of exertional failure with AVS. However, some minor quantitative differences can be observed, probably due to the fact that in the presented EEC, homeostatic (feedback) mechanism(s) is (are) operative until their failure is simulated due to the activation of the RS response during exercise.

Hemodynamic changes effected by AVS were simulated by Korürek et al. [21]. This model also simulated atrial contraction. Results were shown as the time course of left atrial and ventricular pressure and of left ventricular

volume and as ventricular P-V loop diagrams. All data are, qualitatively, readily comparable to data obtained by the presented EEC. However, some quantitative differences can be observed, probably due to the fact that in our EEC, the simulation protocol is different. Our model simulates the physiological negative pressure in the thoracic cavity. Therefore, after vigorous left ventricular contraction, diastolic ventricular pressure may become negative. Furthermore, prior to AVS, left ventricular contractility is decreased, and the homeostatic (feedback) mechanism(s) is (are) operative until the onset of simulated exertional syncope when they are differentially inhibited by the vasodepressor or cardioinhibitory component of the RS response.

Compared to the simulations described above [20, 21], the present EEC allows simulations exactly as in animal experiment. Not only transient phenomena and steady state of various variables can be recorded, but also the rate and magnitude of the homeostatic response can be studied.

4.3. Comparison of the EEC Exertional Syncope Model with Patient Data. There are only a few published reports of exercise-induced syncope in patients with aortic stenosis [1, 3–5]. Consistently, the reports show a reduction in systemic arterial pressure, due to a reduction in both systolic and diastolic blood pressure. Changes in heart rate are variable, ranging from insignificant to tachycardias, bradycardias, or even to a cessation of ventricular contractions. What is important is that, during a RS, hypotension precedes bradycardia [8], thus ruling out the explanation that RS is essentially due to activation of the baroreceptor reflex. Patient with AVS can develop arrhythmias before, during, or after an exercise-induced syncope. However, arrhythmias are not essential for the development of exercise-induced syncope [3]. The exertional syncope of patients with AVS was reported to be associated with ECG signs of myocardial ischemia [1, 4, 5] but also occurred in the absence of left ventricular failure [3].

Our model demonstrates the changes in hemodynamics (a reduction in both systolic and diastolic blood pressure) when the capacity of the heart to maintain a sufficient cardiac output is reduced either due to arrhythmia or to reduced contractility. Therefore, the results of the model are qualitatively in agreement with the published data [1, 3–5]. Since clinical data are available at the level of case series, any statistical comparison with the model is not possible and the results should be evaluated in a descriptive way. The value of the EEC model is its ability to quantify the effect of a selective and gradable change in heart rate, ventricular contractility, or systemic vascular resistance on the hemodynamics during an exertional syncope in patients with severe AVS.

5. Conclusions

The presented lumped-parameter EEC model can differentially simulate the effect of cardioinhibitory and vasodepressor component of the RS response, and the simulated hemodynamic data are in agreement with patient data recorded during exercise-induced syncope. To our knowledge, this

is the first reported computer simulation of an exercise-induced RS in patients with severe AVS.

Conflict of Interests

The authors report no conflict of interests. The authors alone are responsible for the content and writing of the paper.

Acknowledgment

This work was supported by the Slovenian Research Agency of the Republic of Slovenia, Grant no. P3-0171.

References

- [1] M. Šinkovec, P. Rakovec, D. Zorman, G. Antolič, and A. Grad, "Exertional syncope in a patient with aortic stenosis and right coronary artery disease," *European Heart Journal*, vol. 16, no. 2, pp. 276–278, 1995.
- [2] A. Moya, R. Sutton, F. Ammirati et al., "Guidelines for the diagnosis and management of syncope (version 2009): The Task Force for the Diagnosis and Management of Syncope of the European Society of Cardiology (ESC)," *European Heart Journal*, vol. 30, no. 21, pp. 2631–2671, 2009.
- [3] A. M. Richards, M. G. Nicholls, and H. Ikram, "Syncope in aortic valvular stenosis," *The Lancet*, vol. 2, no. 8412, pp. 1113–1116, 1984.
- [4] K. Yano, T. Kuriya, and K. Hashiba, "Simultaneous monitoring of electrocardiogram and arterial blood pressure during exercise-induced syncope in a patient with severe aortic stenosis—a case report," *Angiology*, vol. 40, no. 2, pp. 143–148, 1989.
- [5] E. D. Grech and D. R. Ramsdale, "Exertional syncope in aortic stenosis: evidence to support inappropriate left ventricular baroreceptor response," *American Heart Journal*, vol. 121, no. 2 I, pp. 603–606, 1991.
- [6] P. O. O. Julu, V. L. Cooper, S. Hansen, and R. Hainsworth, "Cardiovascular regulation in the period preceding vasovagal syncope in conscious humans," *Journal of Physiology*, vol. 549, no. 1, pp. 299–311, 2003.
- [7] R. Hainsworth, "Syncope: what is the trigger?" *Heart*, vol. 89, no. 2, pp. 123–124, 2003.
- [8] C. Schroeder, J. Tank, K. Heusser, A. Diedrich, F. C. Luft, and J. Jordan, "Physiological phenomenology of neurally-mediated syncope with management implications," *PLoS ONE*, vol. 6, no. 10, Article ID e26489, 2011.
- [9] B. Oberg and P. Thorén, "Increased activity in left ventricular receptors during hemorrhage or occlusion of caval veins in the cat. A possible cause of the vaso-vagal reaction.," *Acta Physiologica Scandinavica*, vol. 85, no. 2, pp. 164–173, 1972.
- [10] A. P. Fitzpatrick, N. Banner, A. Cheng, M. Yacoub, and R. Sutton, "Vasovagal reactions may occur after orthotopic heart transplantation," *Journal of the American College of Cardiology*, vol. 21, no. 5, pp. 1132–1137, 1993.
- [11] C. Wright, M. J. Drinkhill, and R. Hainsworth, "Reflex effects of independent stimulation of coronary and left ventricular mechanoreceptors in anaesthetized dogs," *Journal of Physiology*, vol. 528, no. 2, pp. 349–358, 2000.
- [12] M. J. Drinkhill, C. I. Wright, and R. Hainsworth, "Reflex vascular response to independent changes in left ventricular end-diastolic and peak systolic pressures and inotropic state in

- anaesthetised dogs,” *Journal of Physiology*, vol. 532, no. 2, pp. 549–561, 2001.
- [13] L. Dell’Italia, “The human story of aortic stenosis: a time for new surrogate markers in clinical decision making,” *Cardiology*, vol. 122, no. 1, pp. 20–22, 2012.
- [14] M. Sever, T. Podnar, F. Runovc, and M. Kordaš, “Analog simulation of two clinical conditions: (1) Acute left ventricle failure; (2) exercise in patient with aortic stenosis,” *Computers in Biology and Medicine*, vol. 37, no. 8, pp. 1051–1062, 2007.
- [15] S. Ribarič and M. Kordaš, “Teaching cardiovascular physiology with equivalent electronic circuits in a practically oriented teaching module,” *American Journal of Physiology*, vol. 35, no. 2, pp. 149–160, 2011.
- [16] M. Sever, S. Ribarič, F. Runovc, and M. Kordaš, “Analog simulation of aortic stenosis,” 2011, <http://www.intechopen.com/books/aortic-stenosis-etiology-pathophysiology-and-treatment/analog-simulation-of-aortic-stenosis>.
- [17] H. T. Milhorn, *The Application of Control Theory to Physiological Systems*, Saunders, Philadelphia, Pa, USA, 1966.
- [18] C. F. Rothe and J. M. Gersting, “Cardiovascular interactions: an interactive tutorial and mathematical model,” *American Journal of Physiology*, vol. 26, no. 1–4, pp. 98–109, 2002.
- [19] R. M. Berne and M. N. Levy, *Physiology*, Mosby, St. Louis, Mo, USA, 6th edition, 2009.
- [20] H. J. Kim, I. E. Vignon-Clementel, C. A. Figueroa et al., “On coupling a lumped parameter heart model and a three-dimensional finite element aorta model,” *Annals of Biomedical Engineering*, vol. 37, no. 11, pp. 2153–2169, 2009.
- [21] M. Korürek, M. Yildiz, and A. Yüksel, “Simulation of normal cardiovascular system and severe aortic stenosis using equivalent electronic model,” *Anadolu Kardiyoloji Dergisi*, vol. 10, no. 6, pp. 471–478, 2010.

Research Article

Simulation of the Frank-Starling Law of the Heart

Samo Ribarič and Marjan Kordaš

Institute of Pathophysiology, Faculty of Medicine, University of Ljubljana, 1104 Ljubljana, Slovenia

Correspondence should be addressed to Samo Ribarič, samo.ribaric@mf.uni-lj.si

Received 22 June 2012; Revised 19 September 2012; Accepted 24 September 2012

Academic Editor: Gangmin Ning

Copyright © 2012 S. Ribarič and M. Kordaš. This is an open access article distributed under the Creative Commons Attribution License, which permits unrestricted use, distribution, and reproduction in any medium, provided the original work is properly cited.

We developed a lumped parameter, computer-based model of an equivalent electronic circuit for a one-atrium one-ventricle (frog) heart attached to a vascular circuit, to simulate a basic concept of cardiovascular physiology, the Frank-Starling Law of the Heart. A series of simulations was performed, to observe changes in cardiovascular variables (e.g., arterial pressure, ventricular volume, and valve flows) if either preload or afterload was increased. The simulated data agreed qualitatively, and quantitatively when experimental data are available, with data obtained on amphibian or on mammalian myocardium. In addition, the data obtained in these simulations improve our understanding of the mechanism(s) whereby the heart muscle adapts itself to increased distension (increased preload) or to impeded systolic contraction (increased afterload). The analysis of the measured valve flows suggests that the ventricle is a highly input sensitive pump because the input pressure determines the diastolic distension and, consequently, the force of ventricular systolic contraction. On the other hand, the ventricle is a relatively output insensitive pump. Therefore, not only atrium contraction, but also predominantly the preceding ventricular systolic contraction is the main mechanism of the subsequent diastolic ventricular filling. We conclude that the presented model enables the study of basic concepts of cardiovascular physiology.

1. Introduction

Originally, cardiovascular physiology was simulated by mathematical [1–4] or analog [5–8] approaches. Recently, computer simulations using lumped parameter models of the cardiovascular system (alone or in combination with numerical methods) have been introduced [9–15]. We have found the use of lumped parameter models with computer-simulated equivalent electronic circuits (EECs) useful for understanding basic physiology concepts and for educational use [16, 17]. By appropriate upgrading, we could use these EECs for simulating qualitatively, in some cases even quantitatively, cardiovascular physiology and cardiovascular pathology, including well-known clinical conditions [18, 19]. This highly upgraded EECs lumped parameter model enables us to record many interesting variables, for example, the time course of atrial and ventricular pressure during systole and diastole, the rate of myocardial contraction and relaxation, the valve flows, the ventricular volume taking into consideration the resetting of the sympathetic nervous tone in the heart and systemic circuit, the fluctuating intrathoracic

pressure during respiration, and the passive relaxation of ventricle during diastole.

In clinical practice, and in whole animal or human studies, the short-term and long-term compensatory mechanisms modify cardiac function thus impeding the study of the basic mechanical properties of the whole heart in isolation. Therefore, it would be of interest to study, by using the EECs model, the basic determinants of myocardial function(s) as it was originally attempted by using the *in vitro* frog heart model [20, 21]. It should be remembered that it is a one-atrium one-ventricle preparation. Its function, determined by atrial pressure (input pressure, preload) and by output pressure (afterload), is formulated as the Frank-Starling Law of the Heart [20].

In the presented simulation of the Law of the Heart it is attempted to answer the following basic questions.

- (1) *What is the role of atrium in the filling of the ventricle, if the latter is subjected to increased preload or increased afterload?*
- (2) *Why is the ventricle a highly input sensitive pump, but at the same time a relatively output insensitive pump?*

- (3) *What is the change in the pressure-volume (P-V) loop diagram if the ventricle is subjected to increased preload or increased afterload?*

2. Methods

In the experimental layout the one atrium-one ventricle heart (e.g., of the frog) should be attached to an artificial “systemic” circuit, featuring three characteristic sections: (a) a high-pressure/low-capacitance “arterial” section, (b) a variable “peripheral” resistance section, and (c) a low-pressure/high-capacitance “venous” section including a blood reservoir. In this circular arrangement pressures, flow, and stroke volume would depend on preload and afterload. Preload is determined by the height of venous reservoir, and afterload is controlled by “resistance to flow” section (Figure 1(a)). If the heart is contracting, flow is unidirectional due to valves, the “input” and “output” valve. In the “arterial,” high-pressure section, pressure depends predominantly on afterload, that is, on the variable resistance to flow and on the cardiac output. Contrary to that, in the “venous” low-pressure section, pressure depends predominantly on preload, that is, the height of blood level in the venous reservoir.

The equivalent electronic circuit (EEC) should have a very similar structure; the “systemic” circuit, preload control subcircuit, afterload control subcircuit, atrial contraction subcircuit, and ventricular contraction subcircuit, as shown in Figure 1(b). Parallel to the scheme in Figure 1(a), electronic subcircuits simulate preload, atrial contraction, ventricular contraction, and afterload. These subcircuits are suitably incorporated into the main circuit simulating the “arterial” section, the “peripheral resistance section,” and “venous” section of systemic circuit.

It should be noted that, for reasons of comparison, in the present EEC both atrium and ventricle are comparable to the adult human left atrium and left ventricle. Therefore, in the latter, in resting pressure and capacitance conditions, its volume (size, EDVV) is about 117 mL and peak “arterial” pressure is about 70 mm Hg. For reasons of simplicity, in simulations the usual terminology is used also for both valves in this one-atrium one-ventricle heart: at the input of the ventricle the mitral and at the output the aortic valve, respectively.

Analysis of the EEC simulating the one-atrium one-ventricle heart, attached to an artificial vascular circuit, is performed by using Electronics Workbench Personal version 5.12 [22]. This software is used because the circuitry can be tailored almost exactly to the simulation needs. The conversion of electrical units to equivalent units used in physiology is shown in Table 1.

The EEC simulating the one-atrium one-ventricle heart and the artificial systemic circuit is shown in Figure 2. The components (as described in Figures 1(a) and 1(b)) are simulated by subcircuits and indicated by dashed-lined boxes.

Details of how to simulate the atrium and ventricle—both as input-sensitive pumps—and the attached vessels are described elsewhere (e.g., [17–19, 23]). To summarize, the main sections of the EECs model are as follows.

- (a) The “systemic” circuit is made up by a chain of resistor/capacitor segments. The direction of flow (current) is indicated by arrows. Resistors are connected in series. One terminal of a single capacitor is connected to the chain of resistors and the other capacitor terminal is connected to ground. Thus, the resistor/capacitor segments simulate “resistance to flow” and capacitance of single segments of the circuit attached to the heart.
- (b) Preload control subcircuit: by applying the 0.6 V, 0.7 V, and 0.8 V batteries (in parallel to the “systemic” circuit) preload can be set as 6 mm Hg, 7 mm Hg, or 8 mm Hg.
- (c) Afterload control subcircuit: by applying the 3 M Ω , 6 M Ω , and 9 M Ω resistors (in series into the “systemic” circuit) afterload can be increased. Because the series resistance of aorta is 1 U (1 M Ω) afterload can be set as 4 U, or 7 U, or 10 U.
- (d) Atrial contraction subcircuit: essentially, it is a feedback loop with a nominal gain of 0.5 and a nominal time constant 0.1 s. It is activated/deactivated by the atrial pacemaker as described below.
- (e) Ventricle contraction subcircuit: it is a complex feedback loop with a nominal gain of 100. Nominal time constant of ventricular contraction is 0.1 s and that of ventricular relaxation is 0.2 s. Duration of systole is 0.2 s because this value has been used in almost all previous simulations. The gain loop is activated/deactivated by the ventricular pacemaker (synchronous—but with a time shift as described above—with the atrial pacemaker) and two voltage-sensitive switches VS.
- (f) Heart valves: the mitral and aortic valves are simulated as diodes (D1; cf. [18, 19]). The corresponding mitral and aortic flow is measured as a voltage drop across the 1 Ω resistor (Figure 2) as described [18, 19].
- (g) Design of the pacemaker circuit: it consists of two parts: an atrial and a ventricular pacemaker. The atrial pacemaker is a sine-wave generator operating at 1 Hz, (60/min), but with a phase shift of 192°, driving two voltage-sensitive switches (VS). The ventricular pacemaker is a square-wave generator operating at 1 Hz (60/min, duty cycle 0.2 s) which drives two voltage-sensitive switches (VS). In this way both generators, although physically separated, act as a single pacemaker, atrial contraction (nominal gain 0.5) preceding the ventricular contraction (nominal gain 100). The time course of simulated variables (e.g., ventricular pressure, volume of the ventricle; see Figures 3–6) is very similar to those described earlier [16].
- (h) Possible modes of simulation: the mode of simulation is determined by 3 switches: S1 and S2 operated by the “space” key, and S3 operated by the “A” key.

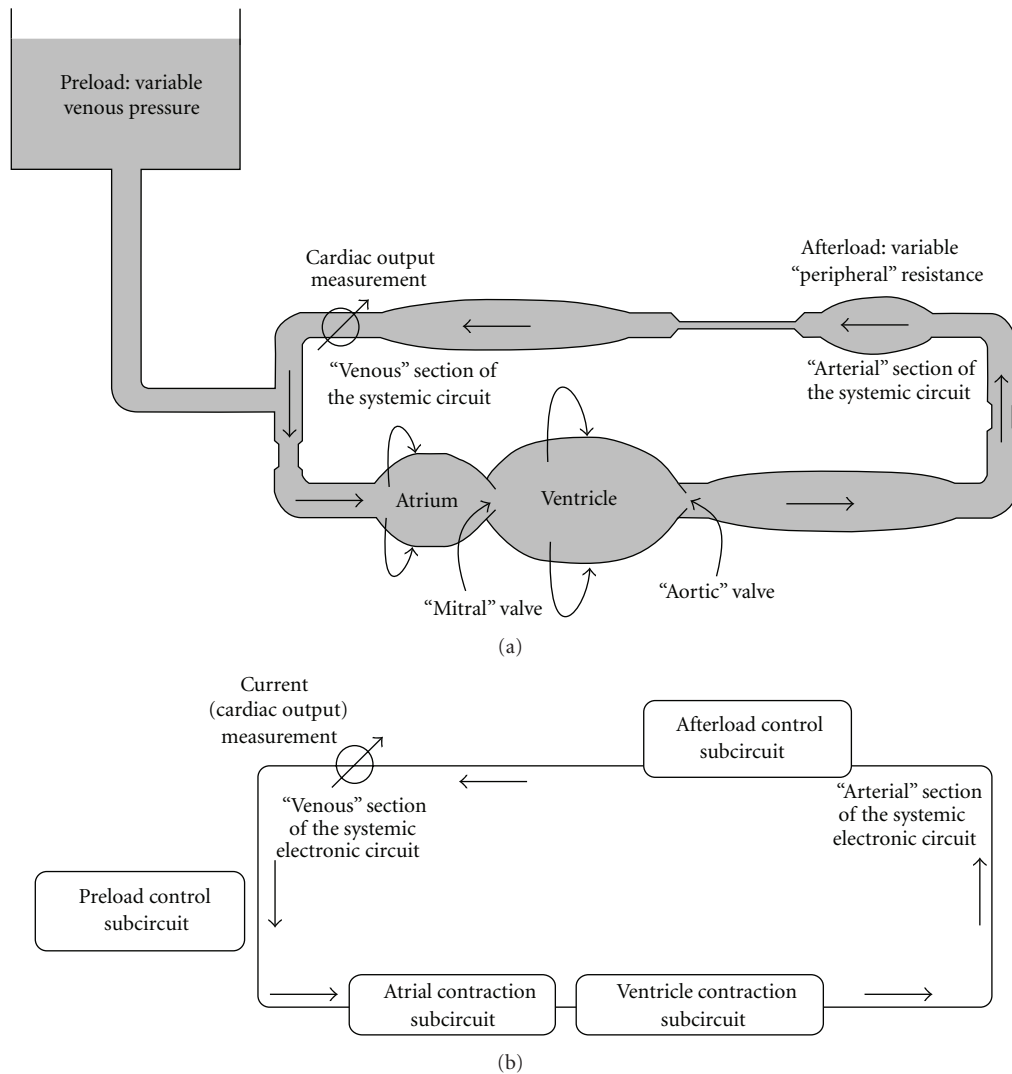


FIGURE 1: Representation of the one-atrium one-ventricle heart preparation. (a) Schematic representation of a one-atrium one-ventricle heart, the contractility of both being determined by their diastolic distension. If it is contracting, flow is unidirectional due to both valves, the “mitral” and “aortic” valves. This one-atrium one-ventricle heart is attached to an artificial circulation, set up by three sections: (1) an elastic “arterial” high-pressure section, (2) a “peripheral,” variable resistance section, and (3) a “venous” low-pressure section. (b) Schematic representation of the EEC simulating the properties of a one-atrium one-ventricle heart attached to an artificial circulation. Current (equivalent to blood flow) is measured at the end of the “venous” section because at this point of the circuit pulsations of the current are minimal.

TABLE 1: Equivalent quantities and arbitrary units in simulation of cardiovascular system.

Electronic circuit	Unit(s)	Cardiovascular system	Unit(s)
Voltage	1 V	Pressure	10 mm Hg
Ground potential (reference for voltage measurements)	0 V	Atmospheric pressure (reference for pressure measurement)	0 mm Hg
Current	1 μA = 60 $\mu\text{As}/\text{min}$	Blood flow	100 mL/s = 6000 mL/min
Resistance	10 V/1 μA = 10 M Ω	Resistance to flow	100 mm Hg/100 mL/s = 1 U
Capacitance	1 μF = 1 $\mu\text{As}/1\text{ V}$	Capacitance	100 mL/10 mm Hg
Charge	1 μAs	Volume	100 mL
Time	1 s	Time	1 s

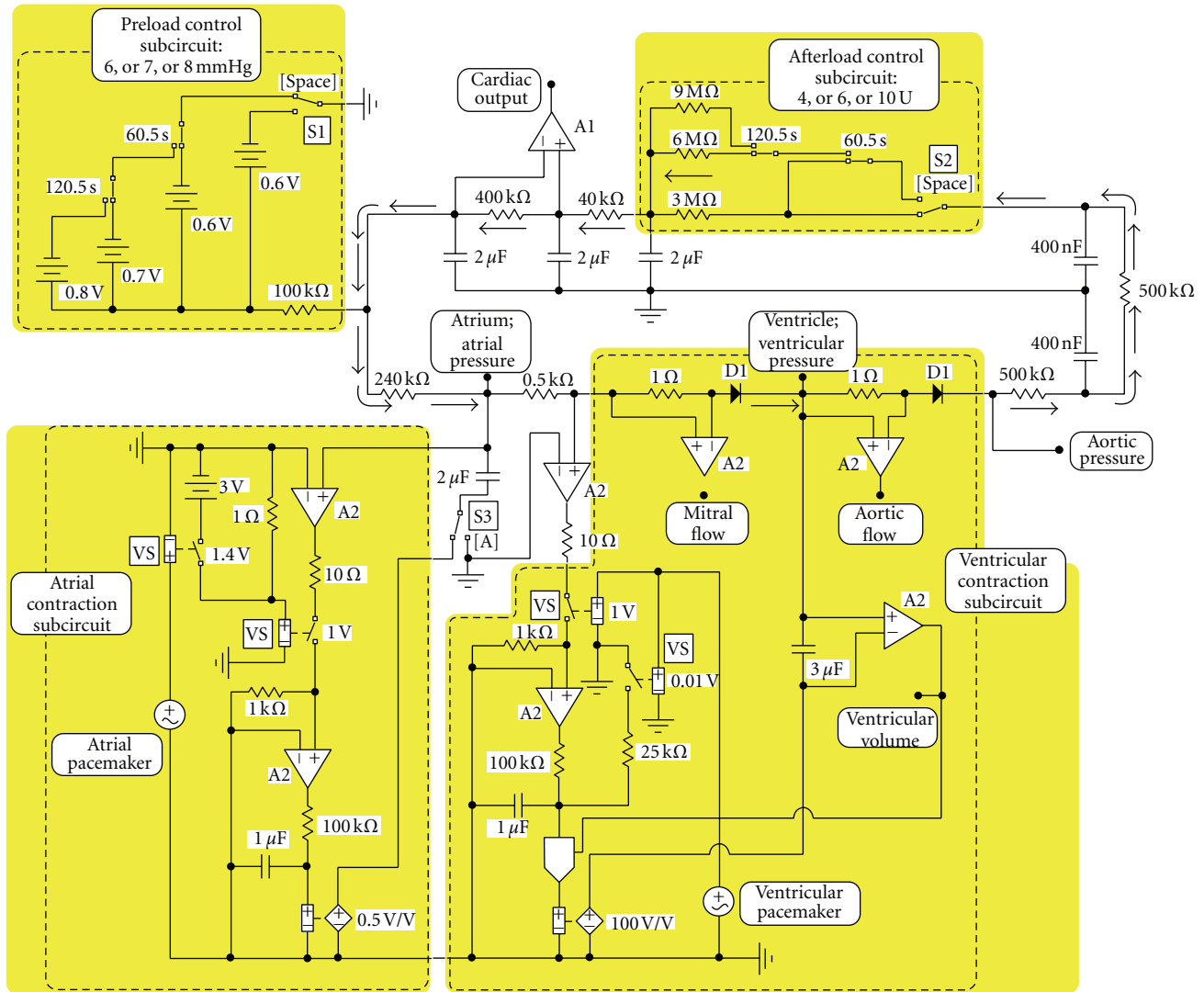


FIGURE 2: Electronic circuit simulating the one-atrium one-ventricle heart and the artificial systemic circuit. Subcircuits (for explanation see Figure 1(b)) are indicated by dashed-lined and shaded boxes. The mode of simulation is determined by 3 switches: S1 and S2 operated by the “space” key, and S3 operated by the “A” key. Various variables can be recorded and measured at points as indicated: pressures (e.g., atrial, ventricular, and “aortic”); flows (e.g., mitral, aortic, and cardiac output); volumes (e.g., ventricular). The “systemic” circuit is made up by a chain of resistor/capacitor segments. The direction of flow (current) is indicated by arrows.

In the setting presented in Figure 2 atrium is contracting. Afterload is constant, 4 U ($3\text{ M}\Omega + 1\text{ M}\Omega$), and preload is stepwise increased: initially 6 mm Hg (0.6 V). At 60.5 s it is increased to 7 mm Hg (0.7 V) and at 120.5 s of simulation time increased to 8 mm Hg (0.8 V). If the “space” key is operated, preload is constant, 6 mm Hg (0.6 V), and afterload stepwise increased: initially 4 U ($3\text{ M}\Omega + 1\text{ M}\Omega$). At 60.5 s it is increased to 7 U ($6\text{ M}\Omega + 1\text{ M}\Omega$) and at 120.5 s of simulation time increased to 10 U ($9\text{ M}\Omega + 1\text{ M}\Omega$). If the “A” key is operated, the capacitor simulating atrium is disconnected from its contractility circuit and connected to ground. Atrium is not contracting.

Variables of interest can be recorded and measured at points as indicated (Figure 2): pressures (e.g., atrial, ventricular, and “aortic”); flows (e.g., mitral, aortic, and cardiac output); volumes (e.g., ventricular).

The acronyms used in text and illustrations are listed in Table 2.

Data are shown as the time course of different variables and as P-V loop diagrams of the ventricle. The work load of the ventricle is calculated in the usual arbitrary units (mm Hg·mL) as well as in joule (J).

3. Results

3.1. EEC Simulation of the Law of the Heart with Contracting Atrium. The effects of increasing preload on the time course of AP, CO, and AtP are shown in Figure 3. In initial conditions (20–60 s of simulation time) preload is 6 mm Hg and afterload is 4 U. When, at 60 s, preload is increased to 7 mm Hg, AP, AtP, and SV are increased (Figure 3(a)). Note also that both AtP max and AtP min are increased; AtP

TABLE 2: The recorded variables and their acronyms.

Aortic pressure	Ap
Atrial pressure	AtP
Maximal atrial pressure	ATP max
Minimal atrial pressure	ATP min
Cardiac output	CO
Ejection fraction of the ventricle	EF
End-diastolic volume	EDVV
End-systolic volume	ESVV
Isovolumic contraction time	ICT
Isovolumic relaxation time	IRT
Maximum velocity of ventricular contraction	dp/dt
Stroke volume	SV
Ventricular pressure	VP
Ventricle volume	VV
Time to peak (time from beginning of systole to peak ventricular pressure)	TtP

pulse pressure is increased. CO is transiently decreased, but within about 10 s it is increased from about 4500 mL/min to almost 6000 mL/min. At the next step, at 120 s, as preload is increased from 7 mm Hg to 8 mm Hg, a similar further increase of these variables occurs. At 180 s, when preload returns to initial conditions, AP, AtP, and VV return to initial conditions level. CO is transiently increased but within about 15 s it also returns to the initial condition level. The performance (i.e., work load) of the ventricle in these simulation conditions is shown by the corresponding P-V loop diagram (Figure 3(b)). If preload is increased, the ESVV is only slightly increased. Contrary to that, EDVV and SV are strongly increased (cf. Figure 3(a)).

The effects of increasing afterload on the time course of AP, CO, and AtP are shown in Figure 4. In initial conditions (20–60 s of simulation time) preload is 6 mm Hg and afterload is 4 U. When, at 60 s, afterload is increased from 4 U to 7 U, AP and AtP are increased, but SV is slightly decreased (Figure 4(a)). Note also that AtP max and AtP min are increased to a different extent; therefore, AtP pulse pressure is decreased. CO is transiently strongly decreased, but within about 20 s it recovers; in steady state it is slightly below the initial conditions level 4500 mL/min. At the next step, at 120 s, as afterload is increased from 7 U to 10 U, a similar further increase of AP and AtP and a slight SV decrease occur. CO is further slightly decreased. AP, AtP, and VV return to initial conditions level. CO is transiently increased but within about 15 s it also returns to the initial condition level. The corresponding P-V loop diagram (Figure 4(b)) shows that, if preload is increased, both ESVV and EDVV are increased, but the latter to a smaller extent. Therefore, SV is slightly decreased (cf. Figure 4(a)).

The time course of cardiovascular variables during a single systole and diastole is presented in Figure 5, in columns A, B, and C, subdivided in four blocks. Upper block: pressures (AP, VP, and AtP) and flow (CO); middle two blocks: atrial and ventricular pressure at an enlarged pressure

scale, and aortic and mitral flow; bottom block: ventricular volume (EDVV, ESVV, and SV).

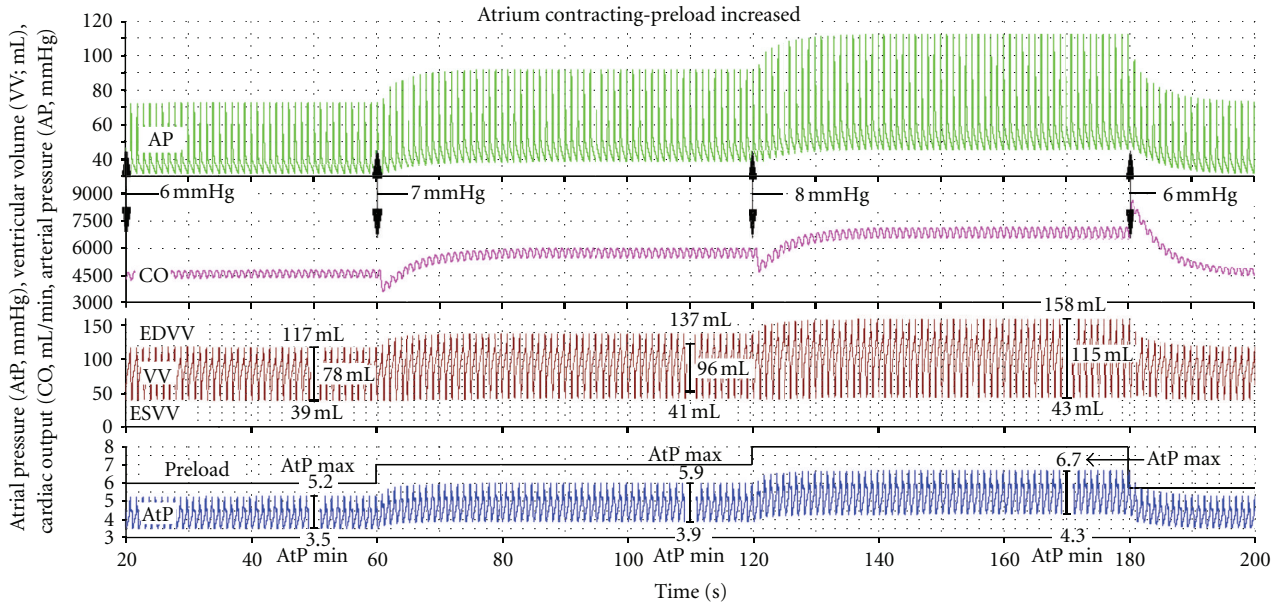
The initial conditions, preload 6 mm Hg and afterload 4 U are shown in Figure 5(a). The time window is 57.6 s to 58.4 s. Peak VP is about 75 mm Hg. Aortic flow coincides with increase of VP-curve. dp/dt is 1886 mm Hg/s; TtP is 72 ms. During ICT and IRT there is no flow. The “effective” diastole starts as soon as VP is lower than AtP, thus inducing mitral flow. It has two peaks: a large early mitral flow in early diastole and a small late mitral flow in late diastole. The latter coincides with an increase in EDVV by about 20 mL. During IRT ventricle volume is constant, at ESVV. EDVV is about 118 mL, ESVV about 40 mL, and SV about 78 mL. End-systolic AtP is 4.5 mm Hg.

Figure 5(b) shows cardiovascular variables at maximum preload (i.e., increased by 33%, from 6 mm Hg to 8 mm Hg; time window is 177.6 s to 178.4). Peak VP is about 115 mm Hg. Aortic flow coincides with increase of VP-curve. The rate of ventricular contraction is strongly increased; dp/dt is increased from the resting value 1886 mm Hg/s to 3125 mm Hg/s; consequently, TtP is decreased from its resting value 72.0 ms to 63.6 ms. Peak VP coincides with peak aortic flow. Note that SV is increased to 115 mL mainly due an increased EDVV, about 158 mL, ESVV being virtually unchanged, about 40 mL. End-systolic AtP is 5.9 mm Hg.

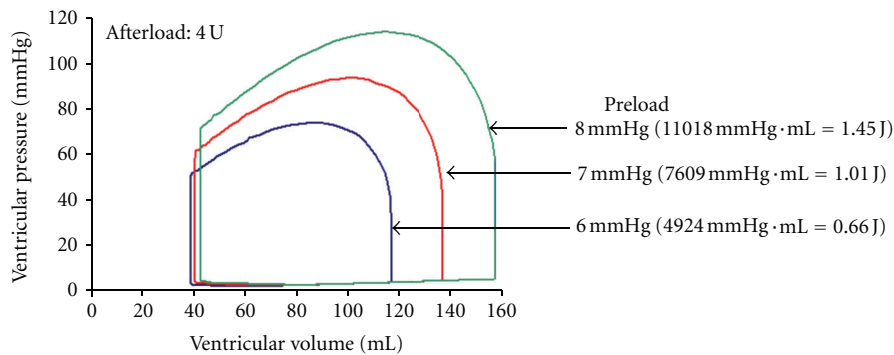
Figure 5(c) shows cardiovascular variables at maximum afterload (i.e., increased by 250%, from 4 U to 10 U; time window is 177.6 s to 178.4). Peak VP is about 100 mm Hg and aortic flow coincides with the increase of VP-curve. The rate of ventricular contraction is mildly increased; dp/dt is slightly increased from the resting value 1886 mm Hg/s to 2127 mm Hg/s; consequently TtP is increased from its resting value 72.0 ms to 90.0 ms. Peak VP coincides with peak aortic flow. Note that EDVV is increased to about 128 mL and ESVV is also increased to about 60 mL. Therefore, SV is mildly decreased to 70 mL. End-systolic AtP is 4.5 mm Hg. The corresponding P-V loop diagram for Figure 5(c) is in Figure 5(d) which shows that, if preload is increased, the loop diagram becomes broader. It shows a high ventricular pressure, a high EDVV and SV. If afterload is increased, the loop diagram becomes narrower; ventricular pressure is increased. While ESVV and EDVV are increased to a different extent, SV is slightly decreased.

3.2. EEC Simulation of the Law of the Heart with Noncontracting Atrium. The effects of increasing preload or afterload on the time course of AP, CO, and AtP are very similar to those shown in Figure 5. The only difference is that CO is lower. Thus, in initial conditions CO is about 4200 mL/min. If atrium is contracting, in initial conditions CO is about 4500 mL/min.

The time course of cardiovascular variables during a single systole and diastole is presented in Figure 6: in initial conditions (Figure 6(a)), in maximum preload (Figure 6(b)), and in maximum afterload (Figure 6(c)). Note that—as atrium is not contracting—in the time course of AtP and of ventricular volume there is no “hump” in late diastole. Also, late mitral flow is absent. However, if atrium is not contracting, early mitral flow is very much pronounced; its



(a)



(b)

FIGURE 3: The time course of aortic pressure (AP), cardiac output (CO), ventricular volume (VV), and atrial pressure (AtP) if afterload is constant (4 U) and preload increased from 6 mm Hg to 8 mm Hg. (a) In initial conditions (20–60 s; preload is 6 mm Hg) all variables are in steady state. Atrial pulse pressure (AtP max/AtP min) is 5.2/3.5 mm Hg. Preload increased first to 7 mm Hg (60–120 s) and then to 8 mm Hg (120–180 s). Note that at each step CO is transiently decreased, but within about 10 s it is increased to a new steady-state level. Similarly, SV and AP are increased. AtP pulse is increased. After preload is returned to 6 mm Hg, AP, AtP, and VV return to initial conditions level. CO is transiently increased but within about 15 s it also returns to the initial condition level. (b) The P-V loop diagram in conditions above. Note that, if preload is increased from 6 mm Hg to 8 mm Hg, ESVV is about 40 mL, while EDVV is increased from 117 mL to about 158 mL. The EF increases from 66% to about 72%. Ventricular work is given in mm Hg·mL and in J.

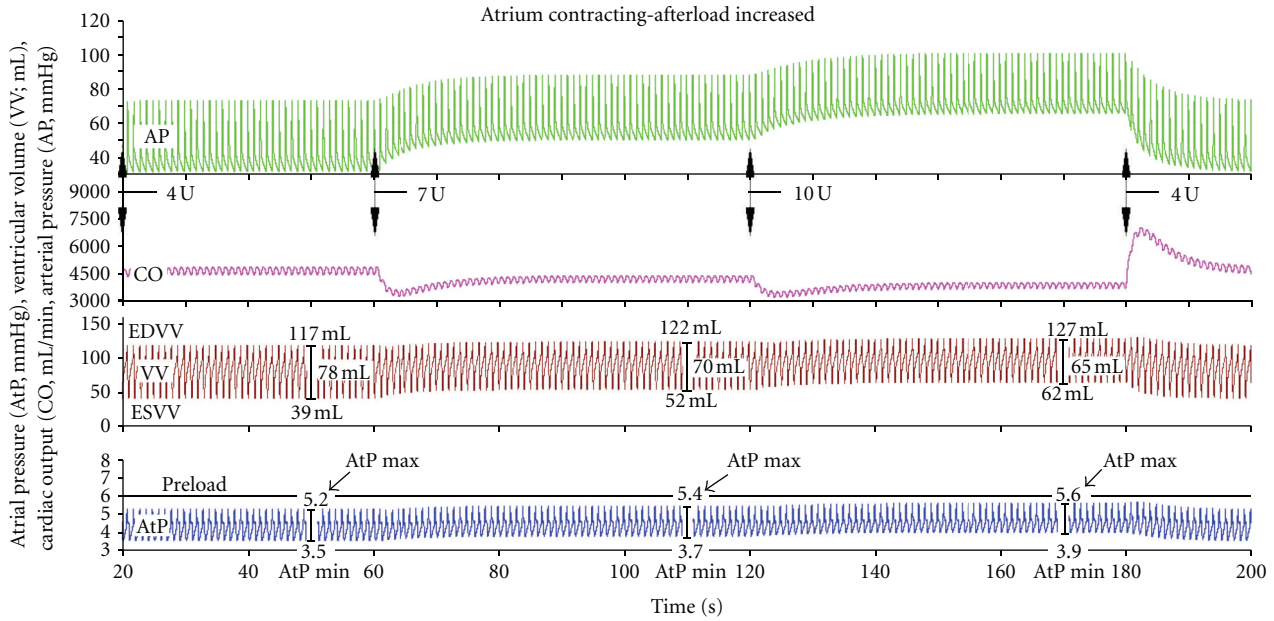
peak value is larger (about 710 mL/s; Figure 6(a)) compared to its peak value when atrium is contracting (about 550 mL/s; Figure 5(a)).

The corresponding P-V loop diagram in Figure 6(d) is qualitatively almost the same as that shown in Figure 5(d). Quantitatively, however, the P-V loop diagram shows a smaller ventricle volume range and slightly lower ventricular pressure.

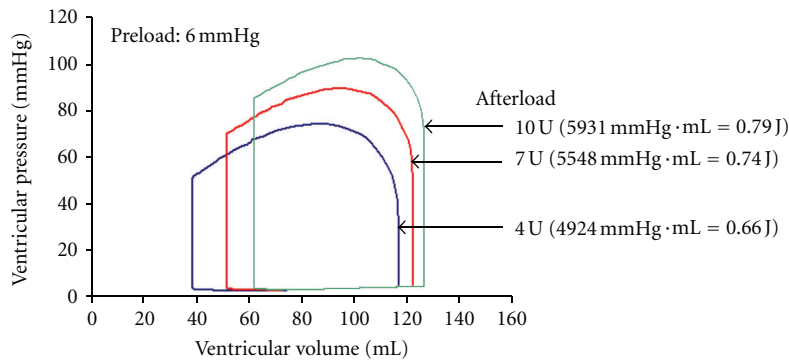
4. Discussion

4.1. General Comments. It should be noted that in the EEC, the heart valves have a negligible “back” flow. However, valve shunts (regurgitation) could be simulated, as has been shown

recently [18]. Because blood inertia is not simulated, there is no diastolic notch in pressure records. The pulse pressure is relatively large because the capacitance of the artificial aorta is relatively low. Therefore, the “Windkessel” effect is relatively small. Heart rate is constant (in the EEC it is 60/min) because in a Frank-Starling preparation there is no nervous or humoral influence. The discontinuities which seem to appear variables in Figures 5 and 6 are due to the fact that they are recorded for time span of 0.4 s and not 1 s (the complete heart cycle). If required, effects of heart rate and velocity of ventricular contraction could be studied as shown [17]. In the earlier simulation of the Starling preparation [16] as well as of the human circulation [17] the duration of systole was 0.25 s. After the circuitry was upgraded (including negative



(a)



(b)

FIGURE 4: The time course of aortic pressure (AP), cardiac output (CO), ventricular volume (VV), and atrial pressure (AtP) if preload is constant (6 mm Hg) and afterload increased from 4 U to 10 U. (a) In initial conditions (20–60 s; afterload is 4 U) all variables are in steady state. Atrial pulse pressure (AtP max/AtP min) is 5.2/3.5 mm Hg. Afterload increased first to 4 U (60–120 s) and then to 10 U (120–180 s). Note that at each step CO is transiently significantly decreased, but within about 20 s it recovers to a new steady state, slightly lower level. Similarly, SV is slightly decreased. AP is increased. AtP max and AtP min are increased to a different extent; therefore, AtP pulse pressure is decreased. After afterload is returned to 4 U, AP, AtP, and VV return to initial conditions level. CO is transiently increased but within about 15 s it also returns to the initial condition level. (b) The P-V loop diagram in conditions above. Note that, if afterload is increased from 4 U to 10 U, ESVV is increased from 39 mL to about 62 mL, while EDVV is increased to a smaller extent, from 117 mL to 127 mL. The EF decreases from 66% to 51%. Ventricular work is given in mm Hg·mL and in J.

intrathoracic pressure and negative feedback) this value was decreased to 0.2 s and used in all simulations which followed.

When discussing the Starling heart-lung preparation it should be borne in mind that its behavior critically depends on the experimental layout; either the so-called “closed-circuit heart-lung preparation” [24] or the so-called called “open-circuit heart-lung preparation” [25] (also reviewed by [20, 21]).

In the “closed-circuit heart-lung preparation” blood volume is constant. The pumping action of the heart is determined not only by preload and afterload, but also by the capacitance of the attached artificial vascular circuit

[16]. Its basic behavior is similar to the simulation of a simplified human cardiovascular system [16] which has been continuously upgraded [18, 19].

To demonstrate The Law of the Heart the so-called “open-circuit heart-lung preparation” (Figure 1(a)) should be used as already reported [16]. The attached “vascular” circuit should be very much simplified and include a venous reservoir [16]. It should be remembered, however, that also in this case vascular circuit is elastic. The blood volume within the circuit is not constant and depends on pressure in various sections. If for example, preload is increased, the “venous” volume and pressure are increased. As in the EEC,

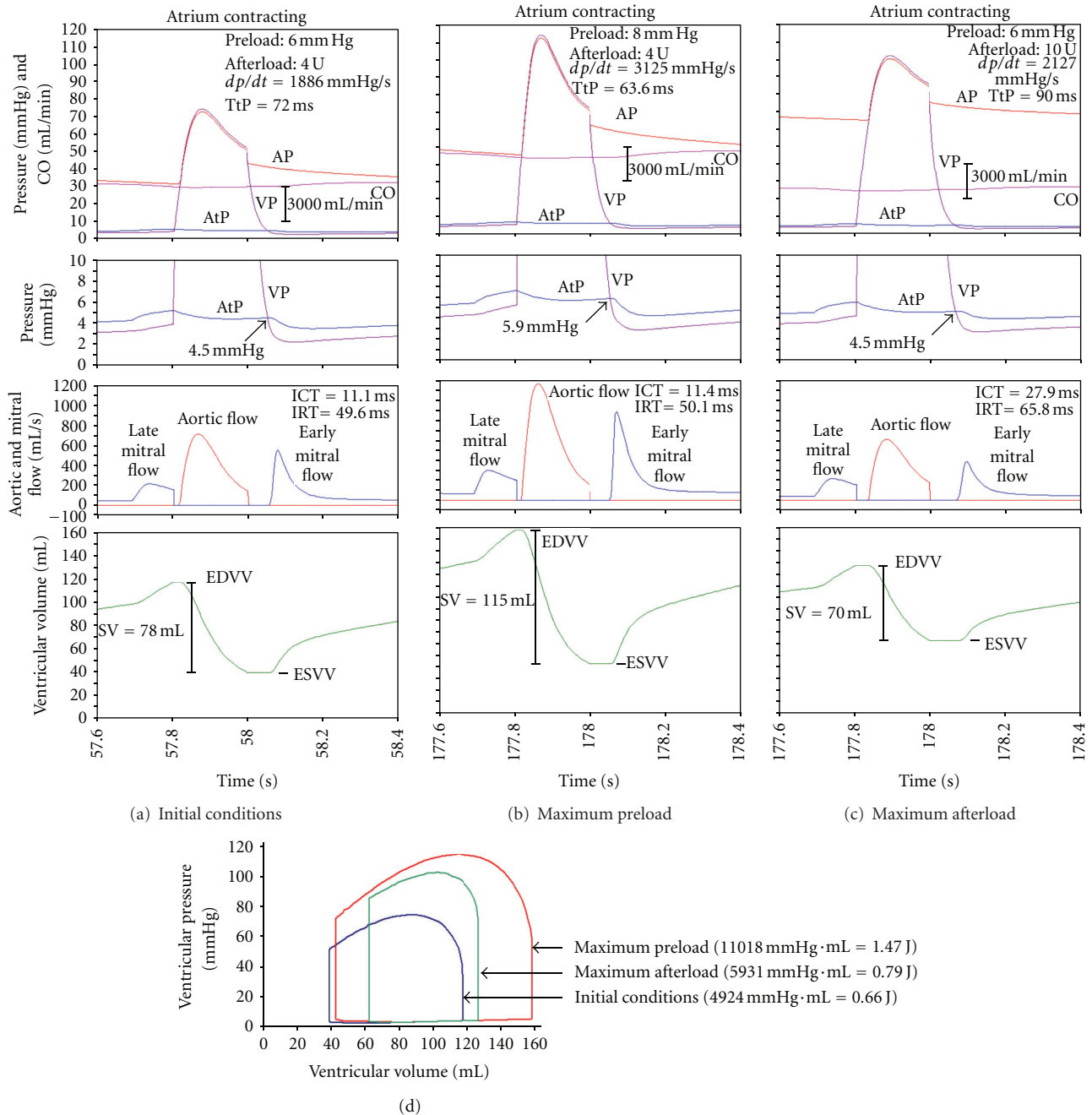


FIGURE 5: Sample values of cardiovascular variables in a single cardiac cycle during initial conditions (column a), maximal preload (column b), or maximal afterload (column c) when atrium is contracting. Each column is subdivided in four blocks. Upper two blocks: AP, VP, AtP, and CO (VP and AtP also at an enlarged pressure scale). Middle block: mitral flow and aortic flow. Bottom block: EDVV, ESVV, and SV. Note the “hump” in AtP in late diastole. Note also that the early mitral flow commences when AtP = VP. The higher is this pressure, the higher is peak early mitral flow. (a) Initial conditions (57.6 s–58.4 s of simulation time). Note that atrial contraction (immediately prior to the ventricular contraction) results in a late mitral flow, increasing EDVV by about 20 mL. Aortic flow is synchronous with ventricular contraction; this flow is stopped abruptly as soon as VP is lower than AP. Early mitral flow starts as soon as VP is lower than AtP. (b) Preload increased to 8 mm Hg (177.6 s–178.4 s of simulation time). Note that AP and VP are strongly increased. Similarly, both mitral flows and aortic flow are increased, and consequently EDVV, SV, and CO are strongly increased. Almost no change in ESVV, in ICT, and in IRT. dp/dt is increased from the resting value 1886 mm Hg/s to 3125 mm Hg/s; consequently, TtP is decreased from its resting value 72 ms to 63.6 ms. (c) Afterload increased to 10 U (177.6 s–178.4 s of simulation time). Note that both AP and VP are strongly increased. However, both mitral flows and aortic flow are decreased. Consequently EDVV and ESVV increase in an unequal extent, so that SV and consequently CO are slightly decreased. Note also that both ICT and IRT are increased. dp/dt is slightly increased from the resting value 1886 mm Hg/s to 2127 mm Hg/s; consequently TtP is increased from its resting value 72 ms to 90 ms. (d) The P-V loop diagram of the conditions above. If preload is increased, the loop diagram becomes broader. Both ventricular pressure and SV are increased. If afterload is increased, the loop diagram becomes narrower. Ventricular pressure is increased, but SV is slightly decreased. Ventricular work is given in mm Hg · mL and in J.

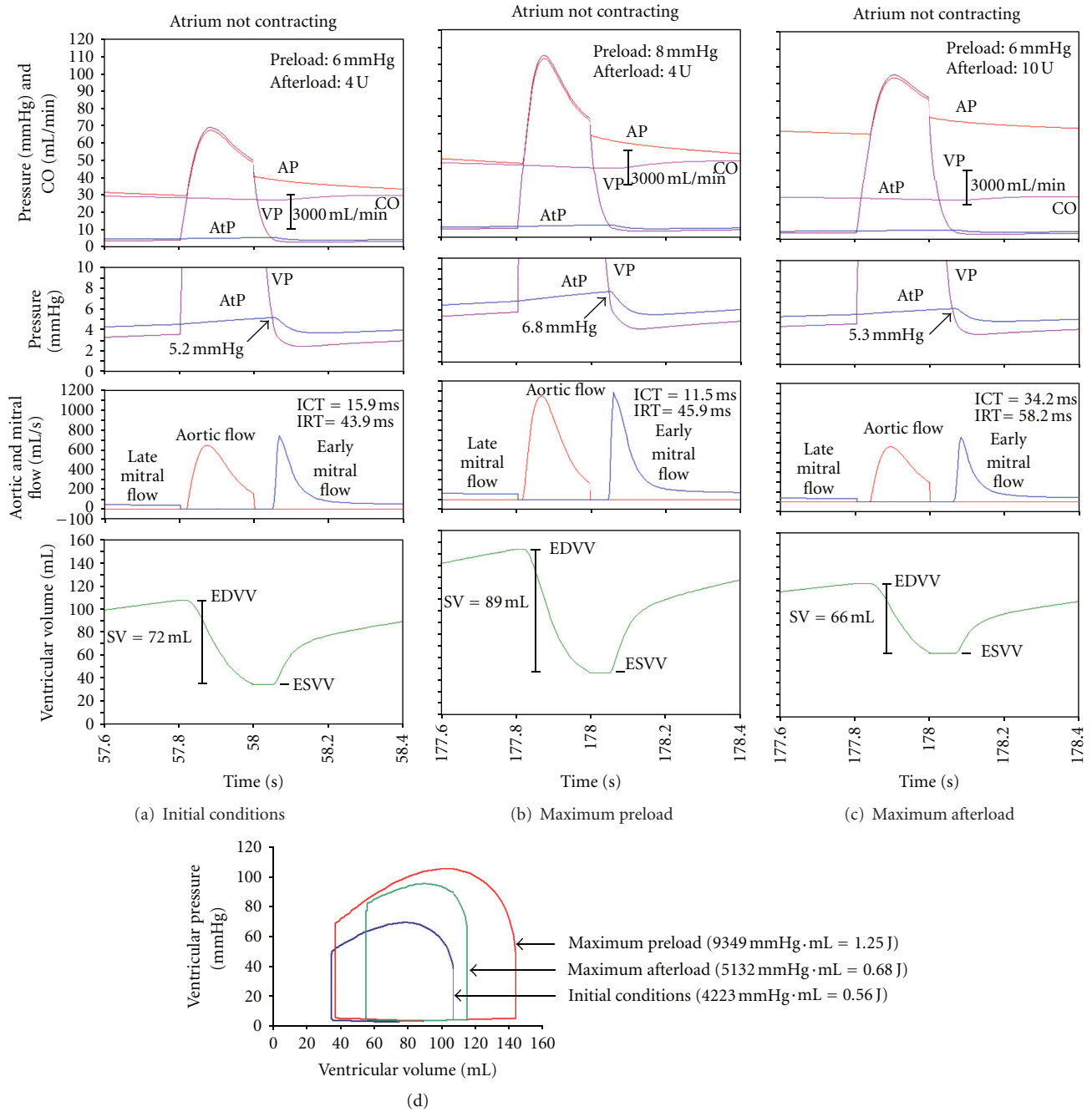


FIGURE 6: Sample values of cardiovascular variables in a single cardiac cycle during initial conditions (column a), maximal preload (column b), or maximal afterload (column c) when atrium is not contracting. Each column is subdivided in four blocks. Details are the same as in Figure 5. If atrium is not contracting, there is no “hump” in AtP in late diastole. However, also in this condition the early mitral flow commences when $AtP = VP$. However, AtP is higher (cf. Figure 5). Therefore, if atrium is not contracting, peak early mitral flow is higher. Data, presented in columns (a, b, and c), are qualitatively similar to those shown in Figure 5. Similarly, the P-V loop diagram (d) is qualitatively similar to that shown in Figure 5.

the blood flow meter is inserted at the end of the “venous” section and the increased preload transiently decreases CO. However, a new, higher steady-state level is established within about 10 s (Figure 3(a)). A similar, transient decrease in CO occurs if afterload is increased. However, as AP begins to increase, CO recovers gradually, in steady-state conditions

CO is only slightly lower compared to initial conditions (Figure 4(a)). Changes in the time course of arterial pressure and ventricular volume agree well with the changes in the corresponding P-V loop diagrams (Figures 3(b) and 4(b)).

Simulations presented in this paper (e.g., aortic and ventricular pressure, ventricular volume) are qualitatively

very similar to those described earlier ([16]; cf. [20, 21]). Quantitatively, however, there are many expected and readily explicable differences (cf. [25]).

4.2. Specific Comments on the Simulation of the Law of the Heart with Contracting Atrium. In the simulation of the Law of the Heart *quantitative* differences are expected because in the simulation circuit it is not possible to exactly match the size and detailed layout of the real heart-lung preparation. As shown in [25–27], the size of the mammalian ventricle (dogs and cats of variable weight) can vary considerably, resulting—even in the real heart-lung preparation—in a considerable variation of arterial pressure. *Qualitatively*, however, the presented simulations of the Law of the Heart agree very well with experimental data. For example, when preload was increased, in the animal heart-lung preparation, from 20 mm H₂O to 210 mm H₂O, cardiac output was increased from 40 mL/10 s to 250 mL/10 s [25]. Contrary to that, within wide limits, cardiac output was independent of arterial resistance (i.e., afterload [27]). If, for example, arterial resistance was increased from 44 mm Hg to 208 mm Hg, cardiac output remained constant at about 820 mL/min–860 mL/min as presented in [26] and reviewed in [20, 21]. In comparison, the corresponding results of the EEC computer simulation are as follows:

- (1) The stroke volume of the ventricle (and consequently cardiac output and AP pulse pressure) is highly increased if preload is increased from 6 mm Hg to 8 mm Hg (increased by a relatively small extent, by 33%). The ventricle is an input-sensitive pump (Figures 3–6).
- (2) The stroke volume of the ventricle (and consequently cardiac output and AP pulse pressure) is only slightly decreased if afterload is increased from 4 U to 10 U (increased considerably, by 250%). The ventricle is an *output-insensitive* pump (Figures 3–6).

To explain the basic findings above it should be remembered that, if atrium and ventricle are contracting/relaxing, blood circulates in the attached circuit. If so, atrial pressure is not exactly equal to preload. Atrial pressure is always slightly lower than preload (Figure 3). Due to blood flow, there is always a small pressure drop across the conduit between the mouth of the venous reservoir and atrium. In initial conditions, for example, when preload is 6 mm Hg, the AtP max/AtP min ratio is 5.2 mm Hg to 3.5 mm Hg (Figure 3). It should also be noted that, as a rule, the AtP pulse changes in parallel to the range of ventricular volume; the changes in EDVV, ESVV, and SV. If preload is increased from 6 mm Hg to 8 mm Hg (by 33%), both atrial pressure and its pulse pressure are increased; the AtP max/AtP min ratio is 6.7 mm Hg to 4.3 mm Hg (Figure 3(a)). End-systolic AtP is increased from 4.5 mm Hg to 5.9 mm Hg (Figures 5(a) and 5(b)). Similarly, SV is increased. Due to the increased ventricular filling (increased EDVV), the force and rate of ventricular contraction are increased and TtP is decreased. Therefore, CO, AP, and AP pulse pressure increase, and ICT remains virtually unchanged.

Afterload is determined predominantly by “peripheral” resistance; its large increase (250%) results in a relatively small decrease in cardiac output (–17%). Therefore, its effect can be neglected. If afterload is increased from 4 U to 10 U (by 250%), AtP is slightly increased while AtP pulse is decreased; the AtP max/AtP min ratio is 5.6 mm Hg to 3.9 mm Hg (Figure 4(a)). However, end-systolic AtP remains virtually unchanged, 4.5 mm Hg (Figures 5(a) and 5(c)). Therefore, EDVV is slightly increased, reflecting a slightly increased diastolic distension. Consequently, peak VP, peak AP are increased. dp/dt and TtP are mildly increased. This means a better filling of left ventricle (reflected by increased EDVV) but, on the other hand, a slightly decreased emptying of left ventricle (increased ESVV). All these changes almost fully compensate the increased afterload. Therefore SV, CO, and AP pulse pressure are only slightly decreased.

Somewhat unexpected is the finding that throughout early and mid diastole the atrial-ventricular pressure difference is very small. But despite this fact the early mitral flow is relatively large. This indicates that the ventricular filling is achieved mainly by its rapid relaxation. The late mitral flow in late diastole, affected by atrial contraction, is relatively large, but very brief, only about 0.1 s. Therefore, in resting conditions, atrial contraction contributes only about 20% to the increased end-diastolic volume of the ventricle; cardiac output is about 4570 mL/min.

4.3. Specific Comments on the Simulation of the Law of the Heart with Notcontracting Atrium. The effects of increasing preload or increasing afterload, when atrium is not contracting, are qualitatively the same as when atrium is contracting (Figure 6). Quantitatively, however, there are differences.

- (1) If atrium is not contracting, cardiac output is about 4200 mL/min, which is slightly lower compared to 4570 mL/min if atrium is contracting.
- (2) Late mitral flow, due to atrial contraction, is absent (Figure 6). However, the early mitral flow is larger compared to that if atrium is contracting. This finding is in agreement with that expressed above: the diastolic filling of the ventricle is achieved mainly through vigorous ventricular contraction followed by ventricle relaxation.
- (3) It should be noted that the early mitral flow commences as soon as atrial pressure equals the ventricular pressure, that is, when AtP = VP. If atrium is not contracting, this pressure equals 5.2 mm Hg (Figure 6(a)). Peak early mitral flow is about 710 mL/s. If atrium is contracting, this pressure is lower; it equals 4.5 mm Hg (Figure 5(a)). Peak early mitral flow is lower, about 550 mL/s (Figure 5(a)). Similar data are obtained by comparing Figures 6(b) (6.8 mm Hg) and 5(b) (5.9 mm Hg), or 6(c) (5.3 mm Hg) and 5(c) (4.5 mm Hg). This finding, although seemingly paradox, is in excellent agreement with the fact that the atrial pressure in late ventricular systole is the higher, the weaker is atrial contraction, and the lower is the cardiac output.

To summarize, if atrium is contracting, cardiac output is about 4500 mL/min and AtP , at the end of ventricular systole, is 4.5 mm Hg. Therefore, maximal early mitral flow is about 550 mL/s and is determined almost exclusively by AtP . If, however, atrium is not contracting, cardiac output is lower, about 4200 mL/min and AtP , at the end of ventricular systole, is higher, 5.2 mm Hg. Therefore, maximal early mitral flow is also higher, about 710 mL/s, and is determined almost exclusively by AtP . The increased early mitral flow is a partial compensation for the decreased total mitral flow, due to the absence of atrial contraction.

4.4. Answers to the Three Basic Questions on the Mechanical Properties of the Ventricle

(1) *What is the Role of Atrium in the Filling of the Ventricle, if the Latter is Subjected to Increased Preload or Increased Afterload?* In resting conditions, the role of atrium in the filling of the ventricle is relatively small since firstly, the absence of atrial contraction is partially compensated with an increased early mitral flow and secondly, the ventricular filling is achieved mainly by its rapid relaxation. If the ventricle is subjected to increased preload or increased afterload, the rapid ventricular diastolic relaxation is the main mechanism for the ventricular diastolic filling.

(2) *Why is the Ventricle a Highly Input Sensitive Pump, but at the Same Time a Relatively Output Insensitive Pump?* The ventricle is a highly input sensitive pump because the input pressure determines the diastolic distension and, consequently, the force of ventricular systolic contraction. On the other hand, the ventricle is a relatively output insensitive pump. Due to mechanisms described above, increased afterload results in an increased ventricular diastolic distension. Therefore, a more vigorous ventricular systolic contraction follows, almost compensating increased aortic pressure. Therefore, in resting conditions, ventricular (cardiac) output is almost independent of afterload.

(3) *What is the Change in the P-V Loop Diagram if the Ventricle is Subjected to Increased Preload or Increased Afterload?* In increased preload the P-V loop diagram becomes broader (i.e., a shift to higher EDV with almost no change in ESV, which strongly increases SV) and higher (with higher ventricular pressure). In increased afterload the P-V loop diagram becomes narrower (i.e., both EDV and ESV are increased, but the former to a larger extent than the latter, which slightly decreases the SV) and higher.

5. Conclusions

To our knowledge, the presented EEC is the first computer simulation to explicitly simulate the Frank-Starling Law of the Heart. With the presented software, the Frank-Starling Law of the Heart can be demonstrated without the need to perform a technically difficult animal preparation that requires skilled staff and access to a suitable live animal model. Also, simulated measurements of selected cardiovascular variables (i.e., mitral or aortic flow) are possible and do

not increase the cost or the complexity of the demonstration. Finally, when live animal preparations are impractical, the presented computer-based simulation offers a technically simple and low-cost alternative for demonstrating the Frank-Starling Law of the Heart. The presented EEC could be an excellent tool in cardiovascular research, on the one hand, to study how the ventricle, during contraction, adapts itself to a resistive or capacitive load, for example, in hypertension or in greatly changed aortic elastance. On the other hand, the ventricular relaxation, the ventricular filling process, and its dependence on the heart rate can be quantitatively studied in great detail.

Conflict of Interests

The authors report no conflicts of interests.

Acknowledgments

This work was supported by the Slovenian Research Agency of the Republic of Slovenia, Grant no. P3-0171. The authors alone are responsible for the content and writing of the article.

References

- [1] J. E. W. Beneken, *A mathematical approach to cardiovascular function. The uncontrolled human system [Ph.D. thesis]*, Institute of Medical Physics TNO, Utrecht, Da Costakade, 1965.
- [2] J. G. Defares, J. J. Osborn, and H. H. Hara, "Theoretical synthesis of the cardiovascular system. Study I: the controlled system," *Acta Physiologica et Pharmacologica Neerlandica*, vol. 12, pp. 189–265, 1963.
- [3] J. G. Defares, J. J. Osborn, and H. H. Hara, "On the theory of the cardiovascular system," *The Bulletin of Mathematical Biophysics*, vol. 27, no. 1, pp. 71–83, 1965.
- [4] F. S. Grodins, "Integrative cardiovascular physiology: a mathematical synthesis of cardiac and blood vessel hemodynamics," *The Quarterly Review of Biology*, vol. 34, no. 2, pp. 93–116, 1959.
- [5] J. E. W. Beneken and B. DeWit, "A physical approach to hemodynamic aspects of the human cardiovascular system," in *Physical Bases of Circulatory Transport*, pp. 1–45, W. B. Saunders, Philadelphia, Pa, USA, 1967.
- [6] J. J. Osborn, W. Hoehne, and W. Badia, "Ventricular function in the basic regulation of the circulation: studies with a mechanical analog," in *Physical Bases of Circulatory Transport, Regulation and Exchange*, pp. 47–60, W. B. Saunders, Philadelphia, Pa, USA, 1967.
- [7] S. Topham and H. R. Warner, "The control of cardiac output during exercise," in *Physical Bases of Circulatory Transport, Regulation and Exchange*, pp. 77–90, W. B. Saunders, Philadelphia, Pa, USA, 1967.
- [8] G. Wright, O. V. Korchazkhina, and S. Zhang, "Evaluation of a lumped parameter model for isolated working rat hearts," *Medical and Biological Engineering and Computing*, vol. 37, no. 2, pp. 190–195, 1999.
- [9] P. Segers, N. Stergiopoulos, N. Westerhof, P. Wouters, P. Kolh, and P. Verdonck, "Systematic and pulmonary hemodynamics assessed with a lumped-parameter heart-arterial interaction model," *Journal of Engineering Mathematics*, vol. 47, no. 3–4, pp. 185–199, 2003.

- [10] B. H. Maines and C. E. Brennen, "Lumped parameter model for computing the minimum pressure during mechanical heart valve closure," *Journal of Biomechanical Engineering*, vol. 127, no. 4, pp. 648–655, 2005.
- [11] M. Korürek, M. Yildiz, and A. Yüksel, "Simulation of normal cardiovascular system and severe aortic stenosis using equivalent electronic model," *Anadolu Kardiyoloji Dergisi*, vol. 10, no. 6, pp. 471–478, 2010.
- [12] T. Korakianitis and Y. Shi, "Numerical simulation of cardiovascular dynamics with healthy and diseased heart valves," *Journal of Biomechanics*, vol. 39, no. 11, pp. 1964–1982, 2006.
- [13] H. J. Kim, I. E. Vignon-Clementel, C. A. Figueroa et al., "On coupling a lumped parameter heart model and a three-dimensional finite element aorta model," *Annals of Biomedical Engineering*, vol. 37, no. 11, pp. 2153–2169, 2009.
- [14] E. Jung and W. Lee, "Lumped parameter models of cardiovascular circulation in normal and arrhythmia cases," *Journal of the Korean Mathematical Society*, vol. 43, no. 4, pp. 885–897, 2006.
- [15] L. Formaggia, D. Lamponi, M. Tuveri, and A. Veneziani, "Numerical modeling of 1D arterial networks coupled with a lumped parameters description of the heart," *Computer Methods in Biomechanics and Biomedical Engineering*, vol. 9, no. 5, pp. 273–288, 2006.
- [16] M. Rupnik, F. Runovc, D. Sket, and M. Kordaš, "Cardiovascular physiology: simulation of steady state and transient phenomena by using the equivalent electronic circuit," *Computer Methods and Programs in Biomedicine*, vol. 67, no. 1, pp. 1–12, 2002.
- [17] T. Podnar, F. Runovc, and M. Kordaš, "Simulation of cardiovascular physiology: the diastolic function(s) of the heart," *Computers in Biology and Medicine*, vol. 32, no. 5, pp. 363–377, 2002.
- [18] J. Dolenšek, T. Podnar, F. Runovc, and M. Kordaš, "Analog simulation of aortic and of mitral regurgitation," *Computers in Biology and Medicine*, vol. 39, no. 5, pp. 474–481, 2009.
- [19] M. Sever, S. Ribarič, F. Runovc, and M. Kordaš, "Analog simulation of aortic stenosis," 2011, <http://www.intecho-pen.com/books/show/title/aortic-stenosis-etiology-pathophysiologyand-treatment>.
- [20] H. G. Zimmer, "Who discovered the Frank-Starling mechanism?" *News in Physiological Sciences*, vol. 17, no. 5, pp. 181–184, 2002.
- [21] A. M. Katz, "Ernest Henry Starling, his predecessors, and the 'Law of the Heart,'" *Circulation*, vol. 106, no. 23, pp. 2986–2992, 2002.
- [22] J. Adams, *Mastering Electronics Workbench*, McGraw-Hill, New York, NY, USA, 1st edition, 2001.
- [23] T. Podnar, F. Runovc, I. Milisav, and M. Kordaš, "Simulation of some short-term control mechanisms in cardiovascular physiology," *Computers in Biology and Medicine*, vol. 34, no. 1, pp. 35–49, 2004.
- [24] I. De Burgh Daly, "A closed-circuit heart-lung preparation. Effects of alterations in the peripheral resistance and in the capacity of the circulation," *Proceedings of the Royal Society*, vol. 99, no. 697, pp. 306–325, 1926.
- [25] S. W. Patterson, H. Piper, and E. H. Starling, "The regulation of the heart beat," *Journal of Physiology*, vol. 48, pp. 465–513, 1914.
- [26] J. Markwalder and E. H. Starling, "On the constancy of the systolic output under varying conditions," *Journal of Physiology*, vol. 48, pp. 348–356, 1914.
- [27] F. P. Knowlton and E. H. Starling, "The influence in temperature and blood-pressure on the performance of the isolated mammalian heart," *Journal of Physiology*, vol. 44, pp. 206–219, 1912.

Research Article

Simulations of Complex and Microscopic Models of Cardiac Electrophysiology Powered by Multi-GPU Platforms

Bruno Gouvêa de Barros,¹ Rafael Sachetto Oliveira,^{2,3} Wagner Meira Jr.,³ Marcelo Lobosco,¹ and Rodrigo Weber dos Santos¹

¹ *Computational Modeling, Federal University of Juiz de Fora, 36036-900 Juiz de Fora, MG, Brazil*

² *Computer Science, Federal University of São João del-Rei, 36307-352 São João del-Rei, MG, Brazil*

³ *Computer Science, Federal University of Minas Gerais, 31270-901 Belo Horizonte, MG, Brazil*

Correspondence should be addressed to Rodrigo Weber dos Santos, rodrigo.weber@ufjf.edu.br

Received 3 August 2012; Revised 28 September 2012; Accepted 1 October 2012

Academic Editor: Ling Xia

Copyright © 2012 Bruno Gouvêa de Barros et al. This is an open access article distributed under the Creative Commons Attribution License, which permits unrestricted use, distribution, and reproduction in any medium, provided the original work is properly cited.

Key aspects of cardiac electrophysiology, such as slow conduction, conduction block, and saltatory effects have been the research topic of many studies since they are strongly related to cardiac arrhythmia, reentry, fibrillation, or defibrillation. However, to reproduce these phenomena the numerical models need to use subcellular discretization for the solution of the PDEs and nonuniform, heterogeneous tissue electric conductivity. Due to the high computational costs of simulations that reproduce the fine microstructure of cardiac tissue, previous studies have considered tissue experiments of small or moderate sizes and used simple cardiac cell models. In this paper, we develop a cardiac electrophysiology model that captures the microstructure of cardiac tissue by using a very fine spatial discretization ($8\ \mu\text{m}$) and uses a very modern and complex cell model based on Markov chains for the characterization of ion channel's structure and dynamics. To cope with the computational challenges, the model was parallelized using a hybrid approach: cluster computing and GPGPUs (general-purpose computing on graphics processing units). Our parallel implementation of this model using a multi-GPU platform was able to reduce the execution times of the simulations from more than 6 days (on a single processor) to 21 minutes (on a small 8-node cluster equipped with 16 GPUs, i.e., 2 GPUs per node).

1. Introduction

Heart diseases are responsible for one third of all deaths worldwide [1]. Cardiac electrophysiology is the trigger to the mechanical deformation of the heart. Therefore, the knowledge of cardiac electrophysiology is essential to understand many aspects of cardiac physiological and pathophysiological behavior [2]. Computer models of cardiac electrophysiology [3, 4] have become valuable tools for the study and comprehension of such complex phenomena, as they allow different information acquired from different physical scales and experiments to be combined to generate a better picture of the whole system functionality. Not surprisingly, the high complexity of the biophysical processes translates into complex mathematical and computational models. Modern cardiac models are described by nonlinear system of partial

differential equations (PDEs) that may result in a problem with millions of unknowns.

Mathematical models for cell electrophysiology are a key component of cardiac modeling. They serve both as standalone research tools, to investigate the behavior of single cardiac myocytes, and as an essential component of tissue and organ simulation based on the so-called bidomain or monodomain models [4]. The cell models can be written as a general non-linear system of ordinary differential equations (ODEs) and may vary in complexity from simple phenomenological models [5] (based on two variables) to complex models describing a large number of detailed physiological processes [6] (based on 40 to 80 differential variables). Simple models focus on the genesis of action potential (AP), that propagates from cell to cell and generates an electric wave that propagates on the heart. Complex models

account not only for the genesis of AP but also describe how this phenomenon is related to cardiac homeostasis and to different sub-cellular components, such as cell membrane's ion channels. Advances in genetics, molecular biology, and electrophysiology experiments have provided new data and information related to the structure and function of ion channels. The Markov Chain (MC) model formalism has been increasingly used to describe both function and structure of ion channels. MC-based models have enabled simulations of structural abnormalities due to genetic diseases and drug-biding effects on ion channels [7–9]. Unfortunately, these modern cardiac myocyte models pose different challenges to both numerical methods, due to the stiffness of the ODEs introduced by MCs, and to high performance computing, due to the size of the problems, since the number of differential variables rises from a couple to near a hundred [10].

On the tissue level, the bidomain model [4] is considered to be the most complete description of the electrical activity. This nonlinear system of PDEs can be simplified to the so-called monodomain model, which may be less accurate but less computationally demanding than the bidomain model. Unfortunately, large scale simulations, such as those resulting from the discretization of an entire heart, remain a computational challenge. In addition, key aspects of cardiac electrophysiology, such as slow conduction, conduction block, and saltatory or sawtooth effects, demand sub-cellular discretization for the solution of the PDEs and nonuniform, heterogeneous tissue electric conductivity. These aspects of cardiac electrophysiology are strongly related to cardiac arrhythmia, reentry, fibrillation or defibrillation, and have been the research topic of many studies [11–20].

However, the demand of sub-cellular discretization for the solution of the PDEs and nonuniform, heterogeneous tissue electric conductivity have prevented the study of the aforementioned phenomena on large-scale tissue simulations. In addition, due to the high computational costs associated with the simulations of these microscopic models of cardiac tissue, previous works have adopted simple myocyte models, instead of modern MC-based models [6, 10].

In this work, we present a solution for this problem based on multi-GPU platforms (clusters equipped with graphics processing units) that allows fast simulations of microscopic tissue models combined with modern and complex myocyte models. The solution is based on merging two different high-performance techniques. We have previously investigated for cardiac modeling: cluster computing based on message passing communications (MPI) [21–24] and GPGPU (General-purpose computing on graphics processing units) [25–30]. We developed a two-dimensional model that is based on the previous work of Spach and collaborators [11, 17] that accounts for the microstructure of cardiac tissue, gap junction heterogeneous distribution, and discretizations of $8\mu\text{m}$. This microscopic tissue model was combined with the model of Bondarenko et al. [6] which is a modern and complex myocyte model based on MCs. Our parallel implementation of this model using a multi-GPU platform was able to reduce the execution times of the simulations from more than 6 days (on a single processor) to 21 minutes

(on a small 8-node cluster equipped with 16 GPUs, that is, 2 GPUs per node). As a result, using this very fast parallel implementation we were able to simulate the formation of spiral waves, a form of self-sustained reentrant activity strongly associated with cardiac arrhythmia. To the best of our knowledge, this is the first time spiral waves are simulated using a cardiac model that accounts for both the microstructure of cardiac tissue and a modern and complex myocyte model.

2. Methods

2.1. Modeling Cardiac Microstructure. We developed a two-dimensional model that is based on the previous work of Spach and collaborators [11, 17] that accounts for the microstructure of cardiac tissue, gap junction heterogeneous distribution, and discretizations of $8\mu\text{m} \times 8\mu\text{m}$. A basic template for myocyte connections was developed and is presented in Figure 1. This basic unit accounts for the connection of a total of 32 cardiac myocytes with different shapes and numbers of neighboring cells. The mean and SD (standard deviation) values for cell length and width are $120.9 \pm 27.8\mu\text{m}$ and $18.3 \pm 3.5\mu\text{m}$, respectively. These values are close to those reported in the literature: [31] (length = $140\mu\text{m}$ and width = $19\mu\text{m}$), [32] (length = $134\mu\text{m}$ and width = $18\mu\text{m}$), and [20] (length = $100\mu\text{m}$ and width = $17.32\mu\text{m}$). On average, each cell connects to other 6 neighboring myocytes. Our two-dimensional model considers a homogeneous depth $d = 10\mu\text{m}$ [11, 17].

This basic unit was created in such a way that it allows the generation of larger tissue preparations via the connections of multiple instances of it. Figure 2 presents how this can be achieved.

Figure 3 presents an example of how the connections between different myocytes can be arranged. The code was developed in a flexible way, so that it allows the user to set up for each discretized volume $\text{Vol}_{i,j}$ (with area = $h \times h$) conductivity or conductance values for the north ($\sigma_{x_{i,j+1/2}}$), south ($\sigma_{x_{i,j-1/2}}$), west ($\sigma_{x_{i-1/2,j}}$), and east ($\sigma_{x_{i+1/2,j}}$) volume faces. These can be any nonnegative values. In this work, we set the discretization h to $8\mu\text{m}$. In addition, based on the work of Spach and collaborators [11, 17], we chose only 5 possible types of connections between neighboring volumes that are membrane ($\sigma_m = 0.0$), cytoplasm ($\sigma_c = 0.4\mu\text{S}/\mu\text{m}$), gap junction plicate ($G_p = 0.5\mu\text{S}$), interplicate ($G_i = 0.33\mu\text{S}$), and combined plicate ($G_c = 0.062\mu\text{S}$), where we use σ for conductivity and G for conductance. For the simulations presented in this work, the distribution of the different gap junctions within the 32 myocytes was not randomly generated. Instead, the gap junction distribution of the basic template unit was manually chosen to reproduce the distribution presented before in [11, 17]. With this setup and conductivity values we found that conduction velocity along the fibers was around $410\mu\text{m}/\text{ms}$ (LP) and was $130\mu\text{m}/\text{ms}$ transversal to fiber direction (TP). This results in a ratio LP/TP of 0.32, which is close to the conduction ratio reported in [11].

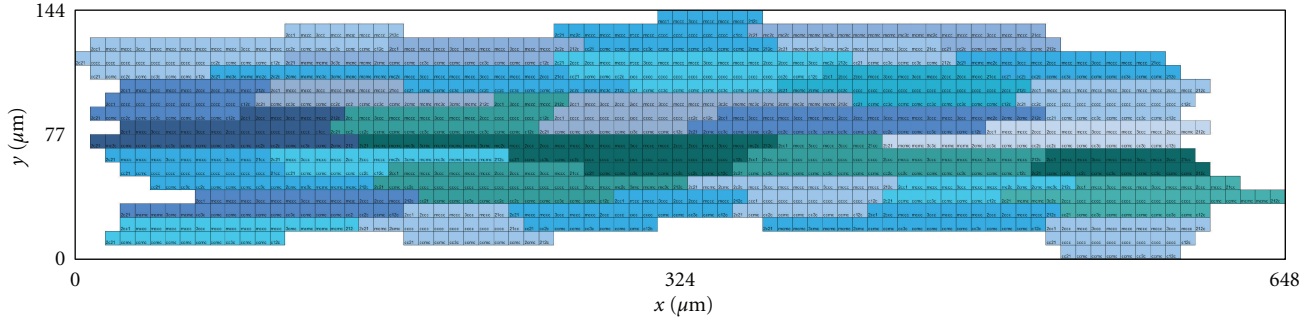


FIGURE 1: Basic unit of cardiac myocyte distribution based on a total of 32 cells. Cells are displayed in different alternating colors along the x -axis. The basic unit spans a total of $648 \mu\text{m}$ in the longitudinal direction versus $144 \mu\text{m}$ in the transversal direction.

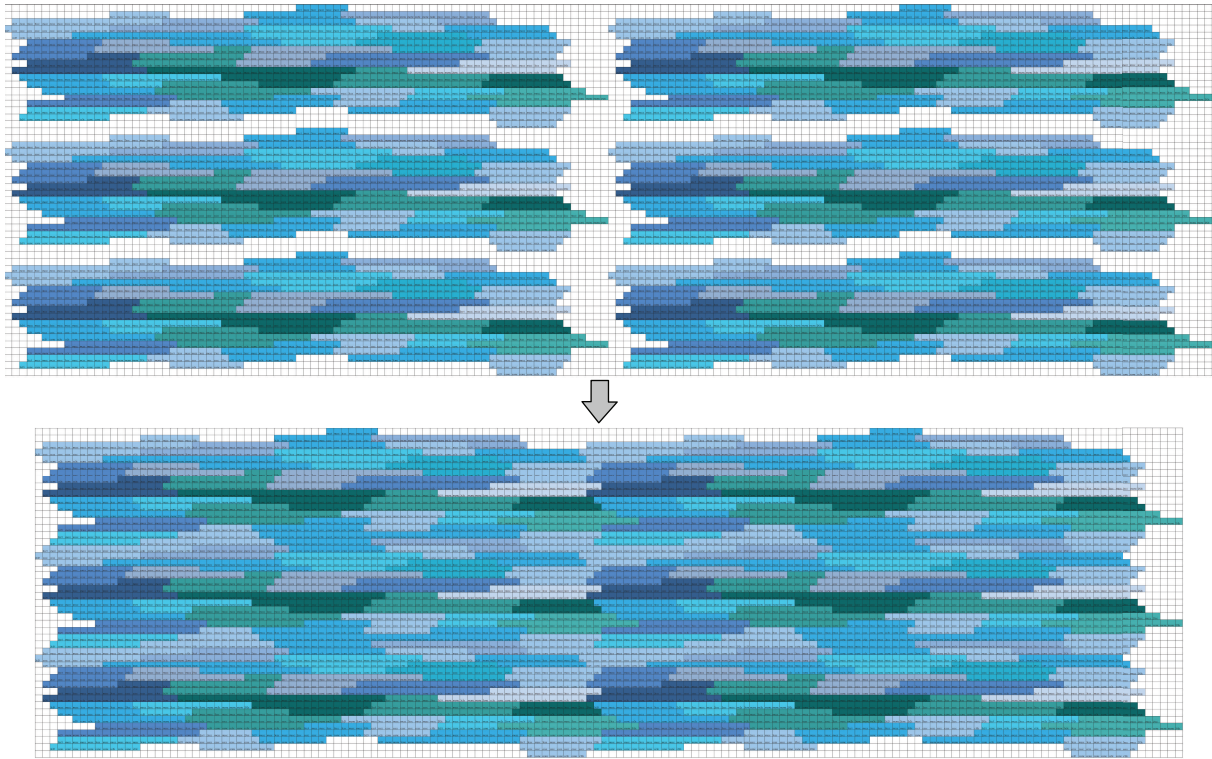


FIGURE 2: Six basic units being combined to form a larger tissue.

2.2. *The Heterogeneous Monodomain Model.* Action potentials propagate through the cardiac tissue because the intracellular space of cardiac cells is electrically coupled by gap junctions. In this work, we do not consider the effects of the extracellular matrix. Therefore, the phenomenon can be described mathematically by a reaction-diffusion type partial differential equation (PDE) called monodomain model, given by

$$\begin{aligned} \beta C_m \frac{\partial V(x, y, t)}{\partial t} + \beta I_{\text{ion}}(V(x, y, t), \boldsymbol{\eta}(x, y, t)) \\ = \nabla \cdot (\boldsymbol{\sigma}(x, y) \nabla V(x, y, t)) + I_{\text{stim}}(x, y, t), \quad (1) \\ \frac{\partial \boldsymbol{\eta}(x, y, t)}{\partial t} = \mathbf{f}(V(x, y, t), \boldsymbol{\eta}(x, y, t)), \end{aligned}$$

where V is the variable of interest and represents the transmembrane potential, that is, the difference between intracellular to extracellular potential; $\boldsymbol{\eta}$ is a vector of state variables that also influences the generation and propagation of the electric wave and usually includes the intracellular concentration of different ions (K^+ , Na^+ , Ca^{2+}) and the permeability of different membrane ion channels; β is the surface-volume ratio of heart cells; C_m is the membrane capacitance, I_{ion} the total ionic current, which is a function of V and a vector of state variables $\boldsymbol{\eta}$; I_{stim} is the current due to an external stimulus, $\boldsymbol{\sigma}$ is the monodomain conductivity tensor. We assume that the boundary of the tissue is isolated, that is, no-flux boundary conditions ($\mathbf{n} \cdot \boldsymbol{\sigma} \nabla V = 0$ on $\partial\Omega$).

In this work, the modern and complex Bondarenko et al. model [6] that describes the electrical activity of left

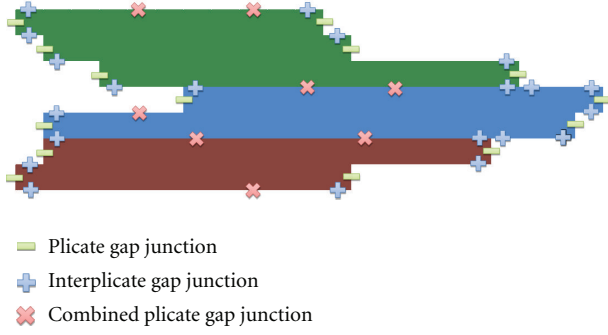


FIGURE 3: In this work, there are only 5 possible types of connections between neighboring volumes that are membrane, which indicates no-flux between neighboring volumes; cytoplasm, which indicates that the neighboring volumes are within the same cell; three possible types of gap junctions, plicate, interplicate, and combined plicate. For the simulations presented in this work, the gap junction distribution of the basic template unit was manually chosen to reproduce the distribution presented before in [11, 17]. This figure presents an example of how different gap junctions are distributed in three neighboring myocytes that belong to the basic unit.

ventricular cells of mice was considered to simulate the kinetics of I_{ion} in (1). The Bondarenko et al. model (BDK) was the first model presented for mouse ventricular myocytes [6]. The ionic current term I_{ion} in this model consists of the sum of 15 transmembrane currents. In short, Bondarenko's model is based on an ordinary differential equation (ODE) with 41 differential variables that control ionic currents and cellular homeostasis. In this model, most of the ionic channels are represented by Markov chains (MCs).

2.3. Numerical Discretization in Space and Time. The finite volume method (FVM) is a mathematical method used to obtain a discrete version of partial differential equations. This method is suitable for numerical simulations of various types of conservation laws (elliptical, parabolic, or hyperbolic) [33]. Like the finite element method (FEM), the FVM can be used in several types of geometry, using structured or unstructured meshes, and generates robust numerical schemes. The development of the method is intrinsically linked to the concept of flow between regions or adjacent volumes, that is, it is based on the numerical calculation of net fluxes into or out of a control volume. For some isotropic problems discretized with regular spatial meshes, the discretization obtained with the FVM is very similar to the one obtained with the standard finite difference method (FDM).

This section presents a brief description of the FVM application to the time and spatial discretization of the heterogeneous monodomain equations. Detailed information about the FVM applied to the solution of monodomain can be found in [34, 35].

2.3.1. Time Discretization. The reaction and diffusion parts of the monodomain equations were split by employing the Godunov operator splitting [36]. Therefore, each time step

involves the solution of two different problems: a nonlinear system of ODEs

$$\begin{aligned} \frac{\partial V}{\partial t} &= \frac{1}{C_m} [-I_{\text{ion}}(V, \boldsymbol{\eta}) + I_{\text{stim}}], \\ \frac{\partial \boldsymbol{\eta}}{\partial t} &= f(V, \boldsymbol{\eta}), \end{aligned} \quad (2)$$

and a parabolic PDE

$$\beta \left(C_m \frac{\partial V}{\partial t} \right) = \nabla \cdot (\boldsymbol{\sigma} \nabla V). \quad (3)$$

Since the spatial discretization of our model, h , is extremely small, the CFL [37] condition that assures numerical stability is very restrictive. Therefore, for the PDE we used the unconditionally stable implicit Euler scheme. The time derivative presented in (3), which operates on V is approximated by a first-order implicit Euler scheme as follows:

$$\frac{\partial V}{\partial t} = \frac{V^{n+1} - V^n}{\Delta t_p}, \quad (4)$$

where V^n represents the transmembrane potential at time t_n and Δt_p is the time step used to advance in time the partial differential equation.

For the discretization of the nonlinear system of ODEs, we note that its stiffness demands very small time steps. For simple models based on Hodgkin-Huxley formulation, this problem is normally overcome by using the Rush-Larsen (RL) method [38]. However, for the most modern and complex models that are highly based on MCs, the RL method seems to be ineffective in terms of allowing larger time steps during the numerical integration. For the case of the Bondarenko et al. model, we tested both methods, Euler and RL, and both demanded the same time step, $\Delta t_o = 0.0001$ ms for stability issues. Since the RL method is more expensive per time step than the Euler method, in this work, we used the simple explicit Euler method for the discretization of the nonlinear ODEs.

However, as already indicated above, we use different time steps for the solution of the two different uncoupled problems, the PDE and the ODEs. Since we use an unconditionally stable method for the PDE, the time step Δt_p could be much larger than that used for the solution of the nonlinear system of ODEs, $\Delta t_o = 0.0001$ ms. In this work, we use $\Delta t_p = 0.01$ ms, that is, a hundred times larger than Δt_o . This has not introduced any significant numerical error. We calculated the L2 relative error for the transmembrane potential between a solution that uses the same time step for both the ODE and the PDE, $\Delta t_o = \Delta t_p = 0.0001$ ms, $V_{m_{\text{ref}}}$ and a solution that uses $\Delta t_o = 0.0001$ ms and $\Delta t_p = 0.01$ ms, V as follows:

$$\text{error} = \frac{\sqrt{\sum_{i=1}^{nt} \sum_{j=1}^{nv} (V(i, j) - V_{m_{\text{ref}}}(i, j))^2}}{\sqrt{\sum_{i=1}^{nt} \sum_{j=1}^{nv} V_{m_{\text{ref}}}(i, j)^2}}, \quad (5)$$

where nt is the number of time steps and nv is the total number of discretized volumes. For the simulation of a tissue of size 0.5×0.5 cm during 20 ms (stimulus at the center of the tissue), the error found was 0.01%.

2.3.2. *Spatial Discretization.* The diffusion term in (3) must be discretized in space. For this we will consider the following:

$$\mathbf{J} = -\sigma \nabla V, \quad (6)$$

where \mathbf{J} ($\mu\text{A}/\text{cm}^2$) expresses the density of intracellular current flow and

$$\nabla \cdot \mathbf{J} = -I_v. \quad (7)$$

In this equation, I_v ($\mu\text{A}/\text{cm}^3$) is a volumetric current and corresponds to the left-hand side of (3), serving as the base for this finite volume solution.

For the space discretization, we will consider a two-dimensional uniform mesh, consisting of regular quadrilaterals (called “volumes”). Located in the center of each volume is a node. The quantity of interest V is associated with each node of the mesh.

After defining the mesh geometry and dividing the domain in control volumes, the specific equations of the FVM can be presented. Equation (7) can be integrated spatially over an individual volume $V_{i,j}$ of size h^2d , leading to

$$\int_{\Omega} \nabla \cdot \mathbf{J} dv = - \int_{\Omega} I_v dv. \quad (8)$$

Applying the divergence theorem yields

$$\int_{\Omega} \nabla \cdot \mathbf{J} dv = \int_{\partial\Omega} \mathbf{J} \cdot \vec{\xi} ds, \quad (9)$$

where $\vec{\xi}$ is the unitary normal vector to the boundary $\partial\Omega$. Then, we have

$$\int_{\partial\Omega} \mathbf{J} \cdot \vec{\xi} ds = - \int_{\Omega} I_v dv. \quad (10)$$

Finally, assuming that I_v represents an average value in each particular quadrilateral, and substituting (3) in (10), we have

$$\beta \left(C_m \frac{\partial V}{\partial t} \right) \Big|_{(i,j)} = \frac{- \int_{\partial\Omega} \mathbf{J}_{i,j} \cdot \vec{\xi} ds}{h^2 d}. \quad (11)$$

For this particular two-dimensional problem, consisting of a uniform grid of quadrilaterals with side h , the calculation of $\mathbf{J}_{i,j}$ can be subdivided as a sum of flows on the following faces:

$$\int_{\partial\Omega} \mathbf{J}_{i,j} \cdot \vec{\xi} ds = (I_{x_{i+1/2,j}} - I_{x_{i-1/2,j}} + I_{y_{i,j+1/2}} - I_{y_{i,j-1/2}}), \quad (12)$$

where $I_{x_{m,n}}$ and $I_{y_{m,n}}$ are calculated at faces $((m,n) = (i + 1/2, j), (i - 1/2, j), (i, j + 1/2), \text{ or } (i, j - 1/2))$ as follows. For the case in which we have defined a conductivity value at face (m,n) , for instance the intracellular, or cytoplasm conductivity, σ_c , as described in Section 2.1, we have

$$\begin{aligned} I_{x_{m,n}} &= -\sigma_c(m,n) \frac{\partial V}{\partial x} \Big|_{(m,n)} hd, \\ I_{y_{m,n}} &= -\sigma_c(m,n) \frac{\partial V}{\partial y} \Big|_{(m,n)} hd. \end{aligned} \quad (13)$$

For the case in which we have defined a conductance value at face (m,n) , for instance a gap junction conduction G , as describes in Section 2.1, we have:

$$\begin{aligned} I_{x_{m,n}} &= -G(m,n) \Delta_x V|_{(m,n)}, \\ I_{y_{m,n}} &= -G(m,n) \Delta_y V|_{(m,n)}. \end{aligned} \quad (14)$$

Using centered finite difference, we have for (13)

$$\begin{aligned} \frac{\partial V}{\partial x} \Big|_{(i+1/2,j)} &= \frac{V_{i+1,j} - V_{i,j}}{h}, \\ \frac{\partial V}{\partial y} \Big|_{(i,j+1/2)} &= \frac{V_{i,j+1} - V_{i,j}}{h}. \end{aligned} \quad (15)$$

For (14), we have

$$\begin{aligned} \Delta_x V|_{(i+1/2,j)} &= V_{i+1,j} - V_{i,j}, \\ \Delta_y V|_{(i,j+1/2)} &= V_{i,j+1} - V_{i,j}. \end{aligned} \quad (16)$$

Equations for $\partial V/\partial x|_{(i-1/2,j)}$, $\partial V/\partial y|_{(i,j-1/2)}$, $\Delta_x V|_{(i-1/2,j)}$ and $\Delta_y V|_{(i,j+1/2)}$ can be obtained analogously.

Rearranging and substituting the discretizations of (4) and (12) in (11) and decomposing the operators as described by (2), and (3) yields

$$\begin{aligned} (\sigma_{i+1/2,j} + \sigma_{i-1/2,j} + \sigma_{i,j+1/2} + \sigma_{i,j-1/2} + \alpha) V_{i,j}^* - \sigma_{i,j-1/2} V_{i,j-1}^* \\ - \sigma_{i+1/2,j} V_{i+1,j}^* - \sigma_{i,j+1/2} V_{i,j+1}^* - \sigma_{i-1/2,j} V_{i-1,j}^* = \alpha V_{i,j}^n, \end{aligned} \quad (17)$$

$$\begin{aligned} C_m \frac{V_{i,j}^{n+1} - V_{i,j}^*}{\Delta t_o} &= -I_{\text{ion}}(V_{i,j}^*, \boldsymbol{\eta}^n), \\ \frac{\boldsymbol{\eta}^{n+1} - \boldsymbol{\eta}^n}{\Delta t_o} &= f(\boldsymbol{\eta}^n, V^*, t), \end{aligned} \quad (18)$$

where $\alpha = (\beta C_m h^2)/\Delta t_p$, n is the current step, $*$ is an intermediate step, and $n+1$ is the next time step. In addition σ can stand for any of the gap junction conductance (G_p, G_i, G_c) divided by the depth d or for any conductivity value (σ_c, σ_m) defined for each volume face as described in Section 2.1. This defines the equations for each finite volume $\text{Vol}_{i,j}$. First we solve the linear system associated with (17) to advance time by Δt_p and then we solve the nonlinear system of ODEs associated with (18) N_o times until we have $N_o \Delta t_o = \Delta t_p$.

2.4. *Parallel Numerical Implementations.* Large scale simulations, such as those resulting from fine spatial discretization of a tissue, are computationally expensive. For example, when an $8 \mu\text{m}$ discretization is used in a $1 \text{ cm} \times 1 \text{ cm}$ tissue and the Bondarenko et al. model (BDK), which has 41 differential variables, is used as cardiac cell model, a total of $1250 \times 1250 \times 41 = 64,062,500$ unknowns must be computed at each time step. In addition, to simulate 100 ms of cardiac electrical activity, 64 millions of unknowns of the nonlinear systems of ODEs must be computed one million times (with $\Delta t_o = 0.0001 \text{ ms}$) and the PDE with 1.5 million of unknowns must be computed ten thousand times.

To deal with this high computational cost, two distinct tools for parallel computing were used together: MPI and GPGPU.

2.4.1. Cluster Implementation. The *cluster* implementation is a parallel implementation tailored to cluster of CPUs. The *cluster* implementation uses the PETSc [39] and MPI [40] libraries. It uses a parallel conjugate gradient preconditioned with ILU(0) (with block Jacobi in parallel) to solve the linear system associated with the discretization of the PDE of the monodomain model. More details about this parallel implementation can be found in our previous works on this topic [21–24].

To solve the non-linear systems of ODEs, the explicit Euler method was used. This is an embarrassingly parallel problem. No dependency exists between the solutions of the different systems of ODEs of each finite volume $\text{Vol}_{i,j}$. Therefore, it is quite simple to implement a parallel version of the code: each MPI process is responsible for computing a fraction Np of the total number of volumes of the simulation, where Np is the number of processes involved in the computation.

2.4.2. Multi-GPU Implementation. In our *multi-GPU* implementation, we have decided to keep the cluster approach for the solution of the linear system associated with the discretization of the PDE of the monodomain model. Therefore, *multi-GPU* also solves the discretized PDE with the parallel conjugate gradient preconditioned with ILU(0) (with block Jacobi in parallel) available in the PETSc library.

However, we have accelerated the solution of the systems of ODEs by using multiple GPUs. This is a different strategy from those we have used before when the full Bidomain equations (elliptic PDE, parabolic PDE, and systems of ODEs) were completely implemented in a single GPU [30], or the full Monodomain equations (parabolic PDE and system of ODEs) were completely implemented in a single GPU [25, 26, 29].

The motivation for choosing a different strategy is based on several reasons. As presented in [29], the monodomain model can be accelerated using a single GPU by 35-fold when compared to a parallel OpenMP [41] implementation running on a quad-core computer. However, this final speedup obtained by the GPU comes from a near 10-fold speedup for the solution of the PDE and a near 450-fold speedup for the solution of the nonlinear systems of ODEs. Nowadays, as manycore architecture evolves, one may easily find in the market a single computer equipped with 64 processing cores. Therefore, we believe that solving the PDE on these new machines with traditional MPI or OpenMP-based parallel implementations may outperform a single GPU implementation. On the other side, for the parallel solution of the nonlinear systems of ODEs a single GPU still easily outperforms these new manycore-based computers. This brings us to focus GPU implementations to the parallel solutions of the millions of nonlinear systems of ODEs. A second motivation is related to the preconditioners that can be easily and efficiently implemented for the conjugate

gradient method in GPUs. For the bidomain equations, efficient geometric multigrid preconditioners [30] were implemented in a single GPU, and sophisticated algebraic multigrid preconditioners [42] were implemented in a multi-GPU platform. However, both implementations are only viable for the solution of the linear system associated with the elliptic PDE of the bidomain equations. Multigrid preconditioners are too expensive and turns out to be an inefficient option for the solution of the parabolic PDE, which is the PDE type of the monodomain model. Until now, the cheap but inefficient w -Jacobi preconditioner has been the best choice for GPU implementations when it concerns the solution of the parabolic PDE [29, 42]. However, it is well known that incomplete LU (ILU) preconditioners combined with block Jacobi or additive Schwarz domain decomposition methods [23] greatly outperform Jacobi-like preconditioners on cluster computing for the solution of the PDE of the monodomain model. This argument favors cluster-like implementations as the best choice for the parallel solution of the parabolic PDE of the monodomain model (see [43] and the references cited therein). Finally, a third and last motivation is related to the particular problem we propose to investigate in this work: models that reveal the microstructure of cardiac tissue. Another recent work presented an implementation for the bidomain model for multi-GPU platforms [44]. Both PDEs and systems of ODEs were implemented on GPUs using explicit methods, Jacobi relaxation, and explicit Euler, respectively. We note that for our particular microscopic tissue model with spatial discretization of $8\ \mu\text{m}$, the approach of using an explicit and cheap solver for the PDE would be very inefficient due to the severe stability restrictions imposed by the CFL conditions [37]. Therefore, once more, this argument also favors cluster-like implementations based on implicit methods for the parallel solution of the parabolic PDE of the monodomain model.

Our *multi-GPU* implementation uses CUDA [45] to implement the numerical solution of the BDK cardiac cell model. The CUDA model extends the C programming language with a set of abstractions to express parallelism, that is, CUDA includes C software development tools and libraries to hide the GPGPU hardware details from programmers that can focus on important issues of the parallelism of their code rather than dealing with unfamiliar and complicated concepts from computer graphics in order to explore the computational power of GPUs for general purpose computation.

In order to run an application, the programmer must create a parallel function called kernel. A kernel is a special C function callable from the CPU but executed on the GPU simultaneously by many threads. Each thread is run by a GPU stream processor. They are grouped into blocks of threads or just blocks. The blocks can be one-, two-, or three-dimensional. A set of blocks of threads form a grid, that can be one- or two-dimensional. When the CPU calls the kernel, it must specify how many blocks and threads will be created at the GPU to execute the kernel. The syntax that specifies the number of threads that will be created to execute a kernel is formally known as the execution configuration and is flexible

to support CUDA's hierarchy of threads, blocks of threads, and grids of blocks. Since all threads in a grid execute the same code, a unique set of identification numbers is used to distinguish threads and to define the appropriate portion of the data they must process. These threads are organized into a two-level hierarchy composed by blocks and grids and two unique coordinates, called *blockId* and *threadId*, are assigned to them by the CUDA runtime system. These two built-in variables can be accessed within the kernel functions and they return the appropriate values that identify a block and thread, respectively. All the threads within a single block are allowed to synchronize with each other via a special barrier operator, called *syncthread*, and have access to a high-speed, per-block shared memory which allows interthread communication. Threads from different blocks in the same grid can coordinate their execution only through the use of atomic global memory operations. No assumptions are made about the execution order of thread blocks, which means that a kernel must execute correctly no matter the order in which blocks are scheduled by the hardware to run.

Some additional steps must be followed to use the GPU: (a) the device must be initialized; (b) memory must be allocated in the GPU and data transferred to it; (c) the kernel is then called. After the kernel have finished its execution, results are transferred back to the CPU.

Two kernels have been developed to solve each of the systems of ODEs related to BDK model. The first kernel is responsible for setting the initial conditions of the systems of ODEs, whereas the second one integrates the systems of ODEs at each time step.

Both kernel implementations were optimized in many different ways. The state variables of M cardiac cells were stored in an array called *SV*, whose size is equal to MN_{eq} , where N_{eq} is the number of differential equations of the ionic model (in this work, N_{eq} is equal to 41). The *SV* array was organized in such a way that the first M entries correspond to the first state variable, followed by M entries of the next state variable, and so on. Moreover, for all ionic models, the first M entries of the *SV* array correspond to the transmembrane potential V . During the solution of the systems of PDEs, after the integration of the ODEs systems, the transmembrane potential of each node should be passed to the PETSC solver. Due to the memory organization chosen for the *SV* array, this is a straightforward task since, as stated before, the M first entries of the array correspond to the transmembrane potential V of each node. This organization allows us to avoid extra memory transactions between CPU and GPU, improving performance. Another implementation choice that impact performance positively was the way the *SV* array has been allocated. The *SV* array was allocated in global GPU memory using the *cudaMallocPitch* routine from the CUDA API. This routine may pad the allocation in order to ensure that corresponding memory addresses of any given row will continue to meet the alignment requirements for the coalescing operations performed by the hardware. In short, a strict coalescing requires that thread j out of n threads has to access data $u[j]$ if $u[0]$ is accessed by thread 0, that is, each thread should perform data access by stride n . Therefore, in the first kernel, to set the initial conditions, each thread

sets the values of all its state variables. The kernel that solves the system of ODEs operates similarly, that is, each thread computes and updates its state variables writing to the right position in memory that corresponds to their variables. In addition, the second kernel was optimized to use as much as local memory operations as possible.

Pure domain decomposition was used for parallelism. The tissue domain was linearly decomposed on Np nonoverlapping subdomains (or Np tasks, T_1 to T_{Np} , see Figure 4), where Np is the number of MPI processes or processing cores. The parallel solution of the PDE is implemented via PETSc (see [21]), with each processing core p responsible for updating the variables associated to subdomain T_p . In our computational environment each machine or node has more CPU cores (8) than GPUs (2). Therefore, for the solution of the ODEs each GPU device will be responsible for processing more than one task. The tasks assigned with one node are distributed to the GPUs in a round-robin fashion. For example, if $Np = 16$ and we have two machines (each with 8 cores and 2 GPU devices), Figure 4 presents how the tissue domain will be partitioned. Four tasks would be assigned to each GPU device. For instance, at node 0, GPU 0 would process tasks $T_1, T_3, T_5,$ and T_7 , GPU 1 the tasks $T_2, T_4, T_6,$ and T_8 .

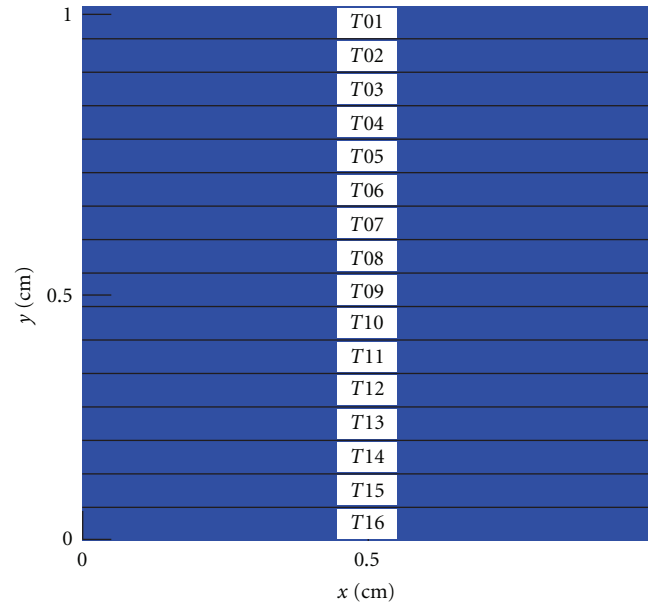
For the solution of the ODEs, both sequential and parallel (CUDA) codes used single precision. For the solution of the PDE we have used double precision. For the case of monodomain simulations, we have shown in [25] that the use of single precision in CUDA does not affect the numerical precision of the solver.

3. In Silico Experiments, Computational Environment, and Metrics

The simulations were performed using the microscopic model with spatial discretization of $8 \mu\text{m}$ and heterogeneous conductivity values as described in Section 2.1. The values used for β and C_m were set to 0.14 cm^{-1} and $1.0 \mu\text{F}/\text{cm}^2$, respectively. The time step used to solve the linear system associated with (17) was set to $\Delta t_p = 0.01 \text{ ms}$ and to solve the nonlinear system of ODEs associated to (18) was set with $\Delta t_o = 0.0001 \text{ ms}$.

Three different tissue setups were used to test our model and parallel implementations: a cardiac tissue of $0.5 \text{ cm} \times 0.5 \text{ cm}$ size that was stimulated in the center and was executed for 10 ms, a cardiac tissue of $1.0 \text{ cm} \times 1.0 \text{ cm}$ size that was stimulated in the center and was executed for 10 ms, and a cardiac tissue of $1.0 \text{ cm} \times 1.0 \text{ cm}$ that was stimulated using the S1-S2 protocol to generate a spiral wave, a form of self-sustained reentrant activity strongly associated with cardiac arrhythmia.

Our experiments were performed on a cluster of 8 SMP computers. Each computer contains two Intel E5620 Xeon quad-core processors and 12 GB of RAM. All nodes run Linux version 2.6.18-194.17.4.el5. The codes were compiled with gcc 4.1.2 and CUDA 3.2. Each node contains two Tesla C1060. The Tesla C1060 card has 240 CUDA cores and 4 GB of global memory.



Linear parallel
partitioning



		Node 0				Node 1			
		Core 0	Core 1	Core 2	Core 3	Core 0	Core 1	Core 2	Core 3
PDE solve		T01	T02	T03	T04	T09	T10	T11	T12
		Core 4	Core 5	Core 6	Core 7	Core 4	Core 5	Core 6	Core 7
		T05	T06	T07	T08	T13	T14	T15	T16
ODE solve		GPU 0		GPU 1		GPU 0		GPU 1	
		T01 + T03 + T05 + T07		T02 + T04 + T06 + T08		T09 + T11 + T13 + T15		T10 + T12 + T14 + T16	

FIGURE 4: Linear parallel decomposition of tissue. Example for the case of two nodes (each with 8 cores and 2 GPU devices, that is, a total of 16 CPU cores and 4 GPU devices). Each CPU core processes one task. Four tasks are assigned to each GPU device. For instance, at node 0, GPU 0 processes tasks T_1 , T_3 , T_5 , and T_7 , and GPU 1 the tasks T_2 , T_4 , T_6 , and T_8 .

All tests were performed three times. The average execution time, in seconds, is then used to calculate the speedup, defined as the sequential execution time divided by the parallel execution time.

4. Results

Figure 5 presents the propagation of a central stimulus on the tissue of size $1 \text{ cm} \times 1 \text{ cm}$ for different time instants. As expected, macroscopically, the propagation looks very smooth and continuous. However, when highlighting a smaller region of size $1 \text{ mm} \times 1 \text{ mm}$, see Figure 6, we can already observe the discrete nature of propagation, that is, the

influence of the cardiac microstructure on the propagation of action potentials.

Table 1 presents the results obtained by the parallel implementations for the experiment with a square tissue of $0.5 \text{ cm} \times 0.5 \text{ cm}$. As one can observe, the time spent solving the ODEs is responsible for near 90% of the execution time. It can also be observed that although the obtained speedups with the *cluster* are respectable and almost linear (near 61 with 64 cores), the total execution time remains high. With respect to the *multi-GPU* implementation, the results are much better. It must be stressed that although 64 cores were used in this simulation, only 16 GPGPU devices were available for executing the simulation, so 8 processes share 2 GPGPU devices per machine. As one can observe,

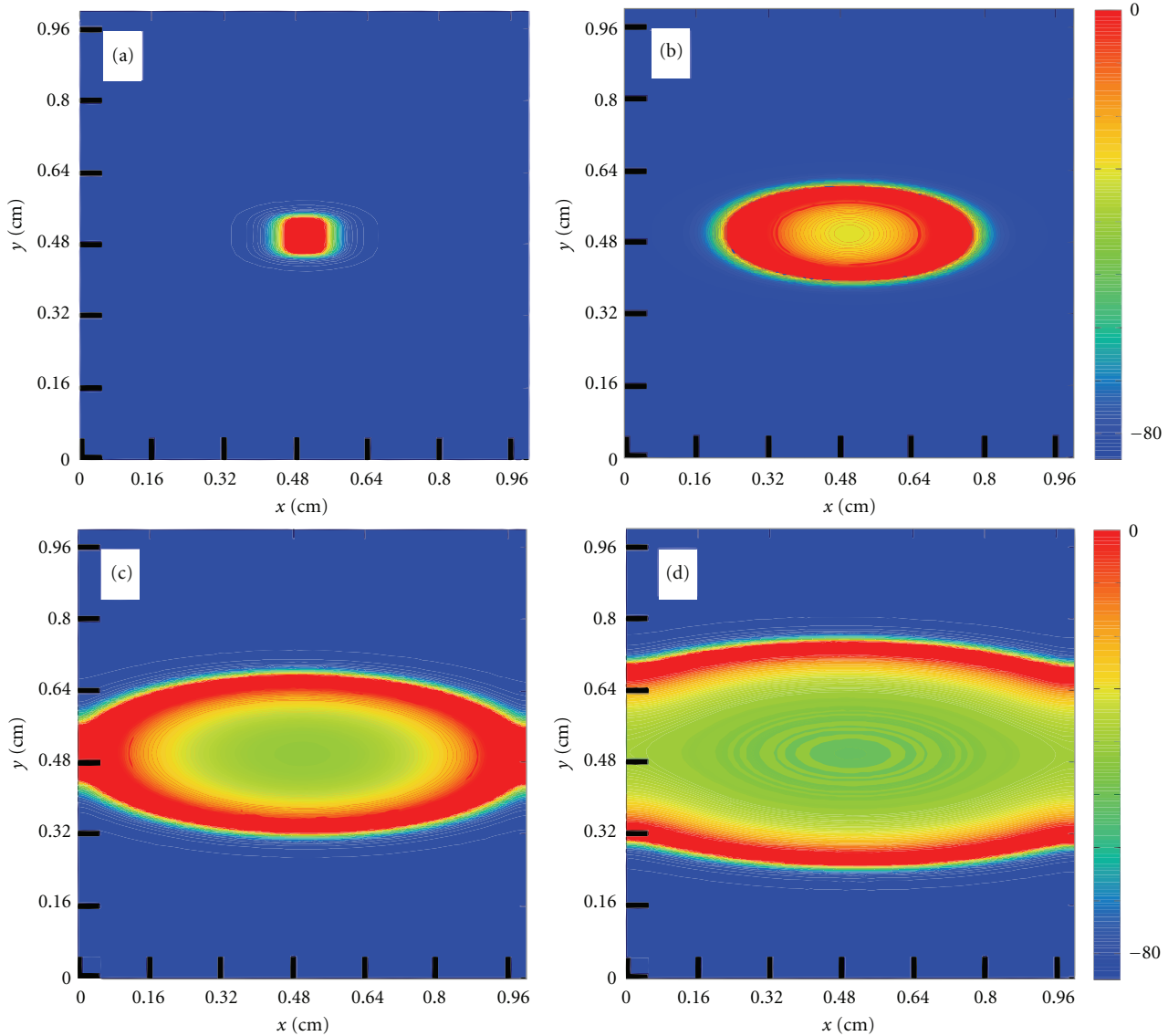


FIGURE 5: Action potential propagation (transmembrane potential) after a central stimulus on a tissue of size $1 \text{ cm} \times 1 \text{ cm}$ for different time instants. (a) $t = 1$ ms, (b) $t = 7$ ms, (c) $t = 13$ ms, and (d) $t = 20$ ms.

the obtained speedup was huge, about 343 times faster than a single core processor. The execution time drops from 1.6 days (using one processing core) to only 6.7 minutes (using the 8-node multi-GPU platform).

Table 2 presents the results obtained by the parallel implementations for the experiment with a square tissue of $1.0 \text{ cm} \times 1.0 \text{ cm}$. Once again, the speedups obtained with the *cluster* implementation, were almost linear (61 with 64 cores). With respect to the *multi-GPU* implementation the results are much better. The speedup was huge, about 420 times faster than a single core processor. The execution time drops from more than 6 days (using one processing core) to only 21 minutes (using the 8-node multi-GPU platform). We can also observe that the *multi-GPU* implementation was near 7 times faster than the *cluster* implementation when running on the 8 computers.

As a result, using this very fast parallel implementation, we were able to simulate the formation of spiral waves, a form of self-sustained reentrant activity strongly associated with cardiac arrhythmia, see Figure 7. To the best of our knowledge, this is the first time spiral waves are simulated using a cardiac model that accounts for both the microstructure of cardiac tissue and a modern and complex myocyte model. After a couple of tries using the S1-S2 protocol to find the correct vulnerable window, we managed to generate a sustained spiral wave using this cardiac model that accounts for both the microstructure of cardiac tissue and a modern and complex myocyte model. The whole process took less than one day (around 13 hours with each simulation taking between 3 and 7 hours). Without our multi-GPU parallel implementation, this process would have taken 227 days using a single core computer or near 4 days using our

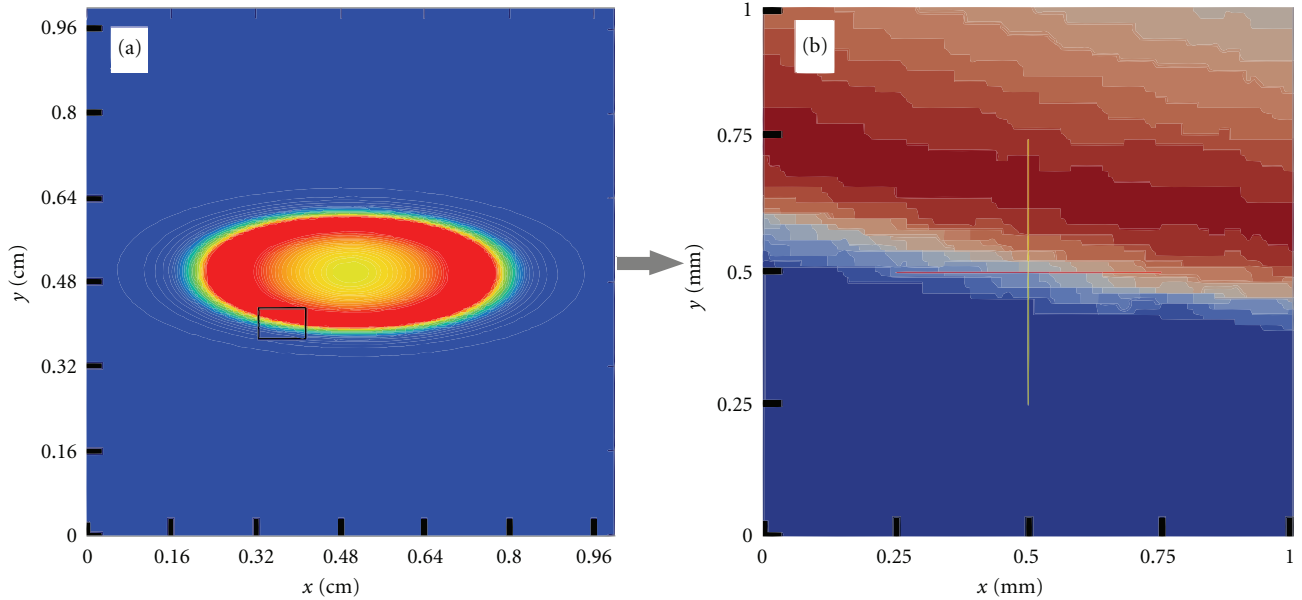


FIGURE 6: (a) Transmembrane potential at $t = 7$ ms after a central stimulus on a tissue of size $1 \text{ cm} \times 1 \text{ cm}$. (b) Microscopic details revealing the discrete nature of AP propagation, that is, the influence of cardiac microstructure on a large tissue size simulation.

TABLE 1: Average execution time and speedup of parallel implementations for a tissue of $0.5 \text{ cm} \times 0.5 \text{ cm}$. The execution times are presented in seconds.

Parallel implementation	Cores	Total Time	ODE time	PDE time	Speedup
Cluster	1	137,964	132,590	5,264	—
Cluster	8	18,492	17,210	1,262	7.5
Cluster	16	9,922	9,316	595	13.9
Cluster	32	4,198	3,884	311	32.9
Cluster	64	2,283	2,087	191	60.4
Multi-GPU	64 + 16 GPUs	401.84	209.4	187	343

TABLE 2: Average execution time and speedup of parallel implementations for a tissue of $1.0 \text{ cm} \times 1.0 \text{ cm}$. The execution times are presented in seconds.

Parallel implementation	Cores	Total Time	ODE time	PDE time	Speedup
Cluster	1	546,507	523,331	23,177	—
Cluster	64	8,934	8,313	607	61.2
Multi-GPU	64 + 16 GPUs	1,302	682	611	420

cluster implementation running with 64 cores but without the GPUs.

5. Discussion and Future Works

Our results show that our *multi-GPU* parallel implementation described in Section 2.4.2 was able to significantly accelerate the numerical solution of a cardiac electrophysiology model that captures the microstructure of cardiac tissue (using a very fine spatial discretization) and is based on a very modern and complex cell model (with Markov chain formulation that has been extensively used for the characterization of ion channels). Speedups around 420 times were obtained, reducing execution times from more

than 6 days (using one processing core) to only 21 minutes (using the 8-node multi-GPU platform). The hybrid *Multi-GPU* parallel implementation presented in this work is even more attractive if one considers that the architectures of GPUs and multicore processors continue to evolve on a fast pace.

Nevertheless, we believe our parallel implementation can be further improved. For instance, in the current implementation, the CPU cores are idle while waiting for the results of the nonlinear ODEs that are being computed by the GPU devices. For future work, we intend to evaluate different load balancing techniques to better distribute the parallel tasks between GPU devices and CPU cores and make a more efficient use of all the computational resources. Another possible improvement is related to the multilevel

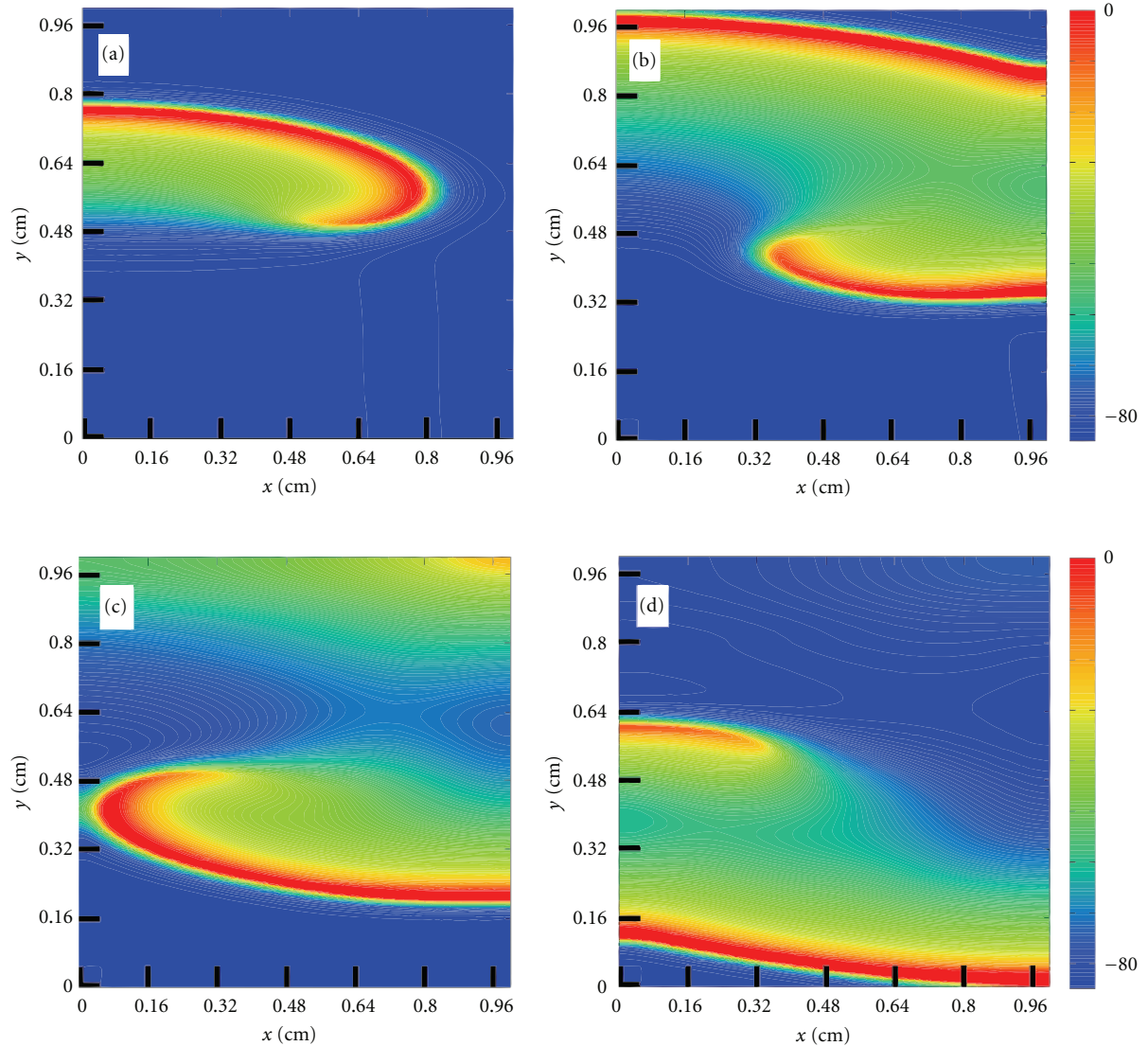


FIGURE 7: Spiral wave formation after an S1-S2 stimulus protocol at different time instants: (a) $t = 80$ ms, (b) $t = 100$ ms, (c) $t = 112$ ms, and (d) $t = 120$ ms.

parallelism introduced for the solution of the bidomain equations [24] that combines task parallelism (via pipeline) and data parallelism (via data decomposition). We believe a similar combination of data and task parallelism could be also exploited for the solution of the monodomain equations to further enhance the parallel efficiency of our algorithms.

Recent studies that focus on the discrete or discontinuous nature of AP propagation have avoided the computational challenges that arise from microscopic models via the development and use of discrete models, where each cardiac myocyte is represented by a single point connected with the neighboring myocytes by different conductivities [46, 47]. This description has allowed the study of the effects of randomly distributed conductivities in the conduction velocity and on the formation of reentry patterns on cardiac tissue. Discrete models were introduced by Keener in [48] to describe the electrical propagation in a 1D cable of nc

connected cells for the case of low gap-junctional coupling. In this model, the cells are assumed to be isopotential. Therefore, only gap junction conductances are considered for the connection of neighboring myocytes, that is, cytoplasmic resistance is considered to be insignificant. Recently, we have compared discrete and microscopic models for a 1D cable of connected cells [49]. We have shown that the numerical results obtained by the discrete model are similar to those obtained by the heterogeneous microscopic model for the case of low gap-junctional coupling (1%–10% of normal coupling). However, the discrete model failed for the case of normal gap-junctional coupling or moderate reduced gap-junctional coupling (50%–100% of normal coupling). The two-dimensional microscopic model developed in this work will allow us to further compare these two approaches (detailed microscopic models versus discrete models) and to better understand the benefits and limitations of each one of

them. In addition, we hope that our microscopic model may also suggest ways to better develop discrete models, which are computationally less expensive than the detailed microscopic ones.

6. Conclusion

In this paper, we developed a cardiac electrophysiology model that captures the microstructure of cardiac tissue by using a very fine spatial discretization and uses a very modern and complex cell model based on Markov chains for the characterization of ion channel's structure and dynamics. To cope with the computational challenges, the model was parallelized using a hybrid approach: cluster computing and GPGPUs. Different *in silico* tissue preparations were used in this work for the performance tests. We have shown that in all cases, our parallel multi-GPU implementation was able to significantly reduce the execution times of the simulations, for instance, from more than 6 days (on a single processor) to 21 minutes (on a small 8-node cluster equipped with 16 GPUs, that is, 2 GPUs per node). We believe that this new parallel implementation paves the way for the investigation of many open questions associated with the complex and discrete propagation nature of action potentials on cardiac tissue.

Authors' Contribution

B. G. de Barros and R. S. Oliveira contributed equivalently in this paper. "Therefore they can be both considered as first authors appearing in alphabetical order".

Acknowledgments

The authors would like to thank CAPES, CNPq, FAPEMIG, FINEP, UFMG, UFSJ, and UFJF for supporting this work.

References

- [1] WHO, World health organization, 2010, <http://www.who.int/>.
- [2] F. B. Sachse, *Computational Cardiology: Modeling of Anatomy, Electrophysiology, and Mechanics*, vol. 2966, Springer, 2004.
- [3] A. L. Hodgkin and A. F. Huxley, "A quantitative description of membrane current and its application to conduction and excitation in nerve," *The Journal of physiology*, vol. 117, no. 4, pp. 500–544, 1952.
- [4] R. Plonsey, "Bioelectric sources arising in excitable fibers (alza lecture)," *Annals of Biomedical Engineering*, vol. 16, no. 6, pp. 519–546, 1988.
- [5] R. R. Aliev and A. V. Panfilov, "A simple two-variable model of cardiac excitation," *Chaos, Solitons and Fractals*, vol. 7, no. 3, pp. 293–301, 1996.
- [6] V. E. Bondarenko, G. P. Szigeti, G. C. L. Bett, S. J. Kim, and R. L. Rasmusson, "Computer model of action potential of mouse ventricular myocytes," *American Journal of Physiology*, vol. 287, no. 3, pp. H1378–H1403, 2004.
- [7] C. E. Clancy and Y. Rudy, "Linking a genetic defect to its cellular phenotype in a cardiac arrhythmia," *Nature*, vol. 400, no. 6744, pp. 566–569, 1999.
- [8] T. Brennan, M. Fink, and B. Rodriguez, "Multiscale modelling of drug-induced effects on cardiac electrophysiological activity," *European Journal of Pharmaceutical Sciences*, vol. 36, no. 1, pp. 62–77, 2009.
- [9] C. E. Clancy, Z. I. Zhu, and Y. Rudy, "Pharmacogenetics and anti-arrhythmic drug therapy: a theoretical investigation," *American Journal of Physiology*, vol. 292, no. 1, pp. H66–H75, 2007.
- [10] V. Iyer, R. Mazhari, and R. L. Winslow, "A computational model of the human left-ventricular epicardial myocyte," *Biophysical Journal*, vol. 87, no. 3, pp. 1507–1525, 2004.
- [11] M. S. Spach and J. F. Heidlage, "The stochastic nature of cardiac propagation at a microscopic level: electrical description of myocardial architecture and its application to conduction," *Circulation Research*, vol. 76, no. 3, pp. 366–380, 1995.
- [12] V. Jacquemet and C. S. Henriquez, "Loading effect of fibroblast-myocyte coupling on resting potential, impulse propagation, and repolarization: insights from a microstructure model," *American Journal of Physiology*, vol. 294, no. 5, pp. H2040–H2052, 2008.
- [13] M. L. Hubbard, W. Ying, and C. S. Henriquez, "Effect of gap junction distribution on impulse propagation in a monolayer of myocytes: a model study," *Europace*, vol. 9, supplement 6, pp. vi20–vi28, 2007.
- [14] A. G. Kléber and Y. Rudy, "Basic mechanisms of cardiac impulse propagation and associated arrhythmias," *Physiological Reviews*, vol. 84, no. 2, pp. 431–488, 2004.
- [15] H. J. Jongasma and R. Wilders, "Gap junctions in cardiovascular disease," *Circulation Research*, vol. 86, no. 12, pp. 1193–1197, 2000.
- [16] Y. Wang and Y. Rudy, "Action potential propagation in inhomogeneous cardiac tissue: safety factor considerations and ionic mechanism," *American Journal of Physiology*, vol. 278, no. 4, pp. H1019–H1029, 2000.
- [17] M. S. Spach and R. C. Barr, "Effects of cardiac microstructure on propagating electrical waveforms," *Circulation Research*, vol. 86, no. 2, pp. e23–e28, 2000.
- [18] R. M. Shaw and Y. Rudy, "Ionic mechanisms of propagation in cardiac tissue: roles of the sodium and L-type calcium currents during reduced excitability and decreased gap junction coupling," *Circulation Research*, vol. 81, no. 5, pp. 727–741, 1997.
- [19] J. Stinstra, R. MacLeod, and C. Henriquez, "Incorporating histology into a 3D microscopic computer model of myocardium to study propagation at a cellular level," *Annals of Biomedical Engineering*, vol. 38, no. 4, pp. 1399–1414, 2010.
- [20] S. F. Roberts, J. G. Stinstra, and C. S. Henriquez, "Effect of nonuniform interstitial space properties on impulse propagation: a discrete multidomain model," *Biophysical Journal*, vol. 95, no. 8, pp. 3724–3737, 2008.
- [21] R. Weber Dos Santos, G. Plank, S. Bauer, and E. J. Vigmond, "Parallel multigrid preconditioner for the cardiac bidomain model," *IEEE Transactions on Biomedical Engineering*, vol. 51, no. 11, pp. 1960–1968, 2004.
- [22] G. Plank, M. Liebmann, R. W. dos Santos, E. J. Vigmond, and G. Haase, "Algebraic multigrid preconditioner for the cardiac bidomain model," *IEEE Transactions on Biomedical Engineering*, vol. 54, pp. 585–596, 2007.
- [23] R. W. dos Santos, G. Plank, S. Bauer, and E. J. Vigmond, "Preconditioning techniques for the bidomain equations," *Lecture Notes in Computational Science and Engineering*, vol. 40, pp. 571–580, 2004.
- [24] C. R. Xavier, R. S. Oliveira, V. Da Fonseca Vieira, R. W. Dos Santos, and W. Meira, "Multi-level parallelism for the cardiac

- bidomain equations,” *International Journal of Parallel Programming*, vol. 37, no. 6, pp. 572–592, 2009.
- [25] B. M. Rocha, F. O. Campos, R. M. Amorim et al., “Accelerating cardiac excitation spread simulations using graphics processing units,” *Concurrency Computation Practice and Experience*, vol. 23, no. 7, pp. 708–720, 2011.
- [26] B. M. Rocha, F. O. Campos, G. Plank, R. W. dos Santos, and M. Liebmann, “Simulations of the electrical activity in the heart with graphic processing units,” in *Parallel Processing and Applied Mathematics*, R. Wyrzykowski, J. Dongarra, K. Karczewski, and J. Wasniewski, Eds., vol. 6067, pp. 439–448, Lecture Notes in Computer ScienceSpringer, Berlin, Germany, 2010.
- [27] R. M. Amorim, B. M. Rocha, F. O. Campos, and R. W. Dos Santos, “Automatic code generation for solvers of cardiac cellular membrane dynamics in GPUs,” in *Proceedings of the 32nd Annual International Conference of the IEEE Engineering in Medicine and Biology Society (EMBC ’10)*, pp. 2666–2669, September 2010.
- [28] R. Amorim, G. Haase, M. Liebmann, and R. W. D. Santos, “Comparing CUDA and OpenGL implementations for a Jacobi iteration,” in *Proceedings of the International Conference on High Performance Computing and Simulation (HPCS ’09)*, pp. 22–32, June 2009.
- [29] R. S. Oliveira, B. M. Rocha, R. M. Amorim et al., “Comparing cuda, opencl and opengl implementations of the cardiac monodomain equations,” in *Parallel Processing and Applied Mathematics*, R. Wyrzykowski, J. Dongarra, K. Karczewski, and J. Wasniewski, Eds., vol. 7204 of *Lecture Notes in Computer Science*, pp. 111–120, Springer, Berlin, Germany, 2012.
- [30] R. M. Amorim and R. W. dos Santos, “Solving the cardiac bidomain equations using graphics processing units,” *Journal of Computational Science*. In press.
- [31] A. M. Gerdes, S. E. Kellerman, J. A. Moore et al., “Structural remodeling of cardiac myocytes in patients with ischemic cardiomyopathy,” *Circulation*, vol. 86, no. 2, pp. 426–430, 1992.
- [32] R. E. Tracy and G. E. Sander, “Histologically measured cardiomyocyte hypertrophy correlates with body height as strongly as with body mass index,” *Cardiology Research and Practice*, vol. 2011, Article ID 658958, 2011.
- [33] R. Eymard, T. Gallouët, and R. Herbin, “Finite volume methods,” *Handbook of Numerical Analysis*, vol. 7, pp. 713–1018, 2000.
- [34] D. M. Harrild and C. S. Henriquez, “A finite volume model of cardiac propagation,” *Annals of Biomedical Engineering*, vol. 25, no. 2, pp. 315–334, 1997.
- [35] Y. Coudiere, C. Pierre, and R. Turpault, “A 2d/3d finite volume method used to solve the bidomain equations of electrocardiology,” in *Proceedings of the Algoritmy*, pp. 1–10, 2009.
- [36] J. Sundnes, *Computing the Electrical Activity in the Heart*, Springer, 2006.
- [37] J. C. Strikwerda, *Finite Difference Schemes and Partial Differential Equations*, Society for Industrial Mathematics, 2004.
- [38] S. Rush and H. Larsen, “A practical algorithm for solving dynamic membrane equations,” *IEEE Transactions on Biomedical Engineering*, vol. 25, no. 4, pp. 389–392, 1978.
- [39] S. Balay, K. Buschelman, V. Eijkhout et al., “PETSc users manual,” Tech. Rep., Citeseer, 2004.
- [40] W. Groop and E. Lusk, “User’s guide for mpich, a portable implementation of MPI,” Tech. Rep., Argonne National Laboratory, 1994.
- [41] L. Dagum and R. Menon, “Openmp: an industry standard api for shared-memory programming,” *IEEE Computational Science and Engineering*, vol. 5, no. 1, pp. 46–55, 1998.
- [42] A. Neic, M. Liebmann, E. Hoetzl et al., “Accelerating cardiac bidomain simulations using graphics processing units,” *IEEE Transactions on Biomedical Engineering*, vol. 59, no. 8, pp. 2281–2290, 2012.
- [43] E. J. Vigmond, R. Weber dos Santos, A. J. Prassl, M. Deo, and G. Plank, “Solvers for the cardiac bidomain equations,” *Progress in Biophysics and Molecular Biology*, vol. 96, no. 1–3, pp. 3–18, 2008.
- [44] V. K. Nimmagadda, A. Akoglu, S. Hariri, and T. Moukabay, “Cardiac simulation on multi-GPU platform,” *Journal of Supercomputing*, vol. 59, no. 3, pp. 1360–1378, 2012.
- [45] D. B. Kirk and W. W. Hwu, *Massively Parallel Processors: A Hands-on Approach*, Morgan Kaufmann, 2010.
- [46] S. Alonso, M. Bär, and A. V. Panfilov, “Effects of reduced discrete coupling on filament tension in excitable media,” *Chaos*, vol. 21, no. 1, Article ID 013118, 2011.
- [47] S. Alonso, M. Bar, and A. V. Panfilov, “Negative tension of scroll wave filaments and turbulence in three-dimensional excitable media and application in cardiac dynamics,” *Bulletin of Mathematical Biology*. In press.
- [48] J. P. Keener, “The effects of gap junctions on propagation in myocardium: a modified cable theory,” *Annals of the New York Academy of Sciences*, vol. 591, pp. 257–277, 1990.
- [49] C. M. Costa and R. W. Dos Santos, “Limitations of the homogenized cardiac Monodomain model for the case of low gap junctional coupling,” in *Proceedings of the 32nd Annual International Conference of the IEEE Engineering in Medicine and Biology Society (EMBC ’10)*, pp. 228–231, September 2010.

Research Article

Coronary Artery Center-Line Extraction Using Second Order Local Features

Farsad Zamani Boroujeni,^{1,2} Rahmita Wirza O. K. Rahmat,² Norwati Mustapha,² Lilly Suriani Affendey,² and Oteh Maskon³

¹ Faculty of Computer Engineering, Islamic Azad University, Khorasgan Campus, Esfahan, Iran

² Faculty of Computer Science and Information Technology, Universiti Putra Malaysia, Serdang, Malaysia

³ Department of Medicine, Universiti Kebangsaan Malaysia, Kuala Lumpur, Malaysia

Correspondence should be addressed to Farsad Zamani Boroujeni, farsad.zamani@ieee.org

Received 22 June 2012; Revised 24 August 2012; Accepted 6 September 2012

Academic Editor: Dingchang Zheng

Copyright © 2012 Farsad Zamani Boroujeni et al. This is an open access article distributed under the Creative Commons Attribution License, which permits unrestricted use, distribution, and reproduction in any medium, provided the original work is properly cited.

Of interest is the accurate and robust delineation of vessel center-lines for complete arterial tree structure in coronary angiograms which is an imperative step towards 3D reconstruction of coronary tree and feature-based registration of multiple view angiograms. Most existing center-line tracking methods encounter limitations in coping with abrupt variations in local artery direction and sudden changes of lumen diameter that occur in the vicinity of arterial lesions. This paper presents an improved center-line tracing algorithm for automatic extraction of coronary arterial tree based on robust local features. The algorithm employs an improved scanning schema based on eigenvalues of Hessian matrix for reliable identification of true vessel points as well as an adaptive look-ahead distance schema for calculating the magnitude of scanning profile. In addition to a huge variety of clinical examples, a well-established vessel simulation tool was used to create several synthetic angiograms for objective comparison and performance evaluation. The experimental results on the accuracy and robustness of the proposed algorithm and its counterparts under difficult situations such as poor image quality and complicated vessel geometry are presented.

1. Introduction

In recent years, the utilization of computerized technologies in cardiovascular examinations has introduced a great deal of precision and speed to the diagnosis of coronary artery disease (CAD). In most of the vascular analysis applications, fast and accurate delineation of the arterial center-lines is a major prerequisite which provides a basis for subsequent image analysis steps. The aim of this study is to develop an efficient algorithm for producing a skeleton representation of whole coronary arterial tree. This is typically performed by either a pixel-based segmentation method followed by a skeletonization of the segmented image or direct exploratory center-line extraction in which coronary arterial segments are extracted through a recursive artery tracking algorithm. The objective of the first approach is to produce a separable representation of the foreground and background that

entails a broad range of vessel enhancement or feature extraction methods such as matched/nonlinear filtering [1, 2], morphological filtering [3], eigenvalues of Hessian matrix [4], hysteresis thresholding [5], pixel classification methods [6], and many others. Unfortunately, most of these methods produce a large number of unconnected clusters of pixels instead of a single connected arterial tree, especially when the images contain nonuniform illumination.

As opposed to the tedious and error-prone pixel based segmentation approach, exploratory tracing methods directly extract the features of interest, circumventing low level processing of every pixel in the image. These algorithms are based on sequential searches through examining a small number of pixels that are close to the vasculature which results in efficient extraction of pixels located on the medial axis of the arterial segments. Several properties such as producing useful partial results, upon the occurrence of

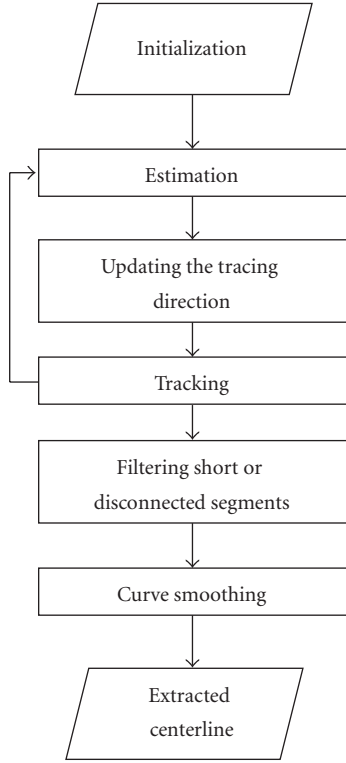


FIGURE 1: The general schema of the center-line extraction procedure.

a deadline, and their computational efficiency make them attractive for real-time, live, and high resolution processing. Figure 1 depicts a general schema of the artery tracing approach followed by most existing methods in the literature. This schema is an iterative process to delineate a sequence of center-line points for each vessel segment. The steps of the process can be described as follows.

- (i) *Initialization*. The initialization step provides preliminary information for starting the tracing procedure. The information typically includes the location of the starting point, the initial direction of the vessel, and distances between the starting point and the left and right boundaries. In manual or semiautomatic algorithms, the location of the seed point and the initial direction are manually defined by the user. In case of fully automatic center-line extraction, however, a valid seed point is selected from a set of validated seed points provided by an automatic seed point detection algorithm.
- (ii) *Estimation*. At the initial point p^k with directions \vec{u}^k , the location of the next center-line point p^{k+1} is estimated simply by linear extrapolation in equation of the form:

$$p^{k+1} = p^k + \alpha \vec{u}^{k+1}, \quad (1)$$

where parameter α is a step size and determines the distance between the current point and the next point. Since an exploratory search produces

a sequence of connected pixels, this distance is filled by a set of intermediary points to connect the two end points using a straight line drawing algorithm [7]. In some algorithms the step size is determined in a self-adaptive manner which yields more accurate results in comparison with the case that the tracing algorithm uses a fixed value for the step size, for example, [8].

- (iii) *Updating the Tracing Direction*. The extrapolation equation uses the vessel direction calculated only at the current center-line point and does not take into account the vessel geometry at the estimated next point. Hence, the estimated tracing direction \vec{u}^{k+1} is not always accurate and needs to be updated according to the local geometric and intensity-based information at the site of estimated next point. The idea of updating the preliminary estimate for the vessel direction has been suggested by many known tracing methods [8–10]. The idea is to refine the first estimate of the vessel direction by adjusting the location of the estimated next point based on its distances from the nearest boundary points.
- (iv) *Tracking*. In this step the tracing algorithm verifies the stopping conditions and repetitious traces and collects information about vessel intersections and branching or crossover points. If the estimated point is still located inside the vessel and the current vessel segment has not already been traced, it returns to the “Estimation” step to collect the subsequent center-line points; otherwise the tracking is terminated and a new trace is started from the next validated seed point.
- (v) *Filtering the Small or Disconnected Segments*. According to the application and required output, the tracing sequences which are smaller than a certain threshold and/or do not have any intersections with other segments are considered as false traces and are removed from the tracing result. In some applications, the operator can be given the ability to complete the tracing results by adding new seed points or deleting false traces.
- (vi) *Curve Smoothing*. Many well-known tracing algorithms produce jaggy or indented center-line due to their coarse angular quantization [9, 11–13]. In the sequel, they require a curve smoothing step to enhance the accuracy of the tracing results at the cost of more computation.

Different tracing algorithms vary primarily in their mechanism to estimate the next center-line point and local orientation of the arterial segment. Bolson et al. [14] proposed a method based on geometric properties of the vessel structures in the image. By manually defining the starting point and an initial direction, the algorithm estimates a new center-line point position and orientation by using a T-shaped structure which is rotated to find the best location for the next center-line point. Another representative algorithm for geometric-based vessel tracing approaches is proposed by

Sun [10] that is the basis of many successful QCA systems. Instead of using directional filters or T-shape structure, their method was based on recursive sequential tracking of the vessel's center-line with the assumption of geometric and densitometric continuity of the arteries in each incremental section. Their algorithm employs an iterative process with two extrapolation-update stages. In the first stage, an initial guess for the location of the next center-line point is made, assuming rectangular pattern for intensity profile defined perpendicular to the initial vessel direction. Then, the previous estimation is corrected by defining another profile at the new center-line point to find the point between two detected edges. Despite its accuracy and robustness, there are some major drawbacks with the Sun's algorithm. Specifically, the algorithm uses matched filtering mechanism for identification of new center-line points in vessel cross-sectional density profiles which performs inefficiently when arterial segments with nonuniform intensity distribution are encountered. Moreover, their edge detection method is based on identification of roll-off points using pure intensity values; this can cause their method to have difficulties in coping with situations such as sudden changes in path-line orientation and vessel diameters [15].

In another study, Haris et al. [16] proposed a recursive tracking algorithm based on circular template analysis and appropriate model of the vessels. Although they showed that their method is very robust and outperforms its predecessors in terms of handling bifurcations and vessel crossings, it heavily depends on the vessel center-line and contour points detected at the artery tree approximation stage which may fail to detect all of the arterial segments in poor quality angiogram images. These drawbacks are stemmed from calculating the vessel direction merely based on the local geometric features extracted from the arteries and neglecting inherent intensity and contrast variations between the two corresponding edge points at the same coronary segment. Xu et al. [8] proposed a method to improve the Sun's algorithm by combining it with a ridge based method proposed by Aylward and Bullitt [17]. In their method, the vessel direction is calculated based on a weighted combination of geometrical topology information obtained from Sun's algorithm and intensity distribution information obtained from Hessian matrix calculation in Aylward's method. They also proposed a self-adaptive look-ahead distance schema to increase the accuracy of the algorithm for extracting highly curved segments, and a dynamic size search window to cope with situations where two arteries are overlapped. Yet, some of the problems originated from Sun's algorithm are still remained unsolved, causing Xu's algorithm to deal with deviations at the site of severe stenoses. Also, there are many other recently published artery tracing algorithms in the literature. However, most of them have been developed for different applications or image modalities such as ophthalmic artery images [18] and CT angiography [19, 20].

The above mentioned limitations have motivated us to propose an improved algorithm which incorporates a semicircular vesselness profile for robust identification of next center-line point in the sequential tracking process. It uses reliable features to discriminate between the true vessel

points and the points that do not coincide with arterial segments in the angiogram. In fact, instead of using pure intensity values to identify the true vessel points, it takes advantage of a feature image based on the eigenvalues of the Hessian matrix. Each pixel in the feature image represents a vesselness measure which associates the likelihood of being a vessel point to the corresponding pixel in the original image, allowing the tracing algorithm to robustly identify the center-line path along the arteries. In addition, an adaptive schema for magnitude of the search profile is incorporated to avoid divergence and premature termination of the tracing process.

The remainder of this paper is organized as follows: a complete explanation of our proposed method is presented in Section 2. In Section 3, the experiments conducted for parameter tuning are described and the results are presented. It also includes the experimental results obtained from comparative performance evaluation. Finally, Section 4 contains the conclusion and our decision for the future work.

2. The Proposed Algorithm

The focus of this study is to propose a robust and accurate algorithm for automatic extraction of complete coronary arterial tree from angiogram images. Toward this aim, a two step solution for fully automatic vessel center-line tracing algorithm is employed which is comprised of two main steps: automatic seed point detection and center-line extraction. In this study, we present those aspects of the tracing approach necessary to extract the center-line of the arterial segments; we do not discuss the details of seed point detection and validation steps as they are previously described in the literature [9, 13, 21].

2.1. Seed Point Detection. In the fully automatic tracing algorithms, the final output of the algorithm highly depends on the initial points that are provided for the tracing algorithm to start its process. In this work, we used our previously published method for fully automatic seed point detection [21] due to its capability to provide optimal balance between the accuracy of the validation procedure and the computational efficiency. To avoid pixel by pixel processing, the seed point detection algorithm samples the image by defining a sparse grid over the image and searching for the edge pixels along the horizontal and vertical lines. The number of grid lines determines the number of edge pixels where the grid lines cut across the vessel segments. The searching process involves identification of candidate boundary points by convolving the profile produced by each grid line with the first derivative of 1D Gaussian low-pass filter. Due to computational efficiency considerations, a 1D kernel of the form $[1, 2, 0, -2, -1]^T$ is considered as a discrete approximation of the continuous filter. By convolving this kernel with the intensity values along each grid line, local peak values of the filter response are identified and collected within a small neighborhood distance. Figure 2 illustrates the result of boundary point collection process in an example angiogram.

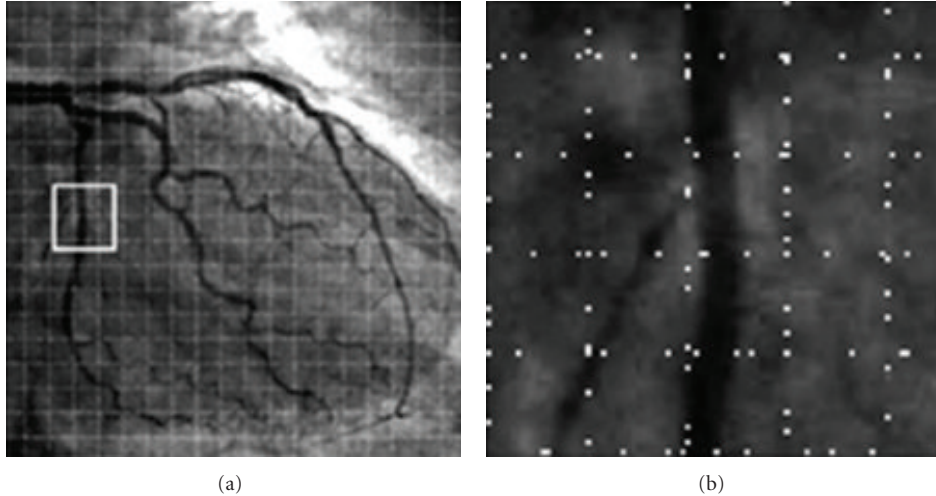


FIGURE 2: (a) Grid search for boundary points and (b) enlarged view of the box region in (a) showing the candidate boundary points without grid lines.

In the validation procedure, the collected boundary points are verified against a set of rules which are defined to discriminate between the actual seed points and mis-detections. The algorithm incorporates the symmetry of geometric properties of the gradient vectors calculated at each candidate boundary point and its neighbors. After the false candidates are removed, the locations of center-line seed points are estimated by calculating the mid-point between the validated seed points and their corresponding point on the opposite edge. Also, the initial direction of the vessel can be represented by a unit vector perpendicular to the gradient vector which is calculated at the validated boundary point. It should be noted that the space between the grid lines is chosen to be much smaller than the longitude of the smallest arterial segments. Hence, the seed point detection algorithm may produce more than one seed point for each single segment which results in repetitious traces. To avoid this problem, an efficient mechanism is applied before validating each candidate seed point to prevent the assignment of a seed point to a previously traced segment; see Section 2.5.

2.2. Estimation. Once a reliable seed point is selected, the next step (so-called the estimation step) is to determine the exact location of the next center-line point. This necessitates the identification of true vessel points in a certain neighborhood of the selected seed point. However, X-ray images suffer from a high level of noise, nonuniform background, and existence of many image artifacts which make the task more difficult to perform. Among many vessel enhancement (and extraction) approaches proposed to overcome these difficulties, the outputs of vessel enhancement methods that are based on eigenvalues of Hessian matrix exhibit more attractive properties for our case. The first reason is that, instead of producing a logical value for each pixel (to show whether or not it is located on a vessel), these methods assign a continuous vesselness value to each pixel allowing the algorithm to identify true vessel point by finding the

maximum vesselness value from a set of candidate next points in a small area surrounding the pixel. The second reason is that the innate computational characteristics of the eigenvalues of Hessian matrix allows for calculating the vesselness value based on local intensity information at each individual pixel in the image. This eliminates the need for low-level pixel processing for the whole image. The Hessian matrix at a given point p is represented by:

$$H(p) = \begin{bmatrix} I_{xx}(p) & I_{xy}(p) \\ I_{yx}(p) & I_{yy}(p) \end{bmatrix}, \quad (2)$$

where $I_{uv}(p)$ denotes the second-order spatial derivative of the image at point p , calculated by convolving the input image with the second-order derivative of the 2-D Gaussian function at a certain scale σ . According to [4], the eigenvalues and eigenvectors of Hessian matrix can be used to extract the principal directions of the local second-order variations at the vessel points. The two-dimensional Hessian matrix has two eigenvalues λ_1 and λ_2 and their corresponding eigenvectors v_1 and v_2 . The eigenvalues are assumed to be ordered such that:

$$|\lambda_1| \geq |\lambda_2|. \quad (3)$$

In coronary angiograms, vessels appear darker than the background. Thus, if we consider the input image $I_{(x,y)}$ as a 3D curvature surface, the vessel center-lines are represented by intensity valleys. Hence, for a given center-line point the eigenvector which corresponds to the stronger eigenvalue, that is, v_1 , reflects the direction of the stronger curvature within the small neighborhood around the center-line which is perpendicular to the vessel's long axis. Since the eigenvectors are orthogonal, the second eigenvector, that is, v_2 , is parallel with the direction of the vessel. Based on the above considerations, the vessel points can be identified by examining the eigenvalues λ_1 and λ_2 as follows:

$$\text{Vessel Point } (p): \lambda_1 > 0, \quad \lambda_2 \approx 0. \quad (4)$$

However, this condition may also be met for some non-vessel points due to noise or line-like background structures. To obtain more deterministic criteria, Frangi, et al. [4] developed a multi-scale vesselness function which provides a value between zero and one for each point at a certain scale. We are interested in the 2-D version of their function which combines the measures of the curvature strength and the ratio of λ_1 and λ_2 to a single value measure as follows:

$$V(p, \sigma) = \begin{cases} 0, & \text{if } \lambda_1 < 0, \\ \exp\left(-\frac{R_B^2}{2\beta_1^2}\right) \left[1 - \exp\left(-\frac{S^2}{2\beta_2^2}\right)\right], & \text{otherwise,} \end{cases} \quad (5)$$

where $S = \sqrt{\lambda_1^2 + \lambda_2^2}$ is the second-order structureness which accounts for the strength of the local contrast and $R_B = |\lambda_1|/|\lambda_2|$ is the blobness measure which differentiates between the tube-like and blob-like structures. The parameters β_1 and β_2 determine the sensitivity of the filter to the measures R_B and S , respectively. In this study, the optimal values of β_1 and β_2 are obtained based on the image characteristics.

2.2.1. Estimating the Vessel Direction. Since there is a wide range of blood vessel diameters in each angiogram, it is required to calculate the vessel resemblance values at various scales and combine them to obtain a single-valued metric. The combination process simply selects the scale which yields the maximum value of function V at a given point p :

$$\sigma_{\max}(p) = \underset{\sigma}{\operatorname{argmax}} V(p, \sigma). \quad (6)$$

The selected scale is then used for selecting the resemblance value and the best estimate of the vessel direction as follows:

$$V_{\text{opt}}(p) = V(p, \sigma_{\max}), \quad (7)$$

$$\varphi_{\text{opt}}(p) = \angle[v_2(p, \sigma_{\max})] \pm \pi. \quad (8)$$

Due to its computational complexity, this multi-scale calculation is considered as a major drawback of this vesselness function, since the core function V only calculates the measure of vessel resemblance at a single scale. In our case, however, the vessel diameter, estimated for the current center-line point, can be used to calculate an appropriate range of discrete scales for the vesselness function, obviating the need for time-consuming calculations for various scales [22].

2.2.2. Semicircular Scanning Profile. In order to find a reliable next point, the value of the vesselness function is calculated for the pixels in a small neighborhood around the current known point p^k where superscript k indicates the k th iteration of the algorithm. For this purpose, a semicircular scanning profile is defined which samples the vesselness measure for neighboring pixels around point p^k within a certain radius r^k . The semicircular scanning profile (S_r) is mathematically described as:

$$S_r(\theta, p^k) = V(p^k + r^k \vec{e}(\hat{u}^i + \theta)), \quad -\frac{\pi}{2} \leq \theta \leq \frac{\pi}{2}, \quad (9)$$

where \hat{u}^i is the angle between the current tracing direction and the x -axis and $\vec{e}(\hat{u}^i + \theta) = [\cos(\hat{u}^i + \theta) \sin(\hat{u}^i + \theta)]^T$ is a unit vector with direction $\angle(\hat{u}^i + \theta)$. The radius r^k , that is, the look-ahead distance, is adapted to the current vessel's half width R^k (the adaptation schema is described later in this section). Specifically, the value of the vesselness function V (as well as the vessel direction φ_{opt}) is calculated at each point on the semicircular search area.

This scanning profile schema has been adopted by many other methods including square scanning profiles [23–25] and complete circumferential profile functions [16, 26] which proved to be useful in providing a uniform look-ahead distance in all directions. Nevertheless, the proposed method employs a semicircular scanning profile instead of a complete circle, employed by the previous methods, to avoid unwanted backward tracing and to maintain the computational efficiency. The proposed scanning profile schema is similar to the method proposed by Schrijver [26]. The main difference between the two methods is that the Schrijver's method suggests the use of a single seed point as a starting point for recursive artery tracing algorithm. He described several conditions in which his seed point detection technique fails to provide a reliable seed point and the user intervention is required for manual selection of the initial seed point. As a consequence of using a single seed point, the scanning process requires relying on confidence scores and many threshold values to choose the potential tracing directions from several candidates for tracing the whole arterial tree. These difficulties make their algorithm unsuitable for real-time tracing applications.

2.2.3. Selecting the Correct Vessel Point. Figure 3 shows the scanning profile drawn at current point p^k to find the next point q at distance r^k from point p^k . In the process of finding the next point q^k , the following situations can be distinguished.

Correct Vessel Point. If a given point q_a is on the vessel, it can be recognized by a local maximum of the scanning profile. However, since some local maximum points may not coincide with the arteries in the image, another criterion should also be verified. Specifically, if the point q_a is on the vessel, the direction of the vessel segment between points p^k and q_a is parallel to the direction field estimated by the second eigenvector of the Hessian matrix calculated at point q_a , that is, $\varphi_{\text{opt}}(q_a)$ in (8). Furthermore, the direction field calculated at point q_a involves vectors with similar directions.

Nonvessel Point. A large part of the scanning profile is occupied by non-vessel points, for example, point q_b , at which the value of the vesselness function is small and their neighboring points constitute a nonuniform direction field.

Points That Belong to a Vessel Branch. The values of scanning profile S_r also attain a local maximum at point q_c . In addition, the direction of the vessel segment between points p^k and q_c is also parallel to the vessel direction $\varphi_{\text{opt}}(q_c)$.

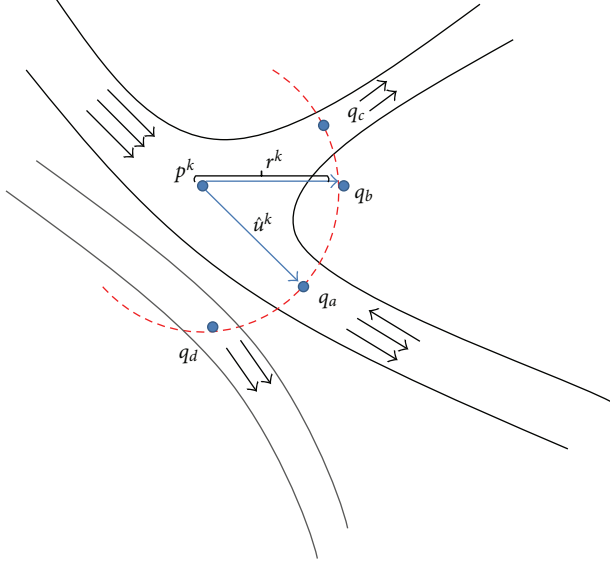


FIGURE 3: Different situations in finding the next point q^k on the semicircle scanning profile defined for the current point p^i and tracing direction \hat{u}^k on a vessel segment. The small arrows indicate the direction fields estimated by the eigenvector of the Hessian matrix.

Therefore, the algorithm should select one point between q_a and q_c . The objective is to select the main vessel segment based on the minimum difference between the angle of current tracing direction \hat{u}^k and the directions calculated by connecting point p^k to each of the two candidate points q_a and q_c . In this situation, the algorithm marks the current point as a bifurcation point and adds point q_c and its initial direction to the list of validated seed points to start a new trace in the next iteration.

Points That Belong to a Neighboring Vessel. Similar to the points that belong to a bifurcation segment, the points that coincide with a neighboring vessel constitute a local maximum in the scanning profile. However, as can be seen in Figure 3, the difference between the vessel direction φ_{opt} at point q_d and the direction of the vessel segment between points p^k and q_d indicate that it is very unlikely that the points p^k and q_d lie on the same vessel. In addition, if small values are chosen for radius r^k , the problem of jumping between the vessels can be greatly avoided.

Figures 4(b) and 4(c) show the vesselness values and vessel directions of the pixels on the profile drawn at a bifurcation point in the example angiogram in Figure 4(a). It can be seen that the vesselness graph has two major local maximum for the vessel points located on the main segment and the branching artery. Further, Figure 4(c) illustrates two sets of uniform directions for points 10–26 and 41–50 which correspond to the points of the lobes in Figure 4(b).

It should be noted that the response of the vesselness filter is decreased at the site of branching points. However, since the global shape of the vesselness filter is of main concern and not its exact values, this does not affect the performance

of the algorithm. Furthermore, if the current centerline point is on the branching point, the range of scales used to calculate the vesselness values for the branching segments is sufficient to identify the local maximum points on the branches.

2.3. Updating the Tracing Direction. Starting from the current center-line point p^k and its initial values of direction \vec{u}^k and radius R^k , a semicircular scanning profile is established to find the first estimate of the next vessel point denoted by q_0^k as described in the previous section. Given the next point q_0^k , the first estimate of vessel direction is calculated based on the geometric direction of the vector that connects the point p^k to the point q_0^k as follows:

$$\vec{u}_0^k = \frac{p^k - q_0^k}{\|p^k - q_0^k\|}, \quad (10)$$

where $\|\cdot\|$ denotes the magnitude of a vector. In most cases, this direction provides an accurate estimate of the vessel direction. Nevertheless, a new estimate is made by adjusting the location of q_0^k such that it is located in the middle of local edges. As shown in Figure 5, to find the middle point, two linear density profiles P_L and P_R are drawn at point q_0^k perpendicular to the direction \vec{u}_0^k . Then, two edge points e_L^k and e_R^k are detected by any edge detection algorithm such as finding the roll-off point based on signal and background levels of intensity values [10], directional low-pass filters [27], weighted sum of first and second derivatives of gray values [23], and many others.

However, our interest is to find the edges based on contribution of more than one pixel to detect the vessel borders in the original image. Therefore, the edges are identified by finding the maximum value of the local gradient magnitude (contrast) calculated for each point on the profiles P_L and P_R as follows:

$$e_L^k = \operatorname{argmax}(|\nabla_x m| + |\nabla_y m|), \quad (11)$$

$$m \in P_L = \{1, 2, \dots, w\},$$

where $|\nabla_x m| + |\nabla_y m|$ is an estimate of gradient magnitude at the m th pixel location on the scan profile P_L and w is the length of the search profiles which is adapted to the current vessel radius R^k . Since the radius of the semicircular scan profile satisfies our need for defining a search window that sufficiently spans the vessel width, the value of parameter w is chosen to be equal to radius r^k . The calculation of right edge point e_R^k is the same as for e_L^k , thus its equations are omitted for the sake of brevity. After calculating the location of local edge points e_L^k and e_R^k , the location of next center-line point can be updated as follows:

$$q_1^k = \begin{bmatrix} q_x^k \\ q_y^k \end{bmatrix} = \begin{bmatrix} q_{0,x}^k \\ q_{0,y}^k \end{bmatrix} + \frac{1}{2} \begin{bmatrix} e_L^k - e_R^k \cdot \vec{u}_{0,x}^k \\ e_R^k - e_L^k \cdot \vec{u}_{0,y}^k \end{bmatrix}. \quad (12)$$

Once the next point q_1^k is identified, the current vessel radius R is updated. Then, the next step is to update the vessel

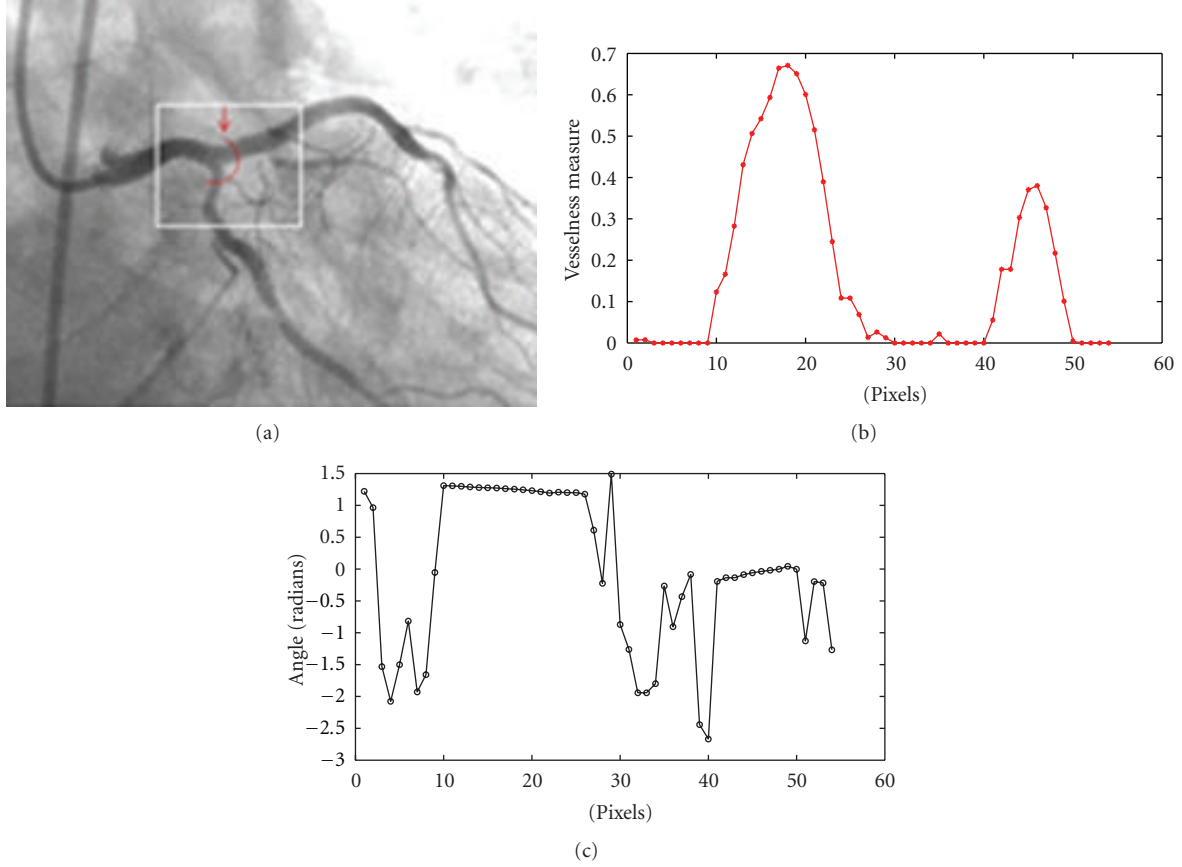


FIGURE 4: (a) A semicircular profile (in red) and its starting point indicated by the small arrow. (b) The graph of the vesselness values calculated for the points of semicircular profile drawn in (a). (c) The direction values of eigenvector v_1 (based on four-quadrant inverse tangent) calculated for the points on the semicircular profile drawn in (a).

direction vector according to the updated next point q_1^k as follows:

$$\vec{u}^{k+1} = \vec{u}_1^k = \frac{p^k - q_1^k}{\|p^k - q_1^k\|}. \quad (13)$$

2.4. The Schema for Adaptation of Step Size. The final position of the next center-line point is determined based on the position of the current point and the value of the step size α . An important challenge is to select an appropriate value for α . Since thin and small vessels are naturally more flexible and tortuous than the large ones, the tracing algorithm should take smaller steps to describe them with larger number of points. One solution is to take the radius of the scanning profile r^k as the step size to control the distance between the current center-line and estimated next point. As depicted in Figure 6, radius r^k should be greater than the current vessel's half width R^k because the semicircular profile should cut across the vessel borders at distance r^k from the current center-line point p^k . Therefore, the radius of the semicircular scan profile r^k is calculated

adaptively based on the size of vessel half width at the current center-line point p^k :

$$r^k = \rho \cdot \left[\max\{R^k, R^{k+1}\} \right], \quad (14)$$

where parameter $\rho > 1$ is a constant factor and R^k and R^{k+1} are the vessel's half width calculated for the current and next center-line points with superscript k denoting the iteration number. The term $\max\{R^k, R^{k+1}\}$ accounts for controlling the magnitude of the step size when a branching point or sudden change in the vessel's radius, that is, high-grade stenosis, is encountered. As shown in Figure 6, once the tracing algorithm reaches to a severe stenosis, the vessel's half width calculated at the next point is much smaller than that of the current center-line point. Thus, if this sudden change is not taken into account, the size of subsequent scan profiles would not be large enough to surround the vessel boundaries. In this situation, it is impossible to detect the two edge points e_L^k and e_R^k , resulting in premature algorithm termination or divergence.

A large difference between the current and previous estimation of vessel's radius yields a large scanning profile, allowing the algorithm to overcome the problem of tracing the high-grade stenosis and handling the branch and crossover points. On one hand, ρ should be kept relatively

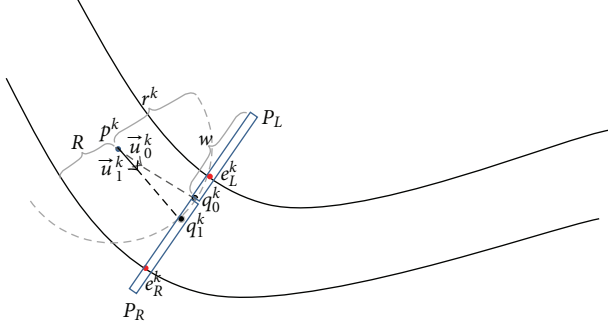


FIGURE 5: Geometric representation of the process for updating the tracing direction: (1) the first next point q_0^k is found on semicircular profile based on maximum vesselness value; (2) the vessel direction \vec{u}_0^k is estimated and two linear profiles P_L and P_R are drawn at q_0^k perpendicular to \vec{u}_0^k ; (3) two edge points e_L^k and e_R^k are detected and the final position of the next center-line point q_1^k is calculated; (4) the final tracing direction \vec{u}_1^k is updated according to the updated center-line point q_1^k .

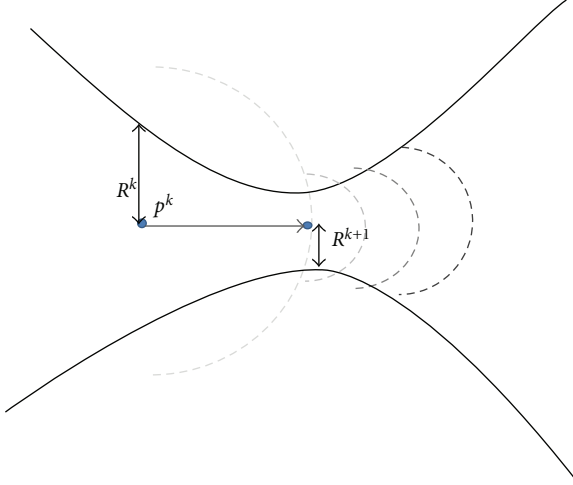


FIGURE 6: A zoom-in view of a severe stenosis. Estimated scan profiles are shown for subsequent center-line point in different gray colors. The most recent profile is represented by dark gray.

small for very large vessels in order to avoid coincidence with neighboring vessels. On the other hand, large values of ρ should be selected for small vessel widths, for example, less than 5 pixels, because significant rounding errors in calculating r^k result in obtaining values that are equal to estimated vessel half width. The experiment conducted to find an optimal value for parameter ρ will be explained later in this paper.

However, as opposed to look-ahead distance r^k , the values of step size α can be less than current vessel radius because it should account for variations of the vessel direction. An alternative solution suggests using the difference between the current and previous vessel directions for adapting the step size α . Let ω^k be the angular difference between the vessel directions \hat{u}^{k-1} and \hat{u}^k calculated for previous and current center-line points p^k and p^{k-1} , respectively, that is,

$\omega^k = \angle(|\hat{u}^k - \hat{u}^{k-1}|)$. The values of ω^k represent the change of local curvature along the current vessel segment such that when the tortuousness is small, the value of ω^k is small, and vice versa. Therefore, the value of ω^k can be used to adopt the step size based on current estimation of the vessel's half width [8]:

$$\alpha^k = \left(1 - \frac{\omega^k}{\pi}\right)R^k, \quad (15)$$

where α^k denotes the step size calculated adaptively for k th center-line point. As the value of angular difference ω^k is between 0 and π , the magnitude of the term $(1 - \omega^k/\pi)R^k$ never exceeds the vessel's half width. The above equation yields a self-adaptive step size such that the tracing algorithm takes smaller steps over the highly curved arteries. Consequently, the proposed schema provides more accurate tracing results by improving the ability of the tracing algorithm to keep up with the abrupt direction changes and coping with complex vessel geometries. The empirical study for setting the optimal value for ρ will be covered later in this paper.

2.5. Preventing Repetitious Traces. Starting from each validated seed point, the tracing process generates a sequence of vessel center-line points called "center-line segment" in the form of N -triplets each of which includes the position of center-line, direction, and local vessel radius as follows:

$$T_k = \{p^k, \vec{u}^k, R^k\}. \quad (16)$$

As mentioned before, validated seed points can be located on any point along the vessel. Hence, starting from each validated seed point, a new center-line segment is created by tracing the vessel once in direction \vec{u}^k and once along $-\vec{u}^k$. The results of several traces are stored in a two-dimensional array of integer values that has the same dimensions as the original image to maintain the center-line segments in a single array called "center-line map".

Initially, the values of all elements in the center-line map are set to zero. When a new segment is traced, a variable called "segment number" is incremented by 1. In order to store a center-line segment, the corresponding pixels in the center-line image are set to the non-zero value of the current segment number. This technique allows the tracing algorithm to prevent repetitious traces. Basically, there are two situations that should be checked to see if the current vessel has already been traced.

- (i) *Before Validating a Seed Point.* Before applying the validation rules to a given seed point, the seed point detection algorithm should check the center-line map for the existence of a previously traced segment in a small neighborhood of the candidate seed point (e.g., 5×5 neighborhood points). The seed point that is found to be located in the neighborhood of an already traced segment is ignored and a new seed point is selected from the collection of the candidate points.
- (ii) *During the Tracing Process.* The center-line image is also used for the detection of intersecting vessel

segments. Before calculating the vesselness values for the pixels on the semicircular scanning profile, their corresponding pixels in the center-line map are checked for a non-zero value. Specifically, the pixels of the scanning profile that encounter a non-zero value are collected in a candidate list and the nearest pixel to the current center-line point is considered as the intersection point. In this situation, all the points that are located on the straight line which connects the current center-line point to the intersection point are added to the current center-line segment and the current trace is terminated accordingly.

There are two points that should be noted here: (1) if the length of a traced segment is shorter than a certain threshold (e.g., less than 20 pixels), the segment is discarded and its pixels should not be added to the center-line map; (2) the segments that intersect with themselves are considered as false traces and should be rejected.

2.6. The Stopping Criteria. The traced segments should be limited to the points that belong to the arteries in the image. Accordingly, the tracing algorithm repeats tracing until one of the following criteria is met.

- (i) One or more of the pixels on the scanning profile does not coincide with the image field.
- (ii) No valid vessel point is found in the scanning profile S_r .
- (iii) The current center-line segment intersects a previously traced segment. This condition is checked for all the pixels on the straight line that connects the point p^k to p^{k+1} .
- (iv) The percent dynamic range (γ^k) of the vesselness values of the points in cross-sectional profiles P_L and P_R is below a certain threshold.

We assume that the vessel segments have continuous densitometric features and the percent dynamic range does not vary significantly along the arteries. Based on this assumption, the percent dynamic range is computed based on the vesselness values of the points of cross-sectional profiles P_L and P_R , and is constantly monitored in the tracing process to check if the stopping condition is met [10]. To calculate the dynamic range of the vesselness measure, the signal level Sg is determined by the average vesselness values between the two edge points e_L^k and e_R^k in the cross-sectional profiles P_L and P_R drawn at point p^{k+1} :

$$Sg = \frac{1}{e_L^k + e_R^k + 1} \left\{ \sum_{i=1}^{e_L^k} V(P_L[i]) + \sum_{i=2}^{e_R^k} V(P_R[i]) \right\}, \quad (17)$$

where e_L^k and e_R^k denote the offsets of the edge points on the cross sectional profiles P_L and P_R , respectively. Also, the background level is defined as:

$$Bk = \frac{1}{2w - e_L^k - e_R^k - 2} \left\{ \sum_{i=e_L^k+1}^w V(P_L[i]) + \sum_{i=e_R^k+1}^w V(P_R[i]) \right\}. \quad (18)$$

Based on the above definition, the percent dynamic range of the vesselness measure can be determined by:

$$\gamma^k = \frac{Sg - Bk}{Bk} \cdot 100\%. \quad (19)$$

The parameter γ^k is used to detect the situations where the estimated point is located on the background. In normal situations, the blood vessels have greater vesselness values than the background. In case of background tracing, however, the value of the signal level would be very close to the background level, resulting in a significant reduction in the value of γ^k . Therefore, the fourth stopping criterion is defined as:

$$\gamma^k \leq \tau, \quad (20)$$

where τ is a threshold value for percent dynamic which is set empirically such that the optimum values for performance measures consistency and discrepancy are achieved.

3. Results and Discussion

The experiments aim at finding optimal settings for parameters used in the proposed algorithm, validating the functionality of the proposed algorithm, and demonstrating the efficiency of the proposed algorithm compared to the conventional methods by conducting comparative performance evaluation. They comprise of two different types of evaluation studies.

3.1. Simulation Study. In this experiment, the synthetic images with known center-line positions and tracing directions are processed by the proposed algorithm. The estimated results are then compared with the optimal results that are generated based on *a priori* data used in the creation of the synthetic images. This comparison is made to evaluate the ability of the center-line extraction algorithms to keep up with producing satisfactory traces in difficult conditions such as complex vessel geometry and low signal-to-noise ratio. The purpose of the simulation study is to analyze the performance of the proposed center-line extraction algorithm under various geometries of the vessel segment, different vessel contrast, and different values of signal-to-noise ratio. For this purpose, a method for generating a synthetic vessel dataset proposed in Greenspan et al. [15] is adopted. As shown by the authors, the method is able to provide an objective way for comparing different center-line extraction algorithms. Nevertheless, the original method is modified to generate a wider range of geometric features such as symmetric and asymmetric lesions, radial dilation of the

vessels, and multiple lesions in a single segment. Figure 7 illustrates sample vessel images in the synthetic dataset. The dataset is composed of the following image groups.

- (i) 19 vessels with zero curvature; zero taper or medium taper value with stenosis.
- (ii) 23 knee-type vessels; no stenosis.
- (iii) 9 vessels with curvature; with stenosis.
- (iv) 9 multiple segment vessels; with stenosis.
- (v) 13 multiple segment vessels with multiple stenosis; zero taper.
- (vi) 13 multiple segment vessels with multiple stenosis; medium taper.

For each image group, four subgroups are generated by adding white Gaussian noise with different variance values to each original image, resulting in 344 synthetic images. The method used to generate synthesized vessels models the coronary angiogram image based on the 2-D geometrical representation of the vessel's projection using four parameters: vessel taper, percent stenosis, and center-line curvature and curve length.

3.2. Clinical Examples. The performance of the proposed algorithm should also be evaluated by comparing the accuracy of the proposed method with existing methods when applied to real-world images. It is worth noting that this experiment requires executing seed point detection algorithm before the automatic center-line extraction. Since our interest is to compare the performance of individual center-line extraction algorithms and not the combination of seed point detection and center-line extraction algorithms, the starting points are provided by the same seed point detection algorithm for all the experiments performed on the clinical dataset. In this study, the final center-line images are achieved by executing the seed point detection algorithm proposed in [21] with the same parameters settings described in the paper, followed by any one of the opponent center-line extraction algorithms.

To obtain a set of reliable center-line images as ground truth data, a set of 315 angiograms were processed by a modified version of the ground truth estimation method proposed by Al-Kofahi et al. [11]. The images were randomly selected from a database of routinely acquired coronary angiograms with anonymous patient information at UKM Medical Center. It consists of a wide variety of vessels, with different types of coronary lesions (types A, B, and C in AHA classification) and different geometries of vessel segments. The selected images have spatial resolution 512×512 and 8-bit quantization acquired by a "GE-Innova 2100-IQ" C-arm system.

This dataset is preprocessed and the vessel center-lines were manually annotated to obtain reference standard center-line images. In the first step, the boundaries of arterial tree in each angiogram are manually traced 5 times by the same person at different times, ignoring small arteries with less than 3 pixels wide. This results in five corresponding edge images for each image in the dataset. Then, the images in

a correspondence set were superimposed on each other such that the pixel value in the resulting image is a function of the number of overlapping pixels. This yields average images with unavoidable discontinuities. To remove the holes and discontinuities, a morphological closing operator with a 3×3 square identity matrix is used as the structuring element. In the next step, the boundary images are filled (with white color) to obtain binary images which illustrate silhouette of the coronary arterial tree. Finally, the skeletonization algorithm developed by Zhang and Suen [28] was used to estimate the location of the true center-line points. Nevertheless, the resulting center-line images were manually modified when needed. A set of angiograms and their corresponding ground truth images are shown in Figure 8.

3.3. Performance Measures. Algorithmic evaluation of center-line extraction techniques requires defining a set of performance measures. In this study, the focus is on improving the robustness of automatic centerline feature extraction while maintaining an accuracy level similar to the existing methods. Accordingly, two different types of performance measures are employed: (1) error estimation measures which provide quantitative metrics to evaluate the robustness of the proposed algorithm against difficult morphologies of the arteries, complex lesions and image degradation which are characterized by synthetic images; (2) accuracy measures which are used to assess the ability of the proposed algorithm in generating accurate tracing results in terms of consistency of the results with the ground truth skeleton images in the clinical dataset.

3.3.1. Error Estimation Measures. As mentioned earlier, in order to create a reliable and accurate synthetic dataset, the authors developed a vessel generating tool based on the method described by Greenspan et al. [15]. In their method, the reference center-line is generated by concatenation of semicircle curves with different lengths and constant curvatures. They defined a parametric equation for the semicircle curve as a function of curve arc length as follows:

$$\bar{r}(l) = \bar{r}_0 + \frac{1}{K} \bar{r}'_0 \cdot \phi_1, \quad (21a)$$

$$\phi_1 = \begin{bmatrix} \sin(lK) & 1 - \cos(lK) \\ \cos(lK) - 1 & \sin(lK) \end{bmatrix}, \quad (21b)$$

where $\bar{r}(l)$ is a position vector, $0 < l < L$ is the curve arc length variable, and L is the total length of the semicircle curve. Further, parameter \bar{r}_0 is the initial position of the semicircle and \bar{r}'_0 denotes the tangent at \bar{r}_0 . The next semicircle curve can be attached to the current curve by using the values of $\bar{r}(L)$ and $\bar{r}'(L)$ as its initial definition. Based on the above formulation, two error estimates are defined as follows.

Normalized Global Distance Error. This error measure reflects the average radial distance between the points on the reference center-line and their corresponding points on the estimated center-line. In order to assure that the two corresponding points lie on the same curvature radius, the

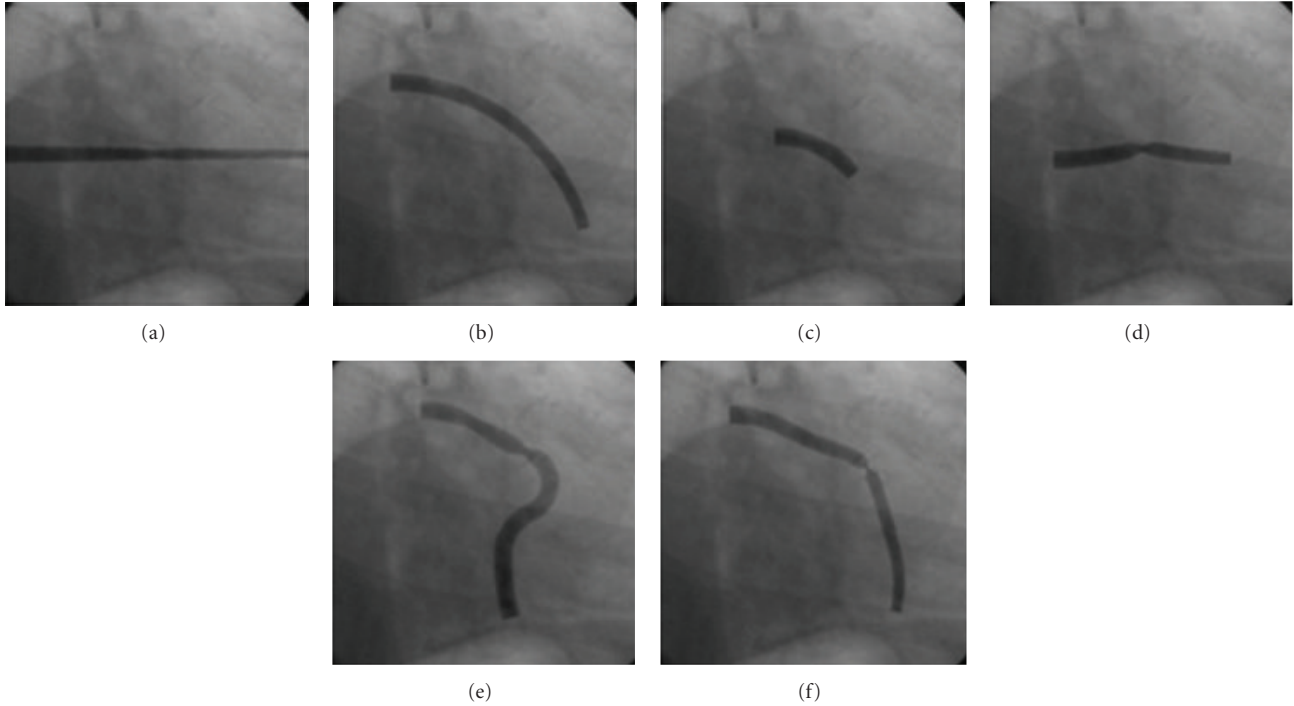


FIGURE 7: Sample vessel images from synthetic dataset, including vessels with different values of taper, curvature, percent stenosis, and number of stenosis.

closest point technique is not used to find the correspondence between points on the two center-lines. Instead, for a given point p^i on the reference center-line, a corresponding point q is identified on the estimated center-line that lies on the profile which is drawn at point p^i perpendicular to the reference center-line, that is, local tangent vector. Therefore, the normalized global distance error is defined as [15]:

$$d_{\text{Norm}} = \sqrt{\frac{1}{N} \sum_{i=1}^N \left(\frac{d_i^2}{r_i^2} \right)}, \quad (22)$$

where d_i is the radial distance in pixels between the two corresponding point, r_i is the vessel's radius at point p^i and N is the number of points contributed in calculations. This formula exhibits more emphasis on the distances where the vessel's diameter is small rather than the distances calculated at vessel areas with large diameter. It is used to evaluate the algorithms against our main objective which is the accurate extraction of vessel center-lines including coronary arterial lesions.

Global Orientation Performance Measure. In addition to the distance error, orientation distance O_i between the corresponding points is also computed as the difference between the corresponding tangents at the selected points. This performance measure is obtained by calculating the mean square orientation error as follows [15]:

$$O_{\text{MSE}} = \sqrt{\left(\frac{1}{N} \right) \sum_{i=1}^N O_i^2}, \quad (23)$$

where O_i is the orientation error in degrees which reflects the difference between the direction of tangent vectors measured in degrees at the i th point of the reference center-line. The traces in which the algorithm fails to cover more than 60% of the ground truth center-line are considered as divergence.

3.3.2. Accuracy Measures. In order to evaluate the accuracy of the proposed algorithm, a validation study is conducted on the accuracy of the tracing results when applied to real world images. In this study, the accuracy is measured with respect to ground truth images obtained from the clinical dataset and is defined based on “discrepancy” and “consistency” measures described in [11]. Discrepancy measures the quality of estimating the true location of the center-line points. It is calculated by computing the average Euclidean distance between the points of the center-line map produced by the algorithm and their corresponding points in the ground truth image.

Let A denote a set of centreline points generated by the proposed tracing algorithm and G be the set of ground truth points. Let two subsets $A_g \subseteq A$ and $G_a \subseteq G$ be the points of sets A and G that have a correspondence in another image. The correspondence indicates that for each point a in subset A_g , there is a corresponding point $C_g(a) \in G$ such that the Euclidean distance between the points is less than a particular number of pixels δ . The correspondence can be described by:

$$C_g(a) = \underset{g \in G}{\operatorname{argmin}} \{ \|a - g\| \}, \quad (24)$$

where notation $\| \cdot \|$ denotes the Euclidean distance. Similarly, for each $g \in G_a$ there is a corresponding point whose

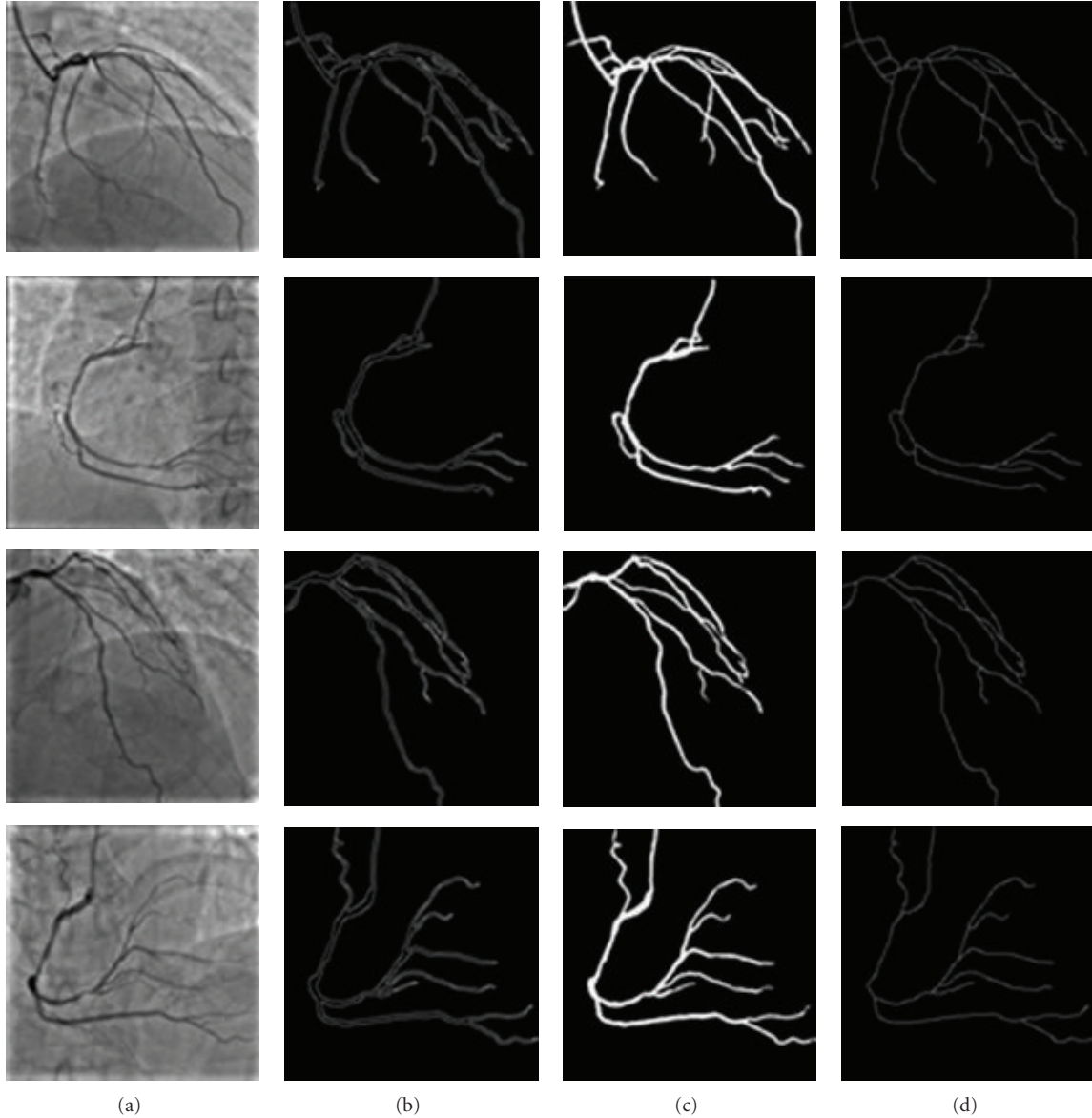


FIGURE 8: Four angiogram images and their corresponding feature images. (a) Original angiogram; (b) average boundary image; (c) silhouette image; (d) center-line image.

Euclidean distance with g is less than δ and is denoted by $C_a(g)$. It should be noted that due to the curved nature of the traces, there is no guarantee to find one-to-one correspondence between the points in A_g and G_a .

The spatial discrepancy between the center-line map produced by the proposed algorithm and the center-line image in the ground truth is defined as follows [11]:

$$\mu = \frac{1}{2|A_g|} \sum_{a \in A_g} \|a - C_g(a)\| + \frac{1}{2|G_a|} \sum_{g \in G_{ga}} \|g - C_a(g)\|. \quad (25)$$

Consistency measures the ability of the algorithm in detection of true segments characterized by the ground truth and avoiding false traces. The consistency between two trace sets is calculated by finding the percentage of points in one

set which has a corresponding point in another set that is within disk radius δ . Observe that the consistency is a mutual measure with similar definitions as follows:

$$\alpha_{ag} = \frac{|A_g|}{|A|} \times 100\%, \quad (26a)$$

$$\alpha_{ga} = \frac{|G_a|}{|G|} \times 100\%. \quad (26b)$$

The first definition refers to the ability of the tracing algorithm in preventing false traces, while the second definition indicates the completeness of the tracing output. These measures are equally important to assess the accuracy of the proposed method, thus to compare the performance of

different algorithms we calculate a single balancing measure called F_1 measure as follows:

$$F_1 = \frac{2\alpha_{ag} \cdot \alpha_{ga}}{\alpha_{ag} + \alpha_{ga}}. \quad (27)$$

The values of F_1 are calculated for each image in the clinical dataset as a function of disk radius δ . The average F_1 values over all clinical images are used as the basis of our comparisons.

3.4. Parameter Tuning. Before performing experiments for performance evaluation, the optimal values of the algorithm's parameters should be found. Primarily, two parameters β_1 and β_2 in (5) are tuned by examining their different value combinations on the performance of the vessel resemblance function. Referring to (5), it is expected that in most cases, the value of R_B is close to 1. This is due to the fact that, on average, the values of $|\lambda_1|$ and $|\lambda_2|$ are similar. Therefore, in order to obtain more discrimination between the line-like and blob-like structures, the value of β_1 should be in the order of 1. On the other hand, β_2 determines the influence of contrast strength in vessel enhancement. By selecting large values for this parameter (e.g., in the order of 10), low-contrast objects are ignored and only vessels with significant contrast are enhanced.

The above conclusions are supported by Figure 9 which shows the effect of selecting different value pairs for β_1 and β_2 within a particular range of scales, that is, $1 \leq \sigma \leq 10$. It can be observed that, high values of β_1 increase the response of the vesselness function for vessel structures than the small values at the expense of enhancing more background structures. The small values of the second parameter, for example, $\beta_2 = 2$, incorporate more noise and background structures in the outcome of the enhancement than the large values. However, the large values, for example, $\beta_2 = 32$, result in significant reduction of the filter response even for the high contrast vessel areas.

The best values of β_1 and β_2 are selected based on the experiment conducted to compare the outcome of applying the vesselness algorithm on the images of the dataset with their corresponding ground truth silhouette images. The comparison procedure involves the following steps.

- (1) Calculating the number of false positives F_p by counting the number of pixels in the vesselness image at which the vesselness value is greater than zero, but their corresponding point in the ground truth image is black.
- (2) The number of false negatives F_n is also calculated as the number of white pixels in ground truth silhouette image which correspond to a zero vesselness value in the vesselness image.
- (3) Calculating the normalized sum of false detections ε_F which is used as an objective discrepancy measure that quantifies the deviation of vesselness images, obtained by applying different values of parameters

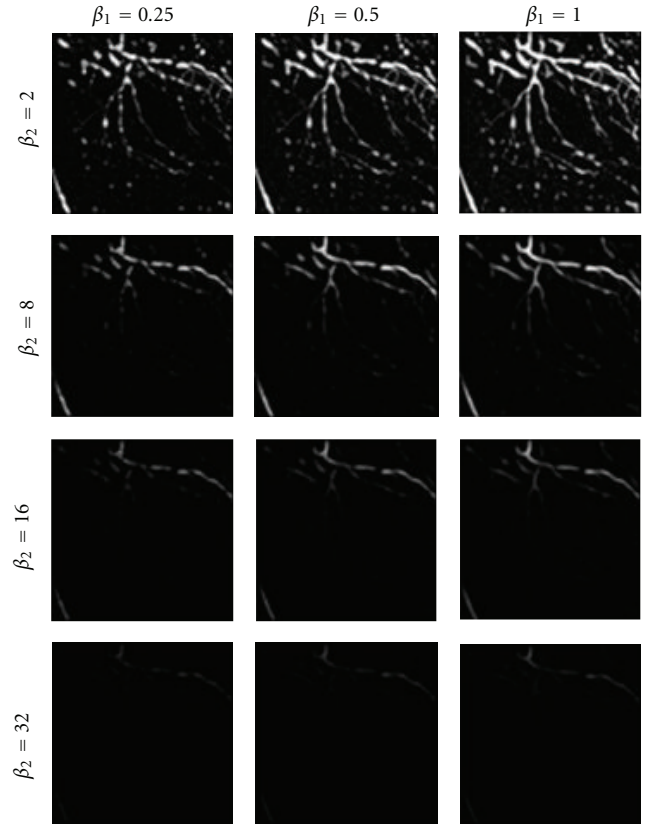


FIGURE 9: Effect of different values of parameters β_1 and β_2 on the output of the vesselness function V .

β_1 and β_2 , from the ground truth silhouette images [29]:

$$\varepsilon_F = \frac{F_p + F_n}{2N}, \quad (28)$$

where N is the number of all pixels in the image.

In this study, a set of 12 vesselness images corresponding to three values for parameter β_1 , that is, $\beta_1 = \{0.25, 0.5, 1\}$ and four values for parameter β_2 , that is, $\beta_2 = \{2, 8, 16, 32\}$ were created. The appropriate values of β_1 and β_2 were chosen from the vesselness image with minimum discrepancy measure ε_F . The result of this experiment showed that the values of $\beta_1 = 1$ and $\beta_2 = 16$ are appropriate for the clinical dataset.

The remaining parameters are constant factor ρ in (14) and τ in (20). To obtain the optimal value for ρ , the proposed algorithm was used to extract the center-lines of clinical images. As mentioned in Section 2.4, a large value of parameter ρ increases the size of the semicircular profile and, accordingly, raises the probability of jumping the tracing point from the current vessel segment to another vessel. Therefore, the value of this parameter should be determined by measuring the consistency and the discrepancy of the algorithm's output with the ground truth center-line on the real-world clinical images in which the problem of jumping between the vessels is probable. We did not use

synthetic images for this purpose since each synthetic image contains a single arterial segment with no side branches.

For each image, a total of 11 center-line segments were obtained, corresponding to different values of ρ ranging from 1 to 2 in a step of 0.1. Then, the average F_1 values are calculated over all images in the clinical dataset within disk radius of 5 pixels. Also, deviations from the ground truth center-line images are measured by calculating average discrepancy as shown in Figure 10.

It can be observed that the value of discrepancy rises as larger values are used for ρ . This is due to the fact that the vessel curvature and vessel diameter varies more slowly within a small vicinity than a large distance along the vessel segment. Therefore, the large radius of scan profile r^k has a negative impact on the accuracy of the estimated vessel direction. By comparing different values of F_1 measure, the value of $\rho = 1.3$ is selected as the optimal value.

However, it should be noted that since r^k is an integer value (number of pixels in semicircular scan profile), a fixed value for ρ results in significant rounding errors for the vessels with small diameter (less than 5 pixels). Figure 11 shows the ratio of rounding error relative to the vessel radius for different values of vessel radius where ρ is set to 1.3. Therefore, a constant value for r^k (e.g., $r^k = 5$) can be used when the vessel half width is less than 5 pixels.

Another parameter is the threshold τ for the percent dynamic range of the vesselness measure which should be set based upon the image characteristics. This parameter is tuned by observing the effect of its different values on the performance measures α_{ag} and α_{ga} by applying the tracing algorithm to the images of the clinical dataset. According to Figure 12, the optimal value for τ is obtained where the performance measure F_1 reaches to its peak at $\tau = 0$. It can be seen that the values of performance measures α_{ag} and α_{ga} almost remain steady when $\tau \leq -2$. After this point, the performance measure α_{ag} starts to grow steeply while the performance measure α_{ga} begins to fall more rapidly. By considering the definition of performance measures in (26a) and (26b), the above observation can be related to the reduction in the number of center-line pixels generated by the proposed algorithm. This reduction affects both performance measures α_{ag} and α_{ga} because setting larger values for parameter τ leads to obtain less false traces as well as less correctly traced segments. However, as the value of threshold τ increases, more correct traces are lost than the false ones. This implies that the proposed algorithm tends to produce less false traces and more true positives regardless of the value selected for parameter τ .

3.5. Experimental Results for Algorithm Validation. In this section, the efficiency of the proposed algorithm is assessed to see if it is able to produce satisfactory results. It should be noted that all heuristic schemas which are proposed for step size and look-ahead distance adaptation are employed in all experiments conducted for algorithm validation except otherwise stated. The synthetic images are divided into 7 groups of arterial segments, with different geometries and varying percentage of stenosis, for comprehensive validation

of the proposed algorithm. The image groups are listed in Table 1. The first group contains the vessels with zero curvature, zero taper value with different percentage of stenosis. This group is used to evaluate the ability of the algorithm in addressing the problem of algorithm's divergence at the site of high-grade stenosis. In this experiment, our focus is on cases in which large deviations occur at the site of stenosis on the straight vessels, that is, zero curvature with constant taper segments. As shown in Figure 13, the effect of percent stenosis on the accuracy of the proposed algorithm is markedly low such that for stenoses between 60–90%, the values obtained for both error measures remain in a reasonably low level and almost equal to each other. Furthermore, no divergence was observed for vessels with 95% stenosis.

The second group of images differs from the first group by changing the taper value from 0 to 0.00145, while almost the same values of percent stenosis are employed. Figures 14(a) and 14(b) present 7 error samples for the second group corresponding to vessels #13 to #19. By comparing the results in Figures 13(a) and 14(a), it can be seen that the distance errors plotted for different values of percent stenosis in group 2 are slightly higher than that of group 1; while approximately similar range of results (less than 1 degree) are obtained for the orientation error measure in Figures 13(b) and 14(b).

The results indicate that the vessel tapering has a trivial effect on the accuracy of the proposed algorithm in terms of estimating the curvature (tangent values) at the center-line points. As expected, for the vessel segments with larger taper values, a slight increase in the distance error measure is observed for all values of percent stenosis. This is due to the sudden change of vessel's half width before and after the stenosed region which causes jittery behaviour in the estimated center-line.

The third image group is used to assay the behaviour of the proposed algorithm when applied to the vessel segments with different curvatures. To attain this goal, the other contributing factors were removed from the third group, that is, no stenosis and constant tapering value. Two experiments were performed on 24 images (corresponding to vessels #20–#43) with different values of curvature ranging from 0.003 to 0.015 radians. In the first experimental run, no adaptation is used for calculating the step size α ; while in the second run the step size is adapted based on angular difference between the current and previous estimates of the vessel direction. Figure 15(a) shows the performance results for the first experimental run by applying the proposed algorithm to the knee-type vessels in group 3. The graphs illustrate the distance and the orientation error performance measures as a function of curvature, that is, vessel segments with varying arc-length (from 50 to 175 pixels) are grouped based on their curvature values. The graph of distance error demonstrates an exponential relationship between the performance and the curvature of the vessel segments. In contrast, the values of orientation error in Figure 15(b), that are obtained from the second experimental run, exhibit more gradual increase in orientation error as a function of curvature value. This indicates that without step size adaptation, the proposed

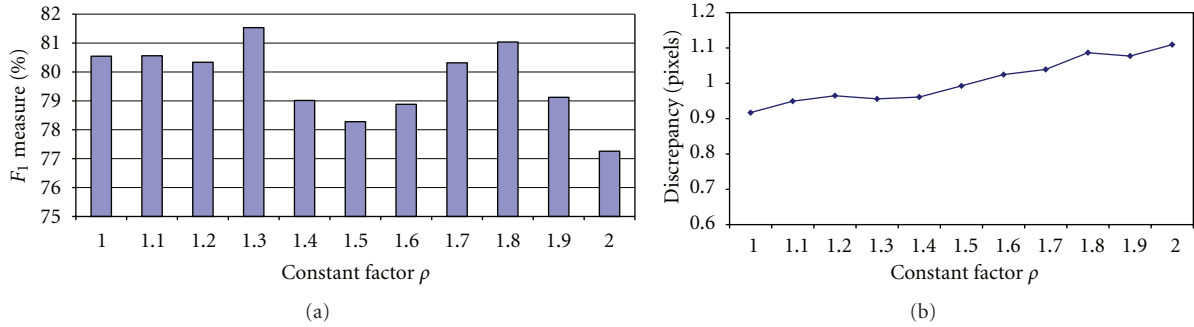


FIGURE 10: Consistency and discrepancy between the estimated center-lines and the ground truth center-lines with different values of constant factor ρ . (a) The values obtained for performance measure F_1 for different values of ρ ; (b) the values of discrepancy versus constant factor ρ .

TABLE 1: Different geometric parameters of synthetic vessel image database.

Group	Image number	Curvature type	Taper	Stenosis	Segment type	Length
1	No. 1–no. 12	No curvature	0	30–95%	Single segment	Constant
2	No. 13–no. 19	No curvature	0.00145	30–95%	Single segment	Constant
3	No. 20–no. 43	Knee-type	0.0008	No stenosis	Single segment	Constant
4	No. 44–no. 52	Variable	0.0008	30–95%	Single segment	Variable
5	No. 53–no. 61	Variable	0.001	30–95%	Multiple segment	Variable
6	No. 62–no. 74	Variable	0	Multiple stenosis	Multiple segment	Variable
7	No. 75–no. 87	Variable	0.00145	Multiple stenosis	Multiple segment	Variable

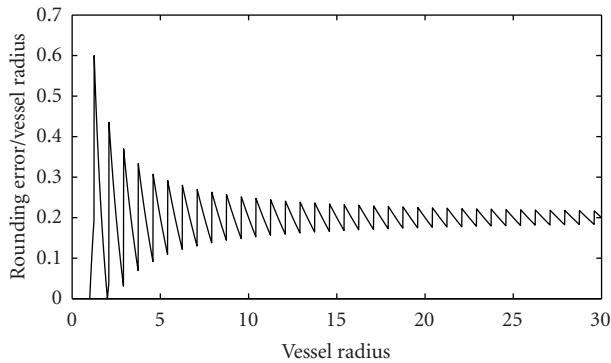


FIGURE 11: Ratio of rounding error to vessel radius versus different values of vessel radius for $\rho = 1.3$.

algorithm is highly sensitive to the vessel's curvature in terms of estimating the distance rather than the orientation. In this condition, the algorithm is more accurate in estimating the direction of the vessel segment than estimating the correct position of the center-line points when highly curved segments are encountered. This is due to large errors in the approximation of the local vessel directions by using large values for the step size at the site of curved segments.

As explained before, the second adaptation schema is based on choosing values smaller than current vessel radius so as to describe the tortuous vessel center-lines with larger number of pixels. The graphs of error measures in Figure 15(b) show the effectiveness of the

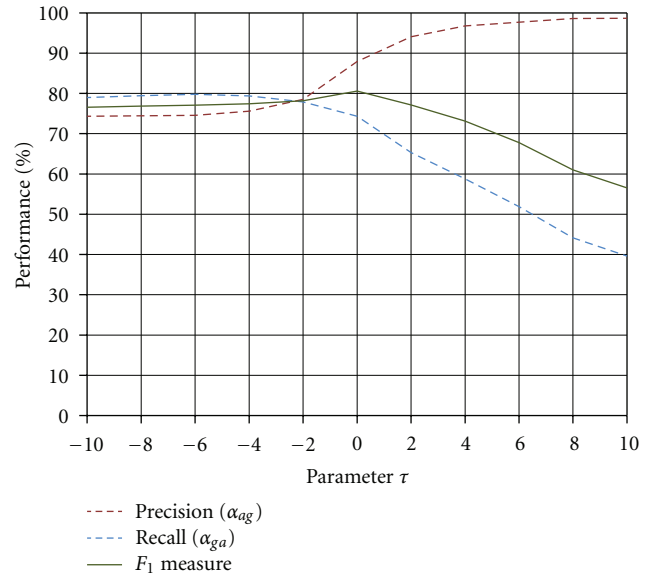


FIGURE 12: Performance measures obtained for different values of parameter τ .

proposed step size adaptation schema. In the second experiment, the value of parameter ρ is kept constant and the proposed algorithm utilizes the step size adaptation schema. In contrast to the graph of distance error in Figure 15(a), the values of distance error in Figure 15(b) increase more gradually as the curvature increases from 0.006 to 0.015. This indicates a considerable reduction in the

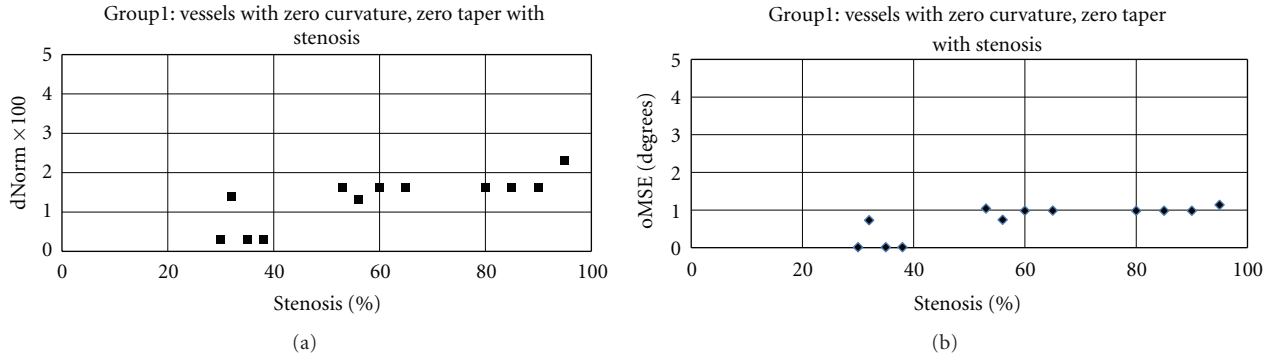


FIGURE 13: Distance performance measures versus percentage of stenosis calculated by applying the proposed algorithm on the images of group 1. (a) Normalized global distance error; (b) global orientation performance measure.

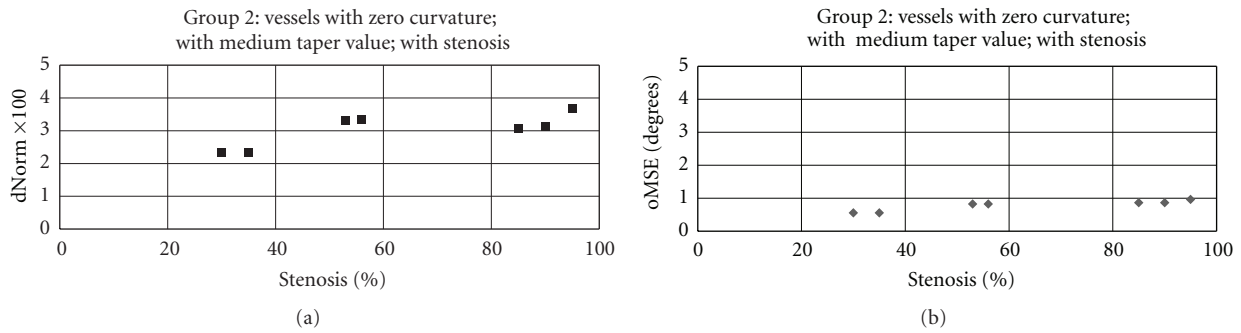


FIGURE 14: Distance performance measures calculated by applying the proposed algorithm on the vessels with zero curvature; medium taper value (0.00145); with stenosis. (a) Normalized global distance error; (b) global orientation performance measure.

distance error when highly curved vessels are encountered. Although no significant reduction is achieved for values of the orientation error in the second graph, a comparison between the slopes of the corresponding graphs indicates that the step size adaptation schema reduces the sensitivity of the tracing algorithm to the vessel curvature and improves its robustness to geometrically complex structures.

Validating the Step Size Adaptation Schema. However, this improvement is obtained at the cost of more divergence at the site of stenoses that causes rapid changes in the vessel's diameter. The divergence is defined as a condition where the center-line produced by the proposed algorithm covers less than 60% percent of the ground truth center-line. To evaluate the ability of the tracing algorithms in extracting the center-line at the site of severe stenoses, we measure the algorithm's success rate as the average number of center-line points in the estimated center-line that have a corresponding point in the ground truth center-line for different values of percent stenosis in vessel groups 4 and 5.

In Figure 16, the success rate of the proposed algorithm is plotted against percent stenosis for two adaptation schemas. In the first schema, only the radius r^k is calculated adaptively and no adaptation is used for the step size α , while in the second schema both radius r^k and step size α are calculated adaptive to the vessel's half width. It can be concluded that

the drawback of using adaptive schema for calculating the step size emerges in difficulties in coping with abrupt changes of the vessel diameter near to the severe stenoses, that is, vessels with percent stenosis above 90%.

3.6. Experimental Results for Performance Evaluation. To evaluate the accuracy and robustness of the center-line extraction algorithm, two experiments were conducted on the proposed algorithm and its three well-established counterparts: Sun algorithm [10], Aylward algorithm [17], and the algorithm proposed by Xu et al. [8].

In the method proposed by Xu et al., the vessel direction is calculated based on a weighted combination of geometrical topology information obtained from Sun's algorithm and intensity distribution information obtained from Hessian matrix calculation in Aylward's method. This combination is achieved by adjusting the weighting factor α whose range is $0 \leq \alpha \leq 1$. Hence, the tracking direction is determined solely by the geometric direction when $\alpha = 1$ and the tracking algorithm becomes very similar to the Sun algorithm; while the tracking direction is determined solely by the intensity direction, that is, the Hessian eigenvector, when $\alpha = 0$ and the tracking algorithm becomes somewhat similar to the Aylward algorithm. Xu et al. suggest that more accurate results can be achieved by changing the weighting factor α to 0.5. Accordingly, we implemented the algorithm developed by Xu et al. and compared our proposed method with the

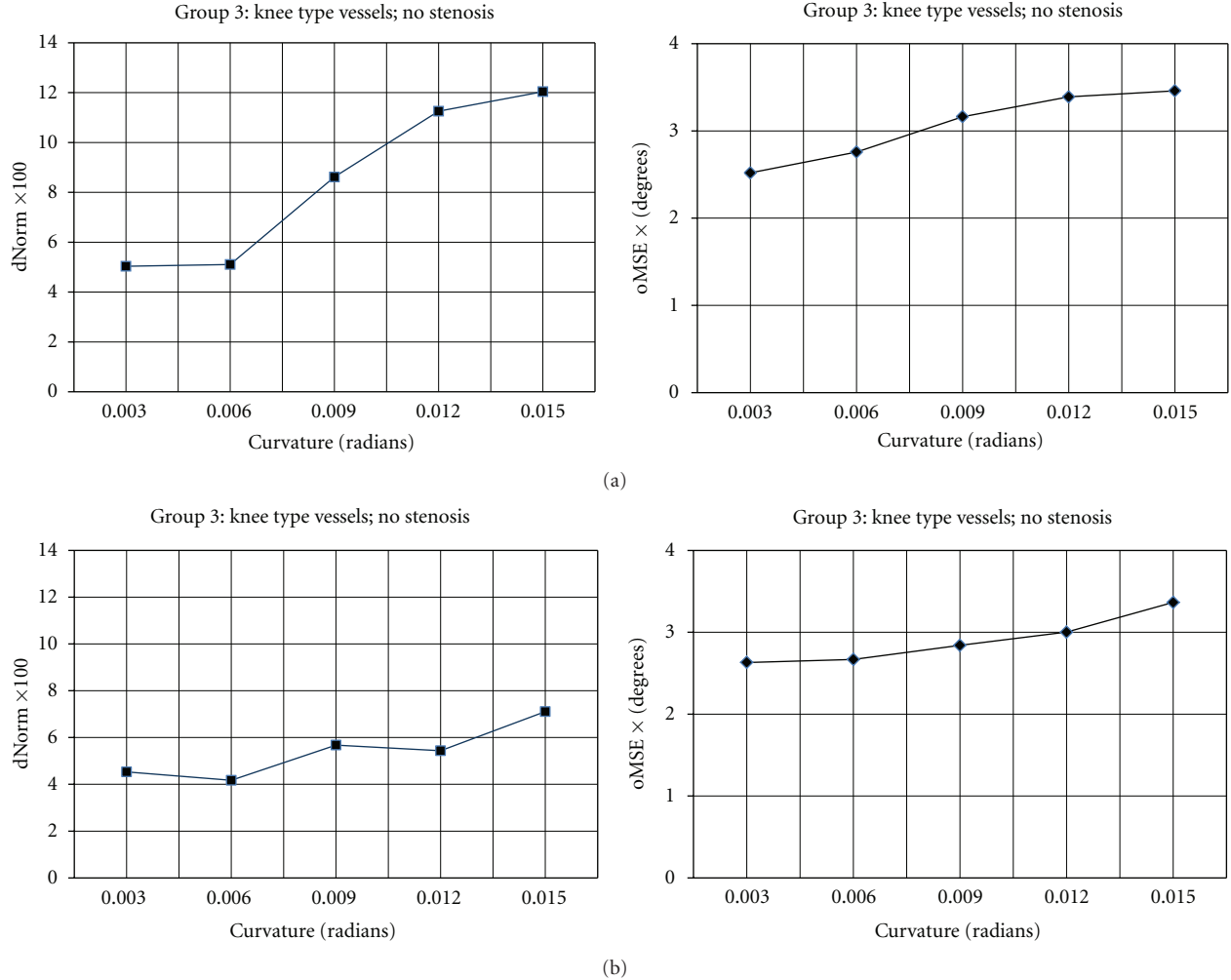


FIGURE 15: The average performance results calculated by applying the proposed tracing algorithm on the vessel segments with equal curvature values, varying arc-length, constant taper value, and no stenosis in image group 3. (a) No adaptation schema is used for the step size. (b) The step size is adapted based on angular difference between the current and previous estimates of the vessel direction.

TABLE 2: List of parameter values set for the other three algorithms used in the comparison.

Parameter	Symbol	Value(s)
Weighting factor for detection of overlapping vessels	β	1.5
Constant factor for adaptive look-ahead distance based on curvature change	ρ	$1/\pi$
Proportionality constant for search window	K_w	2
Proportionality constant for look-ahead distance	K_d	2
Threshold for percent dynamic range	γ_t	0.5%

other three methods by setting parameter α to 0, 0.5, and 1. Other parameters are listed in Table 2.

The first experiment aims to evaluate the accuracy of the algorithms in extracting the center-lines of the coronary vessels in clinical images. In the first step, the proposed seed point detection algorithm was used to provide an equal set of validated seed points for all the tracing algorithms. The optimal parameter values are used to setup the seed point detection algorithm. Given the validated seed points, the proposed algorithm and the three existing algorithms were employed to trace the artery center-lines in the images of the clinical dataset. The original image and the tracing outputs using different algorithms in a small area of an example angiogram are shown in Figure 17.

It can be clearly seen that the proposed algorithm outperforms the earlier solutions in terms of the accuracy of the tracing output. According to the outputs, the Sun algorithm is significantly distracted by the peripheral image artifacts while the Aylward algorithm fails to trace the highly curved segments. Also, the output obtained from the Xu's algorithm is considerably accurate. This can be ascribed to taking advantage of the strength of both geometrical

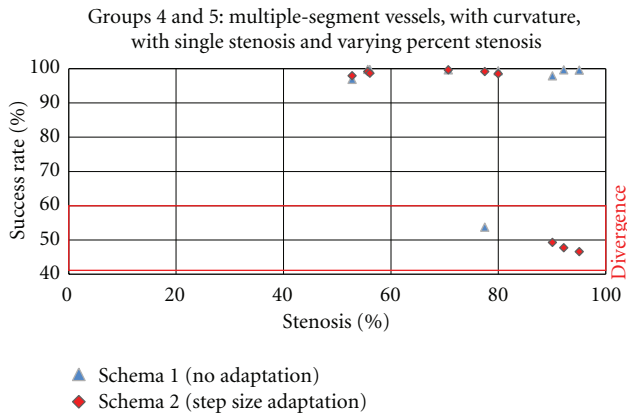


FIGURE 16: The average success rate calculated for the vessel segments with different curvature values, medium taper values, and single stenosis with varying percentage in image groups 4 and 5.

and intensity-based approaches for estimating the vessel direction. Yet, it contains small deviations where the minute branches are encountered.

Figure 18 illustrates the figures of average discrepancy measure over all clinical images at different values of disk radius δ . Observe that the proposed algorithm is superior to its opponents for most values of $\delta > 2$. For example, the average discrepancy calculated for the proposed algorithm is about 0.88 pixel at $\delta = 5$, which is approximately 0.1 pixels less than that of Xu's algorithm at the same disk radius. This can be attributed to the fact that, in contrast to the existing methods, the proposed tracing algorithm uses robust features to identify the location of the next point, and thus it is less sensitive to intensity variations, illumination changes, and image artifacts which increase the discrepancy between the estimated and ground truth center-lines.

In Figure 19, the average of consistency measure over all clinical images is plotted for the proposed algorithm and its opponents. According to the graphs, Aylward has the lowest consistency figures for all values of disk radius. This is due to ignoring the geometric features of the arteries in estimating the location of the next point which results in high estimation error. The plots correspond to the other algorithms run almost closely to each other. However, a more precise observation revealed that, as it was expected, the Sun's algorithm is outperformed by the algorithm proposed by Xu et al. for all values of disk radius δ . This superiority comes from utilizing the advantages of estimating the vessel direction based on eigenvalues and eigenvectors of Hessian matrix. Although Xu's algorithm dominates the competing algorithms in terms of highest values of consistency measure for the first two values of disk radius (26% and 60% resp.), the proposed algorithm exhibits an average of 5% increase in consistency measure where $\delta > 1$. For instance, an average F_1 -measure of 82.1% was obtained for the Xu's algorithm compared with 88.8% recorded for the proposed algorithm at $\delta = 5$. By considering the fact that the consistency measure has two contributing factors, namely precision and completeness of the tracing output, this improvement can

be related to more complete tracing results or higher recall values obtained for the proposed algorithm at higher values of disk radius.

The second category comprises the experiments to assess the robustness of the algorithm to different amounts of impulse noise. The robustness of the algorithms is measured by calculating the algorithm's success rate when an increasing amount of noise is added to the synthetic images. The Poisson noise is simulated by White Gaussian noise with a known range of variance. In this experiment, the noise was gradually added to the synthetic images such that the resulting signal-to-noise ratio declined from 20 dB to 10 dB.

As mentioned earlier in this chapter, the algorithm's success rate refers to the proportion of the true vessel center-line that can be traced by the algorithm without premature termination. Figure 20 shows how different algorithms behave in response to increasing amount of noise which causes the tracing algorithms to diverge and terminate prematurely before the vessel segment is completely traced.

As demonstrated in Figure 20, the Aylward algorithm has the lowest success rates for high signal to noise images, that is, $\text{SNR} \geq 20$ dB. In contrast, the other rivals have almost perfect success rates (at least 94%) within the same range of SNR. By increasing the amount of noise, the success rate of the Sun's algorithm falls significantly, from about 93% at $\text{SNR} = 20$ dB to approximately 69% at $\text{SNR} = 16$ dB and reaches to the bottom of 9% for the images with lowest signal-to-noise ratio (10 dB). Interestingly, the success rate of the Xu's algorithm follows the same pattern as the Sun's algorithm does. However, on average, it exhibits almost 10% improvement in success rate for low quality images. It can be clearly seen that, in images with higher values of additive noise, Aylward algorithm yields more success rates than both methods of Sun and Xu. Also, it can be observed that all existing algorithms diverge if the SNR falls below 16 dB. The figures obtained for the proposed algorithm show the superiority of the proposed method to the existing algorithms in terms of robustness to the inherent noise of angiogram images. The results of this experiment showed that the proposed tracing algorithm obtained about 33% improvement upon the existing methods in terms of algorithm's success rate in processing low quality images.

4. Conclusion and Future Works

All these observations led us to conclude that estimating the vessel direction based on eigenvalues and eigenvectors of Hessian matrix results in improvement in the robustness of the tracing algorithms. On the other hand, utilizing the geometric features of the arterial segments in estimating the location of the center-line points leads to obtaining more accurate results. It seems possible that the promising results obtained for the proposed algorithm are due to combining the advantages of the above mentioned approaches and avoiding the limitations associated with existing methods in handling highly curved segments and sudden changes of vessel diameter at the site of arterial lesions. The results of comparative performance evaluation showed that, according

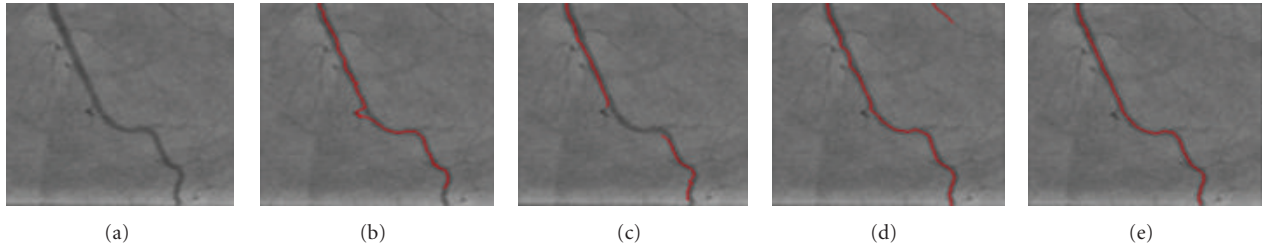


FIGURE 17: A small patch of a clinical arterial image with a curved vessel in (a) original image; and the tracing results using (b) the Sun algorithm (c) the Aylward algorithm (d) the Xu et al. algorithm, and (e) the proposed algorithm.

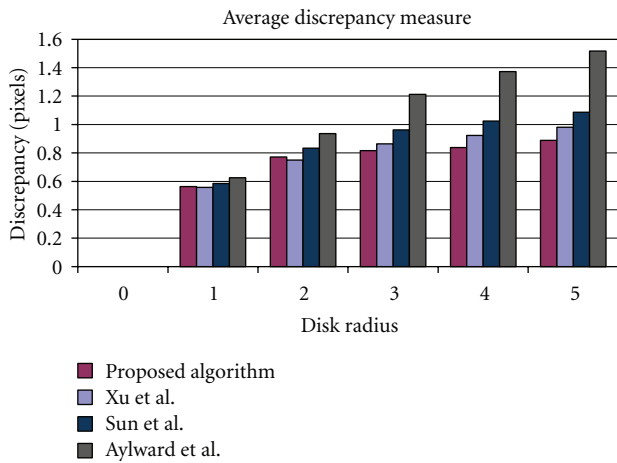


FIGURE 18: Average discrepancy between the ground truth center-line and the output of various tracing algorithms applied to the images of the clinical dataset.

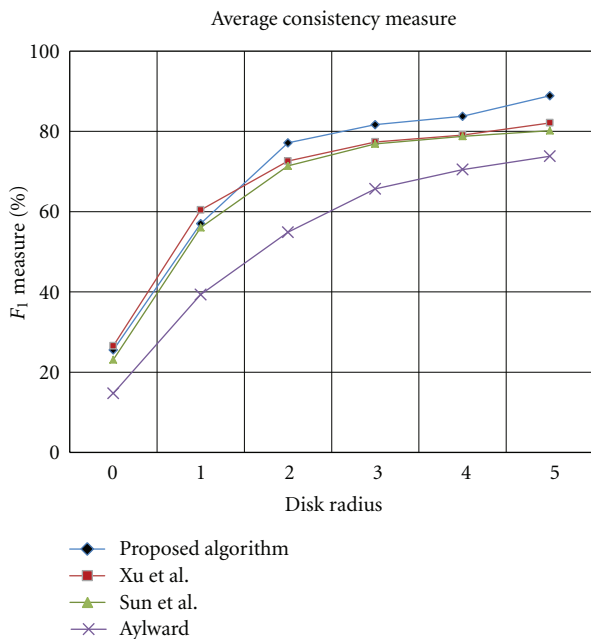


FIGURE 19: Average consistency measure, that is, percentage of points in the estimated center-line that coincides with the ground truth center-line, calculated for various tracing algorithms over all images in the clinical dataset.

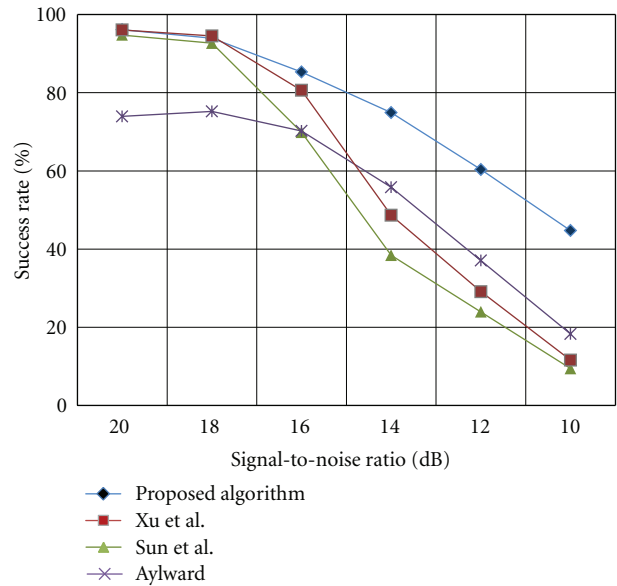


FIGURE 20: The average success rate versus signal-to-noise ratio calculated for all 7 groups of vessel segments in the synthetic dataset.

to expectations, the proposed method achieved a remarkable improvement in the accuracy of the tracing algorithm. Surprisingly, the proposed algorithm was found to be extremely more robust to image noise than existing well-known methods. This makes the proposed algorithm more suitable for feature extraction and quantitative coronary analysis from inherently noisy data in real-world applications. In the future, we plan to conduct a comprehensive study on the effect of utilizing different seed point detection algorithms on the performance of the whole center-line extraction method.

Acknowledgment

The authors wish to thank the medical staff of Cardiology Department of Hospital HUKM Malaysia for their support in the data collection effort.

References

[1] A. D. Hoover, V. Kouznetsova, and M. Goldbaum, "Locating blood vessels in retinal images by piecewise threshold probing

- of a matched filter response," *IEEE Transactions on Medical Imaging*, vol. 19, no. 3, pp. 203–210, 2000.
- [2] Q. Li, J. You, and D. Zhang, "Vessel segmentation and width estimation in retinal images using multiscale production of matched filter responses," *Expert Systems with Applications*, vol. 39, no. 9, pp. 7600–7610, 2011.
- [3] E. R. Dougherty, *Mathematical Morphology in Image Processing*, vol. 34, CRC Press, 1993.
- [4] A. Frangi, W. Niessen, K. Vincken, and M. Viergever, "Multiscale vessel enhancement filtering," in *Medical Image Computing and Computer-Assisted Intervention (MICCAI '98)*, pp. 130–137, 1998.
- [5] A. P. Condurache and T. Aach, "Vessel segmentation in angiograms using hysteresis thresholding," in *IAPR Conference On Machine Vision Applications (MVA '05)*, pp. 269–272, 2005.
- [6] A. Condurache, T. Aach, S. Grzybowski, and H. G. Machens, "Vessel segmentation and analysis in laboratory skin transplant micro-angiograms," in *Proceedings of the 18th IEEE Symposium on Computer-Based Medical Systems*, pp. 21–26, June 2005.
- [7] J. E. Bresenham, "Algorithm for computer control of a digital plotter," *IBM Systems Journal*, vol. 4, pp. 25–30, 1965.
- [8] Y. Xu, H. Zhang, H. Li, and G. Hu, "An improved algorithm for vessel centerline tracking in coronary angiograms," *Computer Methods and Programs in Biomedicine*, vol. 88, no. 2, pp. 131–143, 2007.
- [9] A. H. Can, H. Shen, J. N. Turner, H. L. Tanenbaum, and B. Roysam, "Rapid automated tracing and feature extraction from retinal fundus images using direct exploratory algorithms," *IEEE Transactions on Information Technology in Biomedicine*, vol. 3, no. 2, pp. 125–138, 1999.
- [10] Y. Sun, "Automated identification of vessel contours in coronary arteriograms by an adaptive tracking algorithm," *IEEE Transactions on Medical Imaging*, vol. 8, no. 1, pp. 78–88, 1989.
- [11] K. A. Al-Kofahi, A. Can, S. Lasek et al., "Median-based robust algorithms for tracing neurons from noisy confocal microscope images," *IEEE Transactions on Information Technology in Biomedicine*, vol. 7, no. 4, pp. 302–317, 2003.
- [12] K. A. Al-Kofahi, S. Lasek, D. H. Szarowski et al., "Rapid automated three-dimensional tracing of neurons from confocal image stacks," *IEEE Transactions on Information Technology in Biomedicine*, vol. 6, no. 2, pp. 171–187, 2002.
- [13] Y. Zhang, X. Zhou, A. Degterev et al., "A novel tracing algorithm for high throughput imaging. Screening of neuron-based assays," *Journal of Neuroscience Methods*, vol. 160, no. 1, pp. 149–162, 2007.
- [14] E. L. Bolson, S. Kliman, F. Sheehan, and H. T. Dodge, "Left ventricular segmental wall motion—a new method using local direction information," in *Computers in Cardiology*, pp. 245–248, 1980.
- [15] H. Greenspan, M. Laifenfeld, S. Einav, and O. Barnea, "Evaluation of center-line extraction algorithms in quantitative coronary angiography," *IEEE Transactions on Medical Imaging*, vol. 20, no. 9, pp. 928–941, 2001.
- [16] K. Haris, S. N. Efstratiadis, N. Maglaveras, C. Pappas, J. Gourassas, and G. Louridas, "Model-based morphological segmentation and labeling of coronary angiograms," *IEEE Transactions on Medical Imaging*, vol. 18, no. 10, pp. 1003–1015, 1999.
- [17] S. R. Aylward and E. Bullitt, "Initialization, noise, singularities, and scale in height ridge traversal for tubular object centerline extraction," *IEEE Transactions on Medical Imaging*, vol. 21, no. 2, pp. 61–75, 2002.
- [18] K. K. Delibasis, A. I. Kechriniotis, C. Tsonos, and N. Assimakis, "Automatic model-based tracing algorithm for vessel segmentation and diameter estimation," *Computer Methods and Programs in Biomedicine*, vol. 100, no. 2, pp. 108–122, 2010.
- [19] C. Biermann, I. Tsiflikas, C. Thomas, B. Kasperek, M. Heuschmid, and C. D. Claussen, "Evaluation of computer-assisted quantification of carotid artery stenosis," *Journal of Digital Imaging*, vol. 25, no. 2, pp. 250–257, 2012.
- [20] S. Mittal, Y. Zheng, B. Georgescu et al., "Method and System for Automatic Detection and Classification of Coronary Stenoses in Cardiac CT Volumes," Google Patents, 2011.
- [21] F. Z. Boroujeni, R. Wirza, O. Rahmat, N. Mustapha, L. S. Affendey, and O. Maskon, "Automatic selection of initial points for exploratory vessel tracing in fluoroscopic images," *Defence Science Journal*, vol. 61, pp. 443–451, 2011.
- [22] Y. Sato, S. Nakajima, N. Shiraga et al., "Three-dimensional multi-scale line filter for segmentation and visualization of curvilinear structures in medical images," *Medical Image Analysis*, vol. 2, no. 2, pp. 143–168, 1998.
- [23] A. C. M. Dumay, J. J. Gerbrands, and J. H. C. Reiber, "Automated extraction, labelling and analysis of the coronary vasculature from arteriograms," *International Journal of Cardiac Imaging*, vol. 10, no. 3, pp. 205–215, 1994.
- [24] K. Hoffmann, K. Doi, H. Chan, L. Fencil, H. Fujita, and A. Muraki, "Automated tracking of the vascular tree in DSA images using a double-square-box region-of-search algorithm," in *Application of Optical Instrumentation in Medicine XIV and Picture Archiving and Communication Systems*, vol. 626 of *Proceedings of SPIE*, pp. 326–333, 1986.
- [25] P. M. J. van der Zwet, I. M. F. Pinto, P. W. Serruys, and J. H. C. Reiber, "A new approach for the automated definition of path lines in digitized coronary angiograms," *International Journal of Cardiac Imaging*, vol. 5, no. 2-3, pp. 75–83, 1990.
- [26] M. Schrijver, *Angiographic image analysis to assess the severity of coronary stenoses [Ph.D. thesis]*, Faculty of Electrical Engineering (EL-SAS), University of Twente, 2003.
- [27] Y. Sun, R. J. Lucariello, and S. A. Chiaramida, "Directional low-pass filtering for improved accuracy and reproducibility of stenosis quantification in coronary arteriograms," *IEEE Transactions on Medical Imaging*, vol. 14, no. 2, pp. 242–248, 1995.
- [28] T. Y. Zhang and C. Y. Suen, "Fast parallel algorithm for thinning digital patterns," *Communications of the ACM*, vol. 27, no. 3, pp. 236–239, 1984.
- [29] F. C. Monteiro and A. C. Campilho, "Performance evaluation of image segmentation," *Lecture Notes in Computer Science*, vol. 4141, pp. 248–259, 2006.

Research Article

A Hybrid Model of Maximum Margin Clustering Method and Support Vector Regression for Noninvasive Electrocardiographic Imaging

Mingfeng Jiang,¹ Feng Liu,² Yaming Wang,¹ Guofa Shou,³
Wenqing Huang,¹ and Huaxiong Zhang¹

¹ School of Information Science and Technology, Zhejiang Sci-Tech University, Hangzhou 310018, China

² School of Information Technology and Electrical Engineering, University of Queensland, St. Lucia, Brisbane, QLD 4072, Australia

³ School of Electrical and Computer Engineering, University of Oklahoma, Norman, OK 73019, USA

Correspondence should be addressed to Mingfeng Jiang, jiang.mingfeng@hotmail.com

Received 3 August 2012; Accepted 8 October 2012

Academic Editor: Dingchang Zheng

Copyright © 2012 Mingfeng Jiang et al. This is an open access article distributed under the Creative Commons Attribution License, which permits unrestricted use, distribution, and reproduction in any medium, provided the original work is properly cited.

Noninvasive electrocardiographic imaging, such as the reconstruction of myocardial transmembrane potentials (TMPs) distribution, can provide more detailed and complicated electrophysiological information than the body surface potentials (BSPs). However, the noninvasive reconstruction of the TMPs from BSPs is a typical inverse problem. In this study, this inverse ECG problem is treated as a regression problem with multi-inputs (BSPs) and multioutputs (TMPs), which will be solved by the Maximum Margin Clustering- (MMC-) Support Vector Regression (SVR) method. First, the MMC approach is adopted to cluster the training samples (a series of time instant BSPs), and the individual SVR model for each cluster is then constructed. For each testing sample, we find its matched cluster and then use the corresponding SVR model to reconstruct the TMPs. Using testing samples, it is found that the reconstructed TMPs results with the MMC-SVR method are more accurate than those of the single SVR method. In addition to the improved accuracy in solving the inverse ECG problem, the MMC-SVR method divides the training samples into clusters of small sample sizes, which can enhance the computation efficiency of training the SVR model.

1. Introduction

The technique of noninvasive imaging of the heart's electrical activity from the body surface potentials (BSPs) constitutes one form of the inverse problem of ECG [1, 2]. Approaches to solving the inverse ECG problem have been usually based on either an activation-based model or a potential-based model, which includes epicardial, endocardial, or transmembrane potentials. Activation-based models are used to investigate the arrival time of the propagation wavefront within the myocardium [3, 4]. The potential-based models are used to evaluate the potential values on the cardiac surface [5–7] or within the myocardium [8] at certain time instants. In this study, we explore a new solution for ECG inverse problem using the potential-based approach.

Due to its inherent ill-posed property, the inverse ECG problem is usually solved by “regularization” techniques. In the last decades, numerous regularization methods have been proposed to solve this ill-posed problem, including truncated total least squares (TTLS) [9], GMRes [10], and the LSQR [11, 12]. Most of them are essentially L2-norm based regularization schemes, which inherently lead to considerable smoothness of the inverse solutions. L1-norm regularization method can overcome this drawback of L2-norm regularization method, which has been applied for epicardial potential reconstruction [13–15]. Although the above-mentioned regularization methods can more or less deal with the geometry and measurement noises for the ECG inverse problems, which depends on the regularization parameters, the robustness of the inverse solution is not always guaranteed. In this paper, without seeking assistance

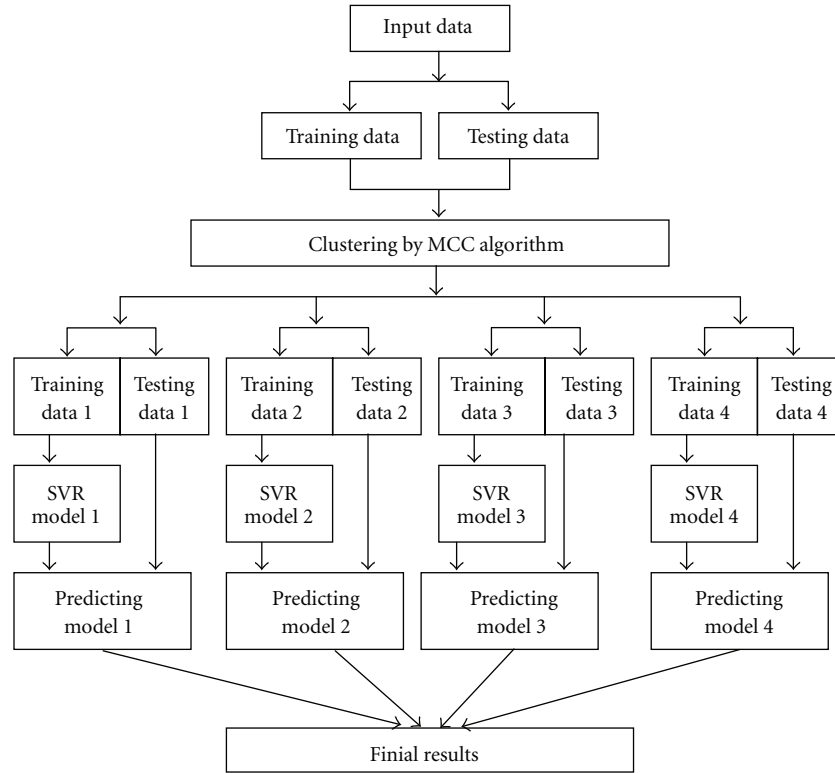


FIGURE 1: The framework of the proposed MCC-SVR method.

from the regularization techniques, we explore an alternative, more robust approach to solve the inverse ECG problem. The method is called Support Vector Regression (SVR) [16]. To find the solution for the inverse ECG problem, a regression model will be set up with multi-inputs (BSPs) and multioutputs (transmembrane potentials, TMPs). This statistic method based solution will be assessed with the quality of the inversely predicated TMPs from the measured BSPs. Compared with conventional regularization methods (e.g., zero order Tikhonov and LSQR), the SVR method can produce more accurate results in terms of reconstruction of the transmembrane potential distributions on epi- and endocardial surface. In addition, when the PCA and KPCA are adopted to extract useful features from the original inputs for building the SVR model, the SVR method with feature extraction (PCA-SVR and KPCA-SVR) outperforms that without the extract feature extraction (single SVR) in terms of the reconstruction of the TMPs [17].

Compared with using single SVR model, the hybrid models by integrating difference methods show better performance. The self-organizing map (SOM) is an unsupervised and competitive learning algorithm, which can be viewed as clustering techniques [18]. Combining the SOM with SVR or LS-SVM, the proposed hybrid method has the potential to find better inverse solutions than using a single SVR model [19, 20]. Xu et al. [21] proposed the Maximum Margin Clustering (MMC) method, which performs clustering by simultaneously finding the large margin separating hyperplane between clusters. The MMC

method has been successfully applied to many clustering problems [22]. However, its efficiency is an issue of concern. Recently, Zhang et al. proposed [23, 24] an efficient approach for solving the MMC via an alternative optimization procedure, which was implemented by using the SVR method with the Laplacian loss in the inner optimization subproblem. The modified MMC algorithm is more accurate, much faster and therefore more practical for solving engineering inverse problems. In this paper, the hybrid model of modified MMC method and SVR is proposed to solve the inverse ECG problem, which is referred to as an MCC-SVR method. The conference version of this submission has appeared in CINC 2011 [25]. This submission has undergone substantial revisions and offers extended experiment results.

The main purpose of this study is to use an MCC-SVR model to investigate the reconstruction capability of TMPs. In this study, based on our previously developed realistic heart-torso model, the equivalent double layer (EDL) source model method was applied to generate the data set for training and testing the SVR model. The proposed algorithm was also compared with a single SVR model for noninvasive ECG imaging.

2. Theory and Methodology

The framework of the proposed MCC-SVR method is shown in Figure 1. The MCC method is used to classify the input data; the SVR is then applied to construct the regression model of each cluster.

- (1) Initialize the labels y by using the k -means;
- (2) Fix y , and perform SVR with Laplacian loss;
- (3) Compute ω from the Karush-Kuhn-Tucker (KKT) conditions;
- (4) Compute the bias b as described above;
- (5) Assign the labels as $y_i = \text{sign}(\omega^T \varphi(x_i) + b)$;
- (6) Repeat steps 2–5 until convergence.

ALGORITHM 1: Iterative SVR procedure for MCC method.

2.1. Maximum Margin Clustering (MMC) Method [23, 24]. The clustering principle is to find a labeling to identify dominant structures in the data and to group similar instances together, so the margin obtained would be maximal over all possible labelings, that is, given a training set $\{(x_i, y_i)\}_{i=1}^n$, where $x_i \in \mathcal{X}$ is the input and $y_i \in \{\pm 1\}$ is the output. The SVM finds a large margin hyperplane to separate patterns of opposite classes by the classify function $f(x)$ [26]:

$$f(x) = \omega^T \varphi(x) + b, \quad (1)$$

where $\varphi(x)$ denotes the high-dimensional feature space, which is nonlinearly mapped from the input space x by the kernel function k , ω is the normal vector of the hyperplane, and b is the offset of the hyperplane. Computationally, this leads to the following optimization problem [24, 26]:

$$\begin{aligned} \min_{\omega, b, \xi} \quad & \|\omega\|^2 + 2C\xi^T e \\ \text{subject to} \quad & \begin{cases} y_i(\omega \varphi(x_i) + b) \geq 1 - \xi_i \\ \xi_i \geq 0, \quad i = 1, \dots, n, \end{cases} \end{aligned} \quad (2)$$

where $\xi = [\xi_1, \dots, \xi_n]^T$ is the vector of a slack variable for the errors, and $C > 0$ is the trade-off parameter between the smoothness $\|\omega\|^2$ and the fitness ($\xi^T e$) of the decision function $f(x)$.

MMC attempts to extend large margin methods to allocate the input data points to different classes, leading to large separation between the different classes. Here, the case with two clusters is considered in this work. Since one could simply assign all the data points to the same class and obtain an unbounded margin, a proper constraint on the class balance needs to be imposed. Xu et al. [21] introduced a class constraint that requires y to satisfy

$$-\ell \leq e^T y \leq \ell, \quad (3)$$

where $\ell \geq 0$ is a user-defined constant controlling the class imbalance. Then the margin is maximized with respect to both unknown y and unknown SVM parameter (ω, b) as follows:

$$\begin{aligned} \min_y \min_{\omega, b, \xi} \quad & \|\omega\|^2 + 2C\xi^T e \\ \text{subject to} \quad & \begin{cases} y_i(\omega \varphi(x_i) + b) \geq 1 - \xi_i \\ \xi_i \geq 0, \quad y_i \in \{\pm 1\}, \quad i = 1, \dots, n \\ -\ell \leq e^T y \leq \ell. \end{cases} \end{aligned} \quad (4)$$

The origin nonconvex MMC problem in (4) can be formulated as a sequence of QPs which can be solved by some efficient QP solvers. However, it suffers from a premature convergence and easily gets stuck in poor local optima. Zhang et al. [23, 24] proposed to replace the SVM by SVR with Laplacian loss, which can lead to a significant improvement in the clustering performance compared to that of iterative SVM procedure. The primal problem of SVR with Laplacian loss can be formulated as

$$\begin{aligned} \min_{\omega, b, \xi_i, \xi_i^*} \quad & \|\omega\|^2 + 2C \sum_{i=1}^n (\xi_i + \xi_i^*) \\ \text{subject to} \quad & \begin{cases} y_i - (\omega^T \varphi(x_i) + b) \leq \xi_i \\ (\omega^T \varphi(x_i) + b) - y_i \leq \xi_i^* \\ \xi_i \geq 0, \quad \xi_i^* \geq 0, \end{cases} \quad \text{for } i = 1, \dots, n, \end{aligned} \quad (5)$$

where ξ_i and ξ_i^* are slack variables. With the obtained labels, the MMC problem based on the iterative SVR with the Laplacian loss becomes

$$\begin{aligned} \min_{\omega, b, \xi_i, \xi_i^*} \quad & \|\omega\|^2 + 2C \sum_{i=1}^n (\xi_i + \xi_i^*) \\ \text{subject to} \quad & \begin{cases} y_i - (\omega^T \varphi(x_i) + b) \leq \xi_i \\ (\omega^T \varphi(x_i) + b) - y_i \leq \xi_i^* \\ \xi_i \geq 0, \quad \xi_i^* \geq 0 \\ y_i \in \{\pm 1\} \\ -\ell \leq e^T y \leq \ell. \end{cases} \quad \text{for } i = 1, \dots, n \end{aligned} \quad (6)$$

After ω is obtained from the optimization of SVR, the problem in (6) is reduced to the form

$$\begin{aligned} \min_{y, b} \quad & \sum_{i=1}^n \left| (\omega^T \varphi(x_i) + b) - y_i \right| \\ \text{subject to} \quad & \begin{cases} y_i \in \{\pm 1\}, \quad i = 1, \dots, n \\ -\ell \leq e^T y \leq \ell. \end{cases} \end{aligned} \quad (7)$$

According to Zhang's proposition [24], for a fixed b , the optimal strategy to determine the y_i 's in (7) is to assign all y_i 's as -1 for those with $\omega^T \varphi(x_i) + b < 0$ and assign y_i 's as 1 for those with $\omega^T \varphi(x_i) + b > 0$. The bias b can be determined as follows. (i) we sort the $\omega^T \varphi(x_i)$'s and use the set of midpoints between any two consecutive sorted values

as the candidates of b ; (ii) from these sorted b 's, the first and the last $(n - \ell)/2$ of them can be dropped, and the middle ℓ can be remained; (iii) for each remaining candidate, we determine the y_i 's according to the above proposition and compute the corresponding objective value in (7); (iv) finally, we choose the b that has the smallest objective. The complete iterative SVR procedure for MCC method is shown in Algorithm 1.

2.2. Support Vector Regression (SVR) Model. The SVR algorithm [26] is only briefly described here; for details, see [16, 26]. As a linear regression model, the SVR algorithm relies on an estimation of a linear regression function:

$$f(x) = \langle \omega, x \rangle + b, \quad (\omega, x \in \mathfrak{R}), \quad (8)$$

where ω and b are the slope and offset of the regression linear, and $\langle \cdot, \cdot \rangle$ denotes the dot product in \mathfrak{R} . The above regression problem can be written as a convex optimization problem:

$$\begin{aligned} \min \quad & \frac{1}{2} \|\omega\|^2 \\ \text{subject to} \quad & \begin{cases} y_i - \langle \omega, x_i \rangle - b \leq \varepsilon \\ \langle \omega, x_i \rangle + b - y_i \leq \varepsilon. \end{cases} \end{aligned} \quad (9)$$

In (9), an implicit assumption is that a function f essentially approximates all pairs (x_i, y_i) with ε precision, but sometimes this may not be the case. Therefore, one can introduce two additional positive slack variables ξ_i, ξ_i^* to refine the estimation of variables ω and b . Now (9) can be reformulated [16] as

$$\begin{aligned} \min \quad & \frac{1}{2} \|\omega\|^2 + C \sum_{i=1}^n (\xi_i + \xi_i^*) \\ \text{subject to} \quad & \begin{cases} y_i - \langle \omega, x_i \rangle - b \leq \varepsilon + \xi_i \\ \langle \omega, x_i \rangle + b - y_i \leq \varepsilon + \xi_i^* \\ \xi_i, \xi_i^* \geq 0, \end{cases} \end{aligned} \quad (10)$$

where the constant C is a trade-off parameter and n denotes the number of samples; ξ_i represents the upper training error, and ξ_i^* is the lower training error subject to ε intensive tube. According to the strategy outlined by Vapnik [26], using Lagrange multipliers, the constrained optimization problem shown in (3) can be further restated as the following equation:

$$\begin{aligned} f(x, \alpha_i, \alpha_i^*) &= \sum_{i=1}^n (\alpha_i - \alpha_i^*) K(x_i, x) + b \\ \text{subject to} \quad & \sum_{i=1}^n (\alpha_i - \alpha_i^*) = 0, \quad 0 \leq \alpha_i, \alpha_i^* \leq C, \end{aligned} \quad (11)$$

where α_i and α_i^* are the Lagrange multipliers. The term $K(x_i, x_j)$ in (11) is defined as the kernel function, whose values are the inner product of two vectors x_i and x_j in the

feature space $\varphi(x_i)$ and $\varphi(x_j)$. And bias b can be computed as follows:

$$b = \begin{cases} y_i - \sum_{j=1}^n (\alpha_i - \alpha_i^*) K(x_j, x_i) - \varepsilon & \text{for } \alpha_i \in (0, C) \\ y_i - \sum_{j=1}^n (\alpha_i - \alpha_i^*) K(x_j, x_i) + \varepsilon & \text{for } \alpha_i^* \in (0, C). \end{cases} \quad (12)$$

The kernel function handles any dimension feature space with no explicit calculation of $\varphi(x)$. In this study, the Gaussian kernel function is chosen as the SVR's application mapping in this study:

$$K(x_i, x_j) = \exp\left(-\frac{\|x_i - x_j\|^2}{2\sigma^2}\right), \quad (13)$$

where x_i and x_j are input vector spaces; σ^2 is the bandwidth of the kernel function.

In this study, an accurate and fast approach based on the GA and the simplex search techniques is presented to determine the optimal hyperparameters of the SVR model [17], as shown in Figure 2. The GA algorithm used here is based on a GA toolbox developed by Chipperfield et al. [27], and the simplex optimization method is implemented using the MATLAB optimization toolbox. The developed SVR model was trained and validated with the software LIBSVM [28].

2.3. Simulation Protocol and Data Set. The SVR model is tested with our previously developed realistic heart-torso model [6, 17]. In this study, an equivalent double layer (EDL) source model is adopted to simulate the cardiac equivalent source, which represents the cardiac electrical activity by means of double layer source on the closed surface (including the endo- and epicardial surface of ventricle). For the ECG inverse problem studies, the ventricular surface TMPs and body surface potentials (BSPs) are evaluated based on the EDL source model. The transfer matrix A between TMPs and BSPs is evaluated by the boundary element method (BEM), and it has the dimension of 412×478 and its condition number (the ratio of largest and smallest singular values) is 5.6×10^{12} . As shown in Figure 3, the EDL source method is used to obtain the BSPs φ_B and the TMPs φ_m . For the construction of the training and testing data set Different Action Potentials (APs) for various myocardial cells and the normal Ventricular Excitation Sequence (VES) are used to calculate the TMPs (φ_m) at different times; from the calculated TMPs, the corresponding BSPs are deduced with the transfer matrix A .

In this study, a normal ventricular excitation data set is prepared for the setup of the SVR model. The considered ventricular excitation period from the first breakthrough to the end is 357 ms and the time step is 1 ms, and, thus, 358 BSPs φ_B and TMPs φ_m temporal data sets are numerically recorded; in addition, the 30 dB simulated Gaussian white noise is added into the BSPs φ_B representing the measurement noises. 60 datasets at times of 3 ms, 9 ms,

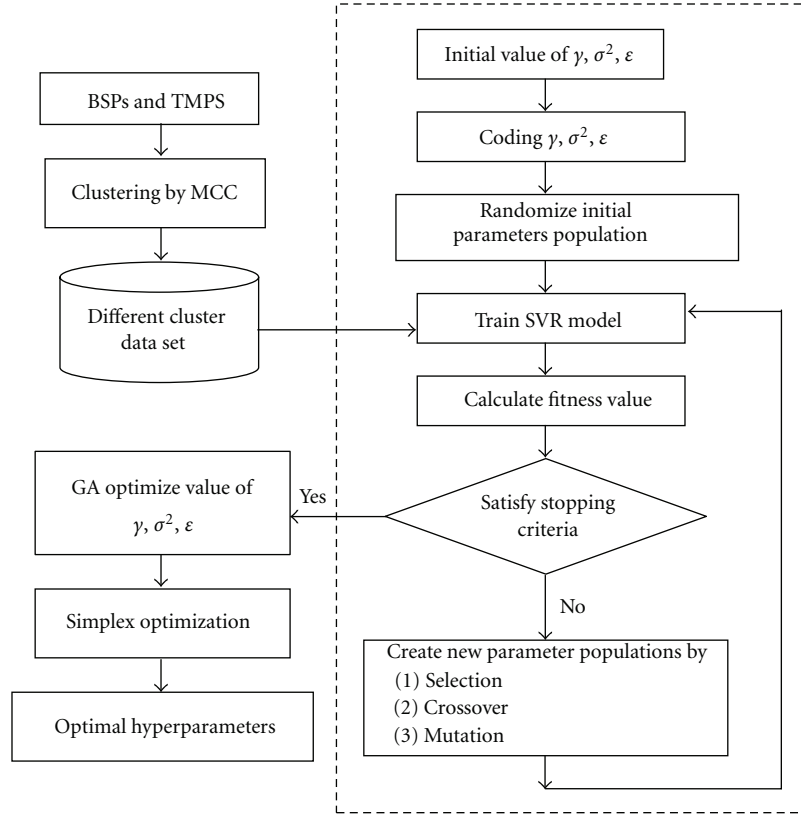


FIGURE 2: GA-Simplex optimization procedure for the parameter selection in the MCC-SVR model.

15 ms, ..., and 357 ms after the first ventricular breakthrough are used as testing samples to evaluate the generalization capacity of the proposed SVR model. The rest 298 in 358 data sets are employed as the training samples for building the SVR model. With the consideration of a wide numerical range of the φ_B values, for each time, the φ_B values can be scaled to the range (0, 1):

$$\varphi_{BtN} = \frac{\varphi_{Bt} - \varphi_{Bt\min}}{\varphi_{Bt\max} - \varphi_{Bt\min}}, \quad (14)$$

where φ_{Bt} are the body surface potentials at time instant t , $\varphi_{Bt\max}$ is the maximum value of BSPs at the time t , and $\varphi_{Bt\min}$ is the minimum value of BSPs at the time t .

As the TMPs are known in advance in the simulation study, the accuracy of reconstructed TMPs at the testing time t can be evaluated by either relative errors (REs):

$$RE = \frac{\|\varphi_t^c - \varphi_t^e\|}{\|\varphi_t^e\|}, \quad (15)$$

or the correlation coefficient (CC), given by

$$CC = \frac{\sum_{i=1}^n [(\varphi_i^c) - \bar{\varphi}_i^c][(\varphi_i^e) - \bar{\varphi}_i^e]}{\|\varphi_i^c - \bar{\varphi}_i^c\| \|\varphi_i^e - \bar{\varphi}_i^e\|}, \quad (16)$$

where n is the number of nodes on the ventricular surface. φ_i^e denotes the simulated TMPs distribution at time t , and φ_i^c are inversely computed. The quantities $\bar{\varphi}_i^c$ and $\bar{\varphi}_i^e$ are the mean value of φ_i^c and φ_i^e over the whole ventricular surface nodes at time t .

3. Results

According to the MCC method, the above 298 training samples are classified four clusters as shown in Figure 4(a), and the numbers of the four clusters is 80, 74, 70, and 74, respectively. Then the individual SVR model is trained for each cluster, and the hyperparameters are determined using the GA-Simplex method. For 60 testing samples, the MCC method is used to find their corresponding clusters, as shown in Figure 4(b).

To illustrate the performances of the reconstructed TMPs, four sequential testing time points (3, 15, 27, and 39 ms after ventricle excitation) are presented. The inverse ECG solutions are shown in Figure 5; in contrast to the conventional regularization methods, such as zero order Tikhonov regularization method and LSQR regularization method, the single SVR method can yield rather better results with lower RE and higher CC. Moreover, it can be seen that the MCC-SVR method offers superior performances than the single SVR method, as its solution is more close to the simulated TMPs distributions. The time courses of the simulated TMPs and reconstructions for one representative source point on the heart surface are depicted in Figure 6. It can be found that, in reconstructing the TMPs for one representative source point over all the testing times, the MCC-SVR method offers better solution compared with single SVR method.

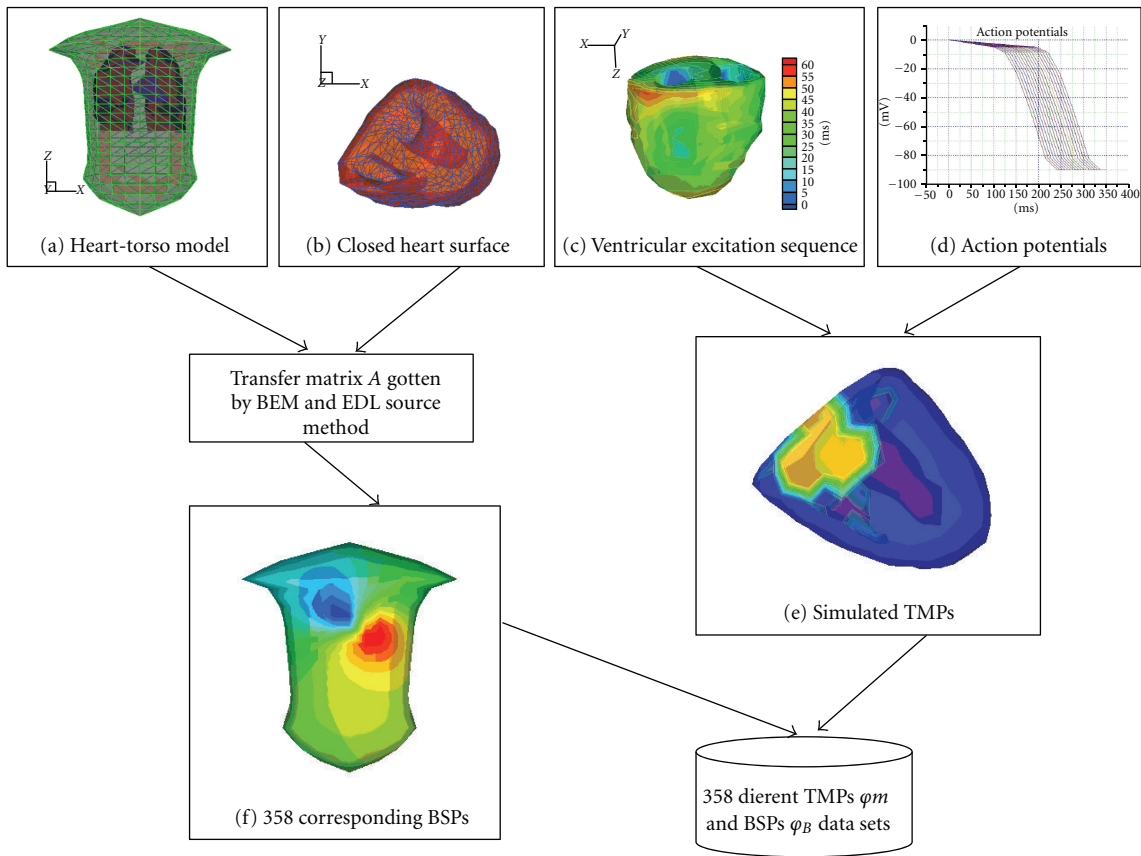


FIGURE 3: The block diagram of the simulation protocol for the construction of the data sets.

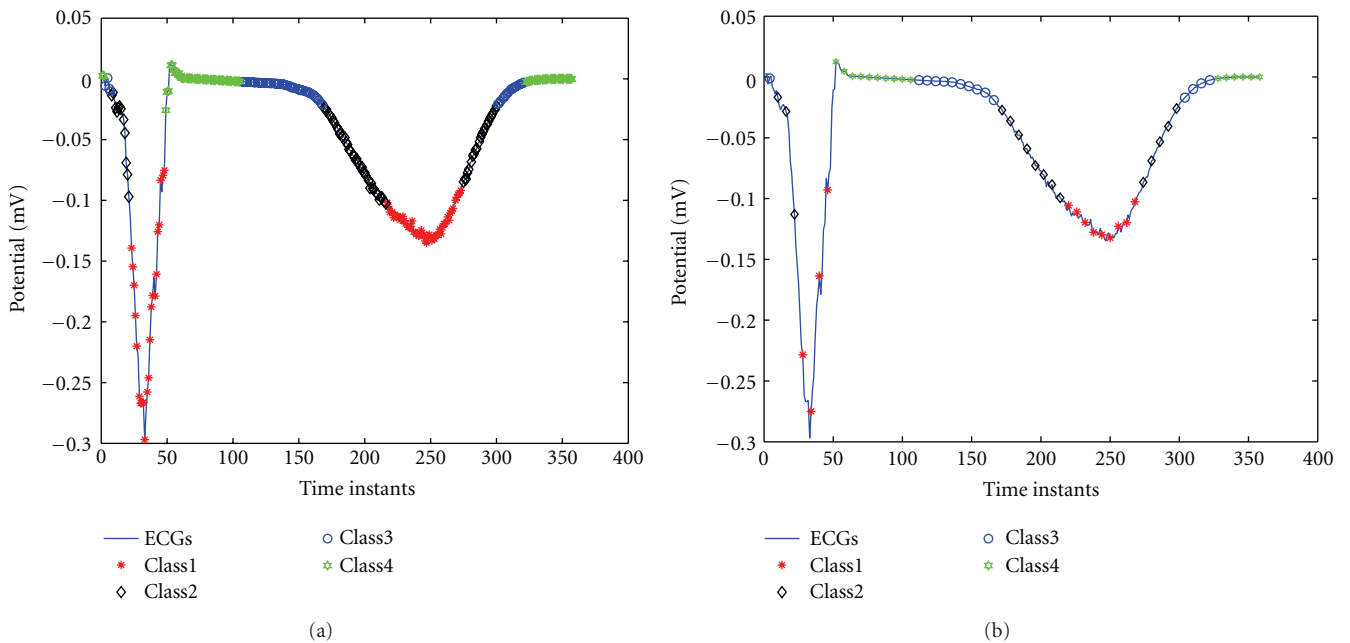


FIGURE 4: On one representative epicardial point, (a) the 298 training samples are classified into four clusters by using MCC method; (b) for the 60 testing samples, the MCC method is used to find their corresponding clusters.

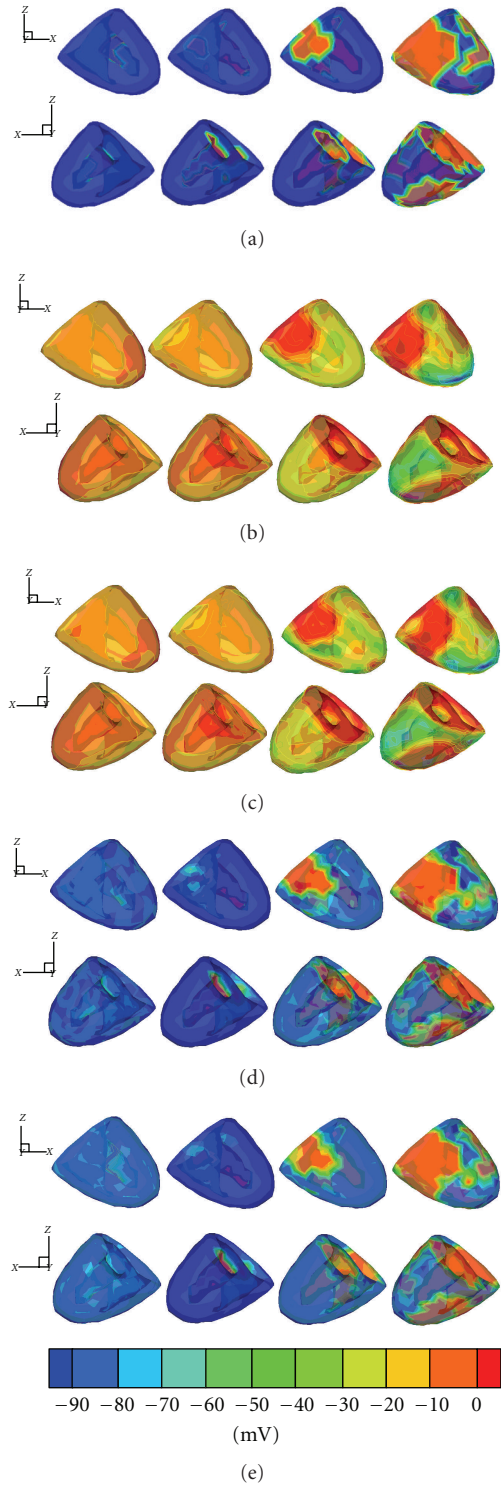


FIGURE 5: The TMPs distribution on the ventricular surface at four sequential testing time points (3, 15, 27, and 39 ms, respectively, after the first ventricular breakthrough). In each subfigure, the upper row shows the TMPs distribution from an anterior view and the lower from a posterior view. (a) The simulated TMPs by using the equivalent double layer (EDL) source model; (b) the reconstructed TMPs by using zero order Tikhonov method; (c) the reconstructed TMPs by using the LSQR method; (d) the reconstructed TMPs by using the single SVR method; (e) the reconstructed TMPs by using the MCC-SVR method.

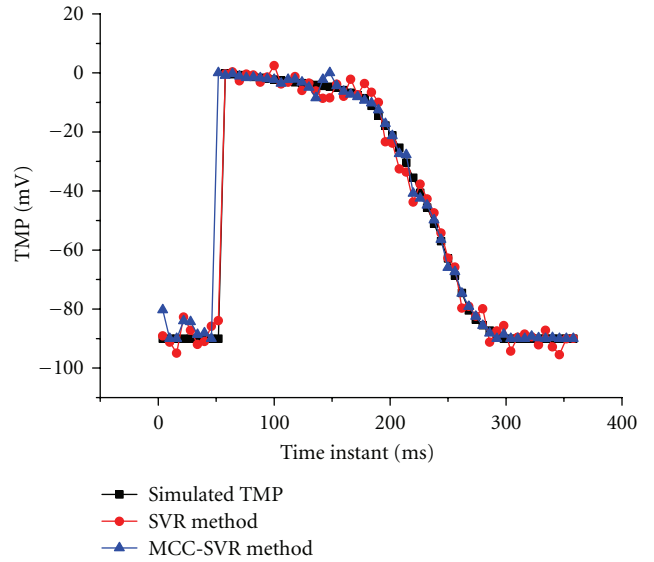


FIGURE 6: The time courses of the TMPs for one representative source point on the heart surface. The reconstruction TMPs over the 60 testing times with SVR method and the MCC-SVR method are all compared with those simulated TMPs.

The RE and CC of the reconstructed TMPs with different methods can be found in Figure 7. In contrast to the single SVR method, the MCC-SVR method can yield improved results with a lower RE and a higher CC over the 60 testing samples.

By dividing the training samples into smaller clusters, the training time for each cluster can be reduced. The training times for each cluster by using the MCC-SVR method are 6715.9 seconds, 6821.1 seconds, 4550.6 seconds, and 5162.4 seconds, respectively, and the total time of the four clusters is 23250 seconds. When using the single SVR model to train the model of the all training samples, it takes 35233.4 seconds.

4. Discussion and Conclusion

In this study, MCC-SVR method is proposed to solve the noninvasive ECG imaging problem. Here, the MMC approach is adopted to cluster the training samples firstly, and then SVR method is applied to construct the model for each cluster. After building different cluster models, for the testing sample, we can find its matched cluster and then use the corresponding SVR model to reconstruct the TMPs. From the reconstructed TMPs as shown in Figures 5 and 6, it can be seen that the MCC-SVR methods offer better solution compared with single SVR method. According to the evaluation indices RE and CC, the performances of the reconstructed TMPs by using the MCC-SVR can constantly converge to a smaller RE and a higher CC on the testing samples than those of the single SVR method, as shown in Figure 7. In terms of the computation efficiency of the training SVR model, for the given training samples, the MCC-SVR method can save about 34% time than the single SVR method. With the increasing of the training samplings,

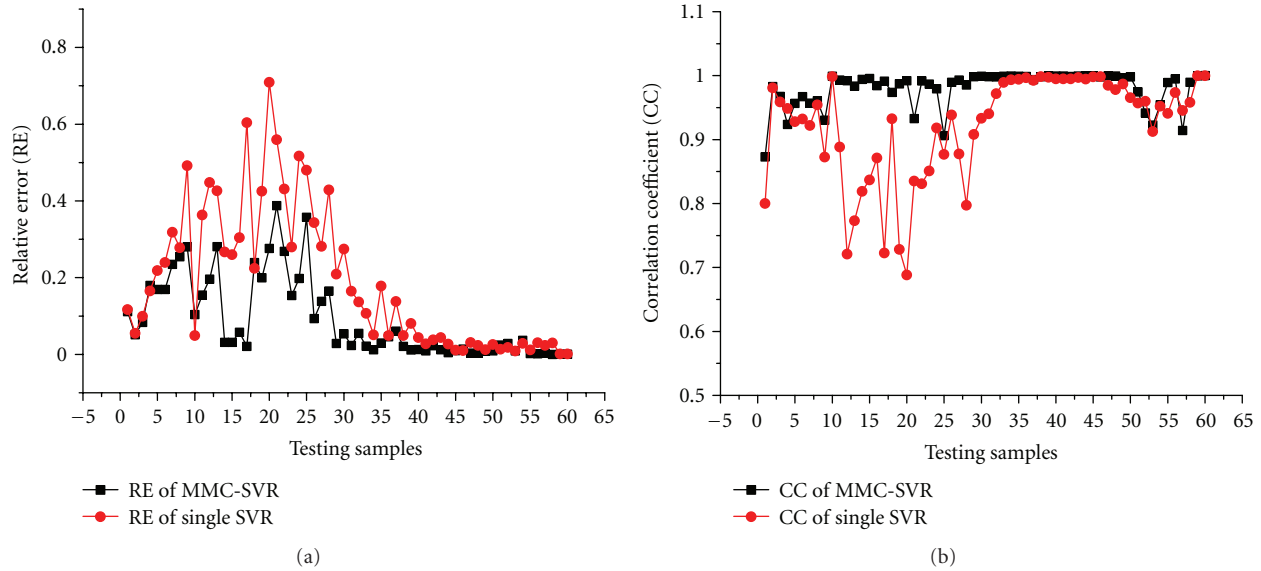


FIGURE 7: The performances of the reconstructed TMPs over 60 sampling times by using SVR and MCC-SVR, respectively. (a) The REs of the reconstructed TMPs; (b) the CCs of the reconstructed TMPs.

the MCC-SVR method lessens more training time than the single SVR method. Moreover, the training process for each cluster can be implemented simultaneously using parallel computing, therefore further enhance the training efficiency.

In summary, this paper proposed the MCC-SVR method for the inverse solutions of the ECG problem. The new algorithm was tested and compared with single SVR schemes using a realistic heart-torso model. The experimental results show that the MCC-SVR can improve the generalization performance of the single SVR in reconstructing the TMPs, leading to a more accurate reconstruction of the TMPs. In our future work, we plan to improve the MCC-SVR method for solving various nonlinear regression problems in noninvasive ECG imaging.

Acknowledgments

This work is supported by the National Natural Science Foundation of China (30900322, 61070063, and 61101046). This work is also funded by the Zhejiang Provincial Natural Science Foundation of China (Y2090398).

References

- [1] L. K. Cheng, J. M. Bodley, and A. J. Pullan, "Comparison of potential- and activation-based formulations for the inverse problem of electrocardiology," *IEEE Transactions on Biomedical Engineering*, vol. 50, no. 1, pp. 11–22, 2003.
- [2] C. Ramanathan, R. N. Ghanem, P. Jia, K. Ryu, and Y. Rudy, "Noninvasive electrocardiographic imaging for cardiac electrophysiology and arrhythmia," *Nature Medicine*, vol. 10, no. 4, pp. 422–428, 2004.
- [3] P. M. Van Dam, T. F. Oostendorp, A. C. Linnenbank, and A. Van Oosterom, "Non-invasive imaging of cardiac activation and recovery," *Annals of Biomedical Engineering*, vol. 37, no. 9, pp. 1739–1756, 2009.
- [4] Z. Liu, C. Liu, and B. He, "Noninvasive reconstruction of three-dimensional ventricular activation sequence from the inverse solution of distributed equivalent current density," *IEEE Transactions on Medical Imaging*, vol. 25, no. 10, pp. 1307–1318, 2006.
- [5] B. F. Nielsen, X. Cai, and M. Lysaker, "On the possibility for computing the transmembrane potential in the heart with a one shot method: an inverse problem," *Mathematical Biosciences*, vol. 210, no. 2, pp. 523–553, 2007.
- [6] M. Jiang, L. Xia, G. Shou, Q. Wei, F. Liu, and S. Crozier, "Effect of cardiac motion on solution of the electrocardiography inverse problem," *IEEE Transactions on Biomedical Engineering*, vol. 56, no. 4, pp. 923–931, 2009.
- [7] M. Jiang, L. Xia, W. Huang, G. Shou, F. Liu, and S. Crozier, "The application of subspace preconditioned LSQR algorithm for solving the electrocardiography inverse problem," *Medical Engineering and Physics*, vol. 31, no. 8, pp. 979–985, 2009.
- [8] L. Wang, H. Zhang, K. C. Wong, H. Liu, and P. Shi, "Physiological-model-constrained noninvasive reconstruction of volumetric myocardial transmembrane potentials," *IEEE transactions on Bio-Medical Engineering*, vol. 57, no. 2, pp. 296–315, 2010.
- [9] G. Shou, L. Xia, M. Jiang, Q. Wei, F. Liu, and S. Crozier, "Truncated total least squares: a new regularization method for the solution of ECG inverse problems," *IEEE Transactions on Biomedical Engineering*, vol. 55, no. 4, pp. 1327–1335, 2008.
- [10] C. Ramanathan, P. Jia, R. Ghanem, D. Calvetti, and Y. Rudy, "Noninvasive electrocardiographic imaging (ECGI): application of the generalized minimal residual (GMRES) method," *Annals of Biomedical Engineering*, vol. 31, no. 8, pp. 981–994, 2003.
- [11] M. Jiang, L. Xia, G. Shou, and M. Tang, "Combination of the LSQR method and a genetic algorithm for solving the electrocardiography inverse problem," *Physics in Medicine and Biology*, vol. 52, no. 5, pp. 1277–1294, 2007.
- [12] M. Jiang, L. Xia, G. Shou, F. Liu, and S. Crozier, "Two hybrid regularization frameworks for solving the electrocardiography

- inverse problem,” *Physics in Medicine and Biology*, vol. 53, no. 18, pp. 5151–5164, 2008.
- [13] S. Ghosh and Y. Rudy, “Application of L1-norm regularization to epicardial potential solution of the inverse electrocardiography problem,” *Annals of Biomedical Engineering*, vol. 37, no. 5, pp. 902–912, 2009.
- [14] G. Shou, L. Xia, F. Liu, M. Jiang, and S. Crozier, “On epicardial potential reconstruction using regularization schemes with the L1-norm data term,” *Physics in Medicine and Biology*, vol. 56, no. 1, pp. 57–72, 2011.
- [15] L. Wang, J. Qin, T. T. Wong, and P. A. Heng, “Application of L1-norm regularization to epicardial potential reconstruction based on gradient projection,” *Physics in Medicine and Biology*, vol. 56, pp. 6291–6310, 2011.
- [16] A. J. Smola and B. Schölkopf, “A tutorial on support vector regression,” *Statistics and Computing*, vol. 14, no. 3, pp. 199–222, 2004.
- [17] M. Jiang, L. Zhu, Y. Wang et al., “Application of kernel principal component analysis and support vector regression for reconstruction of cardiac transmembrane potentials,” *Physics in Medicine and Biology*, vol. 56, no. 6, pp. 1727–1742, 2011.
- [18] M. M. Mostafa, “Clustering the ecological footprint of nations using Kohonen’s self-organizing maps,” *Expert Systems with Applications*, vol. 37, no. 4, pp. 2747–2755, 2010.
- [19] S. Ismail, A. Shabri, and R. Samsudin, “A hybrid model of self-organizing maps (SOM) and least square support vector machine (LSSVM) for time-series forecasting,” *Expert Systems with Applications*, vol. 38, no. 8, pp. 10574–10578, 2011.
- [20] S. H. Hsu, J. P. A. Hsieh, T. C. Chih, and K. C. Hsu, “A two-stage architecture for stock price forecasting by integrating self-organizing map and support vector regression,” *Expert Systems with Applications*, vol. 36, no. 4, pp. 7947–7951, 2009.
- [21] L. Xu, J. Neufeld, B. Larson, and D. Schuurmans, “Maximum margin clustering,” in *Advances in Neural Information Processing Systems*, vol. 17, pp. 1537–1544, MIT Press, Cambridge, Mass, USA, 2005.
- [22] L. Xu and D. Schuurmans, “Unsupervised and semi-supervised multi-class support vector machines,” in *20th National Conference on Artificial Intelligence and the 17th Innovative Applications of Artificial Intelligence Conference, AAAI-05/IAAI-05*, pp. 904–910, usa, July 2005.
- [23] K. Zhang, I. W. Tsang, and J. T. Kwok, “Maximum margin clustering made practical,” in *24th International Conference on Machine Learning, ICML 2007*, pp. 1119–1126, usa, June 2007.
- [24] K. Zhang, I. W. Tsang, and J. T. Kwok, “Maximum margin clustering made practical,” *IEEE Transactions on Neural Networks*, vol. 20, no. 4, pp. 583–596, 2009.
- [25] M. Jiang, J. Lv, C. Wang, W. Huang, L. Xia, and G. Shou, “A hybrid model of maximum margin clustering method and support vector regression for solving the inverse ECG problem,” *Computing in Cardiology*, vol. 38, pp. 457–460, 2011.
- [26] V. Vapnik, *Statistical Learning Theory*, John Wiley & Sons, New York, NY, USA, 1998.
- [27] A. Chipperfield, P. Flemming, H. Pohlheim, and C. Fonseca, *Genetic Algorithm Toolbox for Use with MATLAB*, University of Sheffield, Sheffield, UK, 1994.
- [28] C. C. Chang and C. J. Lin, “LIBSVM: a library for support vector machines,” 2001, <http://www.csie.ntu.edu.tw/~cjlin/libsvm/>.

Research Article

A Fully Coupled Model for Electromechanics of the Heart

Henian Xia,¹ Kwai Wong,² and Xiaopeng Zhao¹

¹Department of Mechanical, Aerospace, and Biomedical Engineering, University of Tennessee, Knoxville, TN 37996, USA

²Joint Institute for Computational Sciences, Oak Ridge National Laboratory, Oak Ridge, TN 37831, USA

Correspondence should be addressed to Xiaopeng Zhao, xzhao9@utk.edu

Received 20 June 2012; Revised 7 September 2012; Accepted 8 September 2012

Academic Editor: Ling Xia

Copyright © 2012 Henian Xia et al. This is an open access article distributed under the Creative Commons Attribution License, which permits unrestricted use, distribution, and reproduction in any medium, provided the original work is properly cited.

We present a fully coupled electromechanical model of the heart. The model integrates cardiac electrophysiology and cardiac mechanics through excitation-induced contraction and deformation-induced current. Numerical schemes based on finite element were implemented in a supercomputer. Numerical examples were presented using a thin cardiac tissue and a dog ventricle with realistic geometry. Performance of the parallel simulation scheme was studied. The model provides a useful tool to understand cardiovascular dynamics.

1. Introduction

Cardiovascular disease is the leading cause of death in America. Computer simulation and visualization of complicated dynamics of the heart have great potentials to provide quantitative guidance for diagnosis and treatment of heart problems. There have been intensive research efforts on developing accurate computer models to advance the understanding on the mechanisms of cardiovascular dynamics [1].

Inspired by the pioneering work of Hodgkin and Huxley [2], many mathematical models have been developed [3]. Meanwhile, a variety of mathematical models have been proposed for electromechanical simulations. Nash and Panfilov [4] presented a computational framework to couple a three-variable FitzHugh-Nagumo-type [5] excitation-tension model to governing equations of nonlinear stress equilibrium employing the electromechanical and mechano-electric feedback. Niederer et al. [6] quantitatively characterized the binding of Ca^{2+} to TnC, the kinetics of tropomyosin, the availability of binding sites, and the kinetics of cross-bridge binding after perturbations in sarcomere length. Gurev et al. [7] illustrated methods to construct finite element electromechanical models of heart and to develop anatomically accurate ventricular mesh based on magnetic resonance and diffusion tensor magnetic resonance imaging of the heart. The work of [7] focused on the construction of the ventricular meshes and did not consider the influence of the mechanical contraction on the cardiac electrophysiology.

Göktepe and Kuhl [8] proposed an implicit and entirely finite element-based approach to the two-way coupled excitation-contraction problem. The electrophysiology was described by a FitzHugh-Nagumo-type (FHN) model in [8]. Doyle et al. [9] applied the parallel computing to the simulation of heart mechanics. They assessed the model's performance using an unstructured mesh, and they achieved the maximum speed-up factor as 15.9 when using 32 threads. Lafortune et al. [10] developed a parallel electromechanical model of the heart. Their model could run efficiently in hundreds of processors using a ventricular mesh of realistic geometry. Lafortune et al. described the electrophysiology by the simple three-variable FitzHugh-Nagumo-type (FHN) model [5] or the three-variable Fenton-Karma (FK) model [11] and employed a "one-way coupling" in which the displacements do not affect the electrophysiology. Moreover, the influence of the heart's mechanical behavior on its electrical behavior, which is termed as mechanoelectric feedback, has drawn researchers' attention [12–15]. Mechanoelectric feedback may be caused by stretch-activated channels or the influence of stretch on electrical signal propagation.

This work aims to develop a two-way coupled electromechanical model for parallel simulation of complex cardiovascular dynamics. Towards that aim, we have developed a fully coupled electromechanical model of the heart, which integrates the cardiac electrophysiology, the cardiac mechanics and the two-way coupling arising from

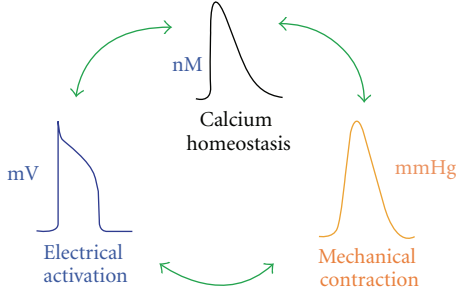


FIGURE 1: Schematic representation of the coupling between electrical, chemical, and mechanical functions of the heart.

the excitation-induced contraction and the deformation-induced generation of current. The cardiac electrophysiology is described by the Beeler-Reuter (BR) model [16]. The coupled electrical and mechanical problem is solved implicitly using finite element method. The computational algorithm is parallelized using the message passing interface (MPI). The model is tested by simulating a thin cardiac tissue and a dog ventricle with realistic geometry.

This paper is organized as follows. In Section 2, we introduce the physiological models. The numerical computation approach to the coupled problems is introduced in Section 3. Section 4 shows the numerical results. We discuss the results and conclude the paper in Section 5.

2. Physiological Models

Hearts beats are the result of a sequence of electrochemical excitation waves that are initiated from the sinoatrial node. The electrical impulses induce intracellular calcium cycling, which in turn causes heart muscle to contract. This process, known as excitation-contraction coupling (ECC), is essential to understanding of the heart. On the other hand, mechanical changes that response to neural and hormonal influences also impact on the electrical properties. This complementary concept is called mechanoelectric feedback. See Figure 1 for the relation between electrical activation, chemical homeostasis, and mechanical contractions.

2.1. Cardiac Electrophysiology. Dozens of models have been proposed over years to simulate cardiac electrophysiology [3]. Most of those models are drawn from the pioneering work of Hodgkin and Huxley [2]. In this work, the Beeler-Reuter (BR) model [16] is adopted for numerical illustrations. The BR model describes the transmembrane voltage in a single cell as follows

$$\frac{dv}{\partial t} = -\frac{I_{\text{ion}}}{C_m}, \quad (1)$$

where, v represents transmembrane voltage, C_m represents membrane capacity, and the total current is described as:

$$I_{\text{ion}} = I_{\text{Na}} + I_{K1} + I_{x1} + I_{\text{Ca}} + I_{\text{sac}} - I_{\text{stim}}. \quad (2)$$

Here, I_{Na} represents the voltage-gated Na current, I_{K1} represents the time-independent outward current, I_{x1} represents

the time-activated outward current, I_{Ca} represents a slow inward current, and I_{stim} represents the external stimulation. Note that the original BR model does not include I_{sac} , the stretch-activated channel, whose details will be discussed later. The stimulus current I_{stim} is selected to be a square wave pulse of $-80 \mu\text{A}/\mu\text{F}$ for 1 ms. We refer readers to [16] for details of the BR model.

In cardiac tissue, (1) is extended into a reaction-diffusion form to include spatial diffusion of currents:

$$\frac{\partial v}{\partial t} + \frac{I_{\text{ion}}}{C_m} - \nabla_{\mathbf{x}} \cdot (\mathbf{D} \cdot \nabla_{\mathbf{x}} v) = 0, \quad (3)$$

where \mathbf{x} represents the spatial coordinate of each material point in the heart; \mathbf{D} is the diffusion tensor, which controls the transduction orientation and speed of the electrical wave of excitation in the cardiac tissue; C_m is the membrane capacitance and is set as $1 \mu\text{F}/\text{cm}$.

2.2. Cardiac Mechanics. We denote the initial configuration (diastole) of the heart by Ω_0 and the deformed configuration (systole) by Ω . The position vector of a material point in the initial configuration is given by $\mathbf{X} = \mathbf{X}_i \mathbf{e}_i$, where \mathbf{e}_i are the unit base vectors of a rectangular Cartesian coordinate system. Denote the position of the material point \mathbf{X} at time t by $\mathbf{x} = \mathbf{x}_i \mathbf{e}_i$. Then, the spatial coordinate of a material point \mathbf{X} can be represented by $\mathbf{x} = \Phi(\mathbf{X}, t)$. The function Φ can be regarded as a map between the initial configuration and the configuration at time t . The two measures, \mathbf{x} and \mathbf{X} , are related by the deformation gradient, as shown in (4). Consider the following:

$$\mathbf{F} = \frac{\partial \mathbf{x}}{\partial \mathbf{X}}. \quad (4)$$

There are two approaches in describing the deformation of a continuum: the Lagrangian description uses the material coordinates \mathbf{X} as independent variables and the Eulerian description uses the spatial coordinates \mathbf{x} as independent variables [17]. The Eulerian description is often adopted for fluid dynamics. In this work, the Lagrangian description approach is utilized. There are two formulations for the Lagrangian approach: total Lagrangian formulation and updated Lagrangian formulation. In the total Lagrangian formulation, equations are discretized with respect to the original configuration. In contrast, the updated Lagrangian formulations are based on the current configuration and are commonly used for nonlinear, large deformations. Thus, we use the updated Lagrangian formulation in this work.

For each time step Δt , the displacement of a material point, denoted by $\mathbf{u}(\mathbf{X}, t)$, is defined by the difference between its current position and its previous position (5). The displacement $\mathbf{u}(\mathbf{X}, t)$ is governed by the equilibrium of the linear momentum, and the equation is described as (6). In (6), $\boldsymbol{\sigma}$ is the Kirchhoff stress tensor; \mathbf{b} accounts for the body force or externally applied stresses. The Kirchhoff stress $\boldsymbol{\sigma}$ is composed of a passive component $\boldsymbol{\sigma}_{\text{pass}}$ and an active component $\boldsymbol{\sigma}_{\text{act}}$. The active force $\boldsymbol{\sigma}_{\text{act}}$ is generated from the electrical excitation and will be explained later in detail. The passive component $\boldsymbol{\sigma}_{\text{pass}}$ is determined by

the equation of the elementary mechanics (7). In (7), $\chi = 0.5$ MPa and $\zeta = 0.2$ MPa are the Lamé constants which govern the isotropic stress response; $\xi = 0.1$ MPa represents the passive stiffness of myofibers. The left Cauchy-Green tensor is denoted as \mathbf{p} and is defined as (8). The parameter values were referred to the work of Nash and Panfilov (2004) [4] and Göktepe and Kuhl (2010) [8]. Consider

$$\mathbf{u}(\mathbf{X}, t) = \Phi(\mathbf{X}, t) - \Phi(\mathbf{X}, t - \Delta t), \quad (5)$$

$$\nabla_{\mathbf{x}} \cdot \boldsymbol{\sigma} + \mathbf{b} = 0, \quad (6)$$

$$\boldsymbol{\sigma}_{\text{pass}} = \left(\frac{\chi}{2} \ln A - \zeta \right) + \zeta \mathbf{p} + 2\delta \xi (B - 1) \boldsymbol{\kappa}, \quad (7)$$

$$\mathbf{p} = \mathbf{F}\mathbf{F}^T. \quad (8)$$

Let us denote the local orientation of a myofiber at initial configuration by a unit vector \mathbf{a}_0 and that at deformed configuration by vector \mathbf{a} . In (7), $\boldsymbol{\kappa}$ represents the deformed structural tensor and is defined as (9). In (9), $\boldsymbol{\kappa}_0$ is the structural tensor at initial configuration. The structural tensors $\boldsymbol{\kappa}_0$ at initial configuration and $\boldsymbol{\kappa}$ at deformed configuration represent dominating directions in a specified neighborhood of a node [18, 19]. Consider the following:

$$\boldsymbol{\kappa} = \mathbf{a} \otimes \mathbf{a} = \mathbf{F}\boldsymbol{\kappa}_0\mathbf{F}^T. \quad (9)$$

In (7), the symbol δ denotes the coefficient that determines whether or not the stiffness of the myofibers is in effect. It indicates that when there is stretch at a material point, δ will be 1, otherwise it is 0. Mathematically, it is defined as (10). In (10), $|\mathbf{a}|$ represents the stretch at a material point of the heart. At initial configuration, $|\mathbf{a}_0| = 1$, while at deformed configuration, there may be stretch at some material points that causes $|\mathbf{a}| > 1$. Moreover, the scalars A and B in (7) are defined as (11). Consider

$$\delta = \begin{cases} 1, & \text{if } |\mathbf{a}| > 1 \\ 0, & \text{otherwise,} \end{cases} \quad (10)$$

$$A = \det(\mathbf{F}^T\mathbf{F}) \quad (11)$$

$$B = |\mathbf{a}|^2.$$

2.3. Electromechanical Coupling. Summarizing Sections 2.1 and 2.2, the coupled problems are governed by the following equations:

$$\frac{\partial v}{\partial t} - \nabla_{\mathbf{x}} \cdot (\mathbf{D} \cdot \nabla_{\mathbf{x}} v) + \frac{I_{\text{ion}}}{C_m} = 0, \quad (12)$$

$$\nabla_{\mathbf{x}} \cdot \boldsymbol{\sigma} + \mathbf{b} = 0,$$

$$\begin{aligned} \frac{\partial \mathbf{n}}{\partial t} &= \nabla_{\mathbf{x}} \cdot \mathbf{n} = 0, \\ \boldsymbol{\sigma} \cdot \mathbf{n} &= 0, \\ \mathbf{x} &= \bar{\mathbf{x}}. \end{aligned} \quad (13)$$

Equations (12) show the full coupling of the cardiac electrophysiology and the cardiac mechanics. The membrane potential and the spatial coordinates of each node are

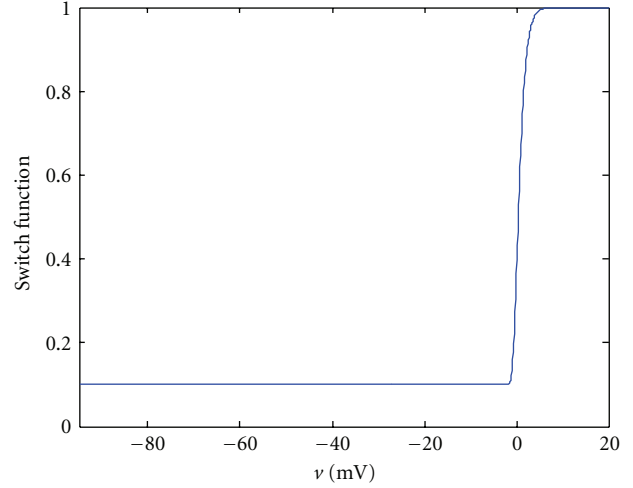


FIGURE 2: Illustration of the switch function with the following parameters: $\varepsilon_0 = 0.1/\text{mV}$, $\varepsilon_\infty = 1/\text{mV}$, $l = 1/\text{mV}$, $\bar{v} = 0$ mV.

solved simultaneously from (12). The first equation of (13) represents the no-flux boundary condition imposed on the surface domain of the heart denoted by $\partial\Omega$. The symbol \mathbf{n} is the outward surface normal on $\partial\Omega$. The second equation of (13) defines the natural boundary condition imposed on $\partial\Omega$. The third equation of (13) shows the essential boundary condition imposed at points which are fixed to ensure that the mechanical problem is well defined. The domain where the essential boundary condition is imposed on is denoted by $\partial\Lambda$.

2.3.1. Excitation-Induced Contraction. In Section 2.2, we introduced the active Kirchhoff stress $\boldsymbol{\sigma}_{\text{act}}$. $\boldsymbol{\sigma}_{\text{act}}$ is generated by the excitation-induced contraction. From the perspective of geometry, the direction of the active Kirchhoff stress should be determined by the structural tensor $\boldsymbol{\kappa}$, and its magnitude is controlled by the transmembrane potential v . Let the magnitude of the active stress be $f(v)$, we have $\boldsymbol{\sigma}_{\text{act}} = f(v)\boldsymbol{\kappa}$.

Quite a few models have been proposed to simulate the voltage-dependent active fiber tension $f(v)$ [4, 18]. In this work, we adopt the simplified equation proposed by [4]:

$$\begin{aligned} \dot{f} &= \varepsilon(v) [k_f(v - v_r) - f] \\ \varepsilon(v) &= \varepsilon_0 + (\varepsilon_\infty - \varepsilon_0) \exp[-\exp(-l(v - \bar{v}))]. \end{aligned} \quad (14)$$

In (14), the symbol $k_f = 0.005$ MPa/mV is the maximum active fiber tension, and v_r is the resting potential which is about -94.7 mV for cardiac cells in the BR ionic model. The switch function is denoted by $\varepsilon(v)$ and it determines how fast the active fiber tension will change with respect to the transmembrane potential v . Parameters' values are $\varepsilon_0 = 0.1/\text{mV}$, $\varepsilon_\infty = 1/\text{mV}$, $l = 1/\text{mV}$, $\bar{v} = 0$ mV. When v changes from -94.7 mV to 20 mV, the function is as Figure 2.

Note that the calcium fluctuation is not studied in this work and the active fiber tension is controlled by the membrane potential directly for simplification, as shown in (14).

2.3.2. Diffusion Tensor. In (3), the interconnection between cells is regulated by the diffusion tensor \mathbf{D} . It controls the transduction speed of the electrical wave of excitation in the cardiac tissue. Due to the anisotropic properties of the heart tissue, it is observed in experiments that the conduction is obviously faster in the myofiber directions than in other directions. To consider the additional speed along the fiber orientations, the diffusion tensor is split into two parts: $\mathbf{D} = d_{\text{iso}}\mathbf{I} + d_{\text{ani}}\boldsymbol{\kappa}$. The symbol \mathbf{I} denotes an identity matrix. The coefficient $d_{\text{iso}} = 0.001 \text{ cm}^2/\text{ms}$ controls the speed of the isotropic transduction to all directions and the coefficient $d_{\text{ani}} = 0.0001 \text{ cm}^2/\text{ms}$ denotes the additional speed along the fiber orientations. Since the structural tensor $\boldsymbol{\kappa}$ is dependent on the spatial coordinate, the diffusion tensor at each material point will change with the reshaping of the heart.

2.3.3. Deformation-Induced Generation of Current. In (3), the total ionic transmembrane current I_{ion} consists of a component I_{sac} . The stretch activated channels are the ion channels which open their pores in response to mechanical deformation of the cell membrane [19]. According to what mechanisms the current is induced, there are different kinds of formulations for the stretch activated channels. In this work, we employ the formulation proposed by [20]:

$$I_{\text{sac}} = \delta G_s (|\mathbf{a}| - 1)(v - v_s). \quad (15)$$

In (15), $G_s = 10 \text{ mS}/\mu\text{F}$ is the maximum conductance; $v_s = -20 \text{ mV}$ is the resting potential of the stretch-activated channels; δ is the coefficient that determines whether or not the stiffness of the myofibers is in effect, as defined in (10); $|\mathbf{a}|$ is the stretch at a material point of the heart.

3. Numerical Computation Approach

The governing equations (12) are solved using the operator splitting method [21]. First, we solve the following nonlinear ordinary differential equation using the forward Euler method [22]:

$$\frac{dv}{dt} + \frac{I_{\text{ion}}}{C_m} = 0. \quad (16)$$

Then, the solution from (16) is used to solve the following partial differential equation in (17) using the implicit Euler method. These two equations are solved iteratively for each time step. Consider the following:

$$\begin{aligned} \frac{\partial v}{\partial t} - \nabla_{\mathbf{x}} \cdot (\mathbf{D} \cdot \nabla_{\mathbf{x}} v) &= 0 \\ \nabla_{\mathbf{x}} \cdot \boldsymbol{\sigma} + \mathbf{b} &= 0. \end{aligned} \quad (17)$$

Weak forms of (17) are constructed following the classical Galerkin procedure. The weak form is obtained by taking the product of (17) with the test functions $\delta \mathbf{x}$ and δv and integrating them over the domain. The time independent test functions are required to be C^0 and satisfy the essential boundary conditions on $\partial\Omega$. Multiplying the test function

$\delta \mathbf{x}$ and δv with the two equations in (18) and carrying out integration by part yield

$$\begin{aligned} G_{\mathbf{x}} &= \int_{\Omega} \nabla_{\mathbf{x}}(\delta \mathbf{x}) : \boldsymbol{\sigma} dV \\ &\quad - \int_{\partial\Omega} \delta \mathbf{x} \cdot \boldsymbol{\sigma} \cdot \mathbf{n} da - \int_{\Omega} \delta \mathbf{x} \cdot \mathbf{b} dV = 0, \\ G_v &= \int_{\Omega} \left[\delta v \frac{\partial v}{\partial t} + \nabla_{\mathbf{x}}(\delta v) \cdot (\mathbf{D} \cdot \nabla_{\mathbf{x}} v) \right] dV \\ &\quad - \int_{\partial\Omega} \delta v \mathbf{D} \cdot \nabla_{\mathbf{x}} v \cdot \mathbf{n} da = 0. \end{aligned} \quad (18)$$

Applying the natural boundary conditions to (18) leads to

$$\begin{aligned} G_{\mathbf{x}} &= \int_{\Omega} \nabla_{\mathbf{x}}(\delta \mathbf{x}) : \boldsymbol{\sigma} dV - \int_{\Omega} \delta \mathbf{x} \cdot \mathbf{b} dV = 0, \\ G_v &= \int_{\Omega} \left[\delta v \frac{\partial v}{\partial t} + \nabla_{\mathbf{x}}(\delta v) \cdot (\mathbf{D} \cdot \nabla_{\mathbf{x}} v) \right] dV = 0. \end{aligned} \quad (19)$$

At each time step, (19) are linearized as follows:

$$\begin{aligned} G_{\mathbf{x}}(\mathbf{x}_{n+1}, v_{n+1}) &= G_{\mathbf{x}}(\mathbf{x}_n, v_n) + \Delta G_{\mathbf{x}}(\mathbf{x}_n, v_n; \mathbf{x}_{n+1} - \mathbf{x}_n, v_{n+1} - v_n), \\ G_v(\mathbf{x}_{n+1}, v_{n+1}) &= G_v(\mathbf{x}_n, v_n) + \Delta G_v(\mathbf{x}_n, v_n; \mathbf{x}_{n+1} - \mathbf{x}_n, v_{n+1} - v_n). \end{aligned} \quad (20)$$

We can then solve for $\Delta \mathbf{x} = \mathbf{x}_{n+1} - \mathbf{x}_n$ and $\Delta v = v_{n+1} - v_n$ from the linearized equations.

The conventional isoparametric Galerkin procedure is followed to discretize the continuous weak form equations. The domain of the heart Ω is decomposed into subdomains Ω_e^h , and each subdomain is an element. Then the field variables \mathbf{x} and v , and the two associated test functions are interpolated in each subdomain as

$$\begin{aligned} \mathbf{x}_e^h(\mathbf{X}, t) &= \sum_{j=1}^{n_{\text{en}}} N^j(\mathbf{X}) \mathbf{x}_j^e(t), \\ v_e^h(\mathbf{X}, t) &= \sum_{j=1}^{n_{\text{en}}} N^j(\mathbf{X}) v_j^e(t) \end{aligned} \quad (21)$$

In (21), n_{en} is the number of nodes per element and $N^j(\mathbf{X})$ is the C^0 interpolants, often called shape functions in finite element literatures. The implicit Euler method is utilized when discretizing time derivative terms in (18). Finally, we achieved a linear system equation in form of:

$$\{A\}_{4N \times 4N} \begin{pmatrix} \Delta x_n \\ \Delta y_n \\ \Delta z_n \\ \Delta v_n \end{pmatrix}_{n=1 \sim N} = \{b\}_{4N}. \quad (22)$$

The linear system equation has a degree of $4 * N$, where N is the number of the nodes in the mesh. For each node, $(\Delta x, \Delta y, \Delta z, \Delta v)$ are solved. They are then used to update the membrane potential and the spatial coordinate of each node.

The model was implemented in C++ and was parallelized using the message passing interface (MPI) [23]. An open

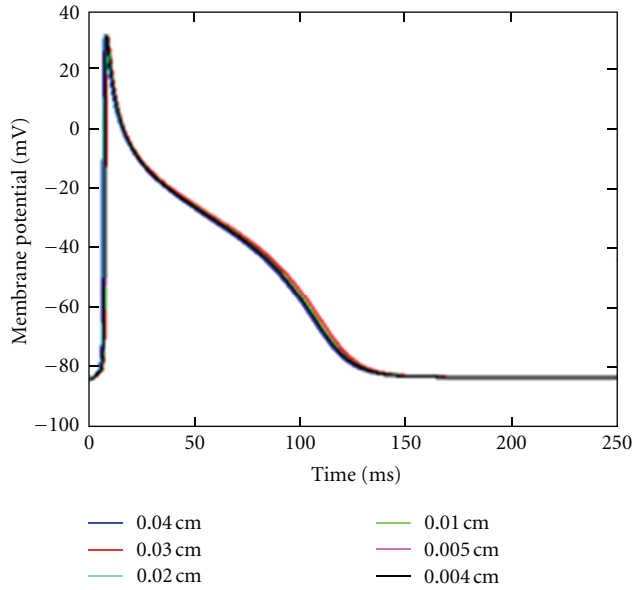


FIGURE 3: Action potential of a node at $(-0.2 \text{ cm}, -0.2 \text{ cm}, 0.0005 \text{ cm})$. Mesh size was decreased from 0.04 cm (blue) to 0.004 cm (black).

source software package called METIS [24] was used to partition the heart mesh so that computational loads are balanced among CPUs. The algorithms in METIS were based on multilevel recursive-bisection, multilevel k-way, and multiconstraint partitioning schemes.

Two parallel solvers were used to solve the final linear system. The two solvers are the hierarchical iterative parallel solver (HIPS) [25] and the solver from the Trilinos package [26]. Both of them implemented the generalized minimal residual method [27]. When using the Trilinos, the linear system was preconditioned by the Jacobi preconditioner. Simulations were run on the supercomputer, Kraken [28]. The open source software VisIt [29] was used for visualization.

4. Numerical Results

4.1. A Thin Cardiac Tissue. We first conducted simulations in a thin square cardiac tissue of the size $0.4 * 0.4 * 0.001 \text{ cm}^3$. In simulations, the top-left and the bottom-right corners were fixed, and the fiber orientation was along vertical direction. We used the Forward Euler method to solve the ODE in (16) at a time step of 0.005 ms. The PDEs in (17) are solved using the implicit Euler method with a time step of 0.1 ms.

Action potential of a node at $(-0.2 \text{ cm}, -0.2 \text{ cm}, 0.0005 \text{ cm})$ as shown in Figure 3 was obtained using different mesh sizes. The numerical results show that consistent action potential responses are obtained using different mesh sizes. Because the cardiac tissue is very thin, it is treated like a 2d tissue. The mesh size is with respect to the x and y directions which are each 0.4 cm in length.

We then performed an electromechanical simulation in the tissue $(0.4 \text{ cm} * 0.4 \text{ cm} * 0.001 \text{ cm})$ with mesh size = 0.004 cm. The stimulation was imposed at the center of the tissue. Figure 4 shows the electrical wave propagation without considering the contraction. The electrical wave propagated symmetrically from the center to the whole tissue. This test validates the part of “reaction-diffusion” in our model by reproducing the basic phenomenon of electrical wave propagation in a square tissue. Note that the coefficient d_{ani} was set to 0 in this simulation so that the tissue was isotropic.

Figure 5 shows the electrical propagation as well as the excitation-induced contraction in a tissue. In this test, the fibers of the tissue were aligned vertically. Thus, the tissue deformed in vertical direction, as clearly shown at time $t = 7 \text{ ms}$ in Figure 5. Moreover, in contrast to the previous test, we considered the additional speed along the fiber orientations, as indicated by $\mathbf{D} = d_{\text{iso}}\mathbf{I} + d_{\text{ani}}\boldsymbol{\kappa}$. The coefficient d_{ani} was set to $0.0001 \text{ cm}^2/\text{ms}$. It is easily observed from Figure 5 that the propagation was obviously faster in vertical direction.

4.2. Dog Ventricle with Realistic Geometry. We also simulated the contraction of a dog ventricle with realistic geometry. Two meshes were examined. The first mesh consisted of 880 Hexahedron elements. The second mesh which had 190080 hexahedron elements was refined from the first one using the software CUBIT which was developed at Sandia National Laboratories [30]. See Figure 6 for the original mesh and the refined one. The ventricle mesh was obtained from [31].

The constitutive and coupling models, the anisotropic electrical conductivity, and other parameters were the same as used earlier. The stimulus was imposed on the superior section of the ventricle as shown in Figure 7. Some nodes on the upper surface were restrained so that the problem would be well defined. We assumed that the normal of the fiber at any point is pointing to the geometric center. Under this assumption, the fibers form layers of muscle in the heart. We note that this assumption may not be close to realistic fiber layouts in the heart. However, the assumed structure allows us to test the efficiency and robustness of the computational algorithms on a heart, on which fiber orientation changes from point to point.

Figure 8 shows an electromechanical simulation of a dog ventricle with realistic geometry. Electrical stimulation was imposed on the upper surface of the septum. The contraction state kept for about 100 ms and then slowly recovered to the resting state.

We also simulated a ventricle with a scar near the outer surface. We have adopted a simplified description of scar. Specifically, we assumed the scar has no conduction capability and can maintain passive mechanical contractions like other cells. The scar had a size as shown in Figure 9. The scar has a radius of about 1cm in the surface area and its thickness was similar to the ventricle wall.

Figure 9 shows the shapes of the contracting ventricle and the spatial distribution of membrane potentials at six moments. Comparing Figure 9 with Figure 8, obvious

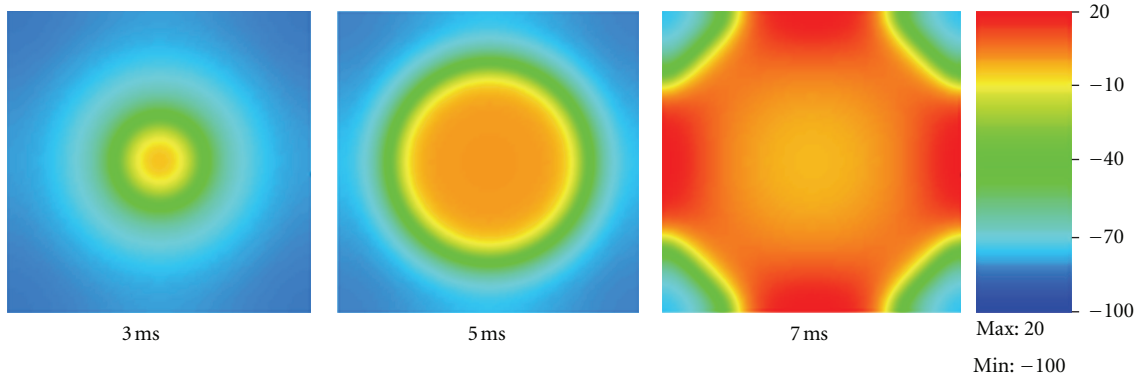


FIGURE 4: Electrical wave propagation in a piece of heart tissue.

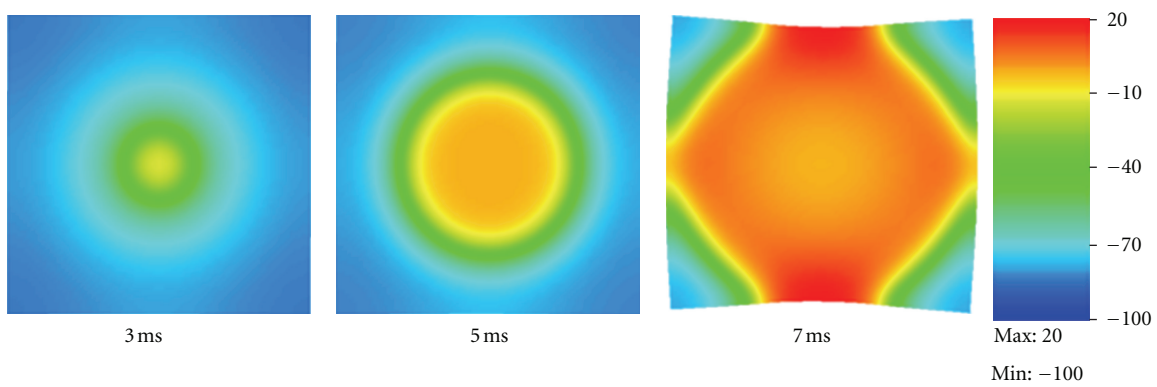


FIGURE 5: Electrical wave propagation and excitation-induced contraction in a piece of heart tissue. Although these tests are simple and straightforward, they demonstrate the model's capability of performing fully-coupled electromechanical simulations.

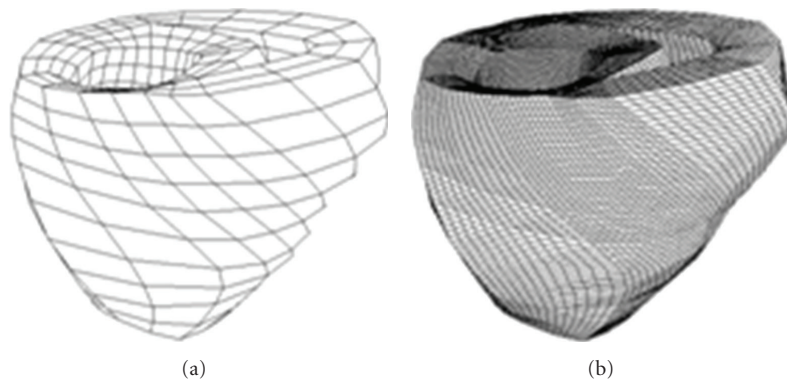


FIGURE 6: Dog ventricle mesh: original (left) and refined (right).

difference can be observed. When the scar was present the membrane potentials was evidently smaller, and this could cause smaller active fiber tension and thus weakened pumping ability. Although no serious physiological conclusion could be given in this study since our simulations were preliminary and lacked experimental validation, the simulations demonstrated the capability of our model to study the real heart.

4.3. Performance Analysis. Parallel efficiency is crucial for our model. The requirements of using meshes with hundreds of thousands of elements to achieve high accuracy and resolution make the computational efficiency a great challenge. The parallel efficiency is measured by the analysis of the scalability. A mesh with 1.56 million Hexahedron elements was used. In this analysis, we used 120, 240, and 480 cores. The time spent when using 120 CPUs was taken as the

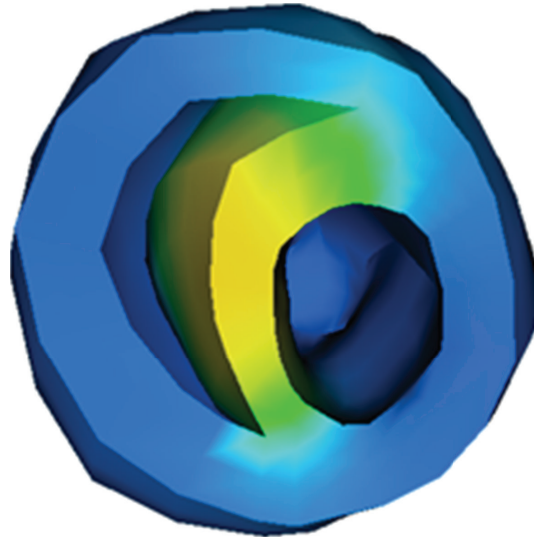


FIGURE 7: Initial stimulus: the stimulus was imposed on the superior section of the ventricle.

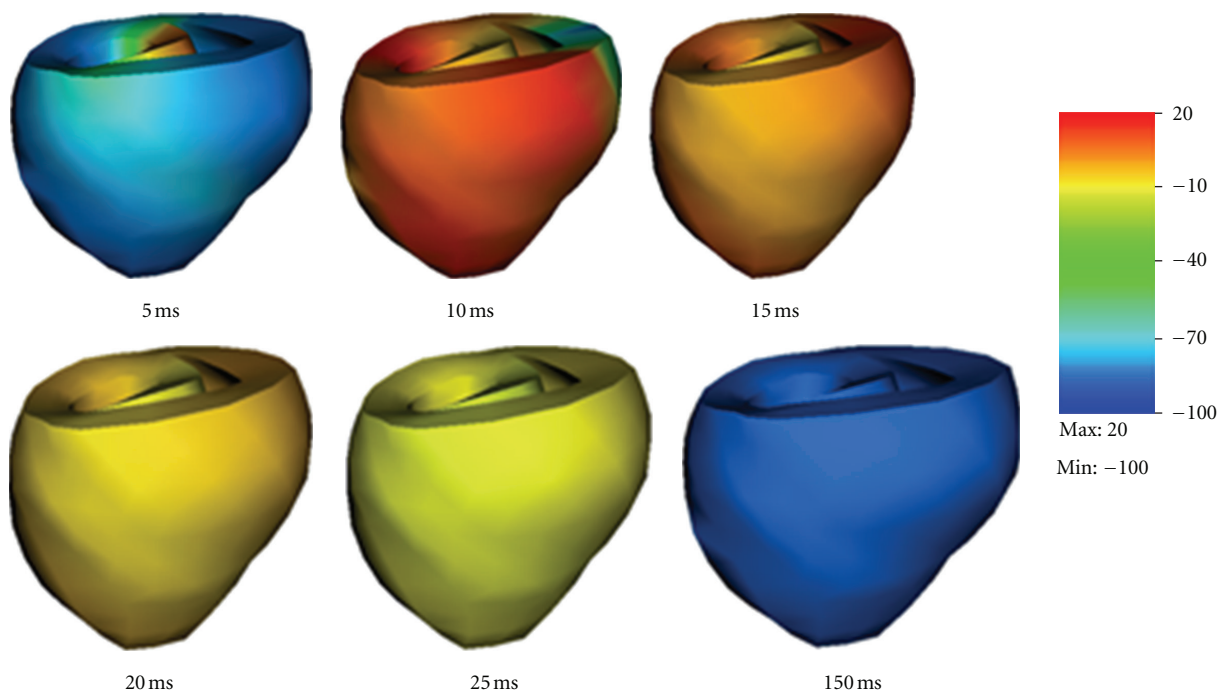


FIGURE 8: Electromechanical simulation of a dog ventricle with realistic geometry.

reference value. Figure 10 shows the strong scalability up to 480 cores on the Kraken supercomputer. In this case, the scalability for 240 cores was about 90% of the ideal and the scalability for 480 cores was about 70% of the ideal. The decrease of the scalability was due to the increase of the proportion of amount of communications per iteration and the increase of the proportion of the number of ghost nodes. The scaling ability was limited by the performance of the PDE solver from the Trilinos package [26]. In future studies, the performance will benefit from choosing a better parallel solving algorithm. Also the performance may be improved if

we take use of the CUDA [32] which is a parallel computing platform and programming model invented by NVIDIA.

5. Discussions and Conclusion

It is a common approach in the literature to solve the electromechanics problem in an iterative manner. In each step, the electrical problem is solved first and then the results from the electrical solution are submitted into the mechanical problem, whose solution is then used to solve the electrical problem in the next step. Since the electrical

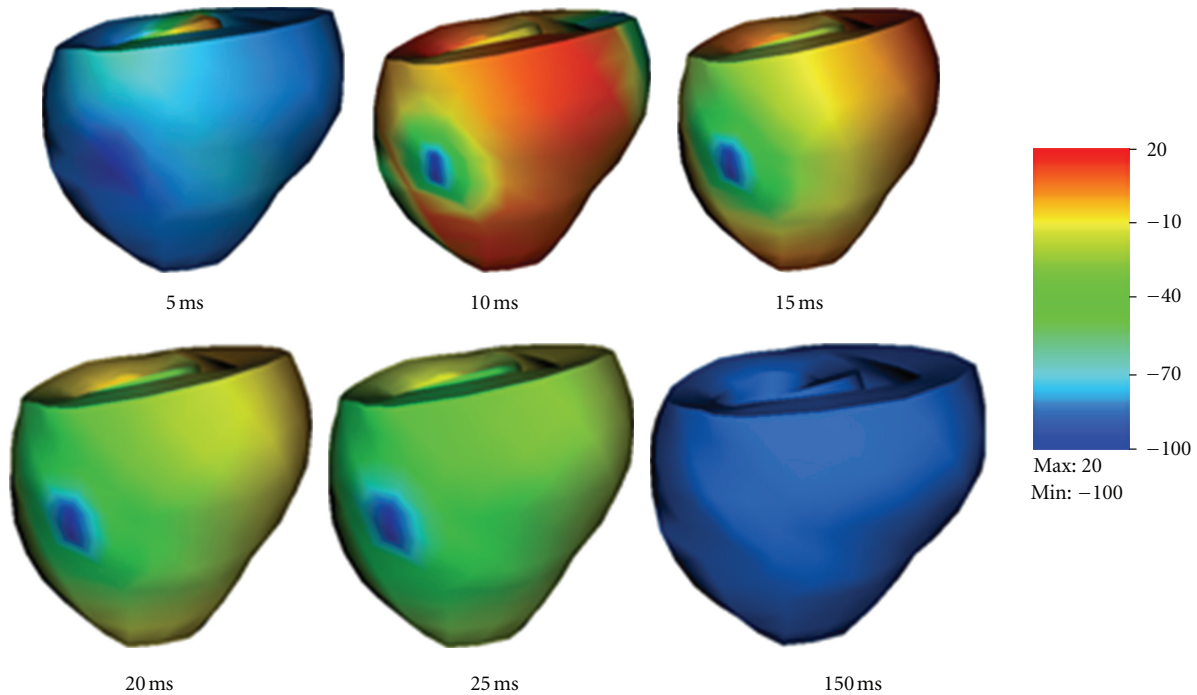


FIGURE 9: Electromechanical simulation of a dog ventricle with a scar near the outer surface.

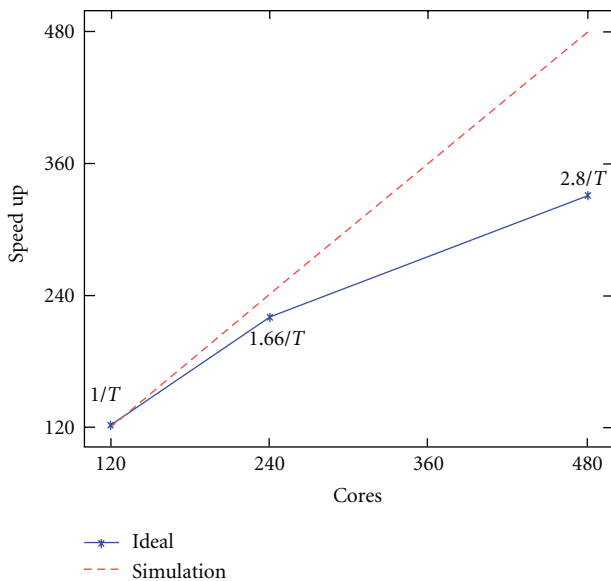


FIGURE 10: Scalability up to 480 CPUs on the Kraken system.

problem and the mechanical problem are solved separately, it is also a common practice to adopt a fine mesh for the electrical field and a much coarser mesh for the mechanical field.

The contribution of this work is to develop a fully coupled scheme to accurately solve the electromechanics of the heart. We have developed a cardiac electromechanics model, which integrates cardiac electrophysiology, mechanical

contraction, as well as their interactions. Realistic physiological models have been adopted to describe the electrical and mechanical functions in the heart. The model has been numerically solved using an implicit, finite element-based approach. Numerical simulations have been conducted using parallel simulation in tissues of different geometries. The cardiac mechanics is described by the updated Lagrangian approach, which views the problem from the current configuration and takes derivatives and integrals with respect to the spatial coordinates. In perspective of mesh description, the updated Lagrangian description is characterized by making the material points remain coincident with mesh points. Therefore, the Lagrangian description simplifies the imposition of boundary conditions since the element boundaries of the mesh remain coincident with material boundaries. The developed model and computer codes have been validated at each step using simple test examples to ensure accuracy in numerical computations. Multiple simulations have been conducted using various meshes and parameters to ensure numerical robustness of the developed model.

Since the computations involve millions of nodes, the current framework has limitations for real-time applications. In future studies, we will further improve the performance of the model using more efficient PDE solvers or implementing the model in CUDA [32]. This paper has adopted a simplified fiber configuration, where the normal of the fiber was assumed to point toward the geometric center of the heart. More realistic heart shape and fiber configurations should be utilized in future work for physiologically faithful parameter studies. Moreover, since Lagrangian meshes deform with material, the mesh may become distorted if the deformation of the heart is too large.

Future work may also consider more detailed models for active stresses such as the hybrid model [18]. In the hybrid model, the active force is dependent on the $[Ca^{2+}]_i$, rather than the transmembrane potential, and this is more biophysically reasonable. Moreover, the hybrid model also takes into consideration binding of intracellular Ca^{2+} to troponin C, configuration change of tropomyosin, and interaction of actin and myosin, which is a more accurate description on excitation contraction interaction. Numerical simulations have been carried out for purpose of validating the model implementation in this paper, but more numerical experiments will be executed using the platform to investigate the interaction of electrical and mechanical functions in the heart and their influences to cardiac arrhythmias.

Acknowledgments

This work was in part supported by the NSF under Grant no. CMMI-0845753. This research was supported by an allocation through the TeraGrid Advanced Support Program, under Grant no. BCS090012. Some simulations are conducted on the Newton High Performance Cluster at UTK. H. Xia is supported through a graduate research assistantship at the National Institute for Mathematical and Biological Synthesis, an Institute sponsored by the National Science Foundation, the U.S. Department of Homeland Security, and the U.S. Department of Agriculture through NSF Award no. EF-0832858, with additional support from The University of Tennessee, Knoxville.

References

- [1] F. Vadakkumpadan, V. Gurev, J. Constantino, H. Arevalo, and N. Trayanova, "Modeling of whole-heart electrophysiology and mechanics: towards patient-specific simulation," in *Patient Specific Modeling of the Cardiovascular System*, R. C. P. Kerckhoffs, Ed., pp. 145–165, Springer Science+Business Media, 2010.
- [2] A. L. Hodgkin and A. F. Huxley, "A quantitative description of membrane current and its application to conduction and excitation in nerve," *The Journal of Physiology*, vol. 117, no. 4, pp. 500–544, 1952.
- [3] F. H. Fenton and E. M. Cherry, "Models of cardiac cell," *Scholarpedia*, vol. 3, no. 8, p. 1868, 2008.
- [4] M. P. Nash and A. V. Panfilov, "Electromechanical model of excitable tissue to study reentrant cardiac arrhythmias," *Progress in Biophysics and Molecular Biology*, vol. 85, no. 2-3, pp. 501–522, 2004.
- [5] R. FitzHugh, "Mathematical models of threshold phenomena in the nerve membrane," *The Bulletin of Mathematical Biophysics*, vol. 17, no. 4, pp. 257–278, 1955.
- [6] S. A. Niederer, P. J. Hunter, and N. P. Smith, "A quantitative analysis of cardiac myocyte relaxation: a simulation study," *Biophysical Journal*, vol. 90, no. 5, pp. 1697–1722, 2006.
- [7] V. Gurev, T. Lee, J. Constantino, H. Arevalo, and N. A. Trayanova, "Models of cardiac electromechanics based on individual hearts imaging data: image-based electromechanical models of the heart," *Biomechanics and Modeling in Mechanobiology*, vol. 10, no. 3, pp. 295–306, 2011.
- [8] S. Göktepe and E. Kuhl, "Electromechanics of the heart: a unified approach to the strongly coupled excitation-contraction problem," *Computational Mechanics*, vol. 45, no. 2-3, pp. 227–243, 2010.
- [9] M. G. Doyle, S. Tavoularis, and Y. Bourgault, "Application of parallel processing to the simulation of heart mechanics," *Lecture Notes in Computer Science*, vol. 5976, pp. 30–47, 2010.
- [10] P. Lafortune, R. Arís, M. Vázquez, and G. Houzeaux, "Coupled electromechanical model of the heart: parallel finite element formulation," *International Journal For Numerical Methods in Biomedical Engineering*, vol. 28, pp. 72–86, 2012.
- [11] F. Fenton and A. Karma, "Vortex dynamics in three-dimensional continuous myocardium with fiber rotation: filament instability and fibrillation," *Chaos*, vol. 8, pp. 20–47, 1998.
- [12] R. H. Clayton, O. Bernus, E. M. Cherry et al., "Models of cardiac tissue electrophysiology: progress, challenges and open questions," *Progress in Biophysics and Molecular Biology*, vol. 104, no. 1-3, pp. 22–48, 2011.
- [13] P. Kohl and F. Sachs, "Mechanoelectric feedback in cardiac cells," *Philosophical Transactions of the Royal Society A*, vol. 359, no. 1783, pp. 1173–1185, 2001.
- [14] C. Cherubini, S. Filippi, P. Nardinocchi, and L. Teresi, "An electromechanical model of cardiac tissue: constitutive issues and electrophysiological effects," *Progress in Biophysics and Molecular Biology*, vol. 97, no. 2-3, pp. 562–573, 2008.
- [15] N. H. L. Kuijpers, H. M. M. Ten Eikelder, P. H. M. Bovendeerd, S. Verheule, T. Arts, and P. A. J. Hilbers, "Mechanoelectric feedback leads to conduction slowing and block in acutely dilated atria: a modeling study of cardiac electromechanics," *American Journal of Physiology*, vol. 292, no. 6, pp. H2832–H2853, 2007.
- [16] G. W. Beeler and H. Reuter, "Reconstruction of the action potential of ventricular myocardial fibres," *Journal of Physiology*, vol. 268, no. 1, pp. 177–210, 1977.
- [17] H. Knutsson, "Representing local structure using tensors," in *Proceedings of the 6th Scandinavian Conference on Image Analysis*, pp. 244–251, 1989.
- [18] F. B. Sachse, K. G. Glänzel, and G. Seemann, "Modeling of protein interactions involved in cardiac tension development," *International Journal of Bifurcation and Chaos*, vol. 13, no. 12, pp. 3561–3578, 2003.
- [19] F. Guharay and F. Sachs, "Stretch-activated single ion channel currents in tissue-cultured embryonic chick skeletal muscle," *Journal of Physiology*, vol. 352, pp. 685–701, 1984.
- [20] R. H. Keldermann, M. P. Nash, and A. V. Panfilov, "Pacemakers in a reaction-diffusion mechanics system," *Journal of Statistical Physics*, vol. 128, no. 1-2, pp. 375–392, 2007.
- [21] M. Bjørhus, "Operator splitting for abstract Cauchy problems," *IMA Journal of Numerical Analysis*, vol. 18, no. 3, pp. 419–443, 1998.
- [22] L. Euler, *Institutionum Calculi Integralis*, vol. 2, Impensis Academiae Imperialis Scientiarum, 1769.
- [23] Message Passing Interface (MPI) standard, 2012, <http://www.mcs.anl.gov/research/projects/mpi/>.
- [24] G. Karypis, 2012, <http://glaros.dtc.umn.edu/gkhome/views/metis>.
- [25] J. Gaidamour and P. Hénon, INRIA team-project Scalapplx, 2010, <http://hips.gforge.inria.fr/index.html>.
- [26] M. Heroux, R. Bartlett, V. Howle et al., *An Overview of Trilinos*, Sandia National Laboratories, 2003, <http://trilinos.sandia.gov/TrilinosOverview.pdf>.
- [27] Y. Saad and M. H. Schultz, "GMRES: a generalized minimal residual algorithm for solving nonsymmetric linear systems," *Journal on Scientific Computing*, vol. 7, no. 3, pp. 856–869, 1986.

- [28] Kraken, National Institute for Computational Sciences(NICS), 2012, <http://www.nics.tennessee.edu/>.
- [29] Department of Energy (DOE), Advanced Simulation and Computing Initiative (ASCI), 2012, <https://wci.llnl.gov/codes/visit/>.
- [30] P. Kohl and U. Ravens, “Cardiac mechano-electric feedback: past, present, and prospect,” *Progress in Biophysics and Molecular Biology*, vol. 82, no. 1–3, pp. 3–9, 2003.
- [31] P. J. Hunter, P. M. F. Nielsen, B. H. Smaill, I. J. LeGrice, and I. W. Hunter, “An anatomical heart model with applications to myocardial activation and ventricular mechanics,” *Critical Reviews in Biomedical Engineering*, vol. 20, no. 5-6, pp. 403–426, 1992.
- [32] NVIDIA, 2012, http://www.nvidia.com/object/cuda_home_new.html.

Research Article

A Study of Mechanical Optimization Strategy for Cardiac Resynchronization Therapy Based on an Electromechanical Model

Jianhong Dou,^{1,2} Ling Xia,² Dongdong Deng,² Yunliang Zang,² Guofa Shou,² Cesar Bustos,² Weifeng Tu,¹ Feng Liu,³ and Stuart Crozier³

¹Department of Anesthesiology, General Hospital of Guangzhou Military Command, Guangzhou 510010, China

²Key Lab of Biomedical Engineering of Ministry of Education, Department of Biomedical Engineering, Zhejiang University, Hangzhou 310027, China

³The School of Information Technology & Electrical Engineering, The University of Queensland, Brisbane, QLD 4072, Australia

Correspondence should be addressed to Ling Xia, xialing@zju.edu.cn

Received 21 June 2012; Accepted 10 September 2012

Academic Editor: Dingchang Zheng

Copyright © 2012 Jianhong Dou et al. This is an open access article distributed under the Creative Commons Attribution License, which permits unrestricted use, distribution, and reproduction in any medium, provided the original work is properly cited.

An optimal electrode position and interventricular (VV) delay in cardiac resynchronization therapy (CRT) improves its success. However, the precise quantification of cardiac dyssynchrony and magnitude of resynchronization achieved by biventricular (BiV) pacing therapy with mechanical optimization strategies based on computational models remain scant. The maximum circumferential uniformity ratio estimate (CURE) was used here as mechanical optimization index, which was automatically computed for 6 different electrode positions based on a three-dimensional electromechanical canine model of heart failure (HF) caused by complete left bundle branch block (CLBBB). VV delay timing was adjusted accordingly. The heart excitation propagation was simulated with a monodomain model. The quantification of mechanical intra- and interventricular asynchrony was then investigated with eight-node isoparametric element method. The results showed that (i) the optimal pacing location from maximal CURE of 0.8516 was found at the left ventricle (LV) lateral wall near the equator site with a VV delay of 60 ms, in accordance with current clinical studies, (ii) compared with electrical optimization strategy of E_{RMS} , the LV synchronous contraction and the hemodynamics improved more with mechanical optimization strategy. Therefore, measures of mechanical dyssynchrony improve the sensitivity and specificity of predicting responders more. The model was subject to validation in future clinical studies.

1. Introduction

Congestive heart failure (CHF) is a common heart disease caused by dilated cardiomyopathy or damage to the excitation conduction system. Biventricular pacing (BiVP), or cardiac resynchronization therapy (CRT), was a major breakthrough in the treatment for patients with advanced CHF complicated by discoordinate contractions caused by inter- or intraventricular conduction delays [1]. CRT has the potential to improve the quality of life and functional capacity, promote left ventricle (LV) reverse remodeling, and reduce heart failure (HF) hospitalizations and mortality in patients with New York Heart Association class III or IV CHF [2–6]. However, up to 20–30% of patients do not respond favourably to CRT using standard clinical selection

criteria [7], and a critical analysis of the data suggests the true nonresponder rate can be estimated at perhaps 40–50% [8]. Data indicate that factors associated with a poor outcome are multifactorial and that inappropriate patient selection, left ventricular pacing site, and inadequate device programming are likely to be important [9]. Therefore, an individual optimal electrode position, atrio-ventricular delay (AV delay, AVD), or interventricular delay (VV delay, VVD) in CRT are needed to improve its success [10, 11]. However, left ventricular lead placement and timing delays continue to pose a number of challenges regarding the delivery of an effective CRT.

Over the past decade, many studies have examined the pathophysiology of cardiac dyssynchrony and tested the effect of cardiac resynchronization on heart functions

and the efficacy of symptoms enhancements. Most of these researches have focused on the ECG characteristic of distinct responders versus nonresponders to CRT. For example, left and right ventricular leads were placed in different locations to attain the shortest QRS duration during biventricular stimulation. Presently, the optimal electrode setups and timing delays are also determined by measuring the cardiac index using magnetic resonance tagging (MR tagging), nuclear imaging (NI) or Doppler flow imaging and so on [12–15], most of which relate to the measurement of interventricular asynchrony (interVA) or intraventricular asynchrony (intraVA).

However, it may be not sufficient for clinicians to formulate a scientific and reasonable treatment scheme for CRT optimization with only physical examination of ECG or medical imaging. Quantitative information and precise programming of the optimal stimulation delays and lead positioning accordant with the physiological function are needed. For example, although it is generally accepted that the posterior-lateral wall is the preferred location for LV lead location in CRT, other LV pacing sites have also been shown to offer superior benefits for selected patient population. In other words, there is no universally accepted best LV pacing site, nor the best V-V interval. Therefore, patient-specific CRT optimization is needed. There are both intersubject variability and intrasubject variability (e.g., compare resting versus exercise conditions). Modeling of heart can provide a useful supplementary tool to investigate the dynamical behaviour of heart quantitatively and thus enhance our understanding of the cardiac electrophysiological and mechanical properties under physical and pathological conditions. Consequently, the computer modeling of a patient-specific heart appears to be a reasonable solution for solving this problem, which can determine the optimal AV and VV timing pre- or postoperatively with respect to the lead positions in patients undergoing CRT.

Many scientists have concentrated on the study of individual optimization of lead position and pacing delays of CRT by means of heart modeling and simulation with the progress of mathematical modeling techniques. The electrical-based optimization approach, for example, minimizing the QRS duration, has been widely accepted due to its simplicity. Therefore, most of researches have concentrated on the electrical strategies of optimizing parameters in CRT. Reumann et al. simulated an atrio-ventricular (AV) and a left bundle branch block (LBBB) with different reductions in the interventricular conduction velocity based on computer models of the Visible Man and a patient's heart [16]. They assumed that the ideal cardiac function is achieved if the excitation of the ventricles is as close as possible to the physiological rhythm. Consequently, the minimum error between the physiological excitation and pathology/therapy, that is, the root mean square error E_{RMS} , was used as an optimization assessment index and automatically computed for 12 different electrode positions with different AV and VV intervals. Their results showed the importance of individually adjusting the electrode position, beside the timing delays, to the patient's anatomy and pathology in accordance with current clinical studies. Mohindra et

al. recorded 120-electrode body-surface potential mapping (BSPM) data and calculated the epicardial potentials and isochrones of activation for different V-V intervals by means of an electrocardiographic inverse solution based on a ventricular computer model [17]. They used the area between the LV and RV percentage surface-activated curves as a measure of interventricular synchrony for a variety of V-V settings. Their results demonstrated that an optimal CRT pacing V-V interval can be selected by aiming to minimize the dyssynchrony in the ventricular activation patterns. However, they found that it was difficult to correlate the heart model results with the clinical recordings and moreover, the BSPM did not provide any information about how these patterns improved the cardiac output. To some extent, these mathematical models carried out well the adjustment of the optimization parameters of CRT. Yet, because the optimization procedure was based on the electrical criterion that was not necessarily equal to the electromechanical coupling [15], the simulations in these works might be wrong if the mechanical activation followed the electrical activation with an unfixed delay, that is, the electromechanical dissociation in the cardiopulmonary resuscitation (CPR) [18]. Thus, we doubt the soundness of the electrical optimization strategy for predicting effect of CRT. A relationship between electrical dyssynchrony and mechanical performance needs to be established. Nowadays, the importance of correcting mechanical dyssynchrony has been more and more realized in the field of CRT optimization. For example, most echo-based CRT optimization approaches target the mechanical synchrony, not the electrical synchrony. Unfortunately, the mechanical optimization strategy for CRT has seldom been investigated in the previous computational models.

Compared with previous electrophysiological models for CRT optimization, the present heart model in this paper is extended to include a mechanical contraction model for the optimization of the pacing lead locations and the interventricular delays (VVds) of CRT. Since the spatial distribution of local wall mechanics was very sensitive to the choice of myofiber orientations, specific data of real fiber orientations were used for true description of cardiac deformation in this study. The ventricular mechanical dyssynchrony is evaluated by the assessment of a circumferential uniformity ratio estimate (CURE) [15, 19]. The aim of this study is to validate the feasibility of CRT optimization with mechanical predictors (CURE) and to make a contrast analysis of cardiac function improvement between mechanical (CURE) and electrical (E_{RMS}) optimization strategy for CRT. The present study resolves this question through the simulation of the cardiac electrical activation spread and the mechanical strain maps based on our previous electromechanical canine model of HF combined with a complete LBBB (CLBBB) [20].

2. Materials and Method

2.1. Heart Model of CHF with CLBBB

2.1.1. Heart Anatomical Model. The anatomical canine heart model used in this study was reconstructed from the MR

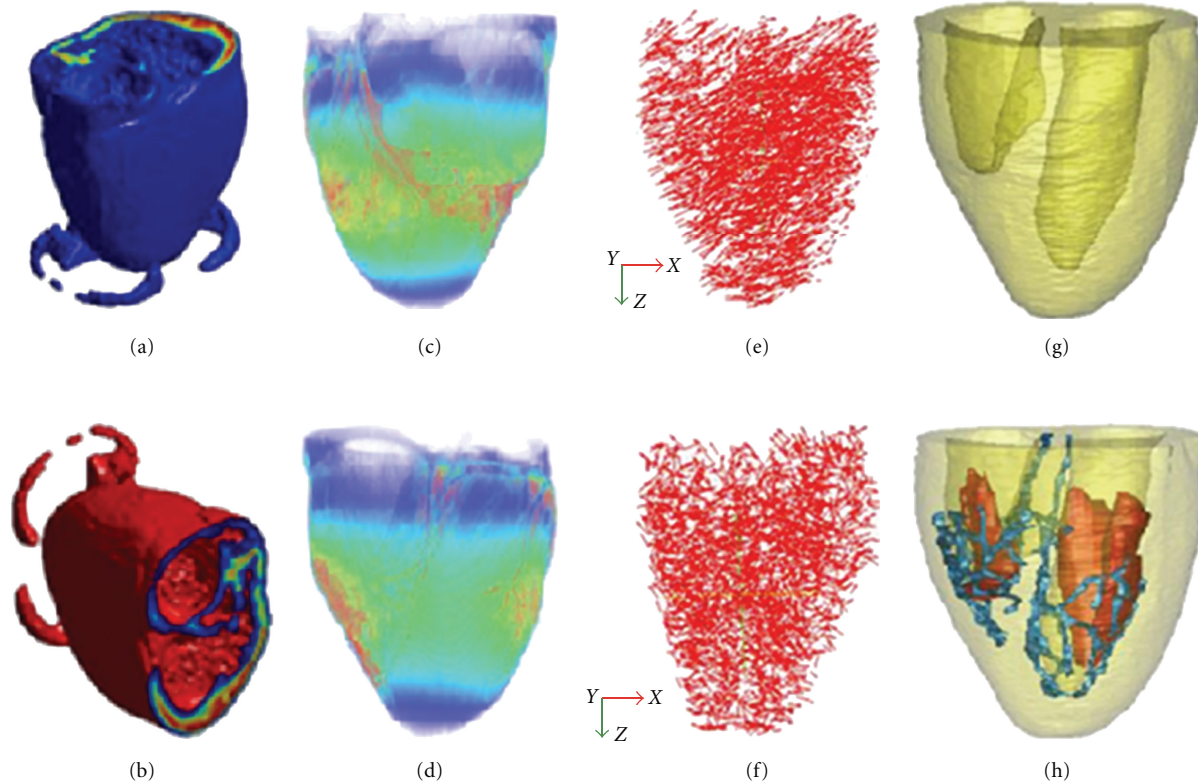


FIGURE 1: 3D view of the canine ventricular anatomical model. The left panel ((a), (b)) shows anatomical geometry from original datasets. (c) and (d) display 3D view of the whole ventricles scanned from DT-MRI at Duke University Center visualized by Volview 2.0. (e) and (f) display distribution of 3-D fiber angles in the space. (g) and (h) display the reconstructed canine heart model.

scans of an intact dog heart derived at the Duke University Medical Center for In Vivo Microscopy, Durham, NC, USA (Figures 1(a), 1(b), 1(c), and 1(d)). The spatial discrete matrix size of the original data was $256 \times 128 \times 128$, corresponding to a pixel size of $0.39 \times 0.78 \times 0.78$ mm. Myocardial fiber orientations were obtained from diffusion tensor MR imaging (DT-MRI) in a 7.1 T MRI scanner (Figures 1(e), 1(f)) and different tissues were manually segmented into functional modules, including papillary muscles and Purkinje fiber networks (Figures 1(g), 1(h)). Full details of this model can be found in [20]. Note that papillary muscles are not used in the simulation.

2.1.2. Heart Electrophysiological Properties. To model electrical propagation in a dilated failing heart with CLBBB, an initial stimulus current with a magnitude of $100 \mu\text{A}/\text{cm}^2$ and duration of 0.5 ms was added to the right bundle branch while blocking the conduction of the left bundle branch, leaving the rest of the conduction tree intact. Latest depolarization time in LBBB simulations occurred at 108 ms (see Figure 2). After these cardiac electrical excitation sequences were obtained, the active forces of myocardium can be calculated.

(1) *Ventricular Cell Model.* The dynamic ionic cell model developed by Winslow et al. [21] was used to simulate the electrophysiology of a single ventricular cell. The cell model

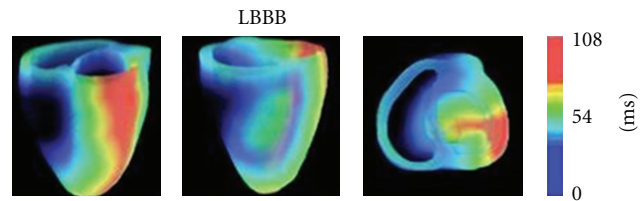


FIGURE 2: 3D maps of simulated complete LBBB activation of the canine ventricles in different views.

with different ionic channel currents could be described by the following differential equations:

$$\begin{aligned} \frac{dV_m}{dt} &= -\frac{1}{C_m} \left(\sum I_{\text{ion}} + I_{\text{app}} \right), \\ I_{\text{ion}} &= G_{\text{ion}} \cdot (V_m - E_{\text{ion}}), \end{aligned} \quad (1)$$

where V_m is the transmembrane potential, C_m is the membrane capacitance, I_x is the current flow through the ion channel x , G_x is the conductance of the channel, and E_x is the reversal potential for the channel [20].

(2) *Reaction-Diffusion Equations.* The asynchronous excitation propagation and intraventricular conduction in

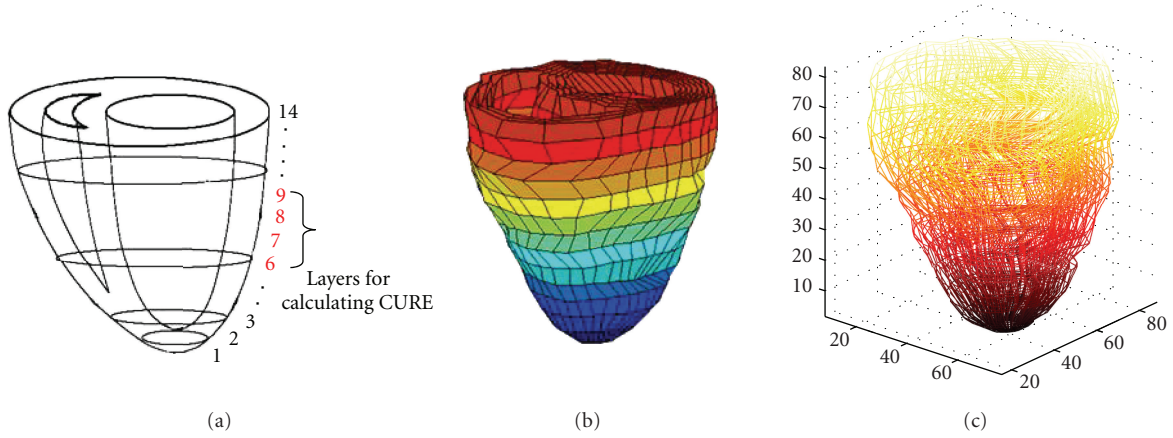


FIGURE 3: Schematic for layer display. (a) Four short slices near the equator site (layer 6 to layer 9) for calculation of CURE. (b) The finite element meshes of biventricular mechanical model of canine. (c) The coordinate system of biventricular mechanical model of canine.

the LBBB were simulated based on solutions of reaction-diffusion equations of the monodomain model as shown in the following with a strategy of parallel computation:

$$\frac{\partial V_m}{\partial t}(\underline{x}, t) = \frac{1}{C_m} \left[- \sum I_{\text{ion}}(\underline{x}, t) - I_{\text{app}}(\underline{x}, t) + \frac{1}{\beta} \left(\frac{k}{k+1} \right) \nabla \cdot (D_i(\underline{x}) \nabla V_m(\underline{x}, t)) \right], \quad (2)$$

where I_{ion} is the sum of all transmembrane ionic currents, I_{app} is the transmembrane stimulating current density, and D_i represents the diffusion coefficient.

In order to solve the monodomain equations, an initial equation (3) as well as boundary condition (4) were required:

$$V(\underline{x}, t = 0) = V(\underline{x}), \quad (3)$$

$$n \cdot \nabla V(\underline{x}, t = 0) = 0. \quad (4)$$

2.1.3. Electromechanical Coupling. In this study, we have modeled the electrical excitation and mechanical contraction as two separate processes weakly coupled together through the use of the excitation wavefront to drive the active tension development.

(1) *Myocardium Mechanical Properties.* After the cardiac electrical excitation sequences were determined by an excitation propagation algorithm in the electrical simulation, the resultant active forces of the myocardium were calculated. The active stress development in the myofibers depended on the time and sarcomere length and was initiated at the timing of the depolarization, as Kerekhoffs et al. [22–24] did. Then the active force along the fiber was calculated.

(2) *Finite Element Method (FEM).* In this work, the ventricular walls were divided into 14 layers from apex to base along the long axis of the LV (see Figure 3). There are in total 2,269 hexahedral elements and 8,736 degrees

of freedom. A 3D 8-node isoparametric element is used as the basic element. Notice that the original reference heart geometry corresponds to the end-diastolic state of a dog heart. Also, muscle alike restriction was added to ventricular base elements due to the constraint of pleura.

To analyze the motion of ventricles, the following equation at time t need to be computed:

$$[K]\{\delta\} = \{F_f\}, \quad (5)$$

where $[K]$ is the total stiffness matrix, $\{\delta\}$ is the volume vector of nodal displacement, and $\{F_f\}$ is the total vector of the active forces:

$$K = \sum_e [K]^e; \quad F_f = \sum_e [F_f]^e, \quad (6)$$

where $[F_f]^e$ is the nodal force vector of an element described above, and $[K]^e$ is the stiffness matrix of an element with the following expression:

$$[K]^e = \sum_{l=1}^{L_e} \int_{\xi_{l-1}}^{\xi_l} \left(\sum_{m=1}^{M_e} \int_{\eta_{m-1}}^{\eta_m} \int_{-1}^1 [B]^T [C]_{lm} [B] |J| d\xi d\eta \right) d\zeta, \quad (7)$$

where $[C]_{lm}$ is the elasticity matrix of layer l and segment m/M_e denotes the number/total numbers of segments in layer l in the circumferential direction, respectively.

In the fiber-coordinate system, the nodal force vector of each element $\{F_f\}^e$ in the direction of fiber can be calculated as shown in the following:

$$\begin{aligned} \{F_f\}^e &= - \sum_{l=1}^{L_e} \int_{\xi_{l-1}}^{\xi_l} \int_{-1}^1 [B]^T T \{0, 0, \sigma'_e, 0, 0, 0\}_l^T |J| d\xi d\eta d\zeta, \end{aligned} \quad (8)$$

where $[B]$ is the geometric matrix of an element, σ'_e is the active myofiber stress as a function of time after

onset of contraction and sarcomere length history, $|J|$ is the determinant of the Jacobin matrix, ξ, η, ζ the local coordinate system with the magnitudes ranging from -1 to 1 , l and L_e are the number and total number of layers in an element, respectively, and T is the transformation matrix between the fiber coordinate and global coordinate (see Appendix A).

These constitutive relations for the cardiac mechanics were then incorporated into a continuum electromechanical model of biventricles to predict the displacement and deformation. From (5) to (7), we can calculate displacement $\{\delta\}$. The equations related to mechanics are solved with eight-node isoparametric element method. Local myocardial circumferential strain ϵ_{cc} of the biventricles is then calculated during the systole phase. As far as mechanical properties are concerned, the material was considered as transversely isotropic at any point in the myocardium. The in-vitro stiffness parameters and material constants were used as before [20].

2.2. Optimization Strategies

2.2.1. Mechanical Index. Mechanical dyssynchrony is a potential indicator for predicting responses to CRT. For example, novel echocardiographic image speckle tracking applied to routine midventricular short-axis images can quantify dyssynchrony by calculating the radial strain from the multiple circumferential points averaged to several standard segments and thus predict the response to CRT [25]. Dyssynchrony for the study was usually defined as the difference in the timing of the peak strain from the earliest to latest segment. However, most clinicians prefer to use the circumferential uniformity ratio estimate (CURE) as the assessment of the mechanical dyssynchrony in the practice of CRT [15, 26, 27]. Therefore, in this study, the CURE is used to index the mechanical dyssynchrony.

According to the report [15], short-axis slices motion near the equator can reflect the actual synchronous systolic process of the ventricular wall; thus, in this study, we chose four short-axis slices near the equator site (layers 6 to 9 in our heart model) to calculate CURE, excluding the most apical and basal regions (Figures 3(a), 3(b)). The coordinate system of biventricular mechanical model of canine was shown in Figure 3(c). The algorithm are as follows.

Step 1. Compute circumferential strain ϵ_{cc} over the entire LV-midwall (y -axis) at 30 circumferentially-distributed locations around each short-axis section (x -axis), and plot ϵ_{cc} versus spatial position for each time-frame. The more oscillatory the plot, the greater was the dyssynchrony among the segments around the short axis. To explain this, we can plot circumferential strain versus spatial location of the segment as Figure 4 showed. Then, from the data, zero-order S0 and first-order S1 terms can be obtained by Fourier series decomposition. A perfectly synchronous heart appeared as a straight line (solely S0 term), whereas one that was perfectly dyssynchronous would appear as a sinusoid (S1 term) (Figure 4).

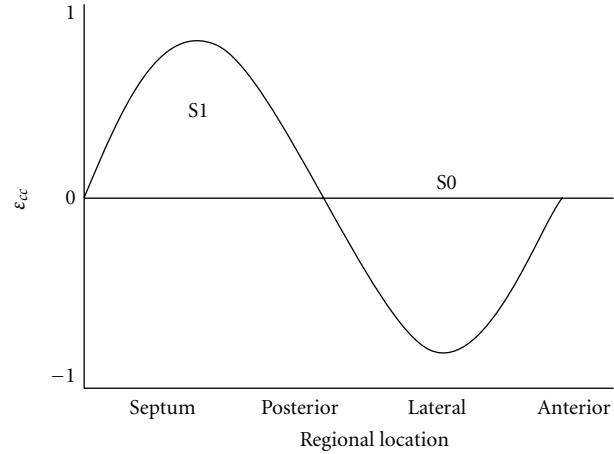


FIGURE 4: Circumferential strain ϵ_{cc} plotted as a function of spatial location of heart segment at a given time. Data were first processed by Fourier series decomposition. The zero-order (S0) and first-order (S1) terms shown plotted versus spatial position.

Step 2. Plots for the four mid-wall short-axis slices are then subjected to Fourier analysis with a function of `fft()` in Matlab7.0.1, and the results are averaged over space and time to yield

$$\text{CURE} = \left(\frac{A_0^2}{A_0^2 + 2A_1^2} \right)^{1/2}, \quad (9)$$

where A_0^2 and A_1^2 are the spatial and temporal sums of the zero- and first-order power terms, respectively. The ratio of mean to “mean plus first-order power” provides the CURE index, and the maximal value for CURE is 1 with all segments contracting synchronously; whereas symmetrically dyssynchronous contractions produce a CURE = 0 [15, 26, 27].

A further description of calculating zero and first-order power terms of layer 6 to 9 around equator sites at a given time was given in Appendix B. Then with (9), CURE can be obtained.

Step 3. Compute the CURE for each electrode pair and each VVD and choose maximum CURE as optimal result of CRT. Because the left ventricular dyssynchrony is an important determinant of CRT response, the CURE calculated from LV and septum is chosen alternatively as the criterion for predicting the response to CRT in the simulation.

The optimization method was then applied to the electromechanical canine heart model of LBBB. The optimization parameter of the CURE was sequentially calculated for each combination of the pacing location and VVD. The optimal result of CRT can be determined by the combination that provided the maximum CURE.

2.2.2. Electrical Index. The description of the electrical optimization strategy with E_{RMS} can be found in many published reports. Briefly, it is assumed that the optimal cardiac

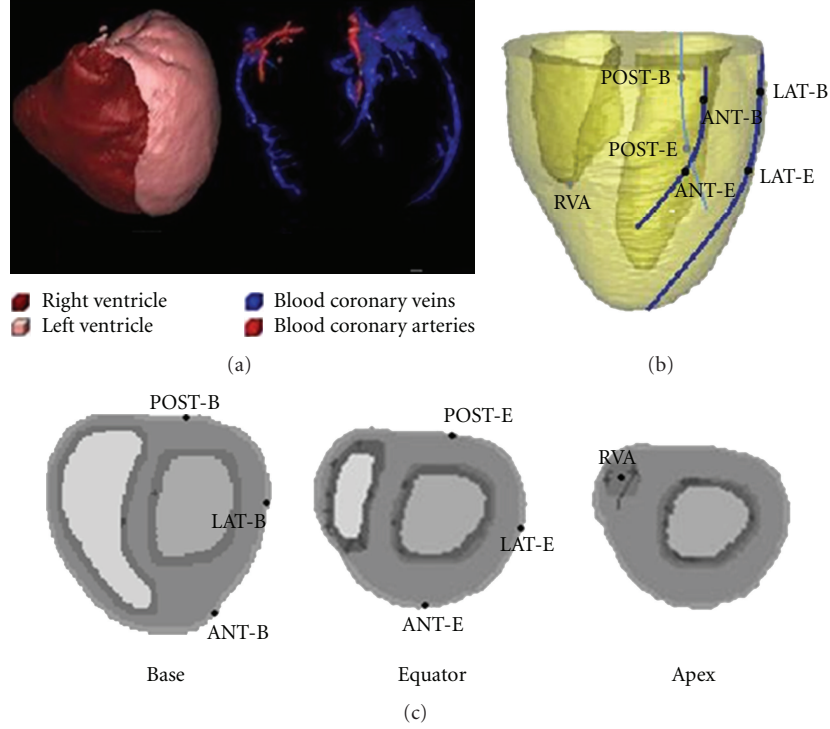


FIGURE 5: A diagram of the electrode positions of pacing leads. (a) Reconstructed LV, RV, blood coronary veins (blue) and blood coronary arteries (red) from USA VHP female dataset. (b) Three-dimensional display of LV and RV pacing lead positions. (c) Display of pacing lead positions on transverse plane.

output is to be achieved through the sinus rhythm and the normal electrophysiological parameters [16]. Therefore, the aim of the pacing therapy is to restore an electrophysiological status as close as possible to the physiological electromechanical coupling. Here, we calculate the root mean square error E_{RMS} between the physiological excitation during the sinus rhythm and pathological excitation as below:

$$E_{RMS} = \sqrt{\frac{1}{N} \sum_{i=1}^N (x_i - e_i)^2}, \quad (10)$$

where N is the whole number of voxel elements, x_i dedicates the activation time of voxel i under the sinus rhythm, and e_i is the activation time of voxel i under the pathological condition. Thus, by minimizing the E_{RMS} , the activation of the heart will be as close as possible to the healthy activation and will provide an optimal combination of the pacing site and timing delay in CRT.

2.3. Objective Function of the Optimization Problem. In order to make a contrast analysis of cardiac function improvement between mechanical (CURE) and electrical (E_{RMS}) optimization strategy for CRT, two objective function are defined as below.

2.3.1. Dyssynchrony Index (DI). Dyssynchrony for the study was usually defined as the difference in the timing of the peak

strain from the earliest to latest segment, as represented by DI, which can be used to describe the contraction synchrony of biventricles. In the clinic research, the radial strain was usually used to substitute for the maximum principal strain. However, they all indicated a thickening of cardiac walls.

2.3.2. Ejection Fraction (EF). The hemodynamic parameter of EF, which is the percentage of blood ejected from the ventricle with each heartbeat, can determine the cardiac function. Since LV is the heart's main pumping chamber, EF is usually measured only in the LV. A measure of the function of LV, also called left ventricular ejection fraction (LVEF), can help determine the cardiac hemodynamics effect. LVEF is defined as

$$LVEF = \frac{(EDV - ESV)}{EDV}, \quad (11)$$

where EDV means LV volume of end-diastole while ESV represents the LV volume of end-systole.

2.4. Pacing Site and VVD

2.4.1. Pacing Site. In this study, BiVP was chosen for CRT simulations. In clinic, doctors often choose the branches of coronary sinus as the LV pacing lead site as shown in Figure 5(a). Here, the anterior, lateral, and posterior branches of the coronary sinus were plotted according to the original anatomical data as shown in Figures 1(c), 1(d). Moreover,

to better contrast the influence of the different LV pacing lead positions to the response of CRT, the optional LV pacing sites were chosen at the base and equator sites of the LV along the branches of the blood coronary veins, as shown in Figure 5(b). The pacing lead positions on the transverse plane are shown in Figure 5(c). The right ventricular apex (RVA) of the endocardium, point RVA (36, 79, 49), was chosen as the position of RV pacing lead. The LV electrodes were placed in the anterior and posterior wall of the LV in addition to the LV free wall (LVFW) as followed, POST-B (77, 98, 89) at the posterior base, POST-E (79, 94, 57) at the posterior equator, LAT-B (114, 62, 89) at the lateral base, LAT-E (108, 53, 57) at the lateral equator, ANT-B (90, 15, 89) at the anterior base, and ANT-E (67, 20, 57) at the anterior equator. Then, pacing was performed for each pair of right and left ventricular pacing positions yielding six electrode setups for the CLBBB model to investigate the influence of the electrode position on the response to CRT.

2.4.2. Pacing Timing Delays. Generally, the activation of the sinus node serves as the reference time for the AV delay. Several studies have pointed out that the VVD should be optimized according to the changes in the AV delay to obtain the maximum hemodynamic benefit [16]. However, because the original canine data did not include the atria, the construction of a whole heart model was infeasible and therefore the AV delay was kept constant in this research. Considering the special features of the canine activation period, we choose -72 ms, -60 ms, -48 ms, -36 ms, -24 ms, -12 ms, 0 ms, 12 ms, 24 ms, 36 ms, 48 ms, 60 ms, and 72 ms as the VVD timings. To contrast with clinic studies, the scope of VVD timings was enlarged to better investigate the influence of VVD on the optimal efficacy of CRT. Positive values indicated that the LV was the first ventricle stimulated and a negative VVD indicated a right-before-left ventricular stimulation. Therefore, there were 78 simulations in whole by multiplying pacing leads numbers and VVD numbers. So, an optimization can be achieved by maximizing the CURE or minimizing the E_{RMS} through adjustment of the pacing location and VVD.

2.5. Numerical Solutions. Simulation of the cardiac excitation anisotropic propagation throughout the ventricular myocardium is computationally very expensive. Thus, high-performance computing techniques should be used. By using an operator-splitting scheme, adaptive time step, and backward differentiation formulation techniques in a parallel implement, we solved the monodomain equations of the cardiac excitation anisotropic propagation successfully [28]. For a combination of the pacing location and VVD, the model of the electrical propagation ran for approximately 10 hours on a Dell computer with four 3.0 GHz Xeon processors running in parallel and with 4 GB of RAM. The computation of the CURE took approximately 190 MB of main memory and 1.5 hours on a Dell computer with a single 3.0 GHz Xeon processor.

3. Results

3.1. The Optimal Result of CRT. The maximal value of CURE was 0.8516, with pacing site at point LAT-E and a VVD of 60 ms (see Figure 6), which could be regarded as the optimal result for CRT. The calculated CURE value of the LBBB model was 0.67. According to clinical reports, cardiac mechanical synchrony was also less in patients with LBBB (CURE in one cardiac cycle: 0.58 ± 0.09) [27]. The value of the maximum CURE significantly increased after BiVP optimization, indicating that CRT could enhance the intrasynchrony of LV for CHF hearts with LBBB.

With the electrical optimization strategy, an optimal pacing location and VVD were also found with a minimal error E_{RMS} of 37.26 ms. The optimal stimulation site was also at point LAT-E, but with a VVD of 0 ms.

To find the potential relationship between CURE and VVD, a diagram of the CURE-VV delay time column map was plotted in Figure 6. It was found that the values of CURE were larger when $VVD \geq 0$ ms, which meant LV was the first stimulated. But for different LV pacing sites, CURE varied disorderly without a continued trend of ascending or descending with the change of VVD. It indicated that there existed a nonlinear relationship between CURE and VVD time. However, with the increasing of VVD, especially when $VVD \geq 48$ ms, CURE varied little and the same thing happened when $VVD \leq -48$ ms. For $VVD \geq 60$ ms, CURE would not rise again. It was obvious that CURE was not the largest with $VVD = 0$ ms that commonly used in the previous VVD setup.

Furthermore, CURE values of LV pacing sites near ventricular equator sites were all larger than those at base for $VVD \geq 12$ ms. However, the CURE of LV pacing location near the lateral wall at equator site, that is, pacing location LAT-E, was always the largest. It can also be found that the CURE values were smaller when the pacing lead was at the anterior wall near base, that is, pacing location ANT-B and ANT-E.

3.2. Optimal Result Contrast of CRT between CURE and E_{RMS} . In order to better contrast with clinical findings, we divided the short-axis LV into four segments, named anterior wall, lateral wall, posterior wall, and septum (Figure 7). Then, the positive maximum principal strain (also called maximum strain) was calculated from the multiple circumferential points averaged to several standard segments near the equator sites (layer 7). Maximum strain was plotted against time under three conditions, including a CHF model with LBBB, a CRT optimization model with maximum CURE and a CRT optimization model with minimum E_{RMS} (Figure 8), and thus predicted their responses to CRT [25]. The maximum strain, $E1$, was used to indicate thickening of the cardiac walls [20]. $E1$ is the maximal eigenvalue of the Green Lagrange strain tensor E with the expression of

$$E = \frac{1}{2(F^T F - I)}, \quad (12)$$

where I represents the identity matrix and the superscript T represents the matrix transpose, and deformation gradient

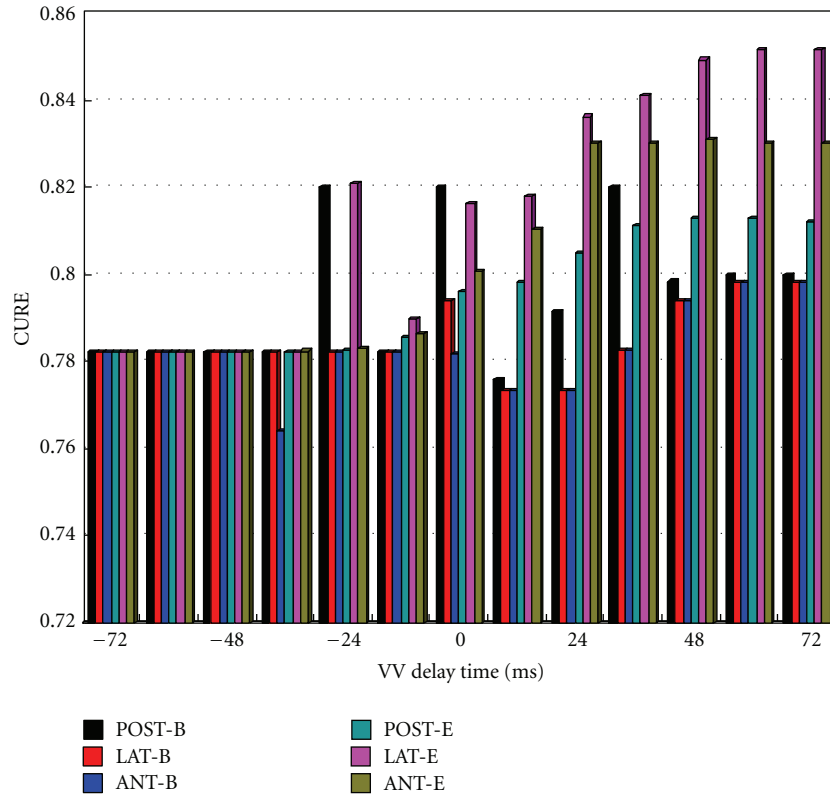


FIGURE 6: A column map of CURE-VV delay time curve.

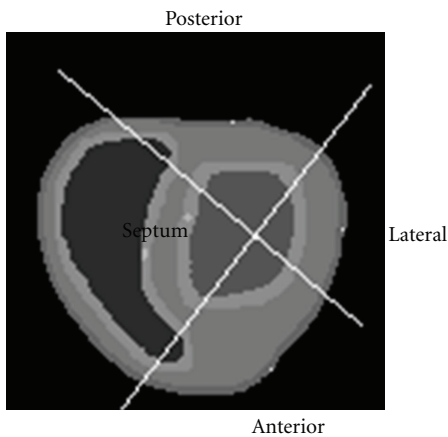


FIGURE 7: Segments division of the short-axis LV, named anterior wall, lateral wall, posterior wall, and septum.

tensor F indicates both the rotation and the deformation around a point.

In the simulation of LBBB, as shown in Figure 8(a), DI equals 60 ms with septum the earliest to the peak strain while lateral and posterior wall the latest to the peak strain. LVEF in the simulation of LBBB is 22%. However, in the simulation of CRT with mechanical optimization strategy (CURE = 0.8516), the time for all four segments (anterior wall, lateral wall, posterior wall, and septum) to peak strain occurs almost simultaneously, as shown in Figure 8(b), and therefore DI

equals 0 ms. LVEF in the simulation of BiVP is 35%, which means an enhancement of LV hemodynamic function after CRT optimization with mechanical strategy.

The “Maximum Strain-Time” curve with the minimum E_{RMS} (37.26 ms) was plotted as the optimal result of CRT from the electrical index (Figure 8(c)). Contrary to the LBBB result, lateral and posterior wall were the earliest to peak strain while septum was the latest to peak strain. The optimal pacing lead was located at the point LAT-E with a VVD of 0 ms. The calculated DI was 30 ms with a LVEF of 30%.

4. Discussions

The clinical findings of CRT have demonstrated that the adjustment of pacing lead position and VVD were very important for an individual to get the best improvement in hemodynamics [29]. However, there still need more quantitative information for determining the optimal VV timing pre- or postoperatively with respect to the lead positions in patients undergoing CRT. Based on a coupled biventricular electromechanical model of the canine with CLBBB, the mechanical and electrical optimization strategies for predicting the effect of CRT were investigated. Unlike previous electrical optimization strategy of CRT (E_{RMS}), we have adopted the mechanical optimization strategy CURE as the synchrony assessment index in the research. As we know, the main function of heart is to pump blood and exchange the metabolites. Therefore, the mechanical

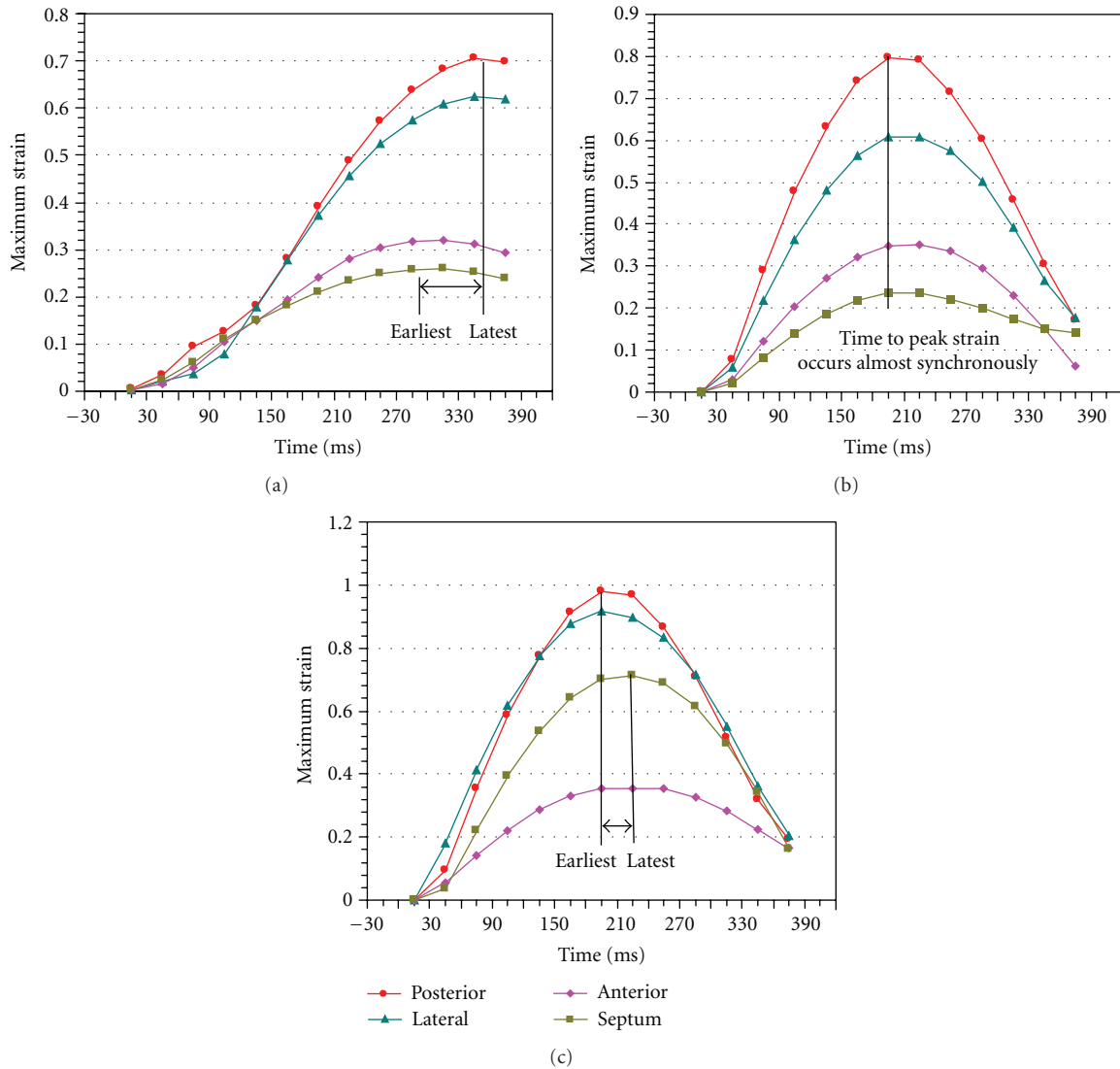


FIGURE 8: An example of maximum principal strain-time curves. (a) a CHF study model with LBBB. (b) a CRT optimization model with maximum CURE. (c) a CRT optimization model with minimum E_{RMS} . The curves are color-coded by the defined myocardial regions as depicted in the figure. An example of dys-synchrony is shown as the difference in the timing of the peak strain from earliest to latest segment (black arrow). (a) shows that DI equals to 60 ms. (b) shows that four segments arrive at the peak-of-strain almost at the same time. (c) shows that DI equals 30 ms.

function of heart and the cardiac hemodynamics were the most basic characteristics and essential criteria for evaluating the cardiac function.

The implantation location of LV pacing lead was proven to be very important for the improvement of the ventricular systolic synchrony [30]. From Figure 6, it indicated that the optimal pacing location was at the LV lateral wall (LVLW) near the equator site (point LAT-E) based on the mechanical index of CURE. It can also be found that a larger CURE could be obtained by placing stimuli at the posterior wall at base (point POST-B) or at the anterior wall near equator sites (point ANT-E). It was suggested by clinicians that the pacing lead should be implanted in the LV posterior or the lateral vein of the coronary sinus during the BiVP in accordance with our simulation results [30]. Thus, the mechanical

synchronous contraction of the myocardium was forced to be better. According to clinical researches [31, 32], the left ventricular posterior wall (LVPW) and LVLW were often the latest activation sites in LBBB patients. In other words, we also validated that the latest activation or mechanical contracting site may be the optimal stimulating site, which was also validated by the mathematical model of Helm et al. [33]. Furthermore, Figure 6 also showed us that a better LV systolic synchrony (LVSS) could be achieved by placing pacing electrodes near the equator sites (points POST-E, LAT-E, and ANT-E) than near the base sites (point POST-B, LAT-B, and ANT-B).

However, with the increasing of VVD, especially for $VVD \geq 48$ ms, CURE varied little and the same thing happened when $VVD \leq -48$ ms. For $VVD \geq 48$ ms, LV was

the first ventricle to be paced. However, when RV was paced, the intrinsic excitation or excitation from LV pacing lead had spread to the RV beforehand. Due to the influence of refractory period, the pacing lead of RV (point RVA) would not play a role. Therefore, CURE values make no variations when VVD was larger than a certain value.

From Figure 6, it showed us that all maximal CURE values were larger than 0.8150 when $VVD \geq 0$ ms. We could also find that a larger CURE may be obtained when the VVD equals 0 ms, especially for those with the LV pacing leads located at the equator sites. It has been observed by clinicians that a larger CURE might be obtained when the LV was first stimulated ($VVD \geq 0$ ms) and about 28.4% of patients might get optimum hemodynamics when a VVD of 0 ms was offered [34]. Under pathological conditions of LBBB, normal rhythm was broken up and depolarization spread more slowly and less uniformly. Due to the spoiled excitation propagation, there was a profound abnormality of contraction sequences of both ventricles, which affected ventricular contractile activity and decreased the heart function. During simulation of LBBB (Figure 2), electrical and mechanical delay was evident in the LVFW segments, which suggested a severe interventricular dyssynchrony [20]. Therefore, LV needs to be paced first to get a coordinate contraction of whole heart during CRT. Before the invention of the second-generation dual-chamber pacemaker, the initial factory setting for the VVD was 0 ms. However, it could be found from our simulation results that the optimal VVD was not 0 ms but 60 ms, based on the mechanical strategy of predicting the response of CRT. Therefore, it will still be necessary for the optimization of VVD.

To further observe the enhancement of LV synchronization after CRT optimization and to contrast the optimal result between mechanical (CURE) and electrical (E_{RMS}) strategy, Maximum Strain-Time curves were plotted in Figure 8. In the simulation of LBBB (see Figure 8(a)), the time to peak strain of all the ventricular segments had various degrees of delays in accordance with the clinic phenomenon [30], with a DI of 60 ms and a LVEF of 22%. Nevertheless, the optimal results with the CURE indicated that LV had a better synchrony (DI = 0 ms, meaning that all the LV segments contract almost simultaneously, as shown in Figure 8(b)) and a higher LVEF (35%), whereas the optimal result of CRT from the electrical criterion (E_{RMS}) had a worse synchrony (DI = 30 ms, meaning that the LV still has some dys-synchrony, as shown in Figure 8(c)) and a lower LVEF (30%). The results proved that mechanical index (CURE) used in this model was superior to the electrical index (E_{RMS}) for the optimal parameters of CRT. It also confirmed the fact that the CURE could better reflect the LV synchrony and hemodynamic result, although biventricles may not obtain the best electrical synchrony [25]. It has been proven by doctors that systolic improvement and mechanical resynchronization does not require electrical synchrony in the dilated failing heart with LBBB [15]. Mechanical coordination plays the dominant role in the global systolic improvement with the BiVP approach. Besides, it may be easier for us to optimize the parameters of CRT using a mechanical criterion with clinic image methods, such as

MRI, intracardiac ultrasound, and so on. Several studies have suggested that the measures of mechanical dys-synchrony by cardiac imaging were superior markers of the response to CRT, compared with the ECG QRS duration [25, 27, 33, 35]. In the practice of CRT optimization, clinicians often use the TDI to trace “tissue velocity-time” with the septal-to-lateral delay of the maximum velocity defined as the LV dyssynchrony, or use echocardiograph techniques to trace “radial strain-time” curves with earliest to latest delay of peak strain defined as the LV dyssynchrony. The VVD that could produce the smallest septal-to-lateral delay and the maximum cardiac output (CO) would be selected as the optimal VVD of CRT, similar to our validation methods [25]. However, note that in this research, improved mechanical coordination and pump function may be observed in the optimal results (DI = 60 ms, LVEF = 22%) with both the CURE and E_{RMS} as optimization strategy for CRT. The thickening of the cardiac walls also improved after CRT with the peak maximum principle strain (PMPS) increased from 0.70 in the LBBB model to 0.77 in CRT optimization model based on the CURE strategy as shown in Figure 8(c). However, the PMPS in CRT optimization model based on the E_{RMS} strategy was larger, with a value of 0.98 as shown in Figure 8(c), indicating a better local myocardium contraction function.

Previous electrical optimization procedures were based on the electrical isochrones, that is, the electrical activation of the cells, which did not necessarily equal the electromechanical coupling, that is, the phenomenon of the delayed electrical uncoupling. Assuming that the mechanical activation followed the electrical activation with a fixed delay, the results with the electrical optimization strategy of CRT might be valid, because the timing offset would be added to all cardiac cells. So long as the delay between the electrical and the mechanical activation per cell varied, the electrical optimization strategy of CRT might be not accurate, because of the pathological prolongation of the mechanical activation influenced by the delayed electrical uncoupling. Damage to the myocardium intercalated disks was another phenomenon of electromechanical dissociation. Because the conduction of the electrical excitation was accomplished by the intercellular “gap junctional communication”, the path of the connection could be closed partly or completely when there was a very low blood calcium level or acidosis causing conduction disturbance in the damaged regions. For a heart with an electromechanical dissociation, the adjustment of the pacing location or VVD might produce profitable results, but the optimization of the pacing site and VVD of CRT with the electrical optimization strategy might be given a great discount [18].

Briefly, the electrical and mechanical activations were not completely equal to each other. However, with the mechanical criterion (CURE or other hemodynamical index) to optimize the parameters of CRT, the problem could be solved. Alternatively, an improved mechanical coordination and function may be inducible in the LBBB-CHF hearts without generating electrical synchrony. The difference of optimal delays and pacing sites was due to the difference of heart geometry, electrical and mechanical properties, and also the

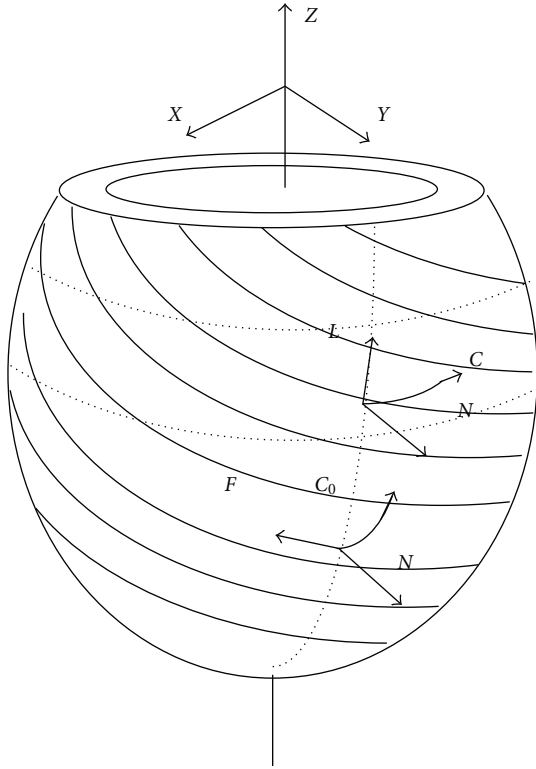


FIGURE 9: Cardiac walls coordinate systems.

time regional differences in the time between electrical excitation and mechanical contraction at one part of the model versus another part. Therefore, clinicians would not always choose the lateral wall for the pacing locations. With the help of a patient-specific computation heart model, quantitative information will be obtained to enhance our understanding of cardiac dyssynchrony and decrease the blindness of CRT.

4.1. Limitations. In this study, however, there are still some defects in our optimization model of CRT. Because of the lack of the atria data, the construction of a whole heart model was not feasible and consequently, the adjustment of the AV delay has not been considered. Furthermore, the hemodynamics parameters should be taken into account in future modeling, such as the cardiac output and the dP_{\max}/dt (maximum value for the first derivative of the LV pressure (peak dP/dt)) that were usually used as the optimal parameters of CRT in clinic [25, 36]. In addition, the heavy computation load might limit the clinical applications of the computation model. Another major limitation of this study is the use of a standard heart model. However, in clinical practice, there are numerous variations, for example, various geometry of the heart, various electrical properties of the heart (conduction velocities, conduction blocks, infarct zones, etc.), various mechanical properties of the heart, various autonomic tones, and so on. Therefore, the results of the single simulation study cannot be extrapolated to clinical patients now.

5. Conclusion

By using a coupled biventricular electromechanical models of the canine heart, the optimization of the electrode positions and VV delay timings for CRT with the BiVP have been investigated, with both the mechanical criterion of CURE and electrical criterion of E_{RMS} . We also demonstrated that the mechanical dyssynchrony measure was able to predicts well the effect of CRT, better than the electrical dyssynchrony measure.

In comparison with other computational optimization models of CRT, the mechanical contraction and deformation was included in our model, and the mechanical index CURE was calculated. The results indicated that the LV pacing lead positioning was a very important factor that affecting the consequence of CRT and the hemodynamic changes. Also, the changes of VVD will lead to a variation in the mechanical synchrony and should be considered in the optimization of CRT. Therefore, it was very important for an individual to adjust the electrode position as well as the timing delays to the patient's anatomy and pathology, in accordance with current clinical studies [34, 37, 38]. In addition, we can conclude from simulation results that the site of the latest mechanical activation may be the optimal left ventricular lead position for the current LBBB-HF model, but it may be limited by the anatomy of the coronary vein. Compared with the electrical optimization strategy, the simulation results showed that the LV synchronous contraction and hemodynamics could be improved more with the mechanical optimization strategy for predicting the effect of CRT. Mechanical dyssynchrony, rather than the electrical dispersion, seems to be the more relevant. Therefore, mechanical dyssynchrony is a potential better means for predicting the response to CRT. However, it does point out that, to apply this modeling approach in clinical practice, patient-specific electromechanical heart model must be established [39].

Appendices

A. Calculation of the Transformation Matrix between the Fiber Coordinate and Global Coordinate

Since fiber orientations vary for different sublayers in an isoparametric element of hexahedron, the transformation between the fiber coordinate and the global coordinate is needed. As shown in Figure 9, we first need to transfer the fiber-coordinate system ($N-C_0-F$, one axis is chosen to coincide with the local muscle fiber direction F , and another one is determined by the epicardium surface normal vector N) to the new surface-coordinate system ($N-C-L$, one axis is chosen to coincide with the epicardium surface normal vector N , and another one is determined by the epicardium circumferential or tangential vector C), with the transformation matrix T_1 determined by the fiber direction angle of a single sublayer; then transfer the surface-coordinate system ($N-C-L$) to the global coordinate system

(X - Y - Z), with the transformation matrix T_2 determined by the direction cosines between two coordinate systems.

Finally, the transformation matrix T between the fiber coordinate and the global coordinate is as follows:

$$T = T_2 T_1. \quad (\text{A.1})$$

B. Calculation of Zero and First-Order Power Terms

The codes for calculating zero and first-order power terms of layer 6 at a given time in Matlab7.0.1 are as follows:

$$\begin{aligned} y &= \text{Sheet6}(1,:); \\ FY &= \text{fft}(y); \\ \text{mag} &= \text{sqrt}(FY * \text{conj}(FY)); \\ \text{s02_6} &= \text{mag}(1); \\ \text{s12_6} &= \text{mag}(2); \end{aligned} \quad (\text{B.1})$$

where $\text{Sheet6}(1,:)$ are the circumferential strains (ϵ_{cc}) over the entire LV-midwall at 30 circumferentially distributed locations in layer 6.

From above, we can get the zero power term (s02_6) and first-order power term (s12_6) of layer 6 at a given time. Then the zero and first-order power terms of layer 7 to 9 during the cycle can be obtained in the same way.

Acknowledgments

This project is supported by the National Natural Science Foundation of China (81171421, 31100671, 61101046), Guangzhou Zhujiang Scientific and Technological New Star Capitals (2011J2200001), and the Program for New Century Excellent Talents in University (NCET-04-0550). The authors would like to thank Prof. Edward W. Hsu, Department of Bioengineering, Duke University, for providing the dataset and technical discussions.

References

- [1] S. Garrigue, P. Bordachar, S. Reuter, P. Jaïs, M. Haïssaguerre, and J. Clementy, "Comparison of permanent left ventricular and biventricular pacing in patients with heart failure and chronic atrial fibrillation: a prospective hemodynamic study," *Cardiac Electrophysiology Review*, vol. 7, no. 4, pp. 315–324, 2003.
- [2] F. A. McAlister, J. A. Ezekowitz, N. Wiebe et al., "Systematic review: cardiac resynchronization in patients with symptomatic heart failure," *Annals of Internal Medicine*, vol. 141, no. 5, pp. 381–390, 2004.
- [3] J. Kron, J. M. Aranda Jr., W. M. Miles et al., "Benefit of cardiac resynchronization in elderly patients: results from the Multicenter InSync Randomized Clinical Evaluation (MIRACLE) and Multicenter InSync ICD Randomized Clinical Evaluation (MIRACLE-ICD) trials," *Journal of Interventional Cardiac Electrophysiology*, vol. 25, no. 2, pp. 91–96, 2009.
- [4] M. G. St John Sutton, T. Plappert, K. E. Hilpisch, W. T. Abraham, D. L. Hayes, and E. Chinchoy, "Sustained reverse left ventricular structural remodeling with cardiac resynchronization at one year is a function of etiology: quantitative Doppler echocardiographic evidence from the Multicenter InSync Randomized Clinical Evaluation (MIRACLE)," *Circulation*, vol. 113, no. 2, pp. 266–272, 2006.
- [5] P. F. Bakker, H. W. Meijburg, J. W. de Vries et al., "Biventricular pacing in end-stage heart failure improves functional capacity and left ventricular function," *Journal of Interventional Cardiac Electrophysiology*, vol. 4, no. 2, pp. 395–404, 2000.
- [6] G. S. Nelson, R. D. Berger, B. J. Fetters et al., "Left ventricular or biventricular pacing improves cardiac function at diminished energy cost in patients with dilated cardiomyopathy and left bundle-branch block," *Circulation*, vol. 102, no. 25, pp. 3053–3059, 2000.
- [7] N. A. Marsan, M. M. Henneman, J. Chen et al., "Left ventricular dyssynchrony assessed by two three-dimensional imaging modalities: phase analysis of gated myocardial perfusion SPECT and tri-plane tissue Doppler imaging," *European Journal of Nuclear Medicine and Molecular Imaging*, vol. 35, no. 1, pp. 166–173, 2008.
- [8] D. H. Birnie and A. S. L. Tang, "The problem of non-response to cardiac resynchronization therapy," *Current Opinion in Cardiology*, vol. 21, no. 1, pp. 20–26, 2006.
- [9] D. A. Kass, "Ventricular resynchronization: pathophysiology and identification of responders," *Reviews in Cardiovascular Medicine*, vol. 4, supplement, no. 2, pp. S3–S13, 2003.
- [10] M. E. Spotnitz, M. E. Richmond, T. A. Quinn et al., "Relation of QRS shortening to cardiac output during temporary resynchronization therapy after cardiac surgery," *ASAIO Journal*, vol. 56, no. 5, pp. 434–440, 2010.
- [11] R. C. Jones, T. Svinarich, A. Rubin et al., "Optimal atrioventricular delay in CRT patients can be approximated using surface electrocardiography and device electrograms," *Journal of Cardiovascular Electrophysiology*, vol. 21, no. 11, pp. 1226–1232, 2010.
- [12] C. M. Yu, E. Chau, J. E. Sanderson et al., "Tissue Doppler echocardiographic evidence of reverse remodeling and improved synchronicity by simultaneously delaying regional contraction after biventricular pacing therapy in heart failure," *Circulation*, vol. 105, no. 4, pp. 438–445, 2002.
- [13] Y. Mishiro, T. Oki, H. Yamada, T. Wakatsuki, and S. Ito, "Evaluation of left ventricular contraction abnormalities in patients with dilated cardiomyopathy with the use of pulsed tissue doppler imaging," *Journal of the American Society of Echocardiography*, vol. 12, no. 11, pp. 913–920, 1999.
- [14] F. Leclercq, F. X. Hager, J. C. Macia, C. J. Mariottini, J. L. Pasquié, and R. Grolleau, "Left ventricular lead insertion using a modified transseptal catheterization technique: a totally endocardial approach for permanent biventricular pacing in end-stage heart failure," *Pacing and Clinical Electrophysiology*, vol. 22, no. 11, pp. 1570–1575, 1999.
- [15] C. Leclercq, O. Faris, R. Tunin et al., "Systolic improvement and mechanical resynchronization does not require electrical synchrony in the dilated failing heart with left bundle-branch block," *Circulation*, vol. 106, no. 14, pp. 1760–1763, 2002.
- [16] M. Reumann, D. Farina, R. Miri, S. Lurz, B. Osswald, and O. Dössel, "Computer model for the optimization of AV and VV delay in cardiac resynchronization therapy," *Medical and Biological Engineering and Computing*, vol. 45, no. 9, pp. 845–854, 2007.
- [17] "Use of body-surface potential mapping and computer model simulations for optimal programming cardiac resynchronization therapy devices," in *Computers in Cardiology*,

- R. Mohindra, J. L. Sapp, J. C. Clements, and B. M. Horáček, Eds., Durham, NC, USA, 2007.
- [18] G. Lecoq, C. Leclercq, E. Leray et al., “Clinical and electrocardiographic predictors of a positive response to cardiac resynchronization therapy in advanced heart failure,” *European Heart Journal*, vol. 26, no. 11, pp. 1094–1100, 2005.
- [19] D. D. Spragg, C. Leclercq, M. Loghmani et al., “Regional alterations in protein expression in the dyssynchronous failing heart,” *Circulation*, vol. 108, no. 8, pp. 929–932, 2003.
- [20] J. Dou, L. Xia, Y. Zhang et al., “Mechanical analysis of congestive heart failure caused by bundle branch block based on an electromechanical canine heart model,” *Physics in Medicine and Biology*, vol. 54, no. 2, pp. 353–371, 2009.
- [21] R. L. Winslow, J. Rice, S. Jafri, E. Marban, and B. O’Rourke, “Mechanisms of altered excitation-contraction coupling in canine tachycardia-induced heart failure, II: model studies,” *Circulation Research*, vol. 84, pp. 571–586, 1999.
- [22] R. C. P. Kerckhoffs, O. P. Faris, P. H. M. Bovendeerd et al., “Electromechanics of paced left ventricle simulated by straightforward mathematical model: comparison with experiments,” *American Journal of Physiology*, vol. 289, no. 5, pp. H1889–H1897, 2005.
- [23] R. C. P. Kerckhoffs, M. L. Neal, Q. Gu, J. B. Bassingthwaite, J. H. Omens, and A. D. McCulloch, “Coupling of a 3D finite element model of cardiac ventricular mechanics to lumped systems models of the systemic and pulmonary circulation,” *Annals of Biomedical Engineering*, vol. 35, no. 1, pp. 1–18, 2007.
- [24] R. C. P. Kerckhoffs, P. H. M. Bovendeerd, F. W. Prinzen, K. Smits, and T. Arts, “Intra- and interventricular asynchrony of electromechanics in the ventricularly paced heart,” *Journal of Engineering Mathematics*, vol. 47, no. 3–4, pp. 201–216, 2003.
- [25] M. S. Suffoletto, K. Dohi, M. Cannesson, S. Saba, and J. Gorcsan III, “Novel speckle-tracking radial strain from routine black-and-white echocardiographic images to quantify dyssynchrony and predict response to cardiac resynchronization therapy,” *Circulation*, vol. 113, no. 7, pp. 960–968, 2006.
- [26] K. C. Bilchick, V. Dimaano, K. C. Wu et al., “Cardiac magnetic resonance assessment of dyssynchrony and myocardial scar predicts function class improvement following cardiac resynchronization therapy,” *Cardiovascular Imaging*, vol. 1, no. 5, pp. 561–568, 2008.
- [27] M. J. Byrne, R. H. Helm, S. Daya et al., “Diminished left ventricular dyssynchrony and impact of resynchronization in failing hearts with right versus left bundle branch block,” *Journal of the American College of Cardiology*, vol. 50, no. 15, pp. 1484–1490, 2007.
- [28] Y. Zhang, L. Xia, Y. Gong, L. Chen, G. Hou, and M. Tang, “Parallel solution in simulation of cardiac excitation anisotropic propagation,” in *Proceedings of the 4th International Conference on Functional Imaging and Modeling of the Heart (FIMH ’07)*, pp. 170–179, June 2007.
- [29] Z. I. Whinnett, J. E. R. Davies, K. Willson et al., “Determination of optimal atrioventricular delay for cardiac resynchronization therapy using acute non-invasive blood pressure,” *Europace*, vol. 8, no. 5, pp. 358–366, 2006.
- [30] A. Rossillo, A. Verma, E. B. Saad et al., “Impact of coronary sinus lead position on biventricular pacing: mortality and echocardiographic evaluation during long-term follow-up,” *Journal of Cardiovascular Electrophysiology*, vol. 15, no. 10, pp. 1120–1125, 2004.
- [31] P. Peichl, J. Kautzner, R. Čihák, and J. Bytešník, “The spectrum of inter- and intraventricular conduction abnormalities in patients eligible for cardiac resynchronization therapy,” *Pacing and Clinical Electrophysiology*, vol. 27, no. 8, pp. 1105–1112, 2004.
- [32] L. M. Rodriguez, C. Timmermans, A. Nabar, G. Beatty, and H. J. J. Wellens, “Variable patterns of septal activation in patients with left bundle branch block and heart failure,” *Journal of Cardiovascular Electrophysiology*, vol. 14, no. 2, pp. 135–141, 2003.
- [33] R. H. Helm, M. Byrne, P. A. Helm et al., “Three-dimensional mapping of optimal left ventricular pacing site for cardiac resynchronization,” *Circulation*, vol. 115, no. 8, pp. 953–961, 2007.
- [34] G. Boriani, C. P. Müller, K. H. Seidl et al., “Randomized comparison of simultaneous biventricular stimulation versus optimized interventricular delay in cardiac resynchronization therapy. The Resynchronization for the Hemodynamic Treatment for Heart Failure Management II implantable cardioverter defibrillator (RHYTHM II ICD) study,” *American Heart Journal*, vol. 151, no. 5, pp. 1050–1058, 2006.
- [35] H. Kanzaki, R. Bazaz, D. Schwartzman, K. Dohi, L. E. Sade, and J. Gorcsan III, “A mechanism for immediate reduction in mitral regurgitation after cardiac resynchronization therapy: insights from mechanical activation strain mapping,” *Journal of the American College of Cardiology*, vol. 44, no. 8, pp. 1619–1625, 2004.
- [36] G. Ansalone, P. Giannantoni, R. Ricci, P. Trambaiolo, F. Fedele, and M. Santini, “Doppler myocardial imaging to evaluate the effectiveness of pacing sites in patients receiving biventricular pacing,” *Journal of the American College of Cardiology*, vol. 39, no. 3, pp. 489–499, 2002.
- [37] M. Bertini, M. Ziacchi, M. Biffi et al., “Interventricular delay interval optimization in cardiac resynchronization therapy guided by echocardiography versus guided by electrocardiographic QRS interval width,” *American Journal of Cardiology*, vol. 102, no. 10, pp. 1373–1377, 2008.
- [38] B. Vidal, D. Tamborero, L. Mont et al., “Electrocardiographic optimization of interventricular delay in cardiac resynchronization therapy: a simple method to optimize the device,” *Journal of Cardiovascular Electrophysiology*, vol. 18, no. 12, pp. 1252–1257, 2007.
- [39] C. A. Taylor and C. A. Figueroa, “Patient-specific modeling of cardiovascular mechanics,” *Annual Review of Biomedical Engineering*, vol. 11, pp. 109–134, 2009.

Research Article

Fast Parameters Estimation in Medication Efficacy Assessment Model for Heart Failure Treatment

Yinzi Ren,¹ Xiao Fu,¹ Qing Pan,¹ Chengyu Lin,¹ Guiqiu Yang,¹ Li Li,² Shijin Gong,² Guolong Cai,² Jing Yan,² and Gangmin Ning¹

¹Department of Biomedical Engineering, Zhejiang University, Hangzhou 310027, China

²Department of Intensive Care Unit, Zhejiang Hospital, Hangzhou 310013, China

Correspondence should be addressed to Jing Yan, yanjingicu@163.com and Gangmin Ning, ninggm@mail.bme.zju.edu.cn

Received 22 June 2012; Accepted 30 August 2012

Academic Editor: Xuesong Ye

Copyright © 2012 Yinzi Ren et al. This is an open access article distributed under the Creative Commons Attribution License, which permits unrestricted use, distribution, and reproduction in any medium, provided the original work is properly cited.

Introduction. Heart failure (HF) is a common and potentially fatal condition. Cardiovascular research has focused on medical therapy for HF. Theoretical modelling could enable simulation and evaluation of the effectiveness of medications. Furthermore, the models could also help predict patients' cardiac response to the treatment which will be valuable for clinical decision-making. **Methods.** This study presents a fast parameters estimation algorithm for constructing a cardiovascular model for medicine evaluation. The outcome of HF treatment is assessed by hemodynamic parameters and a comprehensive index furnished by the model. Angiotensin-converting enzyme inhibitors (ACEIs) were used as a model drug in this study. **Results.** Our simulation results showed different treatment responses to enalapril and lisinopril, which are both ACEI drugs. A dose-effect was also observed in the model simulation. **Conclusions.** Our results agreed well with the findings from clinical trials and previous literature, suggesting the validity of the model.

1. Introduction

Heart failure (HF) is a serious stage of various heart diseases. High incidence and mortality have made it a significant public health problem around the world [1]. Half of the HF patients die within 4 years, and over half of the patients with severe HF die within 1 year [2]. In the United States, HF is the most common age-related disease, and more medical costs are spent on the diagnosis and treatment of HF than any other diseases [3].

Clinical guidelines, technological developments, and pharmacological interventions have intended to diminish the severity of the disease [4]. With the development in medical science, various hemodynamic parameters have been reported to be vital in HF, such as systolic blood pressure (SBP), diastolic blood pressure (DBP), vascular resistance (R), and vascular compliance (C). Among them, blood pressure is the most accessible parameter that effectively reflects the overall hemodynamic status. The Framingham Heart Study [5], which was done on 894 men and 1146 women, revealed that the increase of blood pressure is the major risk

factor of HF. The study by Gheorghide et al. identified SBP as an independent predictor of morbidity and mortality in HF [6].

In clinical practice, pharmacological therapy is the main medical treatment for HF. Angiotensin-converting enzyme inhibitors (ACEIs), beta-blockade, and diuretics improve survival in HF patients. However, an optimal therapy dose for a specific individual is hard to determine. Conventionally, large-scale clinical trials are conducted to assess drug efficacy. However, they usually result in a general guide for the whole population, rather than for individuals. In addition, clinical trials involve high costs and long-term efforts. Therefore, modeling and evaluating drug efficacy by mathematical methods have attracted increasing attention.

Such methods are principally based on mathematical models that mimic the behavior of the hemodynamic parameters under medication in the cardiovascular system. Diaz-Insua et al. simulated blood pressure waves by bond graph methods [7]. Ursino and Magosso established a cardiovascular model with arterial baroreceptor, and using that model, the regulation mechanism of acute hemorrhage

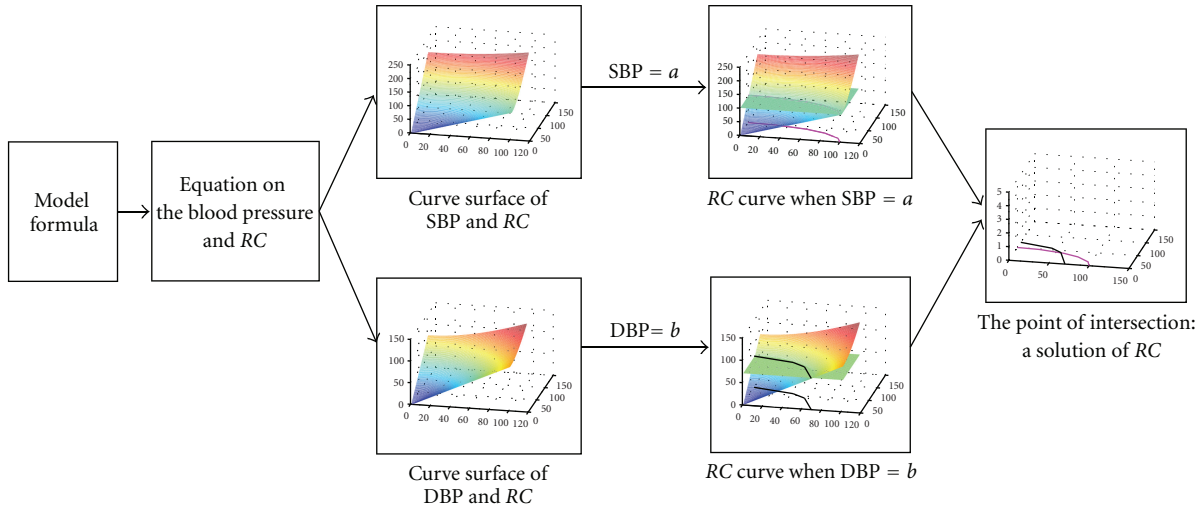


FIGURE 1: The flow-chart of fast parameters estimation algorithm. The flow-chart shows the process from model formula to the solution of RC. The inputs of the process are complex equations and setting conditions. The outputs are the fast estimates of RC parameters.

was simulated [8]. Most cardiovascular models are based on the Windkessel model, constructed by vascular resistance and compliance elements. The resistance and compliance are the primary indicators of the properties of blood vessel, with significant influence on cardiovascular function. Zelis et al. showed that HF may directly increase systemic vascular resistance by altering the mechanical properties and reducing the vasodilation ability of the resistance vessels [9]. Mitchell et al. stated that vessel compliance played a role in the pathophysiology of HF [10]. They explained that the neurohumoral activation increased vascular smooth muscle mass and fibrosis, resulting in decrease of compliance. Under a certain setting of R and C , the models enabled a simulation of vital physiological parameters, such as SBP and DBP. Tsuruta et al. simulated the HF state and predicted the drug efficacy by setting and adjusting the model parameters [11]. In our study, HF is simulated by raising vascular resistance and reducing vascular capacitance to decrease ventricular contractility and increase diastolic stiffness. The response to medicine therapy is emulated by changing resistance and capacitance parameters simultaneously, which are acquired by solving the model inversely from the measured hemodynamic states. Measurable physiological parameters are used to estimate unknown model parameters and derive the changes of model parameters with respect to doses of a particular drug. Consequently, a specific simulation model for individual patient is achieved to predict the medication effect under different doses. These models make the simulation of optimum dose for individual treatment possible. They also provide virtual cases for clinical experiments, facilitate the investigation of cardiovascular functional mechanism, and give us useful information on medical treatment as well as interpretation.

In order to make the simulated physiological parameters match the real ones, the values of RC model parameters must be adjusted by successive approximation. As a consequence, these cardiovascular simulations have a common problem of

large computational time in model parameters estimation. In our previous work [12], a mathematical model consisting of 54 mathematical equations is employed to describe the interaction among the whole body cardiovascular circulation. The work indicates that the estimation of model parameters is the time “bottleneck” of the whole simulation process. In the model, RC values are reiteratively adjusted to minimize the difference between the simulated hemodynamic parameters (e.g., blood pressure) and the true values, until it lies in an acceptable range. Generally, a single simulation costs 20–30 minutes and it may take 2–5 hours to achieve the appropriate RC values. Drug efficacy evaluation and parameters estimation consume 80% of the overall time. For both research and clinical applications, the low efficiency in model parameters estimation needs to be resolved.

The present study aims to address the bottleneck issue of parameter estimation in cardiovascular modeling by developing fast parameters estimation algorithm for pharmacodynamic simulations in predicting HF treatment and individual patient response.

2. Methods

In this section, the fast parameter estimation algorithm and pharmacodynamic simulation model are introduced in detail. ACEI is selected in the present study because it is recommended as the first-line therapy in HF patients [1], producing more hemodynamic and symptomatic benefits for the patients than other conventional medicine. The target of ACEI is the resistance and compliance of the vessels, so the effect of such drug can be simulated by adjusting R and C in a Windkessel model.

2.1. Fast Parameter Estimation Algorithm for Cardiovascular Model. In the cardiovascular system model, the model parameters are estimated from physiological parameters

directly measured from medical examination. Conventionally, one has to repetitively adjust the model parameters to make the simulated physiological parameters approximate the real ones. Essentially, iteration is a method of enumeration, which consumes a great amount of time and reduces the computation efficiency.

As illustrated in Figure 1, the study proposes a novel method to fastly estimate model parameters by constructing a mapping surface of model parameters and physiological parameters. By inputting a set of measured physiological data, the corresponding model parameters can be estimated quickly on the mapping surface. This fast algorithm cannot only overcome the shortcomings of computational complexity but also make the estimation of model parameters more accurate and reliable. In this study, the inputting data are SBP and DBP, and the outputs are the estimates of vascular resistance and vascular compliance.

The details of the method are described as follows.

The cardiovascular model in this study is constructed by bond graph technique, which uses several components to represent real blood vessel. The "0" crunode indicates the elastic chamber of artery blood vessel and the "1" crunode indicates the artery blood vessel with resistance. The bond graph structure of a vessel segment is shown in Figure 2 and a full description of the model can be found in the literature [12].

The equations corresponding to vascular bond graph are given in [13] as follows:

$$\begin{aligned}\frac{dV_i}{dt} &= Q_{i-1} - Q_i, \\ \frac{d\lambda_i}{dt} &= P_i - P_{i+1} - R_i \cdot Q_i, \\ Q_i &= \frac{\lambda_i}{I_i}, \\ P_i &= \frac{V_i}{C_i},\end{aligned}\quad (1)$$

where P , Q , λ , V , R , C , and I represent blood pressure, blood flow, pressure momentum, vascular volume, vascular resistance, vascular compliance, and blood inertia, respectively. These four equations can be combined into a second-order differential equation, as in (2):

$$I_i C_i \frac{d^2 P_i}{dt^2} + R_i C_i \frac{dP_i}{dt} + P_i = I_i \frac{dQ_{i-1}}{dt} + R_i Q_{i-1} + P_{i+1}. \quad (2)$$

Blood flow Q_{i-1} is approximated by a sinusoidal function. Assume the cardiac cycle is 0.8 s, and the systolic period is 0.3 s, the input blood flow wave of the model is defined in (3):

$$Q_{i-1} = \begin{cases} 70 \sin\left(\frac{\pi t}{0.3}\right), & 0 \text{ s} \leq t \leq 0.075 \text{ s}, \\ 70 \sin\left(\frac{\pi}{4}\right) + \frac{70}{12} \sin\left[\frac{2\pi(t - (0.3/4))}{0.3}\right], & 0.075 \text{ s} \leq t \leq 0.225 \text{ s}, \\ 70 \sin\left(\frac{\pi t}{0.3}\right), & 0.225 \text{ s} \leq t \leq 0.3 \text{ s}, \\ 0, & 0.3 \text{ s} \leq t \leq 0.8 \text{ s}. \end{cases} \quad (3)$$

By substituting Q_{i-1} in (2) with the expression of (3), a general solution of the blood pressure in systole period ($t \in [0.075, 0.225]$) is derived as

$$\begin{aligned}P_i &= K_1 \cdot e^{-t(RC - \sqrt{R^2 C^2 - 4CI})/2CI} + K_2 \cdot e^{-t(RC + \sqrt{R^2 C^2 - 4CI})/2CI} \\ &+ \left\{ -2.8\pi \times 10^5 \left(\pi^2 C I^2 - \frac{9I}{400} + \frac{9R^2 C}{400} \right) \cos\left(\frac{20\pi t}{3}\right) \right. \\ &+ 945R \sin\left(\frac{20\pi t}{3}\right) + 5670 + 1.12 \\ &\left. \times 10^7 \left[\pi^4 C^2 I^2 - \frac{9}{200} \left(\frac{-R^2 C}{2} + I \right) C \pi^2 \right] \left(\frac{P_{i+1}}{35} + R\sqrt{2} \right) \right\} \\ &/ [162 + 3.2\pi^4 C^2 I^2 \times 10^5 \\ &+ (-1.44 \times 10^4 C I + 7200 R^2 C^2) \pi^2],\end{aligned}\quad (4)$$

where K_1 and K_2 are coefficients for general solution. According to Luo et al. [13], blood inertia I is set to 0.23 and

the boundary value P_{i+1} is set to 30 mmHg. When $K_1 = 1 \wedge K_2 = 1$, P_i reaches the maximum value at $t = 0.14$ s, so $P_i (t = 0.14 \text{ s})$ is chosen to be the SBP. The expression of $P_i (t = 0.14 \text{ s})$ is also a function of R and C . With reasonable ranges of R and C ($R \in [1.55, 3.60]$, $C \in [0.30, 0.60]$, suggested in Luo et al. [13]), a mapping data surface of SBP and RC is produced, as shown in Figure 3(a).

Blood flow Q_{i-1} in diastolic period ($t \in [0.3, 0.8]$) is 0. Solving (2), a general solution as the expression of blood pressure in diastolic period is derived as

$$\begin{aligned}P_i &= K_3 \cdot e^{-t(RC - \sqrt{R^2 C^2 - 4CI})/2CI} + K_4 \cdot e^{-t(RC + \sqrt{R^2 C^2 - 4CI})/2CI} \\ &+ P_{i+1},\end{aligned}\quad (5)$$

where K_3 and K_4 are coefficients for the general solution. When $K_3 = -200 \wedge K_4 = -400$, the waveform of the function has the maximum value at $t = 0.4$ s, then decreases monotonically till the minimum at $t = 0.8$. Such a waveform is considered to be a classic diastolic pressure wave, so

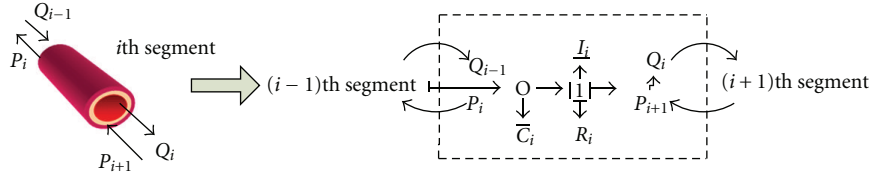


FIGURE 2: The bond graph of i th segment vessel. Bond graph uses several components to represent the real blood vessel. R_i , C_i , and I_i mean vascular resistance, vascular compliance, and blood inertia, respectively. The “0” crunode indicates the elastic chamber of artery blood vessel. The “1” crunode indicates the artery blood vessel with resistance. For the i th segment of blood vessel, the input is the flow Q_{i-1} of the $i - 1$ th vessel segment, which receives the pressure P_i as feedback. The output side transfers the flow Q_i to the $i + 1$ th vessel segment and gets the returned pressure P_{i+1} .

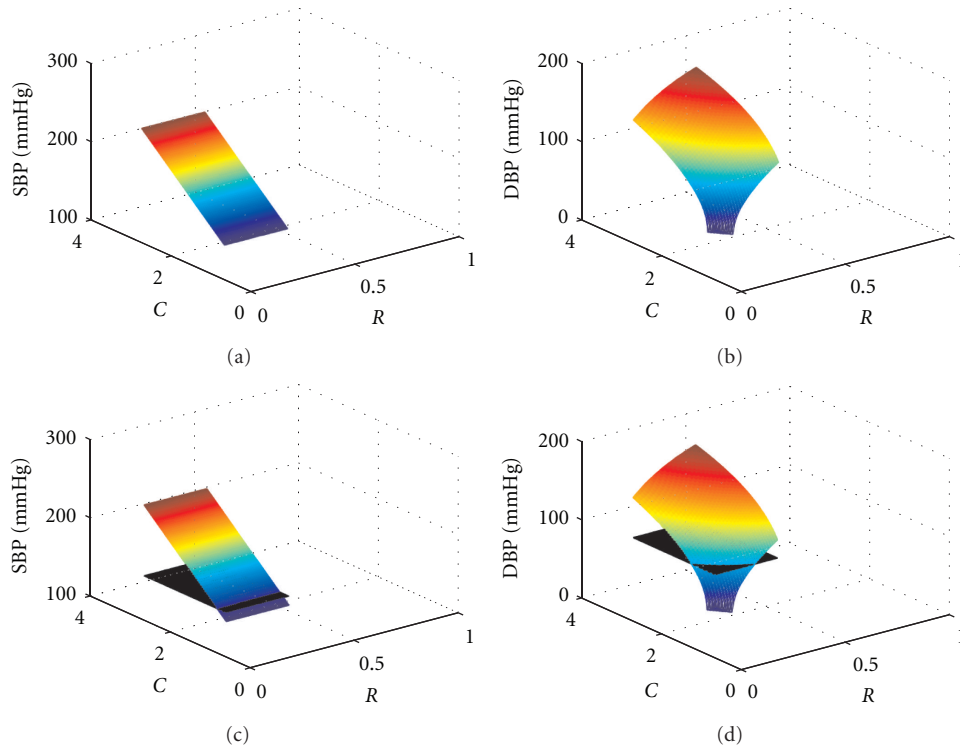


FIGURE 3: ISO surfaces of RC and blood pressure. (a) SBP- RC surface plotting. (b) DBP- RC surface plotting. (c) The plane of SBP = 120 mmHg intersects with SBP- RC surface. (d) The plane of DBP = 70 mmHg intersects with DBP- RC surface.

the specific solution can be regarded as blood pressure in diastolic period and $P(0.8)$ is chosen to be the DBP. The P_i ($t = 0.8$ s) is also a function of R and C . With the same reasonable range of R and C as in systolic period, the mapping data surface of DBP and RC is produced as shown in Figure 3(b).

With SBP and DBP given, the solutions of RC can be directly derived from the data surface. For example, if one’s SBP/DBP is 120/70 mmHg, a plane of $P_i = 120$ mmHg intersects with the SBP- RC surface in Figure 3(a), and an RC curve against SBP is obtained, as shown in Figure 3(c). In a similar manner, an RC curve against DBP is shown in Figure 3(d). When RC versus SBP function and RC versus DBP function are merged to an identical R - C plane, the intersection of them are the R and C values under SBP/DBP = 120/70 mmHg (Figure 4).

2.2. Simulation of HF Treatment Efficacy by ACEI. For simulation of ACEI treatment, two aspects are taken into account: the way ACEI affects hemodynamic state and the assessment of its effect.

It is known that ACEI poses effects mainly on the restoration of vascular property: resistance and compliance [14], so this study focuses on the change in R and C before and after ACEI treatment. By applying the fast parameters estimation algorithm, a unique solution of RC corresponding to HF patients’ blood pressure can be attained. In order to obtain the change of RC under different treatment, we investigate 8 groups of patients with different doses of ACEI. The blood pressure records are from reported trials [15–19], whose baseline characteristics are shown in Table 1.

After the treatment of different doses of ACEI, SBP and DBP are reduced at different levels, leading to a new solution

TABLE 1: The baseline characteristics of 8 groups of HF patients.

Group	Size	Sex		Age in years	Blood pressure		Data source
		Male	Female		SBP (mmHg)	DBP (mmHg)	
1	122	98	24	57	118	78	Nanas et al., 2000 [15]
2	19	8	11	71	136	84	Louis et al., 2009 [16]
3	87	57	30	59	143	95	Bai and Wen, 2009 [17]
4	148	82	64	46	154	93	Hermida et al., 2008 [18]
5	41	38	3	58	158	100	Gomez et al., 1989 [19]
6	41	37	4	56	159	100	Gomez et al., 1989 [19]
7	44	42	2	54	158	102	Gomez et al., 1989 [19]
8	43	37	6	57	161	101	Gomez et al., 1989 [19]

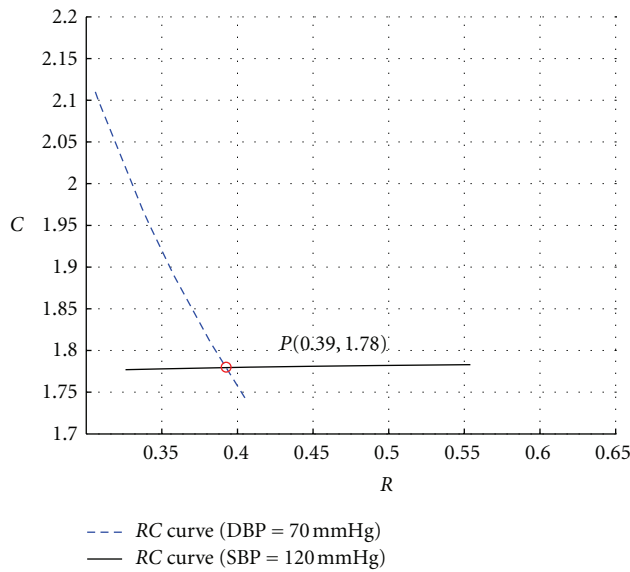


FIGURE 4: Solution of R and C under given SBP and DBP. The solid line is the relationship curve of RC in the case of $SBP = 120$ mmHg and the dotted line is the relationship curve of RC in the case of $DBP = 70$ mmHg. The red point P is the intersection of these two lines, indicating the solution of RC under $SBP = 120$ mmHg and $DBP = 70$ mmHg.

of RC . ΔR and ΔC denote the change percentages of R and C , and the subscripts pre/post denote the parameters before and after treatment:

$$\Delta R = \frac{R_{\text{post}} - R_{\text{pre}}}{R_{\text{pre}}}, \quad (6)$$

$$\Delta C = \frac{C_{\text{post}} - C_{\text{pre}}}{C_{\text{pre}}}. \quad (7)$$

Investigating ΔR and ΔC under different dose treatment helps understand the mechanism of ACEI in altering hemodynamic status. The behavior of vascular resistance and compliance can be depicted by producing a curve of ΔR and ΔC against dose of ACEI. As typical ACEI medicine, enalapril and lisinopril are considered in the study, and the

comparison of their acting manner on R and C leads to better distinguishing diverse mechanisms of ACEI medications.

A cardiovascular system model can then be used to simulate drug efficacy at different doses.

The output parameters of the model are mean arterial pressure (MAP), pulse pressure (PP), heart rate (HR), cardiac output (CO), stroke volume (SV), ejection fraction (EF), stroke work (SW), and so on. These hemodynamic parameters are closely related to cardiac function and are vital for indicating the improvement or deterioration of heart failure. Regarding the outcome of the treatment, a comprehensive index, cardiac integrated index (CII), is produced to assess the hemodynamic state:

$$CII = \sum_{i=1}^7 y_i \times w_i, \quad (8)$$

where y_i is the value of output parameters and w_i is the weighting coefficient of output parameters determined by principal component analysis, as listed in Table 2. Positive weighting coefficient suggests that the smaller the value of the parameter is, the better the cardiac condition will be, so the reduction of CII value is a sign of patient's recovery.

3. Results

By fast parameters estimation algorithm, the dose effect of common ACEIs, enalapril and lisinopril, on R and C is produced. Figure 5 illustrates the change of R and C (ΔR and ΔC in percentage) under different ACEI doses. It is observed that for the lisinopril treatment ΔR and ΔC curves rise sharply and reach the saturation with a dose of 20 mg/d, and both curves run closely. In contrast, ΔR and ΔC under enalapril treatment change gradually but separately at each dose. In addition, for the doses below 40 mg/d, ΔR and ΔC induced by lisinopril are larger than those by enalapril, and the changes of R and C under ACEI treatment tend to be parallel with doses higher than 40 mg/d.

On the basis of ACEI dose and R/C paired data collected from [15–19], the dose-effect relationship curves are fitted. So the variation of R/C under arbitrary ACEI dose is determined. Drug action is simulated by adjusting the RC parameters in the cardiovascular model. Then the output

TABLE 2: The output hemodynamic parameters of the model and weighting coefficients in CII.

Parameter	MAP	PP	HR	CO	SV	EF	SW
Weighting coefficient	0.2333	0.3084	0.0415	-0.3737	-0.3678	-0.3566	0.3266

MAP: mean arterial pressure; PP: pulse pressure; HR: heart rate; CO: cardiac output; SV: stroke volume; EF: ejection fraction; SW: stroke work.

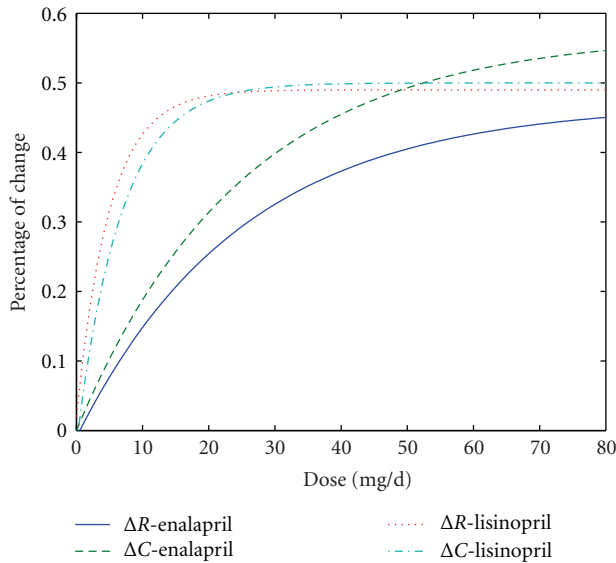


FIGURE 5: The trend curves of ΔR and ΔC under dose-dependent treatment of enalapril and lisinopril. The blue solid line is the trend curve of ΔR under different doses of enalapril; the green dotted line is the trend curve of ΔC under different doses of enalapril; the red dotted line is the trend curve of ΔR under different doses of lisinopril; the blue dotted line is the trend curve of ΔC under different doses of lisinopril.

values of SBP, DBP, MAP, PP, HR, CO, SV, and other parameters can be obtained. Following the process above, specific model is carried out. Just inputting the information of new patient into the model, the hemodynamic parameters can be estimated.

In this study, we applied the model to individual patients [20, 21] and predicted their outcome after medical therapy. The typical results of a subject are shown in Table 3, including the model output and the observed blood pressure in clinical trials. The baselines of hemodynamic parameter and CII before treatment are simulated until the estimated blood pressures are converged to the initial ones, as shown in column 2. The simulation is also done on effects of 20 mg/d of enalapril, and the predicted blood flow condition after drug treatment is shown in column 3. The measured values of SBP and DBP from patients taking 20 mg/d of enalapril are shown in column 4.

It can be seen that the prediction of blood pressure approximates to the situation after treatment in clinical trials [20]. Comparing the hemodynamic parameters and CII of column 2 with those of column 3, we can observe a trend towards better situations. Decrease of blood pressure (SBP, DBP, MAP, and PP) shows the restoration of pressure regulation. The increase of CO, SV, and EF and decrease of

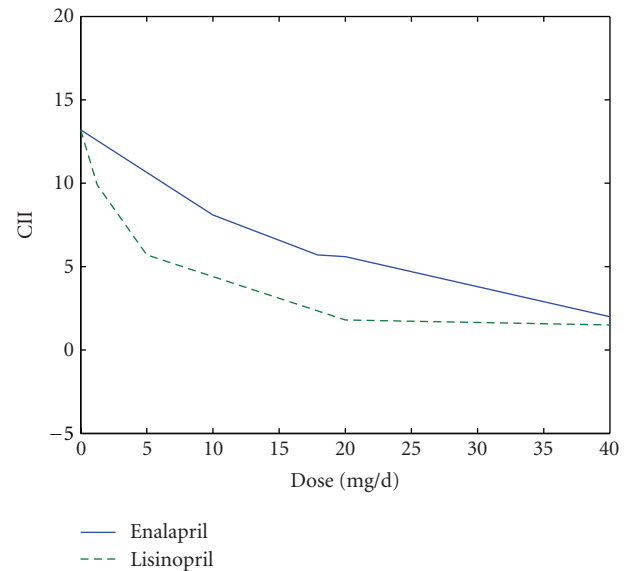


FIGURE 6: The CII at different doses. The solid line is the trend of patients' cardiac integrated index (CII) under different doses of enalapril; the dotted line is the trend of patients' CII under different doses of lisinopril.

SW indicate the enhancement of elasticity of heart muscles, promotion of the pumping function, and reduction of work by heart muscles. The decrease of CII is a sign of overall recovery of cardiac function. Even though there is no real measurement of the hemodynamic parameters (HR, CO, SV, EF, and SW), the simulation is successful on SBP and DBP. Similar results are verified by the simulation of lisinopril.

CII is an integrated parameter representing the hemodynamic status. We studied its performance at different doses of medicine. Simulations on dataset from reference [21] under diverse doses of enalapril/lisinopril are accomplished to obtain hemodynamic parameters after treatment. CII is then derived from those parameters, as shown in Figure 6. The solid line represents the simulated CII under different doses of enalapril, while the dotted line is for lisinopril. In the figure, it is seen that CII does not drop significantly with dose of enalapril lower than 40 mg/d. The CII in lisinopril group falls rapidly when the dose <20 mg/d and then goes almost unchanged with the increase of dose. In general, the results reveal that with a raise of enalapril/lisinopril dose, the CII decreased. This means that the reduction of CII can be an indicator of the recovery of the patient's overall cardiac function. By observing the trends of CII curve, we can evaluate the different impacts of various drugs on cardiac function.

TABLE 3: Comparison of hemodynamic parameters by simulation and clinical observation.

	Baseline value	Simulated value	Measured value
Enalapril 20 mg/d			
SBP (mmHg)	155*	143	137*
DBP (mmHg)	101*	92	88*
MAP (mmHg)	119	109	
PP (mmHg)	54	51	
HR (beat/min)	73	73	
CO (L/min)	5.26	5.48	
SV (mL)	72	75	
EF (%)	28.35	32.05	
SW (J/beat)	2.95	2.70	
CII	9.85	4.01	
Lisinopril 20 mg/d			
SBP (mmHg)	158 ⁺	141	140 ⁺
DBP (mmHg)	94 ⁺	90	88 ⁺
MAP (mmHg)	115	107	
PP (mmHg)	64	51	
HR (beat/min)	73	73	
CO (L/min)	5.11	5.62	
SV (mL)	70	77	
EF (%)	27.24	34.53	
SW (J/beat)	3.03	2.48	
CII	13.22	1.80	

*Data acquired from the literature [20]. ⁺Data acquired from the literature [21]. The rest data are estimated by models.

4. Discussion

In this paper, a new algorithm for fast estimation of vascular model parameters is presented. Vascular resistance and compliance that play important roles in the medical therapy for HF are calculated from the data surfaces constructed by SBP and DBP, which can be easily obtained from regular clinical examination. Compared with the previous method, which will take 2–5 hours to achieve the appropriate RC values, the present one is able to determine a unique approximation of RC considerably faster and more accurate. This novel method of parameter estimation can also be extended to the application in other mathematical physiological models.

Figure 5 shows the diverse mode of enalapril and lisinopril. Since ΔR is greater than ΔC at the same dose of enalapril, it suggests that enalapril affects the cardiac condition mainly by adjusting the vascular resistance. The ΔR and ΔC curves of lisinopril are close to each other indicating that lisinopril works by regulating R and C simultaneously. Therefore, we deduce that enalapril plays an important role in HF treatment mainly through relaxing blood vessel, since it significantly reduces the vascular resistance. Lisinopril exhibits effects in both dilating blood vessel and increasing vascular elasticity, contributing to changes to vascular resistance and vascular compliance.

The simulation results (Figure 6) imply the different patterns of efficacy between enalapril and lisinopril based

on the various modes. The effect of enalapril on patients is mild and smooth, while the effect of lisinopril is rapid. It suggests that, at small doses, lisinopril has a more significant effect on improvement than enalapril. With doses higher than 40 mg/d, the two drugs' performances are similar. These differences result from the diverse effects of enalapril and lisinopril on ΔR and ΔC .

Similar results also have been disclosed in clinical trials and other studies. It has been reported that both ACEI drugs can regulate cardiac situation, and, within a certain range, the larger the dose is, the more amelioration can be seen in cardiac function [22]. Simpson and Jarvis, Menne et al., and Terpstra et al. [23–25] reported that lisinopril would result in a better improvement in HF due to its high tissue affinity, in contrast with enalapril. However, enalapril and lisinopril have a similar efficacy when their doses reach the highest approved level of the treatment [26]. An explanation may be that the binding of ACEI medicine and angiotensin-converting enzyme is a saturation reaction. Regular clinical dose is 10–20 mg for enalapril and 20–40 mg for lisinopril [27]. Our results show that, with 10–20 mg of enalapril or 20–40 mg of lisinopril, simulated blood pressure returns to normal or SBP/DBP decreases by 10 mmHg. Other simulated hemodynamic parameters (such as CO and EF) are also improved. The simulated effects meet the requirement of regular treatment [20].

The difference in the acting manner of ACEIs may provide hints in clinical practice. Our results suggest using lisinopril when patients need a rapid improvement in the physical condition. For acute HF, it is reasonable to use enalapril because it may give a smoother reduction in blood pressure with a lower risk of sudden hypotension. It is worth pointing out that enalapril can be a satisfactory agent for severe HF considering safety, which has been indicated by Dickstein et al. [28].

It is worth noting is that the developed model can also be applied to predict the effect of HF treatment individually. For this purpose, the blood pressure (SBP, DBP) of patients should be first measured and then the fast parameter estimation algorithm is utilized to obtain the corresponding baseline of the model parameters R/C . According to the drug effect curve, which describes the dose effect of ACEI on R/C , the variation of R/C under a given drug dose can be obtained. Finally, knowing the baseline and variation of R/C , we can apply the developed model to estimate the prediction of hemodynamic parameters and overall treatment effect. Referring to Table 3, the results demonstrate a match of predicted and observed blood pressure from reference [20, 21] within an error of 5%, giving proof of the reliability. Though the reference did not provide records of other hemodynamic parameters (such as CO, SV, and EF) measurement, these parameters can be obtained by model simulations. Then the comprehensive index CII will be calculated from them to reflect cardiac function. The predicted CII below the baseline may suggest a better prognosis after the treatment.

The simulation methods can be further used to evaluate other HF medication, that is, beta-blockade, diuretics, angiotensin-in receptor blocker, and so on. For instance, the

drug efficacy of beta-blockade can be simulated by adjusting model parameters: decrease sympathetic nerve activity, increase vagus nerve activity as well as adjust blood volume. With the aiding of the model, the outcome of the treatment can be analyzed.

So far, the present HF simulation model, however, only provides a primary evaluation of ACEI drugs and has certain limitations. First, the model is not applicable to all patients because of the variety in individual reaction to medicines. The current cardiovascular model does not take into account the complicated circulation system. For instance, Sandoval et al. [29] reported that for certain HF patients undergoing lisinopril treatment, there is no significant improvement of blood pressure or cardiac index. The reason may be related to the cardiac antiadrenergic properties of those patients. Second, the applied data in this study are from the reported five large-scale clinical trials with different therapy periods and blood pressure levels, which may lead to bias in parameters estimation. Finally, the model reliability should be confirmed by more verification. We have evaluated the model by estimating the blood pressures, which approach the real ones. In future work, CO, SV, EF, and other hemodynamic parameters should be collected before/after treatments to verify the feasibility of the model. For improving and further validating the model performance, more clinical investigations are expected.

5. Conclusions

HF is a serious cardiovascular disease, which causes an increasing burden on public healthcare. Mathematical modeling and simulation in cardiovascular research have attracted much attention in the recent years. However, the difficulties in parameters estimation hinder the clinical applications of these models. This study presents a novel algorithm for fast estimation of the cardiovascular model parameters. Starting from the pathological parameter setting, the HF treatment can be simulated by adjusting vascular resistance and compliance. The dose effect is evaluated by comparing the model-derived blood pressure with the clinic measurement as well as a comprehensive index CII. The results demonstrate a 5% error between the simulated and measured blood pressure. In addition, we also obtained the CII index which can comprehensively reflect heart condition. We further applied this method to study the dose-effect relationship of ACEI medicine. A relationship curve is produced and the different outcome of enalapril and lisinopril can be distinguished. These results coincide with the conclusions from clinical trials and previously studies. Moreover, this work may offer a quantitative tool for constructing patient-specific treatment plans of HF treatment and can be used in evaluating the dose effect of other HF medications.

Acknowledgments

The work is supported by the National Nature Science Foundation of China (Grant 30970760) and Science & Technology Department of Zhejiang Province (Grant 2006C13018). Special thanks to Qi Shao of the Department of Biomedical

Engineering at University of Minnesota for technical support.

References

- [1] S. A. Hunt, D. W. Baker, M. H. Chin et al., "ACC/AHA 2005 guideline update for the diagnosis and management of chronic heart failure in the adult," *Circulation*, vol. 112, no. 12, pp. 154–235, 2005.
- [2] W. J. Remme and K. Swedberg, "Guidelines for the diagnosis and treatment of chronic heart failure," *European Heart Journal*, vol. 22, no. 17, pp. 1527–1560, 2001.
- [3] B. M. Massie and N. B. Shah, "Evolving trends in the epidemiologic factors of heart failure: rationale for preventive strategies and comprehensive disease management," *American Heart Journal*, vol. 133, no. 6, pp. 703–712, 1997.
- [4] W. J. Remme, J. G. F. Cleland, H. Dargie et al., "The treatment of heart failure," *European Heart Journal*, vol. 18, no. 5, pp. 736–753, 1997.
- [5] A. W. Haider, M. G. Larson, S. S. Franklin, and D. Levy, "Systolic blood pressure, diastolic blood pressure, and pulse pressure as predictors of risk for congestive heart failure in the Framingham Heart Study," *Annals of Internal Medicine*, vol. 138, no. 1, pp. 10–16, 2003.
- [6] M. Gheorghiade, W. T. Abraham, N. M. Albert et al., "Systolic blood pressure at admission, clinical characteristics, and outcomes in patients hospitalized with acute heart failure," *Journal of the American Medical Association*, vol. 296, no. 18, pp. 2217–2226, 2006.
- [7] M. Diaz-Insua and M. Delgado, "Modeling and simulation of the human cardiovascular system with bond graph: a basic development," *Computers in Cardiology*, vol. 11, no. 8, pp. 393–396, 1996.
- [8] M. Ursino and E. Magosso, "Role of short-term cardiovascular regulation in heart period variability: a modeling study," *American Journal of Physiology*, vol. 284, no. 4, pp. H1479–H1493, 2003.
- [9] R. Zelis, D. T. Mason, and E. Braunwald, "A comparison of the effects of vasodilator stimuli on peripheral resistance vessels in normal subjects and in patients with congestive heart failure," *Journal of Clinical Investigation*, vol. 47, no. 4, pp. 960–970, 1968.
- [10] G. F. Mitchell, J. C. Tardif, J. M. O. Arnold et al., "Pulsatile hemodynamics in congestive heart failure," *Hypertension*, vol. 38, no. 6, pp. 1433–1439, 2001.
- [11] H. Tsuruta, T. Sato, and N. Ikeda, "Mathematical model of cardiovascular mechanics for diagnostic analysis and treatment of heart failure—part 2: analysis of vasodilator therapy and planning of optimal drug therapy," *Medical and Biological Engineering and Computing*, vol. 32, no. 1, pp. 12–18, 1994.
- [12] Y. Gong, Q. Hu, G. Ning, S. Gong, and J. Yan, "Simulate heart failure by a mathematical model," in *Proceedings of the 3rd International Conference on Bioinformatics and Biomedical Engineering (iCBBE '09)*, vol. 11, pp. 2447–2450, June 2009.
- [13] Z. Luo, S. Zhang, Y. Yang et al., *Engineering Analysis for Pulse Wave and Its Application in Clinical Practice*, Science Press, Beijing, China, 2006.
- [14] M. Peltier, D. Houpe, A. Cohen-Solal, M. Béguin, F. Levy, and C. Tribouilloy, "Treatment practices in heart failure with preserved left ventricular ejection fraction: a prospective observational study," *International Journal of Cardiology*, vol. 118, no. 3, pp. 363–369, 2007.

- [15] J. N. Nanas, G. Alexopoulos, M. I. Anastasiou-Nana et al., "Outcome of patients with congestive heart failure treated with standard versus high doses of enalapril: a multicenter study," *Journal of the American College of Cardiology*, vol. 36, no. 7, pp. 2090–2095, 2000.
- [16] L. M. Louis, J. Dirk, G. Michael, Z. Zilahi, W. R. Meyer, and R. Willenheimer, "The effect of treatment with bisoprolol-first versus enalapril-first on cardiac structure and function in heart failure," *International Journal of Cardiology*, vol. 40, no. 4, pp. 1–5, 2009.
- [17] J. Bai and S. Wen, "Efficacy of irbesartan versus enalapril in treatment of mild and moderate hypertension," *Modern Medicine & Health*, vol. 25, no. 16, pp. 2421–2422, 2009.
- [18] R. C. Hermida, D. E. Ayala, Y. Khder, and C. Calvo, "Ambulatory blood pressure-lowering effects of valsartan and enalapril after a missed dose in previously untreated patients with hypertension: a prospective, randomized, open-label, blinded end-point trial," *Clinical Therapeutics*, vol. 30, no. 1, pp. 108–120, 2008.
- [19] H. J. Gomez, V. J. Cirillo, J. A. Sromovsky et al., "Lisinopril dose-response relationship in essential hypertension," *British Journal of Clinical Pharmacology*, vol. 28, no. 4, pp. 415–420, 1989.
- [20] R. Botero, H. Matiz, E. María et al., "Efficacy and safety of valsartan compared with enalapril at different altitudes," *International Journal of Cardiology*, vol. 72, no. 3, pp. 247–254, 2000.
- [21] Y. Kaminsky, A. Suslikov, and E. Kosenko, "Specific and pronounced impacts of lisinopril and lisinopril plus simvastatin on erythrocyte antioxidant enzymes," *Journal of Clinical Pharmacology*, vol. 50, no. 2, pp. 180–187, 2010.
- [22] M. D. McMurray and J. V. John, "Systolic heart failure reply," *New England Journal of Medicine*, vol. 362, no. 16, pp. 1545–1546, 2010.
- [23] K. Simpson and B. Jarvis, "Lisinopril: a review of its use in congestive heart failure," *Drugs*, vol. 59, no. 5, pp. 1149–1167, 2000.
- [24] J. Menne, C. Farsang, L. Deák et al., "Valsartan in combination with lisinopril versus the respective high dose monotherapies in hypertensive patients with microalbuminuria: the VALERIA trial," *Journal of Hypertension*, vol. 26, no. 9, pp. 1860–1867, 2008.
- [25] W. F. Terpstra, J. F. May, A. J. Smit, P. A. De Graeff, B. Meyboom-De Jong, and H. J. G. M. Crijns, "Effects of amlodipine and lisinopril on intima-media thickness in previously untreated, elderly hypertensive patients (the ELVERA trial)," *Journal of Hypertension*, vol. 22, no. 7, pp. 1309–1316, 2004.
- [26] I. Enström, T. Thulin, and L. H. Lindholm, "Comparison between enalapril and lisinopril in mild-moderate hypertension: a comprehensive model for evaluation of drug efficacy," *Blood Pressure*, vol. 1, no. 2, pp. 102–107, 1992.
- [27] S. Mazimba, T. Patel, and N. Grant, "Medical advances in the evaluation and treatment of heart failure," *Emergency Medicine Reports*, vol. 31, no. 19, pp. 217–226, 2010.
- [28] K. Dickstein, T. Aarsland, and K. Tjelta, "A comparison of hypotensive responses after oral and intravenous administration of enalapril and lisinopril in chronic heart failure," *Journal of Cardiovascular Pharmacology*, vol. 9, no. 6, pp. 705–710, 1987.
- [29] A. Sandoval, P. Larrabee, D. G. Renlund, J. B. O'Connell, and M. R. Bristow, "Lisinopril lowers cardiac adrenergic drive and increases β -receptor density in the failing human heart," *Circulation*, vol. 88, no. 2, pp. 472–480, 1993.

Research Article

Simulation of Arrhythmogenic Effect of Rogue RyRs in Failing Heart by Using a Coupled Model

Luyao Lu,¹ Ling Xia,² and Xiuwei Zhu¹

¹Department of Biomedical Engineering, Wenzhou Medical College, Wenzhou 325035, China

²Department of Biomedical Engineering, Zhejiang University, Hangzhou 310027, China

Correspondence should be addressed to Ling Xia, xialing@zju.edu.cn

Received 21 June 2012; Accepted 22 August 2012

Academic Editor: Feng Liu

Copyright © 2012 Luyao Lu et al. This is an open access article distributed under the Creative Commons Attribution License, which permits unrestricted use, distribution, and reproduction in any medium, provided the original work is properly cited.

Cardiac cells with heart failure are usually characterized by impairment of Ca^{2+} handling with smaller SR Ca^{2+} store and high risk of triggered activities. In this study, we developed a coupled model by integrating the spatiotemporal Ca^{2+} reaction-diffusion system into the cellular electrophysiological model. With the coupled model, the subcellular Ca^{2+} dynamics and global cellular electrophysiology could be simultaneously traced. The proposed coupled model was then applied to study the effects of rogue RyRs on Ca^{2+} cycling and membrane potential in failing heart. The simulation results suggested that, in the presence of rogue RyRs, Ca^{2+} dynamics is unstable and Ca^{2+} waves are prone to be initiated spontaneously. These release events would elevate the membrane potential substantially which might induce delayed afterdepolarizations or triggered action potentials. Moreover, the variation of membrane potential depolarization is indicated to be dependent on the distribution density of rogue RyR channels. This study provides a new possible arrhythmogenic mechanism for heart failure from subcellular to cellular level.

1. Introduction

Calcium is considered to be the key ion in mediating the process of cardiac excitation-contraction coupling (E-C coupling). Since the discovery of Ca^{2+} sparks in 1993 [1], Ca^{2+} sparks have been widely accepted to be the stereotyped elementary Ca^{2+} release events in the intact myocyte. Sparks arise via clusters of ryanodine receptors (RyRs) localized in the junctional SR (jSR) which is in close apposition to transverse tubules (TTs) [2]. In a diastolic myocyte, spontaneous Ca^{2+} sparks occur randomly at very low frequency, even in the absence of Ca^{2+} influx. During a single muscle twitch, Ca^{2+} influx via sarcolemmal L-type Ca^{2+} channels will trigger synchronously occurrence of thousands of sparks, summation of which in space and time causes a global steep rise of Ca^{2+} concentration named Ca^{2+} transient. However under some pathological conditions, successive recruitment of Ca^{2+} sparks tends to evolve into Ca^{2+} waves propagating across the myocytes which might trigger ventricular arrhythmias [3].

With the improvement of optical methods and innovative techniques, microscopic Ca^{2+} signals at the subcellular level have been extensively investigated and characterized. In

addition to Ca^{2+} sparks via clustered RyRs, nonspark Ca^{2+} release events, named Ca quarks, activated by low-intensity photolysis of Ca^{2+} -caged compounds [4] or by inward Na^+ current, I_{Na} [5], could elicit spatially homogeneous but small Ca^{2+} transient. These quarks are likely to be mediated via one or a few RyR channels called rogue RyRs [6]. Differing from RyR clusters that underly sparks, rogue RyRs are thought to be uncoupled with each other and behave in ways more like the characteristic of single RyR channels [7]. Although detection of these small rogue RyR channels is difficult by conventional instruments, some researchers have suggested that, besides sparks, the nonspark pathway via rogue RyRs explains a part of SR Ca^{2+} leak [8, 9]. Quantitatively, with the optical superresolution technique, Baddeley et al. have indicated that there are greater numbers of rogue RyR groups than large RyR clusters [10]. An experimental study that Ca^{2+} waves are inhibited without affecting Ca^{2+} sparks by ruthenium red suggests a nonspark producing RyR channels which are important to propagation of Ca^{2+} wave [11]. Direct visualization of small local release events has been made possible by recent technical innovations. Brochet et al. claimed that they have directly visualized quark-like or “quarky” Ca^{2+} release events which might depend on the

opening of rogue RyRs (or small cluster of RyRs) in rabbit ventricular myocytes [12].

SR Ca^{2+} leak consists of two components: RyR-dependent leak and RyR-independent leak [8]. The former is thought to be comprised of spark-mediated leak (visible leak) and non-spark-mediated leak (invisible leak). Elevated SR Ca^{2+} leak would contribute to delayed afterdepolarizations (DADs) and consequently arrhythmia in heart failure (HF) [13]. Besides spark-mediated leak, additional Ca^{2+} leak via rogue RyRs may be an important factor in disturbing Ca^{2+} dynamics and triggering Ca^{2+} waves [11, 14]. However, how do these abnormal Ca^{2+} release events affect cellular electrophysiological properties? The precise relationships between property of rogue RyRs and Ca^{2+} handling as well as cellular electrophysiology in failing heart are not completely clear.

In this paper, we developed a coupled mathematical model including Ca^{2+} cycling processes from subcellular to cellular level and electrophysiology of the ventricular myocyte. The proposed coupled model was then applied to study the effects of Ca^{2+} release via rogue RyRs on subcellular spatiotemporal Ca^{2+} cycling and on the possible membrane potential changes in failing heart.

2. Methods

Subcellular Ca^{2+} release events and cellular Ca^{2+} cycling as well as corresponding membrane potential were simulated synchronously by a coupled model. The model consists of two parts: a two-dimensional (2D) spatial Ca^{2+} reaction-diffusion model and an electrophysiological model of the ventricular myocyte.

2.1. A Subcellular Ca^{2+} Reaction-Diffusion Model. The shape of the cardiac myocyte in the model is represented as a circular cylinder $100\ \mu\text{m}$ in length and $10\ \mu\text{m}$ in radius. However, because of quasi-isotropic diffusion of Ca^{2+} on the transverse section [15], a 2D model was used in our simulation work (Figure 1), where x axis denotes the cell's longitudinal direction and y axis is along the Z-line. It could still describe most of the key properties of Ca^{2+} waves, but needs much less computation work than a 3D model. The 2D spatiotemporal Ca^{2+} reaction-diffusion model is described based on a reaction-diffusion system proposed by Izu et al. [16]. Figure 1 shows the subcellular structural representation of RyRs network. The x -axis denotes the cell's longitudinal direction and the y -axis is along the Z-line. The blue dots represent RyR clusters which account for Ca^{2+} sparks. The small red dots are the rogue RyR channels which raise Ca^{2+} quarks. Rogue RyRs are distributed in a stochastic manner. N_{rogue} is referred to the distributing density of rogue RyRs with the unit of rogue RyR/ μm^2 .

The free Ca^{2+} concentration $[\text{Ca}^{2+}]_i$ in the reaction-diffusion is described by a differential equation as follows:

$$\frac{\partial[\text{Ca}^{2+}]_i}{\partial t} = D_x \frac{\partial^2[\text{Ca}^{2+}]_i}{\partial x^2} + D_y \frac{\partial^2[\text{Ca}^{2+}]_i}{\partial y^2} + J_{\text{dye}} + J_{\text{buffers}} + J_{\text{pump}} + J_{\text{leak}} + J_{\text{sub-rel}}, \quad (1)$$

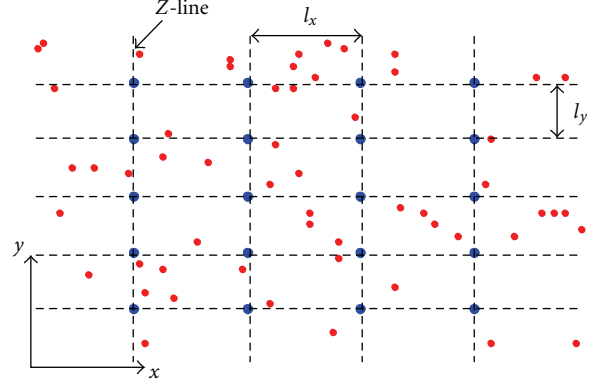


FIGURE 1: Geometry of RyRs distribution. The blue dots represent Ca^{2+} release units consisting of clusters of RyRs. $l_x = 2.0\ \mu\text{m}$ and $l_y = 1.0\ \mu\text{m}$. The small red dots are rogue RyRs which scatter over the plane randomly. In this figure, N_{rogue} is equivalent to 1.0 rogue RyR/ μm^2 .

where D_x and D_y are the diffusion coefficients; J_{dye} and J_{buffers} are due to fluorescent indicator dye and endogenous Ca^{2+} buffer, respectively; J_{pump} is pumping rate of SR Ca^{2+} ATPase; J_{leak} is defined as a RyR-independent leak flux which is small and invisible and persists in the presence of RyR inhibition [8]; $J_{\text{sub-rel}}$ is summation of Ca^{2+} release fluxes in the 2D subcellular model which consists of two types of Ca flows as follows:

$$J_{\text{sub-rel}} = \sum_{i,j} J_{\text{cluster}}(x_i, y_j) + \sum_{m,n} J_{\text{rogue}}(x_m, y_n), \quad (2)$$

$$J_{\text{cluster}}(x_i, y_j) = V_{\text{cluster}} \left([\text{Ca}^{2+}]_{\text{SR}} - [\text{Ca}^{2+}]_{i,(x_i,y_j)} \right),$$

where $J_{\text{cluster}}(x_i, y_j)$ is Ca^{2+} release flux via a cluster of RyRs located on (x_i, y_j) , V_{cluster} is maximal J_{cluster} conductance equivalent to $1.97 \times 10^{-8}\ \text{ms}^{-1}$, and $J_{\text{rogue}}(x_m, y_n)$ is Ca^{2+} release flux via a rogue RyR channel located on (x_m, y_n) , equivalent to $3.3166 \times 10^{-9}\ \text{pmol/ms}$.

Firings of the two types of RyR channels are considered to be stochastic processes and treated by the Monte Carlo simulation in our work. To evaluate the effects of SR luminal Ca^{2+} concentration ($[\text{Ca}^{2+}]_{\text{SR}}$) on SR Ca^{2+} release, we integrate a new parameter k_{CaSR} into the probability of firing of Ca^{2+} sparks or quarks (P_j , $j = \text{cluster}$ for RyR clusters, and $j = \text{rogue}$ for rogue RyRs) as follows:

$$k_{\text{CaSR}} = \frac{k_{\text{max}}}{1 + (D_{\text{SR}}/[\text{Ca}^{2+}]_{\text{SR}})^{n_{\text{SR}}}}, \quad (3)$$

$$P_j = \frac{P_{\text{max}}}{1 + (K_{mj}/[\text{Ca}^{2+}]_i)^{n_j}} k_{\text{CaSR}},$$

where $k_{\text{max}} = 2.0$, the Hill coefficient $n_{\text{SR}} = 4.5$, $P_{\text{max}} = 0.3/\text{event/ms}$, $n_{\text{cluster}} = 1.6$, and $n_{\text{rogue}} = 1.0$ for the less coupled gating of rogue RyRs than RyR clusters. D_{SR} is luminal Ca^{2+} sensitivity parameter of Ca^{2+} release events, and K_{mj} is cytoplasmic Ca^{2+} sensitivity parameter of RyR clusters or rogue RyR channels. In our simulation work,

$K_{m\text{rogue}}$ was always set to be of the same value as $K_{m\text{cluster}}$; thus K_m was used to represent the value of $K_{m\text{cluster}}$ and $K_{m\text{rogue}}$.

In this study, the simulation of subcellular Ca^{2+} handling was performed on the longitudinal section of a cardiac myocyte with the size of $100\ \mu\text{m} \times 20\ \mu\text{m}$ along the cellular longitudinal direction (x -axis) and Z -line (y -axis), respectively. The number of RyR clusters was 49×19 along x and y axes, respectively, and the total number of rogue RyRs was $N_{\text{rogue}} \times 2000\ \mu\text{m}^2$. The diffusion partial differential equation was approximated by the finite difference method (FDM) with a time-step size of 0.01 ms and a mesh size of 0.1 μm .

Because of the stochasticity of opening of RyR clusters and rogue RyRs, the properties of Ca^{2+} signalling were described by statistical results by carrying out repeated Monte Carlo simulations. All averaged data were expressed as mean \pm SEM. One-way analysis of variance (ANOVA) was used for comparison and $P < 0.05$ was taken to indicate statistical significance.

2.2. A Cellular Electrophysiological Model. The electrophysiological behavior of a myocardial cell is modelled based on a cardiac action potential model proposed by Ten Tusscher and Panfilov [17]. The voltage across the cell membrane can be described with the following differential equation:

$$\frac{dV_m}{dt} = -\frac{1}{C_m}(I_{\text{Na}} + I_{\text{CaL}} + I_{\text{to}} + I_{\text{Kr}} + I_{\text{Ks}} + I_{\text{K1}} + I_{\text{NaK}} + I_{\text{NaCa}} + I_{\text{pCa}} + I_{\text{pK}} + I_{\text{bCa}} + I_{\text{bNa}} + I_{\text{stim}}), \quad (4)$$

where C_m is the membrane capacitance, I_{stim} is a stimulus current, and I_x denotes all kinds of ionic currents across the sarcolemma.

However, different from the Ca^{2+} dynamical system by Ten Tusscher et al., global SR Ca^{2+} release current J_{rel} at the cellular level is calculated by the summation of local Ca^{2+} release fluxes in the 2D subcellular model:

$$J_{\text{rel}} = k_{\text{rel}}J_{\text{sub-rel}} = k_{\text{rel}}\left(\sum_{i,j}J_{\text{cluster}}(x_i, y_j) + \sum_{m,n}J_{\text{rogue}}(x_m, y_n)\right), \quad (5)$$

where k_{rel} is a constant multiplier equivalent to 22.25 in our coupled model.

2.3. Heart Failure Model. Changes of Ca^{2+} cycling as well as other ionic currents have been observed in failing heart; thus we modified the parameters of our coupled model to mimic abnormal Ca^{2+} dynamics and electrophysiological properties in heart failure from subcellular to cellular levels.

2.3.1. Ca^{2+} Handling

(a) *SR Ca^{2+} Release Channels.* In HF, RyR channels would become unstable due to phosphorylation of protein kinase A (PKA) [18] or Ca^{2+} /calmodulin-dependent-protein-kinase-I- (CaMKI-) induced hyperphosphorylation [19] and be oversensitive to cytoplasmic Ca^{2+} and SR luminal Ca^{2+} [20].

In our simulation study, K_m was set to be 7.5 μM and D_{SR} was 2.5 mM under the condition of heart failure, while 15 μM and 3.25 mM, respectively, under control condition.

(b) *SR Ca^{2+} Pump.* Pumping activity of SR Ca^{2+} ATPase in failing heart is reduced as shown in experimental studies [21]. A 45% reduction in J_{pump} of a failing myocyte is incorporated into our HF model.

(c) *SR Ca^{2+} Leak.* Spontaneous openings of RyR clusters and rogue RyRs at diastole are the main contributors to SR Ca^{2+} leak as the form of Ca^{2+} sparks and quarks. Because of instability of RyR channels, RyR-mediated Ca^{2+} leak from SR increased in the resting HF myocyte. However, RyR-independent leak was unaltered in our HF model.

2.3.2. Ionic Current across the Sarcolemma

(a) *Inward Rectifier Potassium Current: I_{K1} .* In heart failure, I_{K1} was shown to be reduced in many studies [22, 23]. In our HF model the current density of I_{K1} was assumed to decrease by 20%.

(b) *Slowly Activated Delayed Rectifier Potassium Current: I_{Ks} .* I_{Ks} is the slowly activated component of delayed rectifier potassium current. In the failing canine hearts I_{Ks} has been shown to be downregulated by nearly a half [24]. Therefore, maximal I_{Ks} conduction was changed to 50% of the value used in nonfailing myocytes.

(c) *Transient Outward Potassium Current: I_{to} .* According to an experimental result, the current density of I_{to} in HF declined to 64% of the value in control cardiac cells [25], so that in our simulations I_{to} was reduced to 64% in failing myocytes.

(d) *Fast Na Current: I_{Na} .* It has been reported that the peak density of I_{Na} decreased significantly in heart failure [26]. Therefore, the maximal I_{Na} conductance G_{Na} was set to be 8.902 nS/pF in the failing myocytes, while equivalent to 14.838 nS/pF in the nonfailing myocytes.

(e) *Na-Ca Changer Current: I_{NaCa} .* The activity and/or gene expression of Na/Ca changer was found to be increased obviously in many experiments [27, 28]. Thus we upregulated I_{NaCa} by 65% in the failing myocytes.

(f) *Na-K Pump Current: I_{NaK} .* As shown in the experimental study, the concentration of Na/K ATPase in the failing heart was reduced by 42% [29], so that reduction of I_{NaK} by the same proportion was incorporated in our HF model.

(g) *Ca Background Current: I_{bCa} .* Inward I_{bCa} was considered to balance Ca^{2+} extrusion via Na/Ca exchanger and sarcolemmal Ca^{2+} pump at resting potential. In our HF model the conductance of I_{bCa} was increased due to the increase of I_{NaCa} .

TABLE 1: Parameters in nonfailing versus failing myocyte models.

Parameters	Definition	Nonfailing	Failing
V_{\max}	Maximal SR Ca^{2+} pumping rate	0.006375 mM/ms	0.0035 mM/ms
G_{Ks}	Maximal I_{Ks} conductance	0.392 nS/pF	0.196 nS/pF
G_{K1}	Maximal I_{K1} conductance	5.405 nS/pF	4.324 nS/pF
G_{to}	Maximal I_{to} conductance	0.294 nS/pF	0.185 nS/pF
G_{Na}	Maximal I_{Na} conductance	14.838 nS/pF	8.902 nS/pF
P_{NaK}	Maximal I_{NaK}	2.724 pA/pF	1.57 pA/pF
G_{bCa}	Maximal I_{bCa} conductance	0.000592 nS/pF	0.0009045 nS/pF
k_{NaCa}	Maximal I_{NaCa}	1000 pA/pF	1650 pA/pF
K_m	Ca^{2+} sensitivity parameters of RyR clusters or rogue RyR when they take the same value	15 μM	7.5 μM
D_{SR}	luminal Ca^{2+} sensitivity parameter of Ca^{2+} release events	3.25 mM	2.5 mM

The different values of parameters in nonfailing and failing myocyte models are shown in Table 1.

3. Results

3.1. Ca^{2+} Cycling and V_m in HF. With the proposed coupled model, firstly we simulated the action potential and calcium cycling by applying a stimulus with a frequency of 1 Hz, duration of 1 ms, and an amplitude of 7 pA. Figure 2 shows the simulation results of membrane potential, cytoplasmic Ca^{2+} concentration, Ca^{2+} concentration in SR lumina, and the $\text{Na}^+/\text{Ca}^{2+}$ exchanger current after 10th stimulus. While blue curves in Figure 2 are obtained under the physiological conditions, red curves are under the pathological conditions, that is, heart failure. Compared with that in nonfailing myocytes, the plateau of action potential (AP) shows a larger amplitude and longer duration, causing a significant increase in AP duration ($\sim 45\%$ longer than in normal condition) in heart failure. Meanwhile, decrease of the maximal conductivity of I_{K1} in heart failure makes the resting potential elevate 2 \sim 3 mV. However, the amplitude of AP overshoot is smaller in heart failure, which is due to the reduction of fast inward current I_{Na} . Then at the early stage of rapid repolarization, a weakened notch is observed in heart failure AP, which is caused by a decrease of I_{to} . Moreover, the prolonged plateau is mainly due to decrease of maximal conductivity of I_{Ks} .

For the calcium handling in heart failure, it is mainly characterized by a significant impair of global Ca^{2+} transient and a much slower decay of calcium concentration. Moreover, the SR Ca^{2+} store is smaller in heart failure, that is, $[\text{Ca}^{2+}]_{SR}$ is $\sim 15\%$ lower in resting cells, and the restoring rate of SR calcium is slower than that on control condition. Due to the changes of AP morphology and calcium transient curves together with increase of the activity of Na/Ca exchanger, the curve of I_{NaCa} in heart failure differs significantly from that under normal condition. This can be seen in Figure 2(d); that is, in heart failure, both the inward and outward currents of I_{NaCa} are increased. However, it takes a longer time to reach the peak of inward current, and the amplitude of inward I_{NaCa} in resting stage is also larger compared with that under control conditions.

3.2. Dependence of DAD on Rogue RyR. In heart failure myocytes, the RyR channels become very unstable and are more likely to open with the same values of $[\text{Ca}^{2+}]_i$ and $[\text{Ca}^{2+}]_{SR}$ as those under normal conditions. However, the calcium release current through a RyR cluster decreases as the SR calcium store is partly unloaded, which is observed as reduction of amplitude and area of calcium sparks. Indeed, the simulation results by using our coupled model show that, although more spontaneous calcium sparks occur in failing myocytes, propagating Ca^{2+} waves are seldom found when there is no rogue RyRs on the 2D subcellular space without any stimulus. These spontaneous calcium sparks would slightly elevate global $[\text{Ca}^{2+}]_i$ on the cellular level ($\Delta[\text{Ca}^{2+}]_i = (1.16 \pm 0.06) \times 10^{-4}$ mM, $n = 10$) and depolarize transmembrane potential with a tiny amplitude ($\Delta V_m = 4.21 \pm 0.23$ mV, $n = 10$) as shown in Figure 3(a).

However, how do Ca^{2+} dynamics and electrophysiological properties of a failing myocyte change in the presence of rogue RyR channels? We integrate rogue RyR channels into the 2D RyR grid and vary their distribution density N_{rogue} to investigate the precise effect of rogue RyR channels on Ca^{2+} handling and membrane potential. When the density of rogue RyRs is relatively low, for example, $N_{\text{rogue}} = 0.25$ rogue RyR/ μm^2 , spontaneously occurring calcium sparks are frequently observed in the subcellular region of HF myocytes during the resting state. Occasionally Ca^{2+} waves are formed, albeit at a small area, by recruiting several adjacent Ca^{2+} sparks. Those small Ca^{2+} waves could not propagate across the whole myocyte, but self-abort during a short time. Similar to the condition without rogue RyRs, global $[\text{Ca}^{2+}]_i$ and membrane potential are not affected severely by those Ca^{2+} release events under the condition with low density of rogue RyRs as shown in Figure 3(a) ($\Delta[\text{Ca}^{2+}]_i = (1.61 \pm 0.08) \times 10^{-4}$ mM, $\Delta V_m = 5.95 \pm 0.29$ mV, $n = 10$).

Amplification and increase rate of $[\text{Ca}^{2+}]_i$ and V_m should be two groups of principal parameters to evaluate the effects of rogue RyRs on Ca^{2+} dynamics and electrophysiological properties. Besides $\Delta[\text{Ca}^{2+}]_i$ and ΔV_m , two new parameters T_{peakCa} and $T_{\text{peak}V_m}$ are used in our simulation. T_{peakCa} represents the mean time to reach the peak of $[\text{Ca}^{2+}]_i$ from the end of resting stage, and $T_{\text{peak}V_m}$ is the time to reach the peak of V_m . Increase rate of Ca^{2+} concentration and depolarization velocity could be estimated indirectly

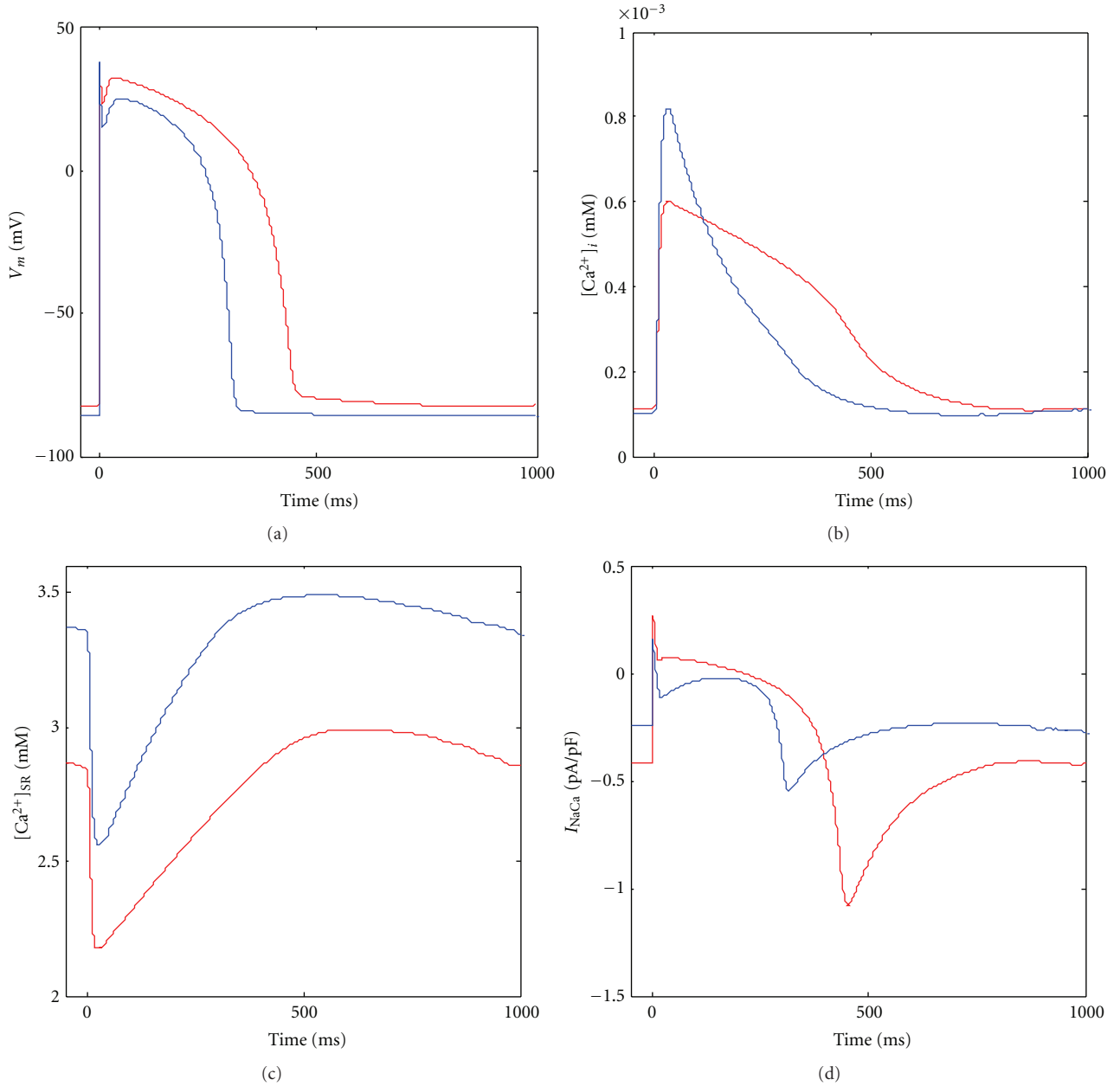


FIGURE 2: Simulation results of membrane potential (V_m) (a), cytoplasmic Ca^{2+} concentration ($[\text{Ca}^{2+}]_i$) (b), SR luminal Ca^{2+} concentration ($[\text{Ca}^{2+}]_{\text{SR}}$) (c), and I_{NaCa} (d) during a single twitch. The red curve represents the time course of those parameters in failing myocytes, while the blue curve is the time course of those parameters in control myocytes.

by the two parameters, which is shown in Figure 3(b). The simulated T_{peakCa} decreases significantly when N_{rogue} is upregulated from 0 to 0.25 rogue $\text{RyR}/\mu\text{m}^2$ ($T_{\text{peakCa}} = 418 \pm 19.7$ ms and 325 ± 15.2 ms ($n = 10$), resp., $n = 10, P < 0.05$). However, decrease of $T_{\text{peak}V_m}$ is slight when N_{rogue} is from 0 to 0.25 rogue $\text{RyR}/\mu\text{m}^2$ ($T_{\text{peak}V_m} = 406 \pm 38.5$ ms and 340 ± 25.1 ms, resp., $n = 10, P > 0.05$). In Figure 3(c) three blue curves when Time > 1000 ms represent repeated simulation results of V_m without any stimulus when $N_{\text{rogue}} = 0.25$ rogue $\text{RyR}/\mu\text{m}^2$. The results indicate a smooth variation without a significant peak in the membrane potential morphology.

When N_{rogue} is increased to 0.5 rogue $\text{RyR}/\mu\text{m}^2$, similar to above, small spontaneous calcium waves cannot propagate in

a long distance and quickly decay as well. The depolarization of membrane potential caused by calcium release events has bigger amplitude compared with that when $N_{\text{rogue}} = 0.25$ rogue $\text{RyR}/\mu\text{m}^2$ ($P < 0.05$), but is also relatively weak with an average of 7.48 ± 0.25 mV. Again, the membrane potential morphology is smooth.

However, as N_{rogue} is further increased, specifically when $N_{\text{rogue}} \geq 0.75$ rogue $\text{RyR}/\mu\text{m}^2$, large calcium waves could be initiated spontaneously in the 2D subcellular region. Moreover, our Monte-Carlo simulation results show that these large calcium release events cause a significant larger calcium transient at the whole cell level and subsequently depolarize the membrane potential to a larger extent when

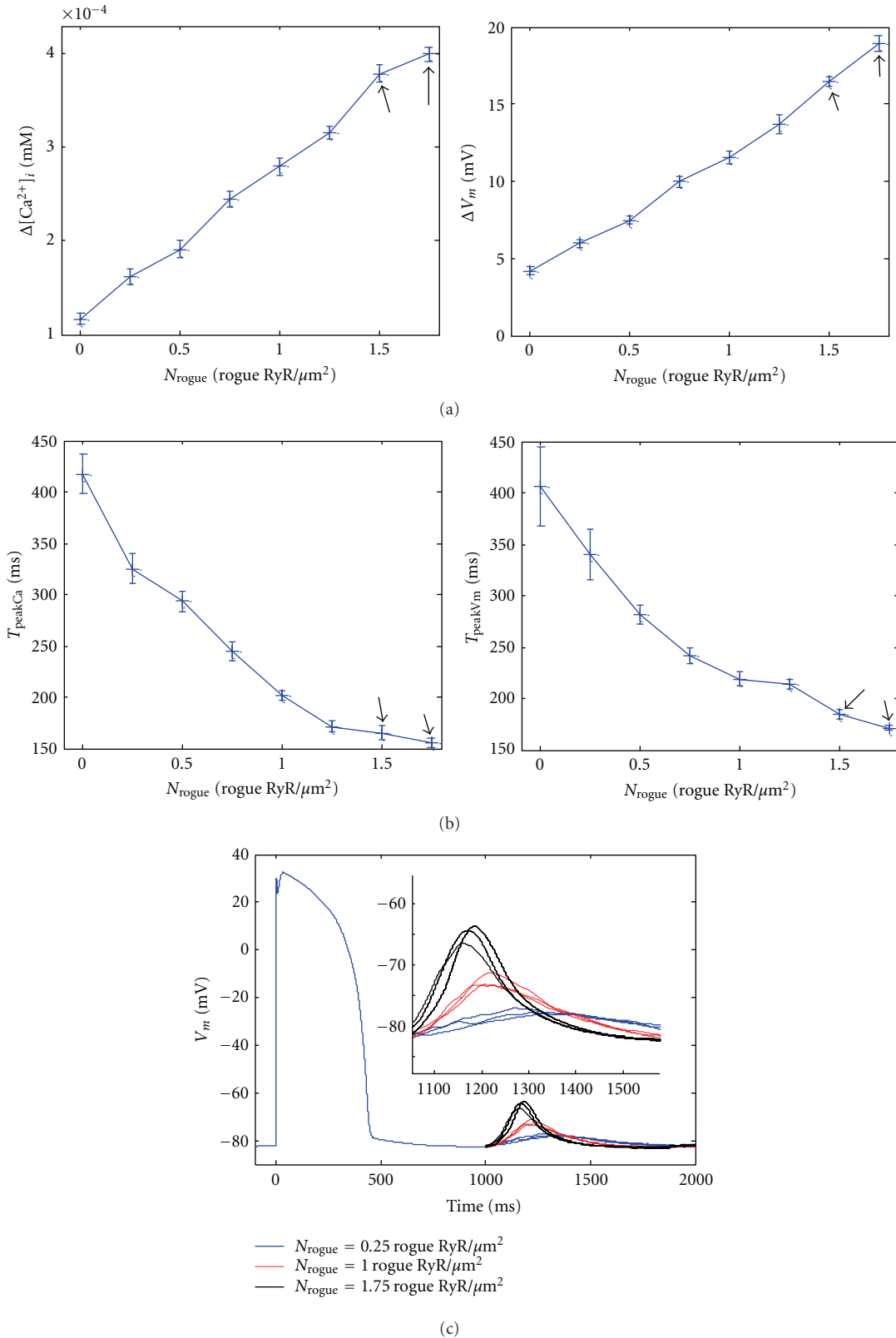


FIGURE 3: (a) Effects of distribution density of rogue RyRs on global change in $[Ca^{2+}]_i$ ($\Delta[Ca^{2+}]_i$, left image) and depolarization of membrane potential (ΔV_m , right image) without any external stimulus in heart failure. (b) Dependence of T_{peakCa} and T_{peakVm} on N_{rogue} . T_{peakCa} represents the time to reach the peak of global $[Ca^{2+}]_i$ from the end of resting stage, and T_{peakVm} is the time to reach the peak of V_m . For each N_{rogue} , we simulated 10 times under the same conditions to get statistical results due to the randomness of opening of RyR channels. The values denoted by arrows in (a) and (b) are recorded when $I_{Na} = 0$ pA. (c) Three groups of simulation results of V_m when $N_{\text{rogue}} = 0.25$, 1.0, and 1.75 rogue RyR/ μm^2 (blue, red, and black curves, resp.). The inset is the enlarged view of depolarization of membrane potential during the period of 1100 ms \sim 1500 ms. I_{Na} is also set to be 0 pA when $N_{\text{rogue}} = 1.75$ rogue RyR/ μm^2 .

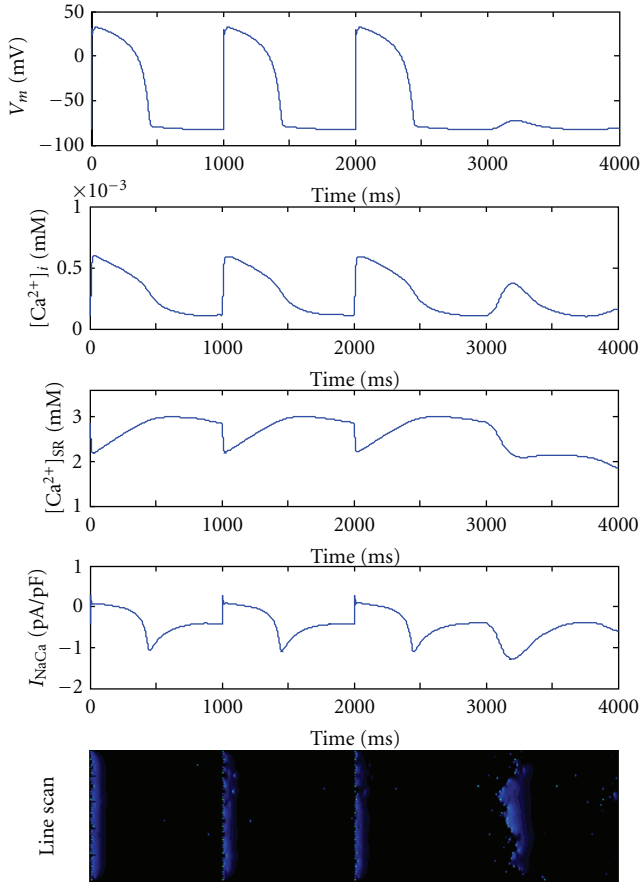


FIGURE 4: Occurrence of DAD following three action potentials in failing myocyte when $N_{\text{rogue}} = 1.0$ rogue RyR/ μm^2 . Five figures from top to bottom represent membrane potential, cytoplasmic $[\text{Ca}^{2+}]_i$, SR luminal $[\text{Ca}^{2+}]_{\text{SR}}$, I_{NaCa} , and line-scan image along longitudinal direction of the cell, respectively, in failing ventricular myocyte.

N_{rogue} is increased by a step of 0.25 rogue RyR/ μm^2 ($P < 0.05$) as shown in Figure 3. Figure 4 shows typical simulation results when $N_{\text{rogue}} = 1.0$ rogue RyR/ μm^2 . After 3 action potentials paced by the cycle length of 1000 ms, a relatively large Ca^{2+} transient is observed, as well as a big inward I_{NaCa} and consequently a DAD without external stimulus in the heart failure myocytes. The linescan image in Figure 4 indicates the underlying microcosmic Ca^{2+} cycling on the subcellular level.

Besides, as N_{rogue} is increased to a larger value, Ca^{2+} transient elicited by spontaneous Ca^{2+} release and the depolarization of membrane potential enlarge further ($P < 0.05$), while the values of T_{peakCa} and $T_{\text{peak}V_m}$ decrease significantly ($P < 0.05$) (as shown in Figure 3). All these results together suggest close relationship between rogue RyRs and DADs.

3.3. Triggered Action Potential. As demonstrated above, the spontaneous Ca^{2+} release from SR causes a Ca^{2+} transient in cytoplasm and subsequently depolarizes the membrane potential even in the resting stage without any stimulus. Furthermore, the amplitude of calcium transient and the

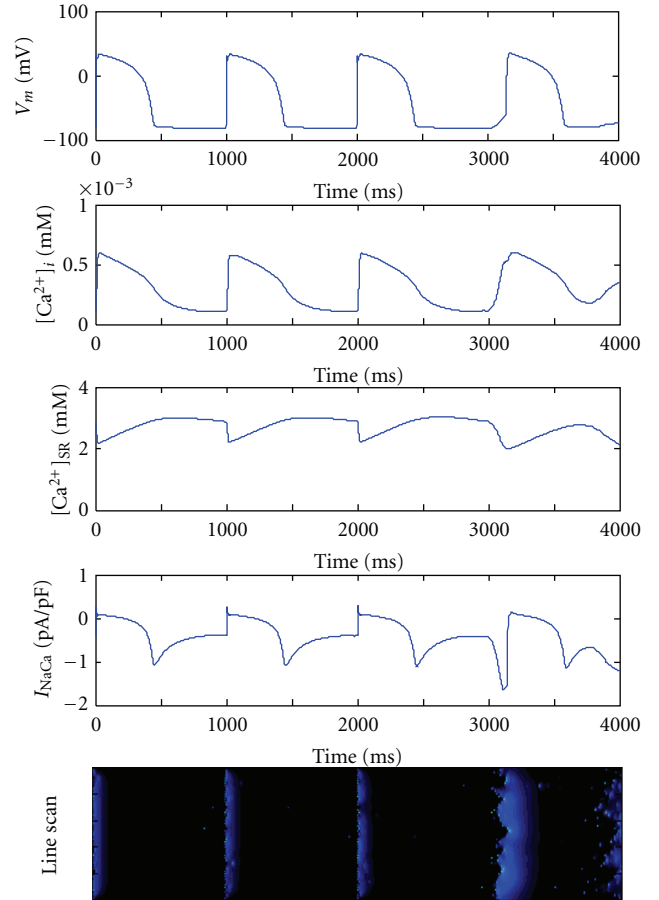


FIGURE 5: Triggered action potential in failing myocyte when $N_{\text{rogue}} = 1.75$ rogue RyR/ μm^2 . Five figures from top to bottom represent membrane potential, cytoplasmic $[\text{Ca}^{2+}]_i$, SR luminal $[\text{Ca}^{2+}]_{\text{SR}}$, I_{NaCa} , and line-scan image along longitudinal direction of the myocyte, respectively, in failing ventricular cell.

degree of depolarization are positively correlated to the distribution density of rogue RyR channels. Therefore, once the density of rogue RyRs is large enough, the membrane potential may be depolarized to reach the threshold that will trigger an action potential.

Figure 5 shows the time course of simulated membrane potentials: cytoplasmic Ca^{2+} concentration, SR Ca^{2+} store, the Na/Ca exchange current, as well as the Ca^{2+} dynamics at subcellular level. From the line-scan image we can see that, along the cellular longitudinal direction, many spontaneous Ca^{2+} waves are initiated nearly at the same time. These Ca^{2+} waves could propagate and diffuse to finally form a large wave. These Ca^{2+} releases rise the $[\text{Ca}^{2+}]_i$ quickly and drive a strong inward component of I_{NaCa} , which causes the depolarization of the membrane potential. When the membrane potential is depolarized to reach the threshold for activation of fast Na^+ channel, the large I_{Na} is produced very fast and induces an upstroke of the membrane potential. Then, the L-type Ca^{2+} channels will be subsequently activated and a flux of extracellular calcium ions burst into cytoplasm via the L-type calcium channels. This inflow of Ca^{2+} together

with the previously released Ca^{2+} from SR can activate the remaining available RyR channels and elicit an even larger Ca^{2+} transient in the cytoplasm. The other ionic channels at the membrane are successively opened and determine the morphology of AP together. Particularly, for the I_{NaCa} , it switches to a weak outward current during the plateau stage, but turns to a strong inward current in the repolarization stage of AP, by which the Ca^{2+} is ejected to the extracellular space.

When $N_{\text{rogue}} = 1.5$ rogue RyR/ μm^2 , triggered APs are observed in 11 simulations (totally 22 Monte Carlo simulations), that is, the probability of triggered AP is 50%. Moreover, when $N_{\text{rogue}} = 1.75$ rogue RyR/ μm^2 , triggered APs are found in 18 out of 21 Monte Carlo simulations, that is, the probability of triggered AP rises to 87.5%. On the contrary, when $N_{\text{rogue}} < 1.5$ rogue RyR/ μm^2 , no triggered AP is seen in our simulations.

To quantitatively investigate the effect of high dense rogue RyRs on Ca^{2+} handling, we also recorded the variations of $[\text{Ca}^{2+}]_i$ and membrane potential ($\Delta[\text{Ca}^{2+}]_i$ and ΔV_m) as well as T_{peakCa} and $T_{\text{peak}V_m}$. However, ΔV_m elicited by intensive Ca^{2+} release events is often large enough to activate I_{Na} . Consequently, the voltage upstroke induced by I_{Na} would overlap the original ΔV_m . Then, $\Delta[\text{Ca}^{2+}]_i$ by Ca^{2+} release events is also overlapped by the following inward-flowing I_{CaL} during a triggered AP. Under those conditions, the measurement of $\Delta[\text{Ca}^{2+}]_i$ and ΔV_m as well as T_{peakCa} and $T_{\text{peak}V_m}$ becomes very difficult. Thus, in our simulation, when $N_{\text{rogue}} \geq 1.5$ rogue RyR/ μm^2 , we set the I_{Na} to be zero after removing the external stimulus. By doing this, triggered AP will not be formed even when a DAD makes the membrane potential more positive than the threshold for I_{Na} . Therefore, we can calculate these parameters easily. Actually, our simulation results are shown in Figure 3 marked by arrows, from which we can conclude that, as N_{rogue} is increased from 1.5 to 1.75 rogue RyR/ μm^2 , the amplitude of $[\text{Ca}^{2+}]_i$ enlarges ($P < 0.05$), whereas the time to reach the peak does not change obviously ($P > 0.05$). However, the amplitude of a DAD increases significantly ($P < 0.05$), while the time to observe the DAD decreases ($P < 0.05$).

4. Discussion

4.1. Mechanism of Ca Handling in HF. Heart failure, a syndrome caused by significant impairments in cardiac function, has become one of the biggest human killers with a poor prognosis [30]. Ca^{2+} handling of cardiac cells in heart failure is always characterized by reduction in the amplitude as well as by slowed decay of Ca^{2+} transient [31]. The primary reason for decrease in the amplitude of Ca^{2+} transient is the partly unloaded Ca^{2+} store in SR. Three factors mainly accounting for the smaller store are (1) increased Ca^{2+} leak in the resting myocyte, (2) decreased activity of SR Ca^{2+} pump, and (3) increase in expression and/or activity of Na^+ - Ca^{2+} exchanger.

Despite the increased activity of Na/Ca exchanger, at the early stage of $[\text{Ca}^{2+}]_i$ decay, the net current of Na/Ca exchanger might be outward current (i.e., Ca^{2+} influx) or

weak inward current, due to longer AP plateau and higher plateau potential in failing myocyte. Therefore, slowed decay of Ca^{2+} transient is mainly due to decreased SR Ca^{2+} pump, which removes major amount of Ca^{2+} at the early stage of $[\text{Ca}^{2+}]_i$ decay. Only when the membrane potential is repolarized to a relatively negative voltage and $[\text{Ca}^{2+}]_i$ is still high that I_{NaCa} turns to a strong inward current and accelerates decay of Ca^{2+} transient at the late stage of $[\text{Ca}^{2+}]_i$ decay.

4.2. Arrhythmogenic Effect of Rogue RyRs. Besides pump failure, patients with severe heart failure are at high risk of sudden cardiac death generally triggered by a lethal arrhythmia [23, 32]. DADs are thought to be the primary mechanism underlying arrhythmia in failing heart [33]. In our simulation work, although the probability of firing of RyR clusters increases in resting failing cardiocytes, the spontaneous Ca^{2+} sparks could not elicit enough amplitude of Ca^{2+} transient to induce an obvious DAD in the absent of rogue RyRs. The existence of rogue RyR channels is of importance in initiation and propagation of spontaneous Ca^{2+} waves in ventricular myocytes with heart failure [14].

In this work, we propose a coupled mathematic model by integrating the spatiotemporal Ca^{2+} reaction-diffusion system into the cellular electrophysiological model. Rogue RyR channels are then incorporated into the coupled model to simulate subcellular Ca^{2+} dynamics and global cellular electrophysiology simultaneously under heart failure conditions. Our simulation results show that, in the presence of rogue RyRs, Ca^{2+} dynamics is more unstable and Ca^{2+} waves are more likely to be initiated than the condition without rogue RyRs. Different from sporadic sparks in a resting myocyte without Ca^{2+} waves, a number of SR Ca^{2+} release events occur intensively during the process of spontaneous occurrence of Ca^{2+} waves. These release events could elevate the amplitude of Ca^{2+} transient effectively and thus induce Ca^{2+} -dependent inward current (mainly via Na/Ca exchanger) which depolarizes the sarcolemma and leads to a DAD, or a triggered AP sometimes. For a given level of Ca^{2+} release in failing myocytes, inward depolarizing current becomes larger due to increased activity of Na/Ca exchanger. And increased membrane resistance owing to reduction of I_{K1} enables the same inward current to produce greater depolarization. Once a DAD elevates membrane potential to the threshold for activation of I_{Na} , a triggered AP is then formed. DADs and triggered AP are the primary triggered activities accounting for arrhythmias in heart failure.

4.3. Dependence of V_m on Density of Rogue RyRs. Without rogue RyR channels or with low distribution density, occurrence of spontaneous Ca^{2+} sparks and/or quarks is independent in time and space, which is unlikely to evolve into propagating Ca^{2+} waves with partially unloaded SR Ca^{2+} store. $[\text{Ca}^{2+}]_i$ variation elicited by these Ca^{2+} release events is slight. In our simulation, when $N_{\text{rogue}} = 0$ or 0.25 rogue RyR/ μm^2 , the amplitude of membrane potential depolarization is very small, only several mV, and the average

$T_{\text{peak}V_m}$ is big and extensive with large SEM. The morphology of membrane potential is very smooth without a distinct peak, so that this type of depolarization could not be referred to a genuine DAD.

However, as more rogue RyRs are distributed over the 2D plane, ΔV_m increases gradually, while the value of $T_{\text{peak}V_m}$ decreases but becomes more intensive. When the value of N_{rogue} is elevated to 1.5 rogue RyR/ μm^2 or bigger, the large membrane potential depolarization tends to evoke a triggered AP, and the probability of occurrence of triggered APs increases with the larger N_{rogue} . The reason is that larger number of rogue RyRs would increase the amplitude and rate of DADs by initiating more Ca^{2+} waves which occur more synchronously. Therefore, depolarization of V_m is indicated to be dependent on the distribution density of rogue RyR channels.

4.4. Limitations and Further Work. Because the rogue RyR remains to be a hypothetical channel rather than a determinate concept, experimental parameters of rogue RyRs are lacked. Some assumptions were made regarding the density, distribution, and kinetic of rogue RyR channels. In our work, a constant was used to represent Ca^{2+} release flux via a rogue RyR channel, while Ca^{2+} release flux via a cluster of RyRs was dependent on global luminal Ca^{2+} concentration ($[\text{Ca}^{2+}]_{\text{SR}}$) and local Ca^{2+} concentration ($[\text{Ca}^{2+}]_{i(x_i,y_i)}$). Besides, different N_{rogue} values were used to evaluate the effect of rogue RyR on Ca^{2+} cycling and membrane potential in failing heart.

Numerous key regulatory proteins, such as protein kinase A (PKA), Calstalin, CaMKII, and phosphatase, are bound to RyR, thus forming the junctional complex. RyR channels would be regulated via different signaling pathways [34]. For example, PKA phosphorylation dissociates FKBP12.6 from the RyR and thus makes the RyR channel unstable in failing hearts [35]. These regulating processes could not be mimiced by our present model. Besides, defective Ca^{2+} handling also occurs in many cardiac diseases, such as myocardial infarction, atrial fibrillation, and various arrhythmogenic paradigms. The coupled model is planned to be improved, and more relevant parameters should be added to investigate the potential mechanisms of Ca^{2+} dynamics in various kinds of cardiac diseases.

5. Summary

By integrating the spatiotemporal Ca^{2+} reaction-diffusion model into the cellular electrophysiological model, appearance of subcellular Ca^{2+} release events and evolution of waves together with dynamics of ionic concentration and membrane potential on the cellular level could be monitored simultaneously. By using the coupled model we investigate the effects of rogue RyRs on Ca^{2+} handling from subcellular to cellular level as well as electrophysiological properties in failing heart. The simulation results suggest that rogue RyR with tiny Ca^{2+} release flux should be an important factor in triggering arrhythmia in failing cardiac cells. Our work suggests the importance of rogue RyRs in

initiation of Ca^{2+} release events (especially Ca^{2+} waves) and consequently DADs or triggered APs. Our study indicates the arrhythmogenic effect of rogue RyRs and helps to elucidate a possible arrhythmia mechanism in failing heart.

Acknowledgments

This project is supported by the 973 National Basic Research & Development Program (2007CB512100) and the National Natural Science Foundation of China (81171421).

References

- [1] H. Cheng, W. J. Lederer, and M. B. Cannell, "Calcium sparks: elementary events underlying excitation-contraction coupling in heart muscle," *Science*, vol. 262, no. 5134, pp. 740–744, 1993.
- [2] C. Franzini-Armstrong, F. Protasi, and V. Ramesh, "Shape, size, and distribution of Ca^{2+} release units and couplons in skeletal and cardiac muscles," *Biophysical Journal*, vol. 77, no. 3, pp. 1528–1539, 1999.
- [3] E. G. Lakatta and T. Guarnieri, "Spontaneous myocardial calcium oscillations: are they linked to ventricular fibrillation?" *Journal of Cardiovascular Electrophysiology*, vol. 4, no. 4, pp. 473–489, 1993.
- [4] P. Lipp and E. Niggli, "Submicroscopic calcium signals as fundamental events of excitation-contraction coupling in guinea-pig cardiac myocytes," *Journal of Physiology*, vol. 492, no. 1, pp. 31–38, 1996.
- [5] P. Lipp, M. Egger, and E. Niggli, "Spatial characteristics of sarcoplasmic reticulum Ca^{2+} release events triggered by L-type Ca^{2+} current and Na^+ current in guinea-pig cardiac myocytes," *Journal of Physiology*, vol. 542, no. 2, pp. 383–393, 2002.
- [6] E. A. Sobie, S. Guatimosim, L. Gómez-Viquez et al., "The Ca^{2+} leak paradox and "rogue ryanodine receptors": SR Ca^{2+} efflux theory and practice," *Progress in Biophysics and Molecular Biology*, vol. 90, no. 1-3, pp. 172–185, 2006.
- [7] W. Xie, D. X. P. Brochet, S. Wei, X. Wang, and H. Cheng, "Deciphering ryanodine receptor array operation in cardiac myocytes," *Journal of General Physiology*, vol. 136, no. 2, pp. 129–133, 2010.
- [8] A. V. Zima, E. Bovo, D. M. Bers, and L. A. Blatter, " Ca^{2+} spark-dependent and -independent sarcoplasmic reticulum Ca^{2+} leak in normal and failing rabbit ventricular myocytes," *Journal of Physiology*, vol. 588, no. 23, pp. 4743–4757, 2010.
- [9] D. J. Santiago, J. W. Curran, D. M. Bers et al., "Ca sparks do not explain all ryanodine receptor-mediated SR Ca leak in mouse ventricular myocytes," *Biophysical Journal*, vol. 98, no. 10, pp. 2111–2120, 2010.
- [10] D. Baddeley, I. D. Jayasinghe, L. Lam, S. Rossberger, M. B. Cannell, and C. Soeller, "Optical single-channel resolution imaging of the ryanodine receptor distribution in rat cardiac myocytes," *Proceedings of the National Academy of Sciences of the United States of America*, vol. 106, no. 52, pp. 22275–22280, 2009.
- [11] N. MacQuaide, H. R. Ramay, E. A. Sobie, and G. L. Smith, "Differential sensitivity of Ca^{2+} wave and Ca^{2+} spark events to ruthenium red in isolated permeabilised rabbit cardiomyocytes," *Journal of Physiology*, vol. 588, no. 23, pp. 4731–4742, 2010.
- [12] D. X. P. Brochet, W. Xie, D. Yang, H. Cheng, and W. J. Lederer, "Quarky calcium release in the heart," *Circulation Research*, vol. 108, no. 2, pp. 210–218, 2011.

- [13] T. R. Shannon, S. M. Pogwizd, and D. M. Bers, "Elevated sarcoplasmic reticulum Ca^{2+} leak in intact ventricular myocytes from rabbits in heart failure," *Circulation Research*, vol. 93, no. 7, pp. 592–594, 2003.
- [14] L. Lu, L. Xia, X. Ye, and H. Cheng, "Simulation of the effect of rogue ryanodine receptors on a calcium wave in ventricular myocytes with heart failure," *Physical Biology*, vol. 7, no. 2, Article ID 026005, 2010.
- [15] L. T. Izu, J. R. H. Mauban, C. W. Balke, and W. G. Wier, "Large currents generate cardiac Ca^{2+} sparks," *Biophysical Journal*, vol. 80, no. 1, pp. 88–102, 2001.
- [16] L. T. Izu, W. G. Wier, and C. W. Balke, "Evolution of cardiac calcium waves from stochastic calcium sparks," *Biophysical Journal*, vol. 80, no. 1, pp. 103–120, 2001.
- [17] K. H. W. J. Ten Tusscher and A. V. Panfilov, "Alternans and spiral breakup in a human ventricular tissue model," *American Journal of Physiology*, vol. 291, no. 3, pp. H1088–H1100, 2006.
- [18] S. E. Lehnart, X. H. T. Wehrens, and A. R. Marks, "Calstabin deficiency, ryanodine receptors, and sudden cardiac death," *Biochemical and Biophysical Research Communications*, vol. 322, no. 4, pp. 1267–1279, 2004.
- [19] X. Ai, J. W. Curran, T. R. Shannon, D. M. Bers, and S. M. Pogwizd, " Ca^{2+} /calmodulin-dependent protein kinase modulates cardiac ryanodine receptor phosphorylation and sarcoplasmic reticulum Ca^{2+} leak in heart failure," *Circulation Research*, vol. 97, no. 12, pp. 1314–1322, 2005.
- [20] S. Nattel, A. Maguy, S. Le Bouter, and Y. H. Yeh, "Arrhythmogenic ion-channel remodeling in the heart: heart failure, myocardial infarction, and atrial fibrillation," *Physiological Reviews*, vol. 87, no. 2, pp. 425–456, 2007.
- [21] R. H. G. Schwinger, M. Bohm, U. Schmidt et al., "Unchanged protein levels of SERCA II and phospholamban but reduced Ca^{2+} uptake and Ca^{2+} -ATPase activity of cardiac sarcoplasmic reticulum from dilated cardiomyopathy patients compared with patients with nonfailing hearts," *Circulation*, vol. 92, no. 11, pp. 3220–3228, 1995.
- [22] D. J. Beuckelmann, M. Nabauer, and E. Erdmann, "Alterations of K^+ currents in isolated human ventricular myocytes from patients with terminal heart failure," *Circulation Research*, vol. 73, no. 2, pp. 379–385, 1993.
- [23] G. F. Tomaselli and D. P. Zipes, "What causes sudden death in heart failure?" *Circulation Research*, vol. 95, no. 8, pp. 754–763, 2004.
- [24] G. R. Li, C. P. Lau, A. Ducharme, J. C. Tardif, and S. Nattel, "Transmural action potential and ionic current remodeling in ventricles of failing canine hearts," *American Journal of Physiology*, vol. 283, no. 3, pp. H1031–H1041, 2002.
- [25] M. Nábauer, D. J. Beuckelmann, P. Überfuhr, and G. Steinbeck, "Regional differences in current density and rate-dependent properties of the transient outward current in subepicardial and subendocardial myocytes of human left ventricle," *Circulation*, vol. 93, no. 1, pp. 168–177, 1996.
- [26] C. R. Valdivia, W. W. Chu, J. Pu et al., "Increased late sodium current in myocytes from a canine heart failure model and from failing human heart," *Journal of Molecular and Cellular Cardiology*, vol. 38, no. 3, pp. 475–483, 2005.
- [27] G. Hasenfuss, W. Schillinger, S. E. Lehnart et al., "Relationship between Na^+ - Ca^{2+} -exchanger protein levels and diastolic function of failing human myocardium," *Circulation*, vol. 99, no. 5, pp. 641–648, 1999.
- [28] K. R. Sipido, P. G. A. Volders, M. A. Vos, and F. Verdonck, "Altered Na/Ca exchange activity in cardiac hypertrophy and heart failure: a new target for therapy?" *Cardiovascular Research*, vol. 53, no. 4, pp. 782–805, 2002.
- [29] O. I. Shamraj, I. L. Grupp, G. Grupp et al., "Characterisation of Na/K-ATPase, its isoforms, and the inotropic response to ouabain in isolated failing human hearts," *Cardiovascular Research*, vol. 27, no. 12, pp. 2229–2237, 1993.
- [30] D. W. Baker, D. Einstadter, C. Thomas, and R. D. Cebul, "Mortality trends for 23,505 medicare patients hospitalized with heart failure in Northeast Ohio, 1991 to 1997," *American Heart Journal*, vol. 146, no. 2, pp. 258–264, 2003.
- [31] Z. Kubalova, D. Terentyev, S. Viatchenko-Karpinski et al., "Abnormal intrastore calcium signaling in chronic heart failure," *Proceedings of the National Academy of Sciences of the United States of America*, vol. 102, no. 39, pp. 14104–14109, 2005.
- [32] D. M. Roden, "A surprising new arrhythmia mechanism in heart failure," *Circulation Research*, vol. 93, no. 7, pp. 589–591, 2003.
- [33] S. M. Pogwizd and D. M. Bers, "Cellular basis of triggered arrhythmias in heart failure," *Trends in Cardiovascular Medicine*, vol. 14, no. 2, pp. 61–66, 2004.
- [34] M. Yano, Y. Ikeda, and M. Matsuzaki, "Altered intracellular Ca^{2+} handling in heart failure," *Journal of Clinical Investigation*, vol. 115, no. 3, pp. 556–564, 2005.
- [35] S. O. Marx, S. Reiken, Y. Hisamatsu et al., "PKA phosphorylation dissociates FKBP12.6 from the calcium release channel (ryanodine receptor): defective regulation in failing hearts," *Cell*, vol. 101, no. 4, pp. 365–376, 2000.

Research Article

Impact of Competitive Flow on Hemodynamics in Coronary Surgery: Numerical Study of ITA-LAD Model

Jinli Ding, Youjun Liu, Feng Wang, and Fan Bai

College of Life Science and Bioengineering, Beijing University of Technology, Beijing 100124, China

Correspondence should be addressed to Youjun Liu, lyjlma@bjut.edu.cn

Received 20 June 2012; Revised 27 July 2012; Accepted 30 July 2012

Academic Editor: Ling Xia

Copyright © 2012 Jinli Ding et al. This is an open access article distributed under the Creative Commons Attribution License, which permits unrestricted use, distribution, and reproduction in any medium, provided the original work is properly cited.

Competitive flow from native coronary artery is considered as a major factor in the failure of the coronary artery bypass grafts. However, the physiological effects are not very clear. The aim is to research the impact of competitive flow caused by different left anterior descending (LAD) artery stenosis degrees on hemodynamics in internal thoracic artery (ITA) bypass graft. An idealized ITA-LAD model was built in CAD tools. The degree of the competitive flow was divided into five classes according to different LAD stenosis degrees: higher (no stenosis), secondary (30% stenosis), reduced (50% stenosis), lower (75% stenosis) and no competitive flow (fully stenosis). Finite volume method was employed for the numerical simulation. The flow velocity distributions, wall shear stress and oscillatory shear index were analyzed. Results showed that higher competitive flow in the bypass graft would produce unbeneficial wall shear stress distribution associating with endothelial dysfunction and subsequent graft failure. The coronary bypass graft surgery was preferred to be carried out when the LAD stenosis was higher than 75%.

1. Introduction

In the treatment of coronary artery stenosis, the arterial grafting causes the blood of the bypass graft flowing into the native coronary artery, and competitive flow is often observed near the end-to-side anastomosis region. Several reports provided that competitive flow in the native coronary artery was related to the occlusion or narrowing of the bypass graft supplying this coronary vessel. For example, Pevni et al. suggested competitive flow was the cause for nonfunctioning grafts to vessels with noncritical stenosis (70%), when grafts were occluded or severely stenotic [1]. Nordgaard et al. assessed whether coronary graft flow patterns are affected differently by native coronary competitive flow or by stenosis of the coronary anastomosis based on nine pigs underwent off-pump grafting of the left internal thoracic artery to the left anterior descending artery (LAD). And it was concluded that the mammary graft flow was significantly reduced by native coronary competitive flow, but marginally decreased by a stenotic anastomosis of 75% mean luminal stenosis [2]. Kawamura et al. studied the effect of competitive flow on patency rate of the internal thoracic artery to the left anterior descending artery bypass from the concomitant saphenous

vein (SV) graft in the left coronary artery, based on 313 patients who had two bypasses to the left coronary artery including 1 in situ ITA-LAD graft. It was also concluded that competitive flow from SV graft could play an important role in occlusion of the in situ arterial graft [3]. Runwei et al. studied the relation between competitive flow and graft flow in coronary artery bypass grafting based on twelve adult healthy dogs and concluded that competitive flow would restrain the graft flow [4]. The patency of coronary artery bypass grafts (CABGs) is mainly determined by the progression of atherosclerosis and intimal hyperplasia within the grafts as well as technical failures [5]. It has been reported that competitive flow is associated with graft failure, and it is considered to be one of the major factors affecting early arterial graft patency and causing the graft to constrict and fail [6]. Moreover, competitive flow is thought to determine the narrowing of the whole length of the left internal thoracic artery graft, the so-called “string phenomenon” [7].

Although, the negative impact of competitive flow on graft patency or failure has been reported in several studies, the exact pathophysiological effects are not fully understood because most of these studies do not provide clear explanations for their findings. Hemodynamics has been widely

acknowledged to have significant influence on the arterial diseases. Flow disturbances are confirmed to be related to the intimal hyperplasia and arterial thrombosis [8, 9]. Wall shear stress (WSS) may play an important role in graft patency after CABG [10]. The association between competitive flow and hemodynamics is still unclear. There is rare literature focusing their study on this area, except Qiang et al. who investigated the impact of competitive flow on wall shear stress in mammary artery bypass grafts and confirmed graft flow was highly dependent on the degree of competitive flow [11]. In that paper, competitive flow was simply divided into three degrees and the degree of LAD stenosis was not fully studied. The associations between the degree of LAD stenosis and hemodynamics were not clear.

The aim of the present study is to numerically research the impact of competitive flow on hemodynamics in ITA-LAD model with different degrees of LAD stenosis. This study will give bright understanding of competitive flow and clinical help to surgeons in the treatment of proximal LAD stenosis.

2. Method

2.1. Model. An idealized coronary artery bypass graft models were built according to the common ITA-LAD bypass design in the treatment of the LAD stenosis (Figure 1). The diameter of the bypass graft was 4.6 mm. The diameter of the native LAD was 4.5 mm [12, 13]. The anastomosis angle of the bypass graft was approximately 45° . The model was imported into the commercial software ANSYS-CFX for meshing. A hexahedral mesh was mainly generated. In order to highlight the hemodynamic features near the wall, the boundary mesh was refined. A mesh sensitivity analysis was carried out using a simple steady computation by comparing the mean pressure and wall shear stress distributions to ensure the accuracy of the simulations. Based on the principle of the acceptable error less than 1%, finally, approximately 1,018,002 grid numbers were generated for the ITA-LAD model.

2.2. Computational Fluid Dynamics. Finite volume method was employed for the computational fluid dynamics (CFD). The duration of a cardiac cycle is 0.8 s. The density and dynamic viscosity of blood fluid are 1050 kg/m^3 and $0.0035 \text{ Pa}\cdot\text{s}$, respectively. The blood flow velocity profile of the LAD artery and the bypass graft (Figure 2) were measured from in vivo experiments of eighteen pigs [12, 13]. The degree of the competitive flow in each option was divided into five classes according to different LAD stenosis: higher (no stenosis), secondary (30% stenosis), reduced (50% stenosis), lower (75% stenosis), and no competitive flow (fully stenosis). A relative pressure of zero was set at the outlet. All the arterial walls were assumed to be rigid with the nonslip conditions. The maximum Reynolds number in all the simulations was approximately 1050, and, therefore, laminar flow was studied. The blood flow was assumed as nonsteady, Newtonian and incompressible flow. The adopted cyclic convergence criterion was based on the velocity components and pressure calculations. In addition, a relative error of less

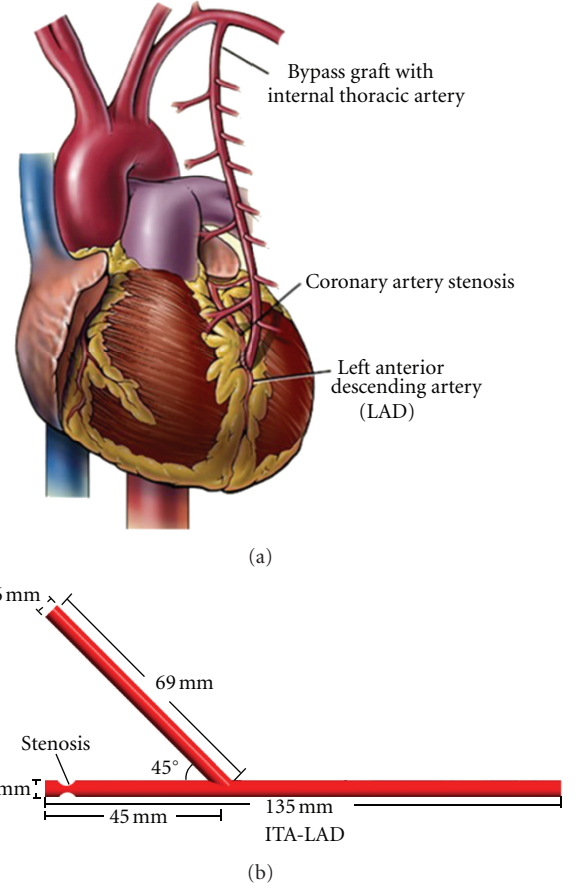


FIGURE 1: The schematic diagram of ITA-LAD bypass graft (a) and the idealized ITA-LAD model (b).

than $1e - 6$ for each calculation was accepted. The Navier-Stokes equations were solved using the ANSYS-CFX package (version 12) on a Microsoft Windows XP 32-bit PC with 4 GB RAM and a dual-core 2.83 GHz CPU. Three cardiac cycles with a fixed time step of 0.001 s were adopted. Comparing the results between the third and the second cardiac cycles, the errors of pressure and wall shear stress were all less than 0.8%. In our opinion, these errors became acceptable, and the results in the third cardiac cycle were used in this study.

2.3. Definition of Time-Averaged Wall Shear Stress and Oscillatory Shear Index. Wall shear stress plays an important role in graft patency after CABG [10]. The oscillatory shear index (OSI) is a measure which allows quantifying the change in direction and magnitude of the wall shear stress [10]. And areas of high OSI are predisposed to endothelial dysfunction and atherogenesis [14]. Therefore, time-averaged wall shear stress (TAWSS) and OSI were calculated according to their expressions [11]:

$$\begin{aligned} \text{TAWSS} &= \frac{1}{T} \int_0^T |\vec{\tau}_w| dt \\ \text{OSI} &= \frac{1}{2} \left(1 - \frac{\left| \int_0^T \vec{\tau}_w dt \right|}{\int_0^T |\vec{\tau}_w| dt} \right), \end{aligned} \quad (1)$$

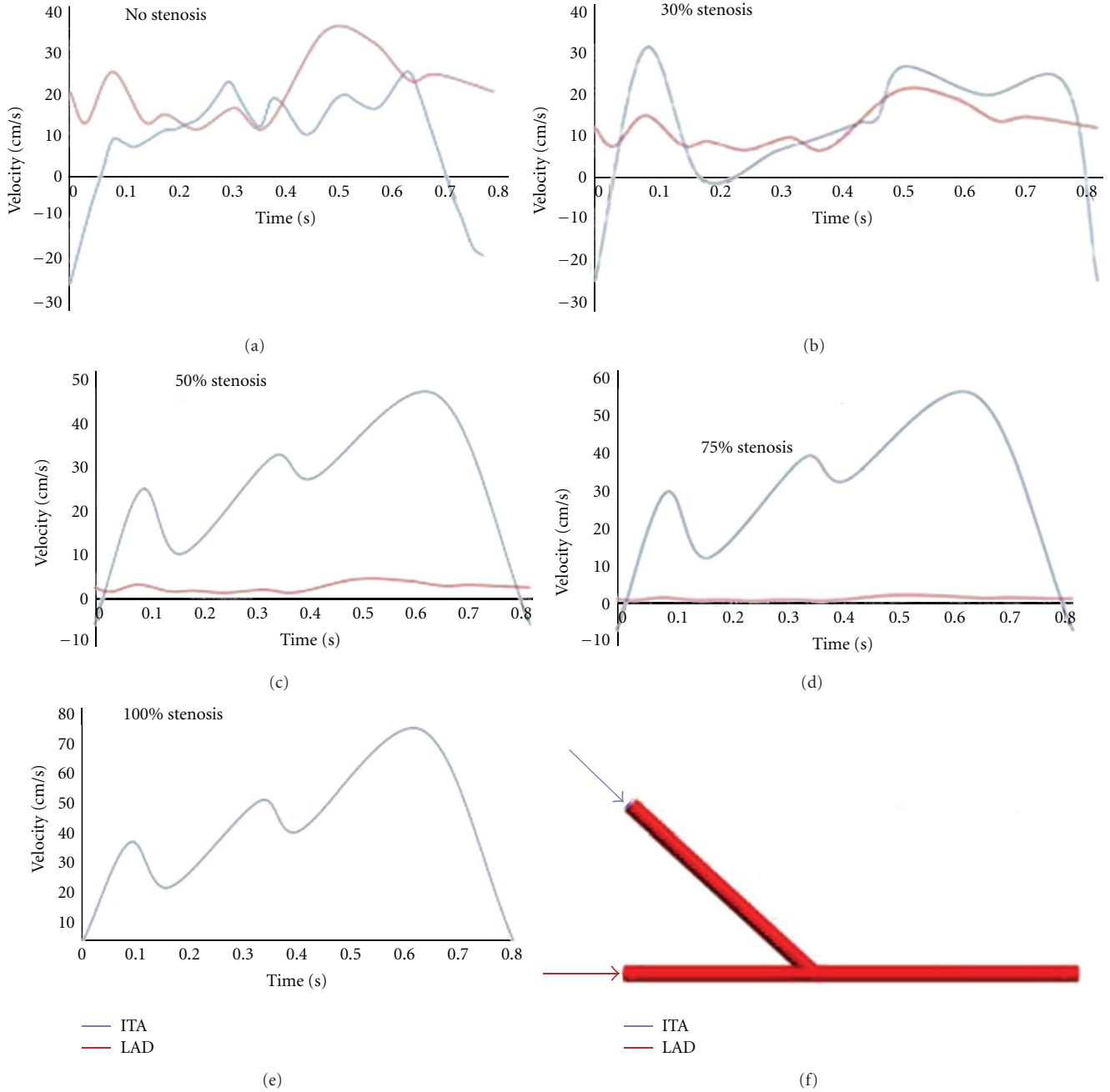


FIGURE 2: The flow conditions.

where $\vec{\tau}_w$ is the wall shear stress vector, T is the time period of the flow cycle, and τ_0 is the wall shear stress for Poiseuille flow at the mean flow Reynolds number. OSI ranges from 0 to 0.5, where 0 describes a total unidirectional wall shear stress and 0.5 means an oscillatory shear flow with a net amount of zero wall shear stress [11].

3. Results

3.1. Flow Pattern. Three typical times including 0.05 s, 0.55 s, and 0.75 s are assigned for the analysis of the flow details. The flow velocity vector maps in the middle section of the

five conditions are shown in Figure 3. It is obvious that the flow velocity distributions in the proximal LAD and ITA were mainly influenced by the flow conditions on LAD and ITA inlets, respectively. The higher the degree of LAD stenosis was, the lower the mean velocity in the proximal LAD artery was. And the opposite phenomena were observed in the bypass graft.

At the initial and final periods of the cardiac cycle when the stenosis was lower than 50%, obvious reverse flow was observed in ITA (Figure 2). This would result in lower velocity flow or even reverse flow in the distal LAD artery (Figure 3). However, this phenomenon was hardly observed

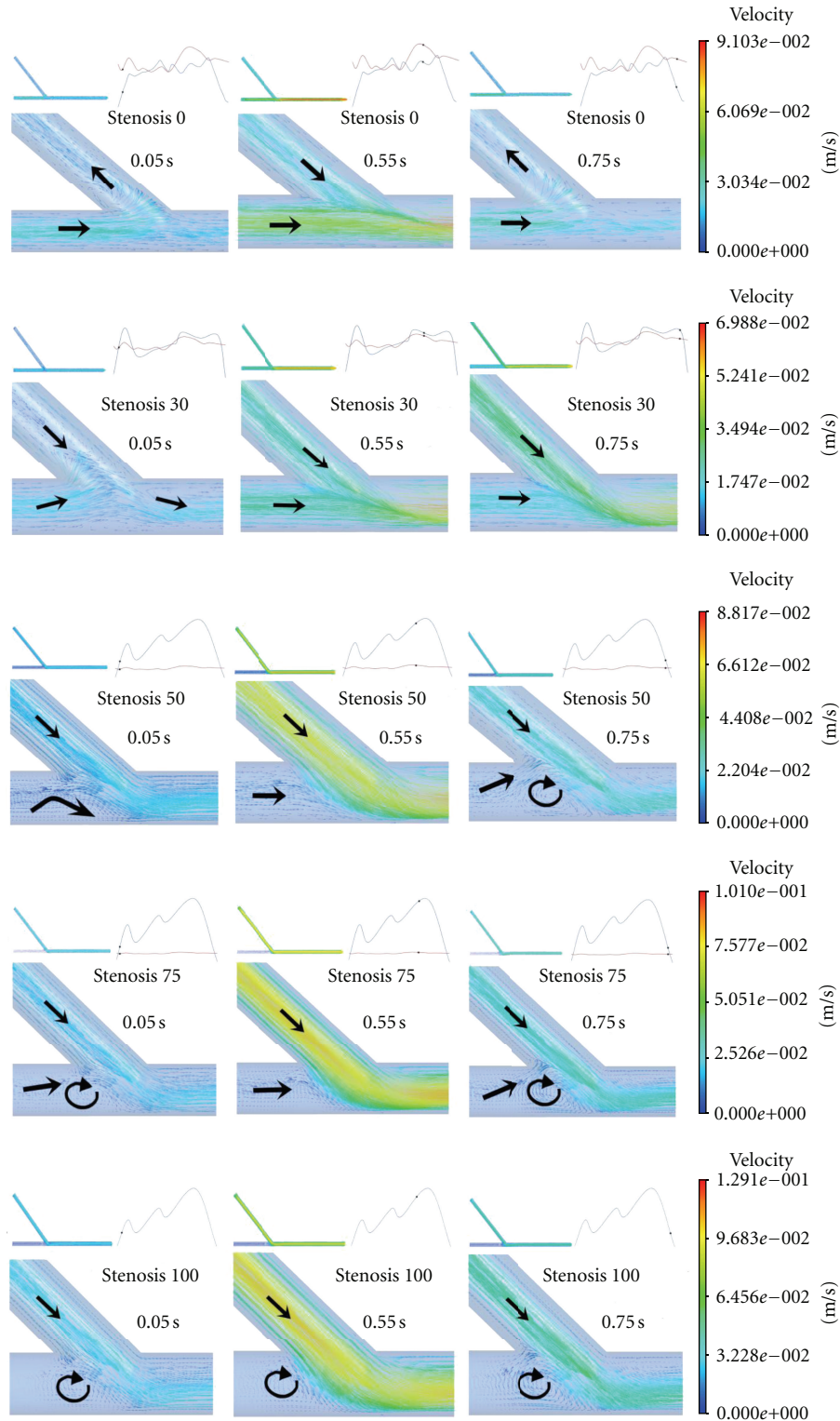


FIGURE 3: The flow velocity contour maps in the middle section for the nine conditions.

when the stenosis was higher than 75%. The flow velocity distributions were different according to different inlet conditions, especially near the anastomotic region where disturbed flows, including flow recirculation and flow separation, were observed.

3.2. Wall Shear Stress Distributions. The wall shear stress distributions in the five conditions are shown in Figure 4. Obviously, the highest wall shear stresses are all concentrated on the toe or bed of the anastomosis. The quick variation of wall shear stress mainly appeared near the anastomosis

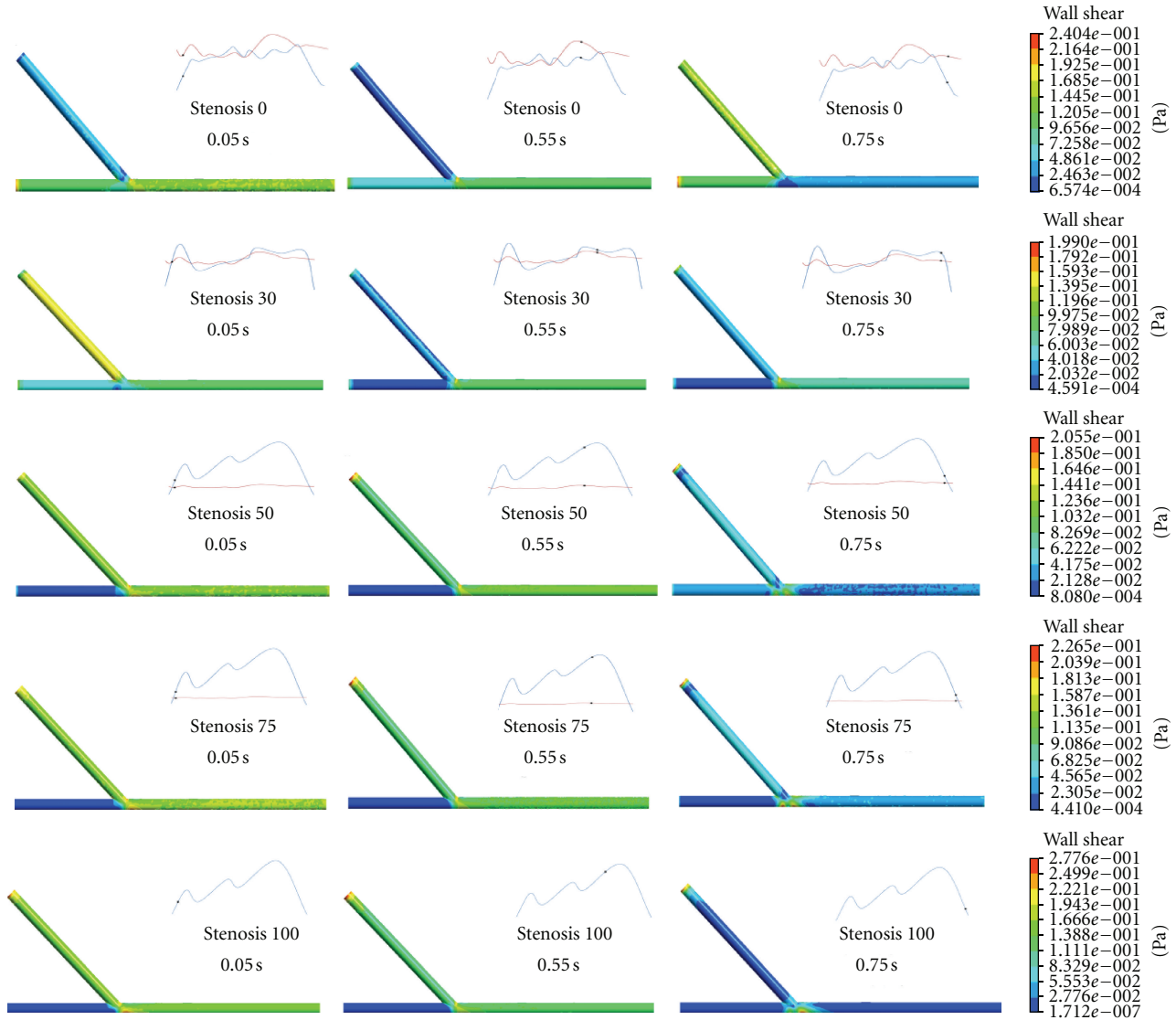


FIGURE 4: The wall shear stress distributions in the five conditions.

region. The TAWSS and OSI were calculated in the bypass graft, as Figure 5 shows. The TAWSS ranged from 0.1–0.24 Pa, while OSI ranged from 0.02–0.25 for the five conditions.

4. Discussions

The purpose of this study is to investigate the physiological effect of competitive flow on hemodynamics in coronary artery bypass graft. Different degrees of the competitive flow caused by different LAD stenosis were studied in this study.

The flow results shown in Figure 3 revealed that the flow details in the bypass graft were mainly affected by their inlet flow conditions. No disturbed flow was observed inside of each graft except the region near the anastomosis. This may indicate that the degree of competitive flow has significant influence on the flow pattern near the anastomosis. Obvious reverse flow was observed in ITA in the higher, secondary

and reduced competitive flow, and this would result in lower velocity flow or even reverse flow in the distal LAD artery. This coincides with the research from Bezon et al. and Berger et al. who reported that the patency rate of the internal thoracic artery to the left anterior descending artery bypass is reduced by competitive flow [15, 16].

The aetiology of graft failure due to competitive flow has not been thoroughly investigated. Wall shear stress plays an important role in graft patency after CABG [10, 17]. Also, areas of high OSI are predisposed to endothelial dysfunction and atherogenesis [14]. Results of our study showed that the TAWSS increased gradually and OSI decreased gradually as the degree of LAD stenosis became higher. Comparing to the TAWSS for no competitive flow, it decreased 7.8%, 34.6%, 53.4%, and 57.3% for that of lower, reduced, secondary, and higher competitive flow, respectively. Comparing to the OSI for no competitive flow, it increased 16%, 102.4%, 685.8%, and 1035.8% for that of lower, reduced, secondary, and

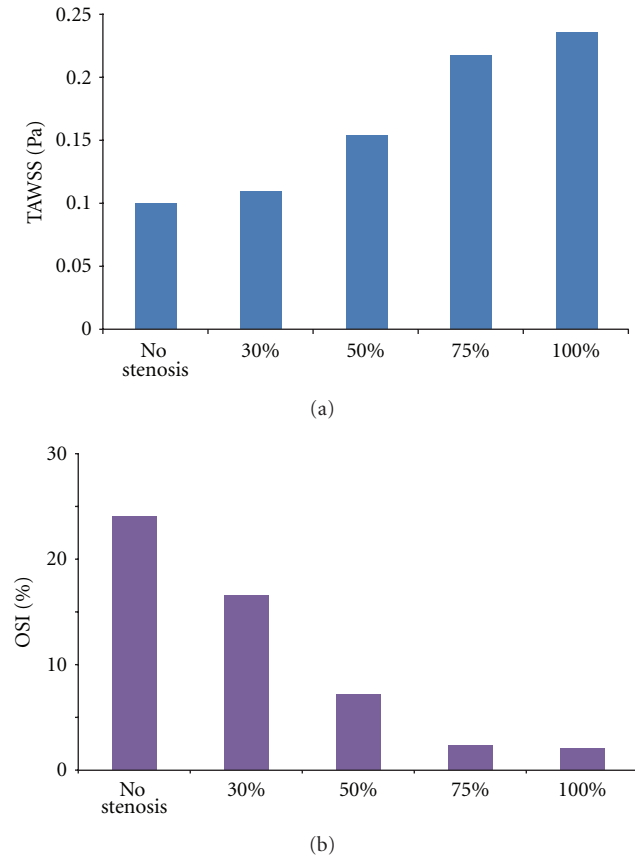


FIGURE 5: The TAWSS (a) and OSI (b) distributions.

higher competitive flow, respectively. It can be seen that the higher competitive flow resulted in the least TAWSS and the OSI in the ITA graft, which indicated that higher competitive flow in the bypass graft would lead to unbeneficial wall shear stress distributions on the bypass graft for low TAWSS and high OSI would increase the probability of intimal hyperplasia and atherogenesis. This might explain why the higher competitive flow would result in the high risk of bypass failure.

There are also rare researches reporting the clinical associations between CABG and degree of stenosis. Results in this study showed that TAWSS was highest and OSI was lowest for the no competitive flow condition. From the view point of hemodynamics, the probability of intimal hyperplasia and atherogenesis was less when the LAD was fully occluded. Furthermore, the differences of TAWSS and OSI between the lower competitive flow (75% stenosis) condition and no competitive flow (100% stenosis) condition were slight. This indicated that lower competitive flow resulted in TAWSS and OSI similar to the no-competitive flow condition, which agreed well with Nordgaard's reports [2]. Unfortunately, when the stenosis was lower than 75%, the TAWSS decreased and OSI increased fast towards an unbeneficial situation. It might be concluded that, from the comparisons of TAWSS and OSI, the CABG was preferred to be carried out when the LAD stenosis was higher than 75%.

CFD has been widely used for the recreation of flow fields existing in idealized or complex geometries of pulsatile flow conditions [18, 19]. The accuracy of a CFD simulation is highly dependent on the quality of geometry and boundary conditions used. However, there are some limitations in this study. The time-dependent pressure conditions were ignored in the CFD simulation. Although the conclusions in this study agreed well with other literatures, it seemed difficult in generalizing our findings to actual one or every patient and describing the detailed hemodynamic features in every coronary bypass anastomosis due to large variation in the anastomotic structure of coronary arteries. Other limitations are related to the CFD models and material assumptions. Firstly, the geometrical models were idealized models rather than the realistic anatomy. This simplification could affect the flow details inside the bypass graft. Secondly, compressible blood, non-Newtonian rheology, and elastic wall were not considered in the CFD simulations as lots of researches did [10, 17, 19]. All these have certain influences on the simulation results and will be considered in the future work. Thirdly, no clinical validation was provided. Future work will dedicate to the clinical experiments and fluid-structure interactions.

5. Conclusions

Physiological effect of competitive flow on hemodynamics in coronary artery bypass graft was studied in this paper. Different degrees of the competitive flow caused by different stenosis in the ITA-LAD option were considered. It was concluded that higher competitive flow in the bypass graft would produce unbeneficial wall shear stress distributions consistent with endothelial dysfunction and subsequent graft failure. Lower competitive flow generated higher TAWSS and lower OSI similar to the no-competitive flow condition. The coronary bypass graft surgery was preferred to be carried out when the LAD stenosis was higher than 75%.

Conflict of Interests

The authors declare that there is no conflict of interests.

Acknowledgments

This work was supported by the National Natural Science Foundation of China (11172016) and Natural Science Foundation of Beijing (3092005).

References

- [1] D. Pevni, I. Hertz, B. Medalion et al., "Angiographic evidence for reduced graft patency due to competitive flow in composite arterial T-grafts," *The Journal of Thoracic and Cardiovascular Surgery*, vol. 133, no. 5, pp. 1220–1225, 2007.
- [2] H. Nordgaard, D. Nordhaug, I. Kirkeby-Garstad, L. Løvstakken, N. Vitale, and R. Haaverstad, "Different graft flow patterns due to competitive flow or stenosis in the coronary anastomosis assessed by transit-time flowmetry in a porcine model," *European Journal of Cardio-Thoracic Surgery*, vol. 36, no. 1, pp. 137–142, 2009.

- [3] M. Kawamura, H. Nakajima, J. Kobayashi et al., "Patency rate of the internal thoracic artery to the left anterior descending artery bypass is reduced by competitive flow from the concomitant saphenous vein graft in the left coronary artery," *European Journal of Cardio-Thoracic Surgery*, vol. 34, no. 4, pp. 833–838, 2008.
- [4] M. Runwei, W. Ruobin, G. Huiming, and Z. Shaoyi, "Relation between competitive flow and graft flow in coronary artery bypass grafting," *Chinese Journal of Clinical Thoracic and Cardiovascular Surgery*, vol. 12, pp. 335–338, 2005.
- [5] O. N. Nwasokwa, "Coronary artery bypass graft disease," *Annals of Internal Medicine*, vol. 123, no. 7, pp. 528–545, 1995.
- [6] J. F. Sabik and E. H. Blackstone, "Coronary artery bypass graft patency and competitive flow," *Journal of the American College of Cardiology*, vol. 51, no. 2, pp. 126–128, 2008.
- [7] R. P. Villareal and V. S. Mathur, "The string phenomenon. An important cause of internal mammary artery graft failure," *Texas Heart Institute Journal*, vol. 27, no. 4, pp. 346–349, 2000.
- [8] J. Chiu and S. Chien, "Effects of disturbed flow on vascular endothelium: pathophysiological basis and clinical perspectives," *Physiological Reviews*, vol. 91, pp. 327–387, 2011.
- [9] L. C. H. John, "Biomechanics of coronary artery and bypass graft disease: potential new approaches," *The Annals of Thoracic Surgery*, vol. 87, pp. 331–338, 2009.
- [10] H. Nordgaard, A. Swillens, D. Nordhaug et al., "Impact of competitive flow on wall shear stress in coronary surgery: computational fluid dynamics of a LIMA-LAD model," *Cardiovascular Research*, vol. 88, no. 3, pp. 512–519, 2010.
- [11] F. Qiang, B. Yanwen, Y. Jianmin et al., "Effects of competitive blood flow from differently stenotic coronary artery on internal mammary artery graft flow," *Journal of Shandong University*, vol. 44, pp. 364–367, 2006.
- [12] Y. Jianmin, *The experimental study of the effect of competitive flow and vasoactive drugs on arterial and veinal grafts flow after coronary artery bypass grafting [Ph.D. dissertation]*, Shandong University, 2006.
- [13] Y. Fukumoto, T. Hiro, T. Fujii et al., "Localized elevation of shear stress is related to coronary plaque rupture. A 3-dimensional intravascular ultrasound study with in-vivo color mapping of shear stress distribution," *Journal of the American College of Cardiology*, vol. 51, no. 6, pp. 645–650, 2008.
- [14] P. F. Davies, "Hemodynamic shear stress and the endothelium in cardiovascular patho-physiology," *Nature Clinical Practice Cardiovascular Medicine*, vol. 6, pp. 16–26, 2009.
- [15] E. Bezon, J. N. Choplain, Y. A. Maguid, A. A. Aziz, and J. A. Barra, "Failure of internal thoracic artery grafts: conclusions from coronary angiography mid-term follow-up," *Annals of Thoracic Surgery*, vol. 76, no. 3, pp. 754–759, 2003.
- [16] A. Berger, P. A. MacCarthy, U. Siebert et al., "Long-term patency of internal mammary artery bypass grafts: relationship with preoperative severity of the native coronary artery stenosis," *Circulation*, vol. 110, no. 11, pp. II36–II40, 2004.
- [17] P. Vasava, P. Jalali, M. Dabagh, and P. J. Kolari, "Finite element modelling of pulsatile blood flow in idealized Model of human aortic arch: study of hypotension and hypertension," *Computational and Mathematical Methods in Medicine*, vol. 2012, Article ID 861837, 14 pages, 2012.
- [18] I. E. Vignon-Clementel, A. L. Marsden, and J. A. Feinstein, "A primer on computational simulation in congenital heart disease for the clinician," *Progress in Pediatric Cardiology*, vol. 30, no. 1-2, pp. 3–13, 2010.
- [19] T. Chaichana, Z. Sun, and J. Jewkes, "Computational fluid dynamics analysis of the effect of plaques in the left coronary artery," *Computational and Mathematical Methods in Medicine*, vol. 2012, Article ID 504367, 9 pages, 2012.

Research Article

An Image-Based Model of the Whole Human Heart with Detailed Anatomical Structure and Fiber Orientation

Dongdong Deng,¹ Peifeng Jiao,² Xuesong Ye,¹ and Ling Xia¹

¹Key Lab of Biomedical Engineering of Ministry of Education, Department of Biomedical Engineering, Zhejiang University, Hangzhou 310027, China

²Institute of Clinical Anatomy, Southern Medical University, Guangzhou 510515, China

Correspondence should be addressed to Ling Xia, xialing@zju.edu.cn

Received 13 June 2012; Accepted 20 July 2012

Academic Editor: Feng Liu

Copyright © 2012 Dongdong Deng et al. This is an open access article distributed under the Creative Commons Attribution License, which permits unrestricted use, distribution, and reproduction in any medium, provided the original work is properly cited.

Many heart anatomy models have been developed to study the electrophysiological properties of the human heart. However, none of them includes the geometry of the whole human heart. In this study, an anatomically detailed mathematical model of the human heart was firstly reconstructed from the computed tomography images. In the reconstructed model, the atria consisted of atrial muscles, sinoatrial node, crista terminalis, pectinate muscles, Bachmann's bundle, intercaval bundles, and limbus of the fossa ovalis. The atrioventricular junction included the atrioventricular node and atrioventricular ring, and the ventricles had ventricular muscles, His bundle, bundle branches, and Purkinje network. The epicardial and endocardial myofiber orientations of the ventricles and one layer of atrial myofiber orientation were then measured. They were calculated using linear interpolation technique and minimum distance algorithm, respectively. To the best of our knowledge, this is the first anatomically-detailed human heart model with corresponding experimentally measured fibers orientation. In addition, the whole heart excitation propagation was simulated using a monodomain model. The simulated normal activation sequence agreed well with the published experimental findings.

1. Introduction

Heart modeling can quantitatively study the physiological and pathological mechanism of the heart diseases, such as arrhythmias, atrial, and ventricular fibrillation, and hence to help improve their diagnosis and treatment. These developed models can also be used for medical teaching [1]. In the last several decades, a lot of research has been done on the heart modeling, from genes to the whole organ [2–4]. The hearts used for modeling were mainly from canines [5, 6], rabbits [7–9], mice [10], pigs [11], or humans [3, 12–17].

Mathematical modeling of the heart anatomy is a prerequisite for cardiac electro-mechanical simulations. Simulating the main cardiac features, including cardiac rhythms [18], mechanics [19–21], hemodynamics [22], fluid-structure interaction, energy metabolism [23], and neural control [24], can only be achieved with detailed heart structure information. It needs to be emphasized that these properties

are interrelated so that any changes in one property may influence others, which makes the virtual heart modeling complicated. Therefore, giving full consideration to the anatomical structure of the heart is essential.

Several mathematical human heart models have been constructed to study its electrophysiological properties using the computed tomography and other modern medical imaging methods [25, 26]. However, the space resolution of these computed tomography-based heart models was not very high [12, 27]. It was 1 mm for the model developed by Lorange and Gulrajani, and the final model contained approximately 250, 000 points. The model developed by Weixue et al. [27] contained approximately 65,000 myocardial discrete units with a spatial resolution of 1.5 mm. Furthermore, neither of the two models included the conduction system. Later, human atrial models were constructed from the MRI images [16], and some of them included the atrial conduction system [14]. A human ventricular model with

fiber orientations and laminar structure was constructed by Rohmer et al. [17] using the DT-MRI. In addition, the Visible Human Project provides a useful data source for detailed human heart anatomical modeling [15]. However, none of the above-mentioned models described the complete geometry of the human heart, including both the atria and the ventricles, the conduction system, and the fiber orientation.

The conduction system plays an important role in the electrical propagation. It contains SAN, interatrial pathways, AVN, and intraventricular conduction pathways. Conduction system abnormalities could lead to cardiac arrhythmias. However, it is practically difficult to distinguish the conduction system from the surrounding tissues based on the current computed tomographic or MRI images. The heart models in early days mainly focused on the geometry of the heart without considering its conduction system [28–30]. Recently, researchers have attempted to construct the atrial conduction system [14, 31] as well as the ventricular conduction system with the His-Purkinje system [32]. However, none of the previously published models contain both the atrial and ventricular conduction systems.

Myofiber orientation also plays an important role in the electrical conduction and mechanical contraction. Many experimental procedures have been developed to measure myofiber orientation. In early days, the measurement was usually restricted into small areas. After full thickness blocks were removed from different sites of the heart, they were cut into serial slices from epicardium to endocardium. The fiber orientation was measured from each slice [33–36]. In the early 90s, a quantitative method was developed to measure the whole ventricular fiber orientations [5], which has been widely used by other studies [6, 7, 11]. However, this method is still very time-consuming. Advanced imaging technique, including the automated confocal microscopy, polarization microscopy and two-photon tissue cytometry, and DT-MRI, makes the measurement of fiber orientation and laminar structure possible [37–39]. However, most of these methods have been only applied to the measurement on the ventricle, not the atria.

In order to validate the function of the anatomic model, the cardiac action potential (AP) and the simulation of cardiac electrophysiology should be simulated and validated with experimental data. Until now, different AP models have been developed from different species. They were mainly based on the Hodgkin-Huxley (HH) equation, which could be used to calculate the flow of ions in the membrane and hence calculate the membrane potential changes. There are also a lot of human AP models, which include atrial working muscles [40–44], SAN [31, 45], Purkinje fibers [46, 47], and ventricle [48–51]. In our simulation, because the newly developed models are much more time-consuming and less robust in the three-dimensional simulation, the commonly used CRN model [41] and the ten Tusscher model [49] were applied to the atrial and ventricular cells.

Regarding the simulation of cardiac electrophysiology, the reaction-diffusion equations were commonly used in combination with the anatomic and AP models. Modeling of the electrical conduction in early days was usually based

on the cellular automata [2, 3, 27, 52, 53]. Later, with the enhancement of computation capacity, ionic models have been gradually applied to small-scale simulation of excitation conduction. In 1978, Tung introduced the “bidomain model” to simulate the propagation of excitation [54]. However, the bidomain model requires a major dimension of the matrix inversion, and very large computing capacity. Therefore, the monodomain model was often used [55–59] because only the changes of cell membrane potential are calculated. Studies have also shown that there were no obvious differences for the computed excitation sequence between the bidomain model and monodomain model [60].

The aim of this study is to construct a whole human heart model with detailed anatomical structure which contains atrial and ventricular conduction systems and fiber orientations. Based on the constructed heart model, the human AP models will be assigned to different parts of the heart. Finally, the normal electrical propagation will be simulated and compared with the experimental data.

2. Materials and Methods

2.1. Cardiome-CN Human Heart Anatomical Model

2.1.1. Data Acquisition. After the confirmation of brain death, the heart specimen (Figures 1(a), 1(b)) from a healthy male adult with a tragic accident was donated to Zhujiang Hospital, Southern Medical University, P.R. China, by his family members. They gave the written consent. The use of the heart for research purpose was approved by the Ethics Committee of the Southern Medical University. The National Rules and Regulations on Heart research were strictly followed. The pretreatment of the heart and image data collection were performed at the Southern Medical University, and the follow-up works including image processing, the three-dimensional (3D) heart anatomical reconstruction was completed at Zhejiang University.

Firstly, the pericardium was carefully stripped off and removed with the large blood vessels (aorta and pulmonary arteries) retained for perfusion. The lead oxide and gelatin solution (gelatin and water ratio was 5%; lead oxide solution and water ratio was 25%) were then injected into the chambers of the heart through the aorta [61]. After the solution was cooled down, the heart specimen was scanned using a spiral CT (Philips/Brilliance 64). The raw CT images had a resolution of 512 pixels by 512 pixels, and the total number of images was 531 with the spatial resolution of $0.3574 \text{ mm} \times 0.3574 \text{ mm} \times 0.33 \text{ mm}$ (Figure 1).

2.1.2. Image Processing Procedure for the Construction of Human Heart Model. The commercial software ScanIP (Simpleware Inc.) was used to segment and reconstruct the anatomy of the human heart with some manual intervention to achieve the maximum accuracy. The processing procedure is briefly summarized as follows.

- (1) Contrast adjustment: as can be seen in Figure 2(a), the contrast between myocardium and gelatin inside the heart cavity was not obvious in the original CT

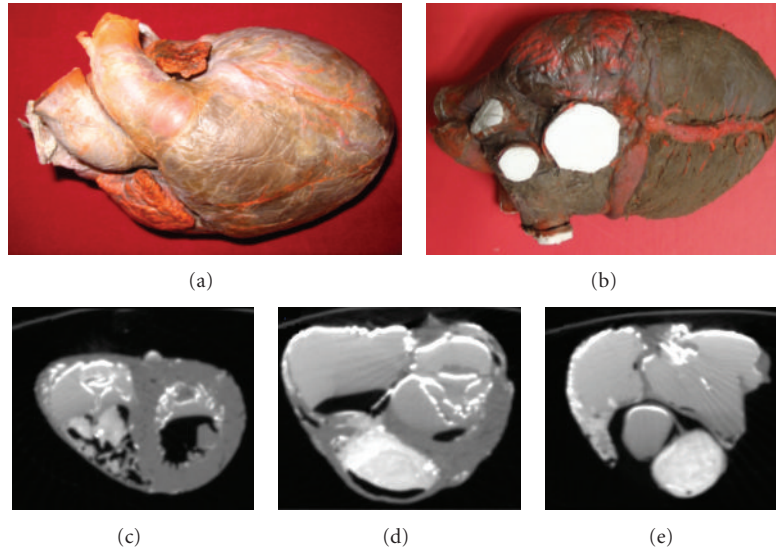


FIGURE 1: Specimen of human heart and its computed tomography (CT) images. Upper row: frontal view (a) and back view (b) of the original human heart pictures. Bottom row: three CT images from different layers of the heart, including (c) ventricle, (d) both atria and ventricle, and (e) atria.

image. After the contrast adjustment, they could be distinguished obviously (Figure 2(b)).

- (2) Image cropping: since a large portion of the original CT image was from the background, they were cropped to define the area of interest and to reduce the image size to 233×301 (Figure 2(c)). After image cropping, the required computer memory was reduced, and the reconstruction speed was improved.
- (3) Contour extraction: the threshold segmentation was firstly applied to the cropped images to obtain the myocardium (Figure 2(d)). Unfortunately, some nonmyocardial tissues were wrongly included. To overcome this limitation, manual check was performed to exclude these nonmyocardial tissues. The connective tissues linked with the endocardium, such as mastoid muscle, trabecula, and so forth, were also excluded. A regional growing method was then applied to generate a clear myocardial image, as shown in Figure 2(e).
- (4) Image reconstruction: the above image processing procedure was repeated to all the CT images to reconstruct the heart with a surface mesh (Figures 2(f) and 2(g)).

2.2. Construction of Conduction System of the Cardiome-CN Human Heart Model. Mimics software (Materialise Inc) was used to construct the cardiac conduction system based on prior knowledge of the human heart anatomy. The conduction system in our model contained sinoatrial node (SAN), crista terminalis, pectinate muscles (PM), Bachmann's bundle (BB), intercaval bundles, atrioventricular node (AVN), atrioventricular ring (AVR), His bundle, bundle branches, and Purkinje network. As an example, the detailed

process to construct crista terminalis is summarized as follows.

- (1) Reconstruct 3D heart model from the segmented CT images: after this step, the manipulation of the voxels in the 3D model directly reflected the corresponding pixels in 2D images. However, at this stage, the conduction system was not distinguished from the heart wall, as shown in Figure 3(a).
- (2) Edit the CT images interactively: to separate the conduction system, the reconstructed model was depicted based on prior knowledge of the anatomical structure of the human heart. The heart model was extended from the anteromedial wall on the right side of the entrance of the superior caval vein to the right side of the entrance of the inferior caval vein [62, 63]. The voxels from the right side of the superior caval vein and downwards to the right side of the inferior caval vein were then selected as shown in Figure 3(b).
- (3) Project to 2D image: after the voxels of crista terminalis were obtained, they were deleted from the 3D model (the white banding in Figure 3(c)). The corresponding 2D image pixels were also deleted as marked with the green rectangle in Figure 3(c).
- (4) Edit the 2D images: an image erosion operation was performed to locate crista terminalis under the epicardium, and a dilation operation was used to spread crista terminalis out of the endocardium. The final 3D model was obtained as shown in Figure 3(d). The blue pixels in the upper image of Figure 3(d) show a cross-sectional image of the crista terminalis.
- (5) Classification and visualization: the other conduction bundles were also obtained similarly by repeating the above 4 steps.

2.3. Construction of Fiber Orientation of the Cardiome-CN Human Heart Model

2.3.1. Fiber Orientation Acquisition. In order to obtain the fiber orientation, some atrial muscles were peeled off along the fiber orientation after the CT scan (Figure 4(a)). The heart was then scanned by a 3D laser scanner (RealScan USB Scanner model 200) with a spatial resolution of 0.01 mm. Geomagic software (Geomagic, Inc) was used to trace the fiber orientation [64]. As shown in Figure 4(b), different curves represent the fiber orientation with its coordinate information. A registration method was then applied to obtain three layers of fiber orientation at the same coordinate. The details of this method has been described in our previous publication [65].

2.3.2. Construction of Ventricular Fiber Orientation. After the registration, the orientations of the endocardial and epicardial fibers had the same coordinate. Figure 5(b) shows all the measured points with the fiber orientation data. These data were used to construct the whole ventricular fiber orientation. The construction steps are summarized as follows.

- (1) Identify the center of gravity of the left and right ventricles (the red lines in Figure 5(a)).
- (2) Calculate the angle of each measured point: the center of gravity was set to be origin, with z axis on the right side and y axis on the upside. Figure 5(c) shows the angles of all the points on a single layer, with different colors representing different angles in degrees from 0° – 360° .
- (3) Calculate the angle of each point on the direction from the apex to the base of the heart: for each layer, the points having fiber orientation at the endocardium and epicardium are marked, respectively, with yellow and green in Figure 5(d). The angle of each point was then calculated as described in step 2.
- (4) Match the endocardial and epicardial fiber angles with the corresponding CT data for each layer (Figure 5(e)): the linear interpolation was then used to calculate the fiber orientation of all the points on the epicardium and endocardium for each layer, as shown in Figure 5(f).
- (5) Calculate the fiber orientation between the epicardium and endocardium over the myocardial wall, as shown in Figure 5(g).
- (6) Follow steps 2–5, the fiber angles of all the layers were obtained. Figure 5(h) shows the fiber angles in a coronal plane (xz plane).

2.3.3. Construction of Atrial Fiber Orientation. Due to the complexity of atrial myoarchitecture, its fiber orientation has not been well quantified. The published qualitative studies concluded that right atrial fiber orientation is obliquely aligned and has different regularity at different layers.

In this study, only the epicardial myofiber orientation of the atria was measured. With the measured atrial fiber orientation data, the interpolation technique was applied to the whole atrial points. The construction steps are summarized as follows.

- (1) Calculate the inclination and transverse angles of each point with measured fiber orientation in the atria.
- (2) For the points without measured fiber orientation, the inclination and transverse angles from their closest point having measured fiber orientation were assigned.

2.4. Electrophysiological Cell Models. For the atrial SAN, the cell model developed by Chandler et al. was used [45]. For the crista terminalis, PM, BB, and atrial working muscles, the models developed by Courtemanche et al. [41] were used. The detailed description has been given in our recently published study [66].

Modeling of human AVN cells is difficult, partially because there is no published study and there is no physiological parameter of human AVN cells available. In this study, a modified AP model of the atria was used to represent the AVN cell model to have the conduction time in the AVN within the physiological range [41]. There are also no existing AP models of the His bundle and bundle branches. It has been reported that Purkinje cell is the principal cell in His bundle, particularly for the left bundle branch [67, 68]. Therefore, the human Purkinje cell AP model developed by [46] was used to represent the AP models of the His bundle, left and right bundle branches. For the ventricles, the cell model developed by ten Tusscher et al. was used [49, 69].

2.5. Numerical Simulation of Excitation Conduction. The monodomain equation was used to simulate the excitation conduction, which is expressed as [70]:

$$\frac{\partial V_m}{\partial t} = \nabla \cdot (\mathbf{D} \nabla V_m) - \frac{I_{\text{ion}} + I_{\text{applied}}}{C_m}, \quad (1)$$

$$\mathbf{D} = \frac{\mathbf{G}_i}{S_v C_m},$$

where S_v is the surface volume ratio of cells (μm^{-1}), C_m is the specific capacitance (pF), \mathbf{G}_i is the bulk intracellular conductivity (mS/cm), V_m is the transmembrane potential (mV), I_{applied} is the transmembrane stimulating current density, and I_{ion} is the sum of all transmembrane ionic currents (pA/pF).

In this study, the finite difference method was used to calculate (1) because of its simplicity and suitability for the parallel computation. The time step was 0.01 ms, the anisotropy of the atrial working muscles was set as 1.3:1 [66], the conduction system was set as 9:1 [31], and the ventricular working muscles were set as 2:1 [55, 71].

The simulation was performed on a Dawning TC4000L server, which had symmetric multiprocessor shared memory and contained one management node and 10 computation nodes. Each computation node contained two Intel

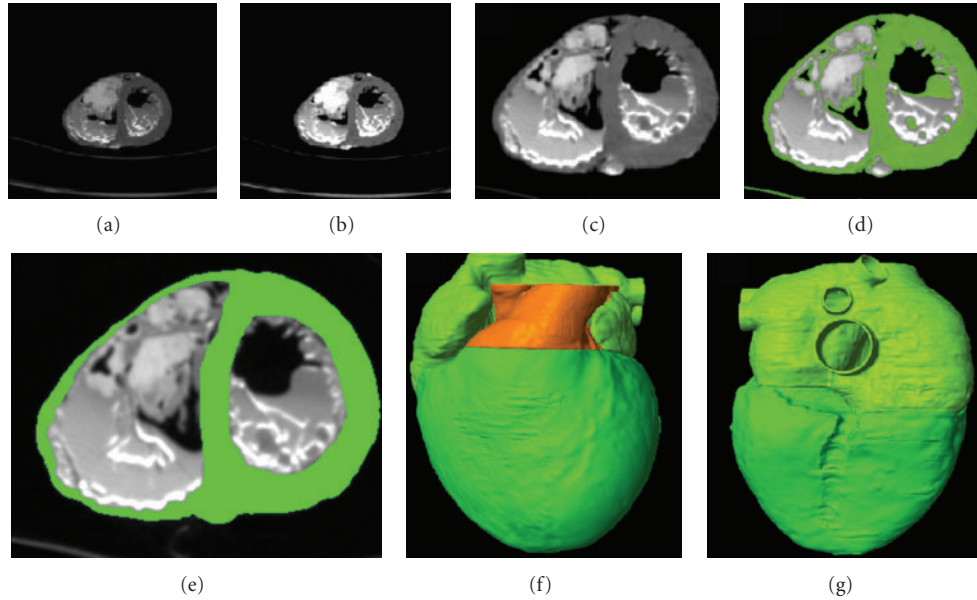


FIGURE 2: Image processing of the construction of human heart model: (a) the original CT image; (b) after contrast adjustment; (c) after cropping; (d) after contour extraction using threshold segmentation; (e) after segmentation; (f) frontal view of the reconstructed model; (g) back view of the reconstructed model.

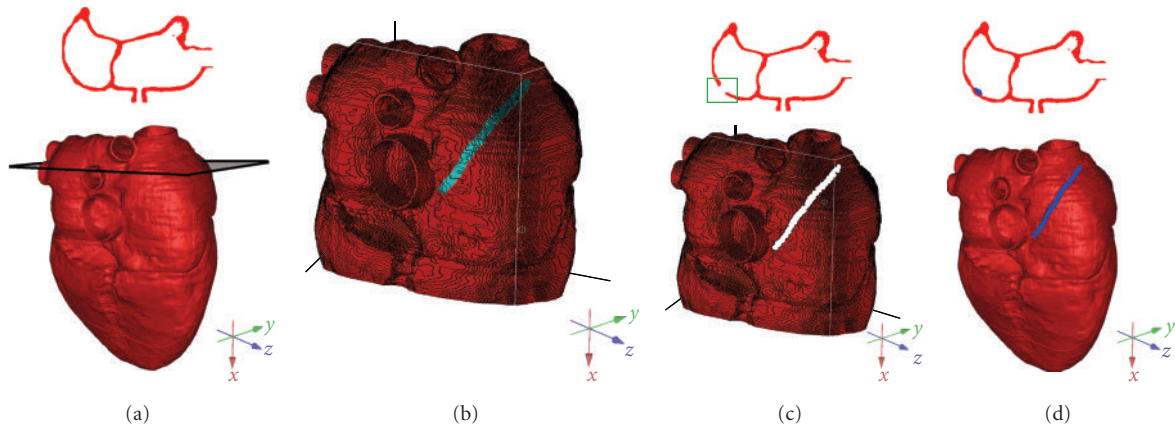


FIGURE 3: Construction of the cardiac conduction system. (a) Reconstructed 3D heart model and one cross-sectional slice of the 3D model; (b) selection of the voxels of crista terminalis in the 3D model; (c) after deletion of the voxels of crista terminalis and the corresponding 2D image; (d) final 3D heart model with one cross-sectional slice; the blue pixels show the conduction bundle.

Xeon 5335 processors, 4 G memory, and 160 G hard disk. The total theoretical computing capacity was up to 184 Gflops. MPICH2 was used to implement the communication between the computational nodes [66].

3. Results

3.1. Reconstructed Anatomical Model of the Human Heart. The reconstructed human heart anatomical model, including both the ventricles and atria, is shown in Figure 6(b). From the segmented images (Figure 6(a)), it can be seen that the left ventricular wall is much thicker than that of the right ventricle (average value: 8–10 mm versus 2–4 mm), and

different layers of the ventricle have different thicknesses. The wall thickness of the atria is slightly thinner than the right ventricle.

3.2. Reconstructed Conduction System of the Cardiome-CN Heart Model. The final conduction system contained the following.

- (1) SAN (Figure 7(b)): including the center and periphery part. It locates at the superior poster lateral wall of the right atrium with the size of about 10 mm × 4 mm × 1 mm, which matches the published experimental data [56–59].

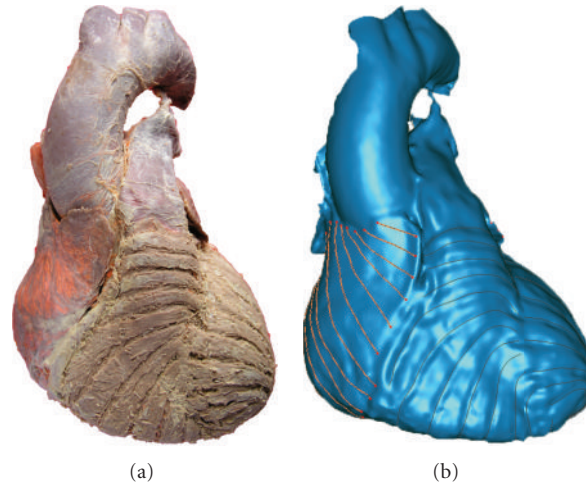


FIGURE 4: Fiber orientation acquisition. (a) The heart before laser scanning. Some atrial muscles were peeled off to make the fiber orientation visible. (b) The heart after laser scanning. The fiber orientation is represented by the red curves.

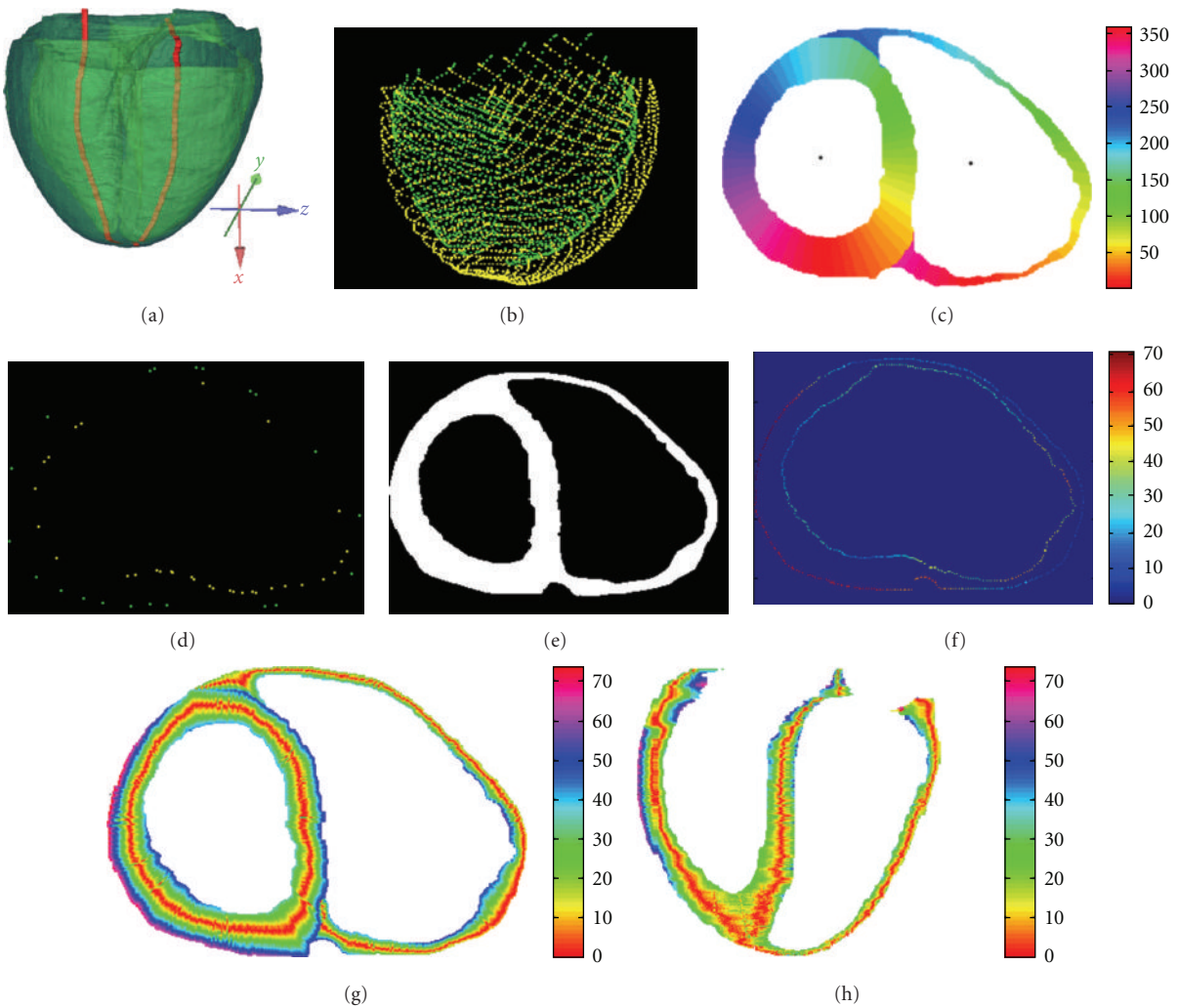


FIGURE 5: (a) Identified center of gravity of the left and right ventricles; (b) all the measured points with fiber orientation data; (c) angel of each point on a single layer; (d), (e) sorting the fiber data and the CT data of the corresponding layer; (f) fiber orientation of all the points on the epicardium and endocardium; (g) fiber orientation of the myocardial wall between epicardium and endocardium; (h) fiber orientation in a coronal plane (xz plane).

- (2) AVN (Figure 7(e)): including fast conduction region, slow conduction region, and central region [57, 72–78]. The slow conduction region was similar to the inferior nodal extension [78, 79], the fast conduction region was similar to the transitional tissue, and the central region was similar to the compact node. In our model, the size of the AVN was about $7\text{ mm} \times 4\text{ mm} \times 1\text{ mm}$.
- (3) Crista terminalis and PM (Figure 7(b)): There is little quantitative data about the crista terminalis and PM, in this study, they were reconstructed from the qualitative description of the position and anatomic structure [62, 63]. The crista terminalis was extended from the anteromedial wall on the left side of the entrance of the superior caval vein to the right of the entrance of the inferior caval vein. PM are parallel alignment of the muscle bulges on the appendage wall and the posterior wall of the right atria [62].
- (4) Intercaval bundles (Figure 7(b)): one bundle connects the origin of the crista terminalis and the anterosuperior rim of FO, and the other connects the origin of the crista terminalis and CS. The details have been reported in our previous publication [66].
- (5) BB (Figure 7(b)): the length of the BB is 14.7 mm, and the maximum diameters of the anteroposterior and superoinferior are 4.5 mm and 3.7 mm [62, 80–82].
- (6) His bundle, left and right bundle branches, and Purkinje fiber system (Figure 7(e)): they were constructed from the published data [68, 83–88]. Left bundle branch starts from the bifurcation of the atrioventricular bundle, descends along the interventricular septum about 1.5 cm, and is then divided into three branches. The right bundle branch starts from the end of the bifurcation of the atrioventricular bundle, moves downward along the membranous part of interventricular septum, and passes the papillary muscle of the conus to the moderator band. After reaching the root of prepapillary muscles, it is divided into three branches. The Purkinje fibers reach into the ventricular myocardial to form the subendocardial network. It is mainly located in the lower part of the interventricular septum, apex, papillary muscles, and free wall. In our model, the Purkinje fiber system, not the His bundle and left and right bundle branches, conducts the excitation to the surrounding ventricular working muscles.

3.3. Reconstructed Fiber Orientation of the Cardiome-CN Heart Model. On the ventricular epicardium (see the first two images from the left in Figure 8(a)), fibers start from the atrioventricular junction and extend obliquely to the cardiac apex along the blunt edge. Near the atrioventricular junction area, longitudinally oriented fibers are observed. When crossing the blunt edge and close to the posterior sulcus, the fiber orientation is transverse. The fiber orientation of the diaphragmatic surface of the right ventricle is nearly

circumferential until it crosses the sharp edge. When close to the outlet of the right ventricle, it is perpendicular to the plane. The fiber orientation in the anterior interventricular groove does not continue, but it forms an angle.

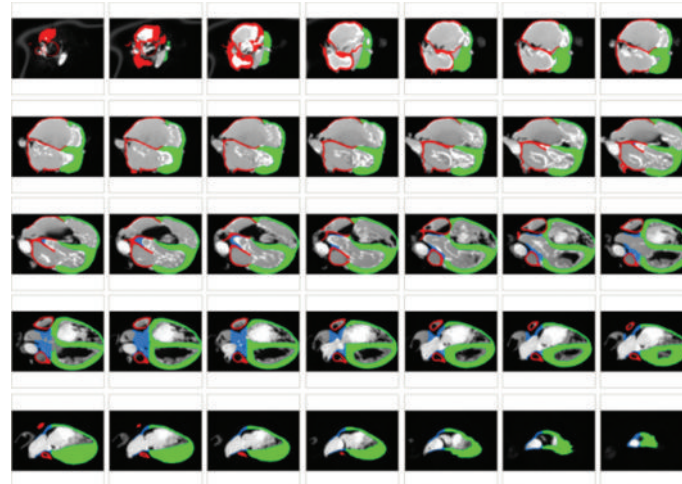
On the middle layer of the anterior and on the posterior and lateral walls of the left ventricle, the fibers are nearly circumferential (see the middle two images in Figure 8(a)), and the fiber in the diaphragmatic surface of the right ventricle middle layer is also circumferential. But when crossing the blunt edge, the fiber orientation is a little oblique, then changes to circumferential again in the anterior wall. When close to the outlet of the right ventricle, the fiber becomes steep and the orientation is longitudinal. Different with the ventricular epicardial junctional area, the fiber continues on the middle layer junctional area of the right and left ventricles.

On the endocardium (see the two images from the right in Figure 8(a)), the fiber orientation is more oblique on the anterior wall than the posterior wall. Overall, from the apex to the base of the heart, the epicardial fibers are arranged clockwise, and the endocardial fibers are counterclockwise. From the epicardium to endocardium, the fiber orientation changes continuously, but inconsistently at different parts.

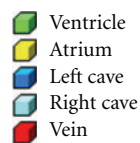
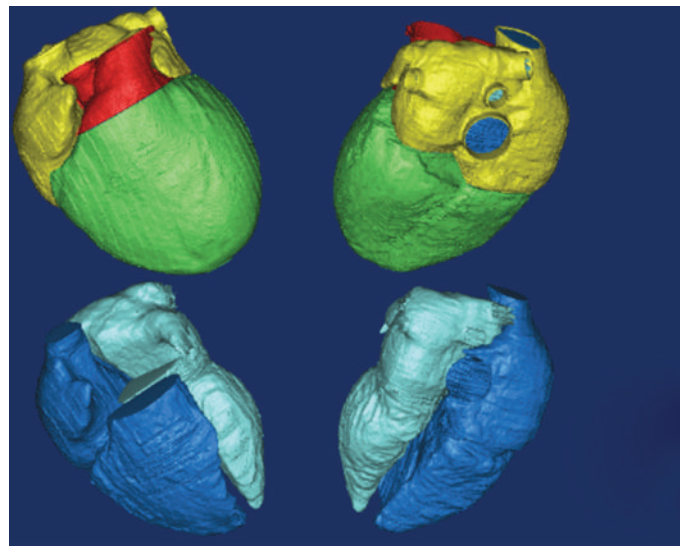
Figure 8(b) gives the comparison between our results and these from other groups. The first row in Figure 8(b) is one cross-section of the fiber orientation from our model, the second row is the published human ventricular DTMRI data [8, 55, 89], and the third row is the data extracted from [55]. It clearly shows that our result was very similar with the DIMRI data. Figure 8(c) shows the constructed fiber orientation of the cross-sections of the ventricle, with the inclination and transverse angles given.

Figure 9 shows the atrial anatomical model with the fiber orientation. The atrial fiber orientation is much more complex than the ventricle. On the posterior and lateral wall of the right atrium, the main fiber direction is longitudinally aligned. The fibers begin in the junction area of the superior vena cava and extend to the atrioventricular junction. Because of the pulmonary veins in the left atrium, the fiber orientation is not as regular as the right atrium. On the posterior and upper posterior wall of the left atrium, fiber orientation is inclined, with a greater inclination on the upper posterior wall. On the lateral wall of left atrium from the left superior pulmonary vein to the apex of the left auricular appendage, it is also inclined. At the top of the left atrium, it is inclinable from the left and right pulmonary veins to the left atrial appendage and interatrial septum, respectively, and is fused on the anterior wall of the atrium. Figures 9(a) and 9(b) are the atrial anatomic model with the fiber orientation, and Figure 9(c) is the final atrial fiber orientation of some selected layers of the atrial model; each layer is represented by inclination and transverse angles.

3.4. Simulation Results of the Cardiac Electrical Propagation. The excitation sequence of the human heart is shown in Figure 10. The frequency of the pacemaker in our model was 1.19 Hz. The excitation starts from the SAN, reaches the BB and crista terminalis in right atrium after approximately



(a)



(b)

FIGURE 6: Reconstructed human heart model. (a) The segmented images. (b) The top two images show the four chambers of the heart model; the bottom two images are the inner cavity of the heart.

10 ms, and conducts to AV junction via the FP, SP, and crista terminalis. It then quickly conducts to the APG. After about 50 ms the left atrial septum close to the fossa ovalis is activated.

The current originated in the SAN also conducts excitation to the left atrium via the BB. In the left atrium, the excitation initiates from the region near the BB, then conducts to the APG via the right PM and to the posterior part of the right atrium, and ends at the posterior-inferior left atrium. The complete activation time is 30 ms for BB, 81 ms for the right atrium, 79 ms for left atrium, and 109 ms for

the entire atrium. The conduction velocity is about 115 cm/s, 76 cm/s, 125 cm/s, and 107 cm/s in the crista terminalis, atrial muscles, PM, and BB, respectively.

When the excitation conducts to the AVN, with a delay of about 15 ms, it reaches the His bundle, left and right bundle, and then to the Purkinje network. The first breakthrough in the endocardium is at about 136 ms in the lower septum, and then the excitation conducts to the ventricular cells via Purkinje network. The first breakthrough point in the epicardium is at the anterior and posterior septal region, which is consistent with clinical measurements

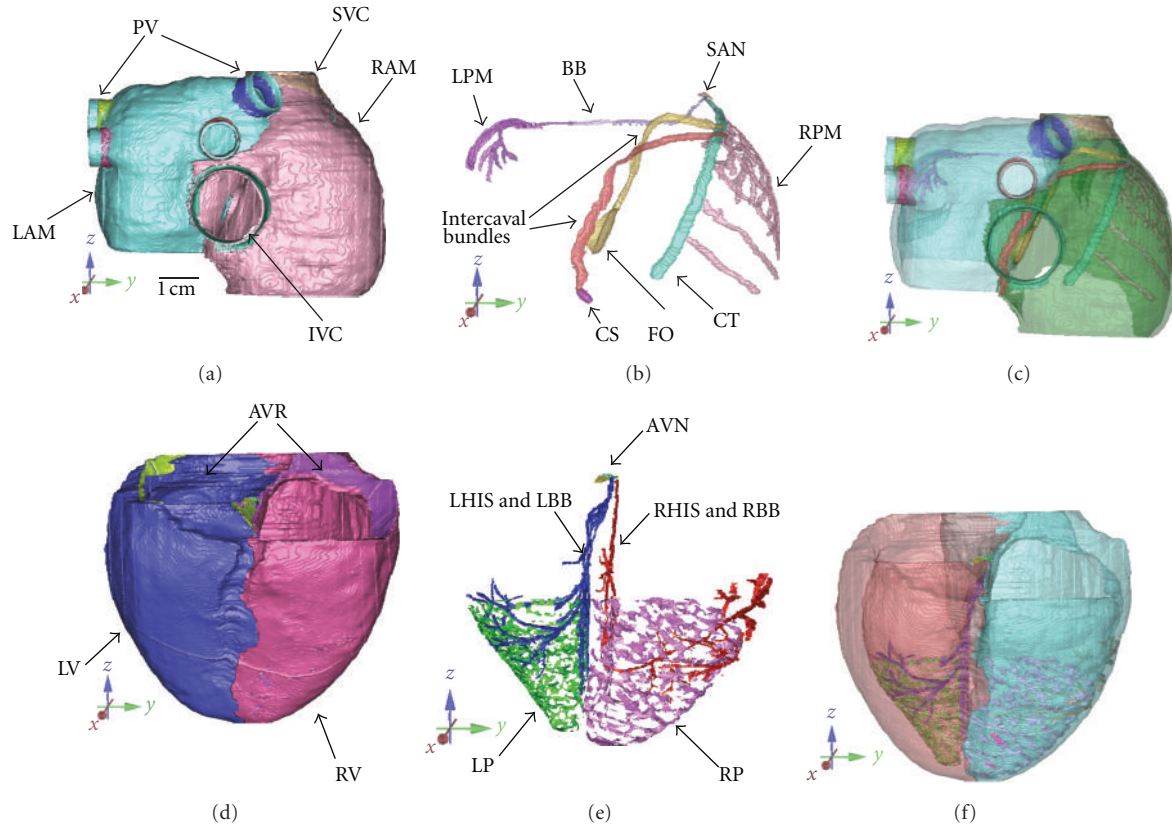


FIGURE 7: The Cardiome-CN human heart conduction system. (a) The posterior view of the atria; (b) the conduction bundles in the atria; (c) the transparent display of the conduction bundles and atrial muscles; (d) the posterior view of the ventricle; (e) the conduction bundles in the ventricle; (f) the transparent display of the conduction bundles and ventricular muscles. Note: PV: pulmonary veins; LHIS: left His bundle; RHIS: right His bundle; RBB: right bundle branches; LBB: left bundle branches; RP: right Purkinje fiber system; LP: left Purkinje fiber system; AVR: atrioventricular ring.

[90]. In the left and right ventricles, the last activated regions are the posterolateral area and the pulmonary conus and posterobasal area. It happens at about 228 ms. The conduction velocity varies at different parts, with the slowest speed of 40 cm/s at the apex, about 70 cm/s at the middle part of the heart and, about 80 cm/s at the upper part close to the base of the ventricle.

4. Discussion

4.1. Fiber Orientation Modeling. The fiber orientations of the ventricles and atria have been investigated in this study. The human ventricular fiber orientation has been widely studied with the range of $+60^\circ \sim -60^\circ$, depending on the different species used [5, 8, 91–93]. Our results agreed well with what has been published [17, 36, 94, 95]. Moreover, our results quantitatively showed that the fiber orientation is not homogeneous on the same layer and also varies at different parts of the heart. It is more inclined near the orifice of pulmonary trunk than the middle and bottom parts of the ventricles, and on the diaphragmatic surface of the epicardium, the left ventricular fiber has steeper angles than the right ventricle.

In this present study, the epicardial fiber orientation of the atrium was quantitatively measured, and the result shows that the atrial fiber orientation in general is less regular than that of the ventricle. On the right atrial epicardium, the fiber has some patterns, but in the left atrium, it is quite irregular because of the pulmonary veins. Our data was consistent with other experimental data [62, 96, 97].

4.2. Conduction System Modeling. A detailed cardiac conduction system has been constructed in this study. It is very difficult to distinguish different conduction pathways using the anatomic or morphological methods. In our model, it has been assumed that muscle bundles exist between the origin of crista terminalis and CS and FO, and they compose of normal atrial muscles, but have high anisotropy ratio. The geometry of the two pathways agreed the general description of the experimental data [96–98]. To the best of our knowledge, this is the first model containing the two pathways in biatrial conduction simulation. Due to the lack of accurate experimental data, the accurate geometry of the two pathways can not be obtained in our simulation, but our simulation showed that they could make the conduction pattern in the atria more close to the clinic data [66].

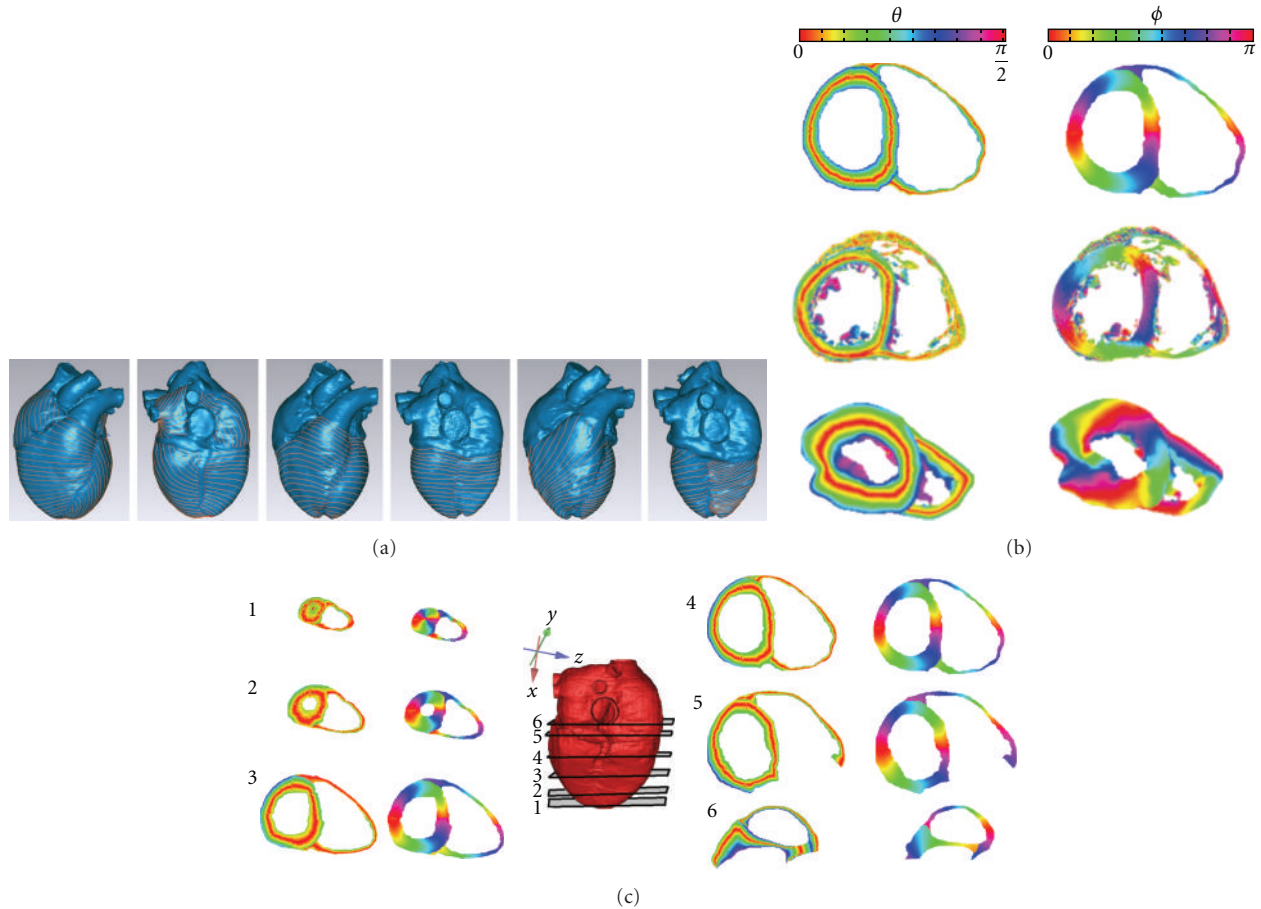


FIGURE 8: (a) Original fiber direction with frontal and back view: the two images from the left are the epicardial fiber orientation; the middle two images are the middle layer fiber orientation; the two images from the right are the subendocardial fiber orientation. (b) Ventricular fiber orientation, with θ the inclination angle and ϕ the transverse angle. The first row is the constructed fiber orientation of our model, the second row is the published human ventricular DTMRI data, and the third row was the data extracted from [55]. (c) Constructed fiber orientation of the cross sections of the ventricle. The numbers represent the position of cross sections in the whole heart model.

Recently, it has been reported that the SAN structure was functionally insulated from the atrium by the connective tissues, fat, and coronary arteries [99]. It has also been reported that the atrial myocardium was excited via the superior, middle, and/or inferior sinoatrial conduction pathways. Therefore, in our simulation the excitation from the periphery cell only conducts to the crista terminalis, and the two internodal bundles are supposed to be from near the SAN. In the other atrial simulations [14, 31], the SAN could conduct electricity to the surrounding atrial working muscles, because the SAN was considered not to be insulated from the surrounding tissues.

Due to the complexity of the AVN, its anatomy and morphology have not been fully understood. In our model, based on the theory of the dual AVN pathways [78, 100–102], the AVN is divided into three parts: fast and slow conduction regions, and central region. The fast conduction region receives the electrical excitation from the transitional cells, and the slow conduction region receives the electrical excitation from the isthmus. These settings may have some

differences with the real anatomic structure, but it made the whole heart modeling become feasible.

Many models have been constructed to simulate the electrical conduction in the ventricle and they have different resolutions and the construction methods varies too, but the majority of them were artificially depicted based on the prior knowledge of the anatomical structure [103, 104] or special algorithms [105, 106]. The His-Purkinje system is important for the ventricular conduction, and there are many qualitative anatomical descriptions [84–88, 107–109]. In our model, the His-Purkinje system was artificially depicted based on the prior knowledge. The His and bundle branches are separated from the Purkinje network, and the Purkinje fibers are connected each other. Our model was also close to the recently constructed His-Purkinje system of a rabbit from macroscopic images [110].

4.3. Excitation Conduction Modeling. The simulated excitation sequences of the atria and ventricles in our model agreed well with the published experimental data [30, 111]. The

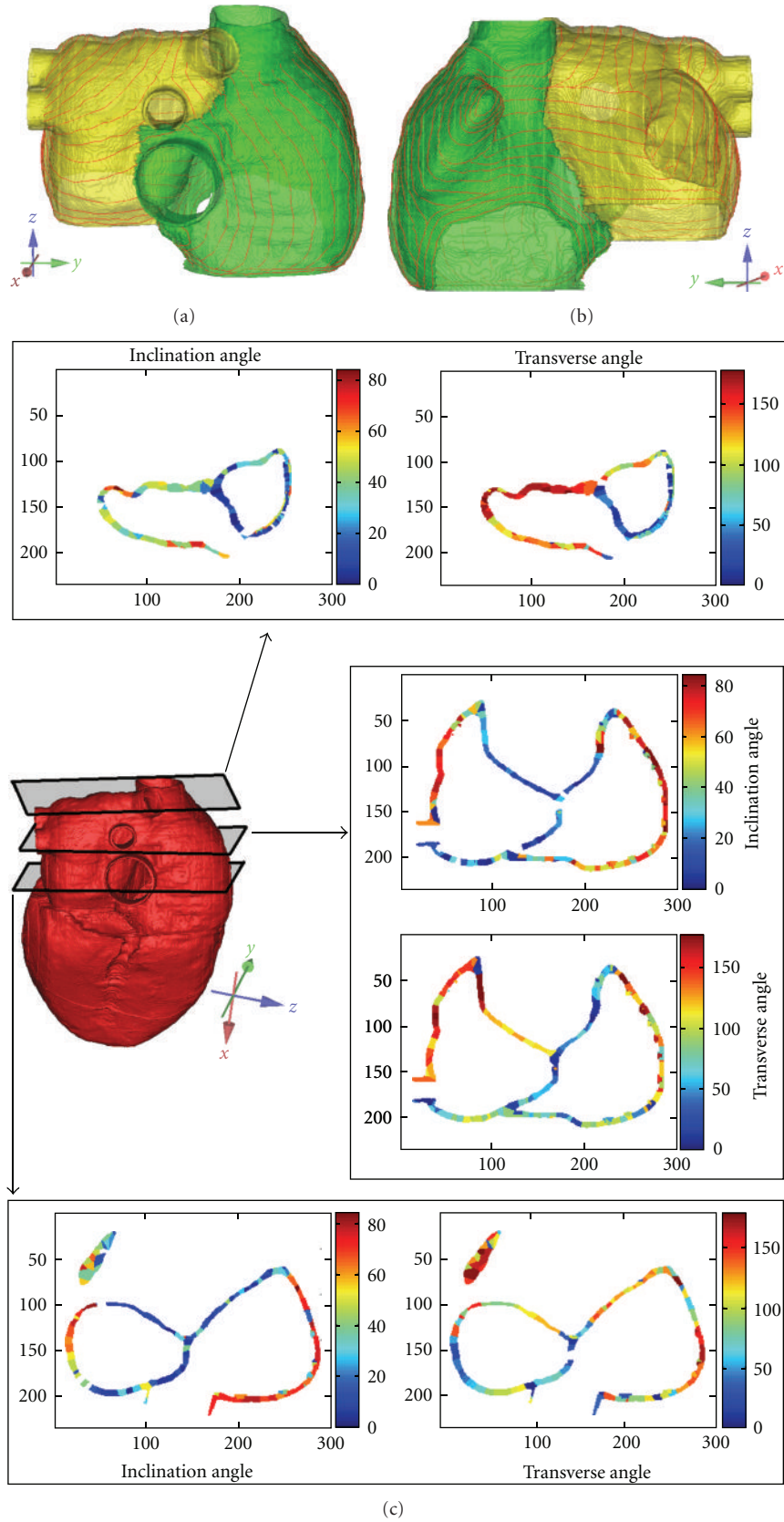


FIGURE 9: Constructed atria fiber orientations. (a), (b) Anterior view and posterior view of the fiber orientation within the atrial anatomical model; (c) the constructed fiber orientation of three cross-sectional images of the atria model. The fiber orientation in each layer is represented by inclination and transverse angles.

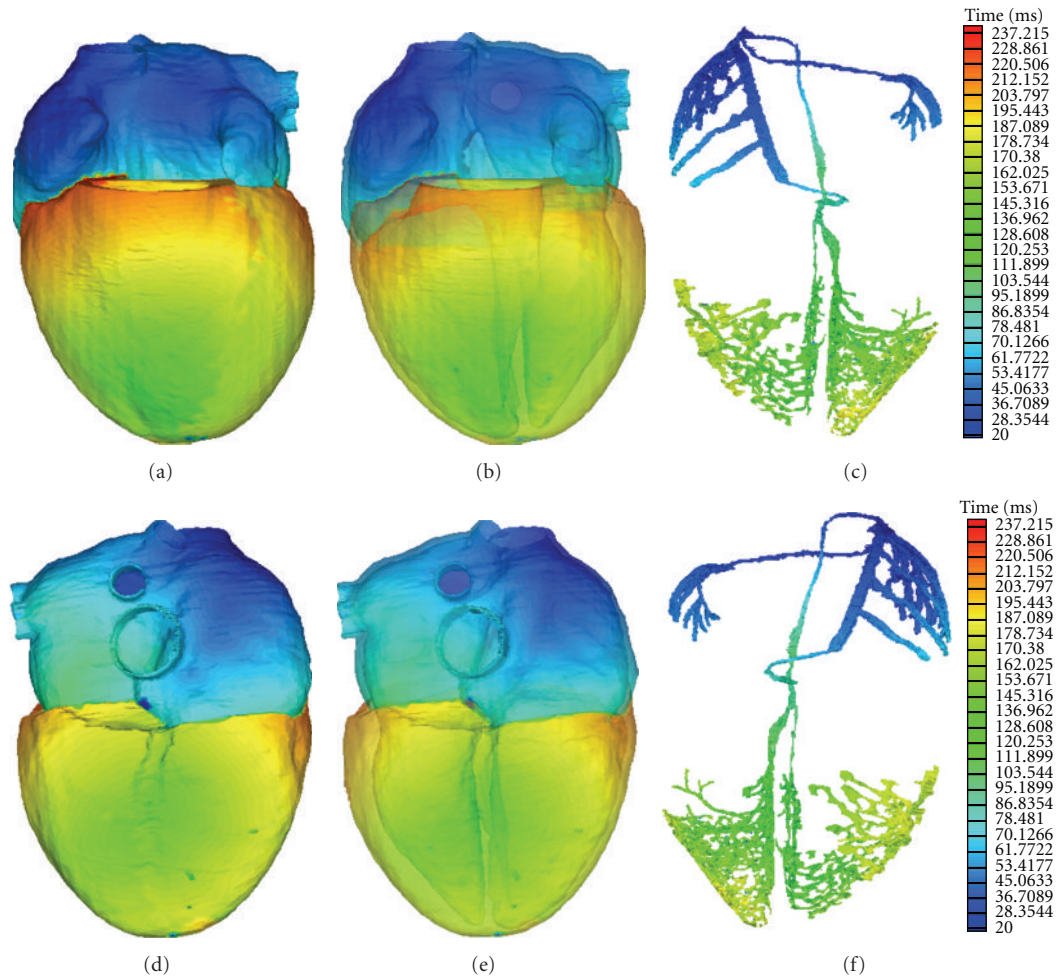


FIGURE 10: The simulated excitation sequences of the whole human heart. Different colors represent different excitement time. (a, d) the front and back views of the excitation sequence; (b, e) the transparency view; (c, f) the excitation sequence of the conduction systems.

conduction velocity in the right atrial wall is not homogeneous; the velocity of the posterolateral wall with PM is 70 to 100 cm/s and the average velocity is close to 95 cm/s, which is within the range of 0.68–1.03 m/s [112]. The velocity of crista terminalis is 1.15 m/s, which is also consistent with the experimental data of 0.7–1.3 m/s [113]. Lemery et al. [111] reported that the total BB conduction time was 23 ± 15 ms, our result of 16 ms is slightly shorter than the average value, but is within the range. The conduction speed of BB in our simulation is between 95 to 150 cm/s, and the average velocity is 113 cm/s; it is within the range reported by Dolber and Spach [114].

De et al. [115] reported that the duration of left atrial propagation and whole atria was 81 ± 10 and 105 ± 9 ms, respectively. The experimental data in [111] showed the activation time of LA and whole atria were 80 ± 11 ms and 120 ± 24 ms, respectively, while the results of [116] were 84 ± 14 ms and 119 ± 14 ms, respectively. In our simulation, the total activation time of left atrial and whole atria are 79 ms and 109 ms, respectively, which is similar to these experimental data.

For the ventricle, the conduction time from the onset of His to the onset of ventricular working muscles is about 41 ms, which is within the range of 47 ± 7 ms [117] and close to another simulation result [32]. After the excitation of lower septum in endocardium, the electricity spread to the epicardium and then upward to the base of ventricle; the whole conduction time of the ventricular working muscles is about 92 ms, which is close to the experimental data of about 100 ms [30, 117] and another model study [118]. The conduction speed of ventricular muscles is about 0.7 m/s, close to 0.6 m/s [119] and fall in the range of 0.3–1.0 m/s [120].

5. Limitation

Firstly, the mastoid muscles could not be clearly distinguished from the ventricular muscles. This is especially obvious in the right ventricle, therefore the mastoid muscles were not included in our heart model. Secondly, our model only contained the atrial epicardial fiber orientation, since the atrial wall is too thin and the endocardial fiber is

complex. Thirdly, the AP model of the AVN was based on the human atrial model. It may not effectively represent the physiological parameters of human AVN cells and may influence the simulation accuracy. In addition, the anatomy of whole heart conduction system was constructed based on the priori knowledge of the heart anatomy, which may affect the simulation.

6. Conclusion

In conclusion, a human heart model with detailed anatomical structure, conduction system, and fiber orientations have been constructed. To the best of our knowledge, this is the first anatomically-detailed human heart model with corresponding experimentally measured fibers orientation. Different AP cell models have been assigned to different parts of the heart, and the simulated normal activation sequence agreed well with the published experimental data. Such detailed anatomical heart model could be very useful for future research on understating of the mechanisms influencing cardiovascular function and its physiological and pathological processes.

Acknowledgments

This project is supported by the 973 National Basic Research & Development Program (2007CB512100), the 863 High-tech Research & Development Program (2006AA02Z307), the National Natural Science Foundation of China (81171421), and the Nature Science Foundations of Zhejiang Province of China (Z1080300).

References

- [1] K. C. Wong, L. Wang, H. Zhang, H. Liu, and P. Shi, "Integrating functional and structural images for simultaneous cardiac segmentation and deformation recovery," in *Proceedings of the Medical Image Computing and Computer-Assisted Intervention (MICCAI '07)*, vol. 4791, pp. 270–277, 2007.
- [2] L. Weixue and X. Ling, "Computer simulation of epicardial potentials using a heart-torso model with realistic geometry," *IEEE Transactions on Biomedical Engineering*, vol. 43, no. 2, pp. 211–217, 1996.
- [3] L. Weixue and X. Ling, "Three-dimensional simulation of epicardial potentials using a microcomputer-based heart-torso model," *Medical Engineering and Physics*, vol. 17, no. 8, pp. 625–632, 1995.
- [4] D. Noble, "Modeling the heart—from genes to cells to the whole organ," *Science*, vol. 295, no. 5560, pp. 1678–1682, 2002.
- [5] P. M. F. Nielsen, I. J. Le Grice, B. H. Smaill, and P. J. Hunter, "Mathematical model of geometry and fibrous structure of the heart," *American Journal of Physiology—Heart and Circulatory Physiology*, vol. 260, no. 4, pp. H1365–H1378, 1991.
- [6] I. J. LeGrice, P. J. Hunter, and B. H. Smaill, "Laminar structure of the heart: a mathematical model," *American Journal of Physiology—Heart and Circulatory Physiology*, vol. 272, no. 5, pp. H2466–H2476, 1997.
- [7] F. J. Vetter and A. D. McCulloch, "Three-dimensional analysis of regional cardiac function: a model of rabbit ventricular anatomy," *Progress in Biophysics and Molecular Biology*, vol. 69, no. 2-3, pp. 157–183, 1998.
- [8] D. F. Scollan, A. Holmes, J. Zhang, and R. L. Winslow, "Reconstruction of cardiac ventricular geometry and fiber orientation using magnetic resonance imaging," *Annals of Biomedical Engineering*, vol. 28, no. 8, pp. 934–944, 2000.
- [9] R. A. B. Burton, G. Plank, J. E. Schneider et al., "Three-dimensional models of individual cardiac histoanatomy: tools and challenges," *Annals of the New York Academy of Sciences*, vol. 1080, pp. 301–319, 2006.
- [10] C. S. Henriquez, J. V. Tranquillo, D. Weinstein et al., "Three dimensional propagation in mathematic models: integrative model of the mouse heart," in *Cardiac Electrophysiology from Cell to Bedside*, D. P. Zipes and J. Jalife, Eds., pp. 273–281, Saunders, Philadelphia, Pa, USA, 2004.
- [11] C. Stevens, E. Remme, I. LeGrice, and P. Hunter, "Ventricular mechanics in diastole: material parameter sensitivity," *Journal of Biomechanics*, vol. 36, no. 5, pp. 737–748, 2003.
- [12] M. Lorange and R. M. Gulrajani, "A computer heart model incorporating anisotropic propagation. I. Model construction and simulation of normal activation," *Journal of Electrocardiology*, vol. 26, no. 4, pp. 245–261, 1993.
- [13] R. Hren, J. Nenonen, and B. M. Horáček, "Simulated epicardial potential maps during paced activation reflect myocardial fibrous structure," *Annals of Biomedical Engineering*, vol. 26, no. 6, pp. 1022–1035, 1998.
- [14] D. Harrild and C. Henriquez, "A computer model of normal conduction in the human atria," *Circulation Research*, vol. 87, no. 7, pp. E25–E36, 2000.
- [15] F. B. Sachse, C. D. Werner, M. H. Stenroos, R. F. Schulte, P. Zerfass, and O. Dössel, "Modeling the anatomy of the human heart using the cryosection images of the Visible Female dataset," in *Proceedings of the 3rd User Conference of the National Library of Medicine's Visible Human Project*, Bethesda, Md, USA, 2000.
- [16] O. Blanc, *A computer model of human atrial arrhythmia [M.S. thesis]*, Ecole Polytechnique Fédérale de Lausanne, 2002, Chapter 6: Model of Human Atria.
- [17] D. Rohmer, A. Sitek, and G. T. Gullberg, "Reconstruction and visualization of fiber and laminar structure in the normal human heart from ex vivo diffusion tensor magnetic resonance imaging (DTMRI) data," *Investigative Radiology*, vol. 42, no. 11, pp. 777–789, 2007.
- [18] P. Colli-Franzone, L. Guerri, and B. Taccardi, "Modeling ventricular excitation: axial and orthotropic anisotropy effects on wavefronts and potentials," *Mathematical Biosciences*, vol. 188, no. 1-2, pp. 191–205, 2004.
- [19] L. Xia, M. Huo, Q. Wei, F. Liu, and S. Crozier, "Analysis of cardiac ventricular wall motion based on a three-dimensional electromechanical biventricular model," *Physics in Medicine and Biology*, vol. 50, no. 8, pp. 1901–1917, 2005.
- [20] Q. Long, R. Merrifield, X. Y. Xu, P. Kilner, D. N. Firmin, and G. Z. Yang, "Subject-specific computational simulation of left ventricular flow based on magnetic resonance imaging," *Proceedings of the Institution of Mechanical Engineers H*, vol. 222, no. 4, pp. 475–485, 2008.
- [21] J. Dou, L. Xia, Y. Zhang et al., "Mechanical analysis of congestive heart failure caused by bundle branch block based on an electromechanical canine heart model," *Physics in Medicine and Biology*, vol. 54, no. 2, pp. 353–371, 2009.
- [22] N. P. Smith, "A computational study of the interaction between coronary blood flow and myocardial mechanics," *Physiological Measurement*, vol. 25, no. 4, pp. 863–877, 2004.

- [23] S. Matsuoka, N. Sarai, S. Kuratomi, K. Ono, and A. Noma, "Role of individual ionic current systems in ventricular cells hypothesized by a model study," *Japanese Journal of Physiology*, vol. 53, no. 2, pp. 105–123, 2003.
- [24] M. S. Olufsen, H. T. Tran, J. T. Ottesen et al., "Modeling baroreflex regulation of heart rate during orthostatic stress," *American Journal of Physiology—Regulatory Integrative and Comparative Physiology*, vol. 291, no. 5, pp. R1355–R1368, 2006.
- [25] Y. Rudy, "From genome to physiome: integrative models of cardiac excitation," *Annals of Biomedical Engineering*, vol. 28, no. 8, pp. 945–950, 2000.
- [26] P. J. Hunter, E. J. Crampin, and P. M. F. Nielsen, "Bioinformatics, multiscale modeling and the IUPS Physiome Project," *Briefings in Bioinformatics*, vol. 9, no. 4, pp. 333–343, 2008.
- [27] L. Weixue, X. Zhengyao, and F. Yingjie, "Microcomputer-based cardiac field simulation model," *Medical and Biological Engineering and Computing*, vol. 31, no. 4, pp. 384–387, 1993.
- [28] W. T. Miller and D. B. Geselowitz, "Simulation studies of the electrocardiogram. I. The normal heart," *Circulation Research*, vol. 43, no. 2, pp. 301–315, 1978.
- [29] W. T. Miller III and D. B. Geselowitz, "Simulation studies of the electrocardiogram. II. Ischemia and infarction," *Circulation Research*, vol. 43, no. 2, pp. 315–323, 1978.
- [30] D. Durrer, R. T. van Dam, G. E. Freud, M. J. Janse, F. L. Meijler, and R. C. Arzbaecher, "Total excitation of the isolated human heart," *Circulation*, vol. 41, no. 6, pp. 899–912, 1970.
- [31] G. Seemann, C. Höper, F. B. Sachse, O. Dössel, A. V. Holden, and H. Zhang, "Heterogeneous three-dimensional anatomical and electrophysiological model of human atria," *Philosophical Transactions of the Royal Society A*, vol. 364, no. 1843, pp. 1465–1481, 2006.
- [32] K. H. W. J. T. Tusscher and A. V. Panfilov, "Modelling of the ventricular conduction system," *Progress in Biophysics and Molecular Biology*, vol. 96, no. 1–3, pp. 152–170, 2008.
- [33] D. D. Streeter, H. M. Spotnitz, D. P. Patel, J. Ross, and E. H. Sonnenblick, "Fiber orientation in the canine left ventricle during diastole and systole," *Circulation Research*, vol. 24, no. 3, pp. 339–347, 1969.
- [34] D. D. Streeter and W. T. Hanna, "Engineering mechanics for successive states in canine left ventricular myocardium. II. Fiber angle and sarcomere length," *Circulation Research*, vol. 33, no. 6, pp. 656–664, 1973.
- [35] T. E. Carew and J. W. Covell, "Fiber orientation in hypertrophied canine left ventricle," *The American Journal of Physiology*, vol. 236, no. 3, pp. H487–H493, 1979.
- [36] R. A. Greenbaum, S. Y. Ho, and D. G. Gibson, "Left ventricular fibre architecture in man," *British Heart Journal*, vol. 45, no. 3, pp. 248–263, 1981.
- [37] A. A. Young, I. J. Legrice, M. A. Young, and B. H. Smaill, "Extended confocal microscopy of myocardial laminae and collagen network," *Journal of Microscopy*, vol. 192, no. 2, pp. 139–150, 1998.
- [38] H. Axer and D. G. V. Keyserlingk, "Mapping of fiber orientation in human internal capsule by means of polarized light and confocal scanning laser microscopy," *Journal of Neuroscience Methods*, vol. 94, no. 2, pp. 165–175, 2000.
- [39] G. B. Sands, D. A. Gerneke, D. A. Hooks, C. R. Green, B. H. Smaill, and I. J. Legrice, "Automated imaging of extended tissue volumes using confocal microscopy," *Microscopy Research and Technique*, vol. 67, no. 5, pp. 227–239, 2005.
- [40] E. Grandi, S. V. Pandit, N. Voigt et al., "Human atrial action potential and Ca^{2+} model: sinus rhythm and chronic atrial fibrillation," *Circulation Research*, vol. 109, no. 9, pp. 1055–1066, 2011.
- [41] M. Courtemanche, R. J. Ramirez, and S. Nattel, "Ionic mechanisms underlying human atrial action potential properties: insights from a mathematical model," *American Journal of Physiology—Heart and Circulatory Physiology*, vol. 44, no. 1, pp. H301–H321, 1998.
- [42] A. Nygren, C. Fiset, L. Firek et al., "Mathematical model of an adult human atrial cell: the role of K^+ currents in repolarization," *Circulation Research*, vol. 82, no. 1, pp. 63–81, 1998.
- [43] M. M. Maleckar, J. L. Greenstein, W. R. Giles, and N. A. Trayanova, " K^+ current changes account for the rate dependence of the action potential in the human atrial myocyte," *American Journal of Physiology—Heart and Circulatory Physiology*, vol. 297, no. 4, pp. H1398–H1410, 2009.
- [44] J. T. Koivumäki, T. Korhonen, and P. Tavi, "Impact of sarcoplasmic reticulum calcium release on calcium dynamics and action potential morphology in human atrial myocytes: a computational study," *PLoS Computational Biology*, vol. 7, no. 1, article e1001067, 2011.
- [45] N. J. Chandler, I. D. Greener, J. O. Tellez et al., "Molecular architecture of the human sinus node insights into the function of the cardiac pacemaker," *Circulation*, vol. 119, no. 12, pp. 1562–1575, 2009.
- [46] P. Stewart, O. V. Aslanidi, D. Noble, P. J. Noble, M. R. Boyett, and H. Zhang, "Mathematical models of the electrical action potential of Purkinje fibre cells," *Philosophical Transactions of the Royal Society A*, vol. 367, no. 1896, pp. 2225–2255, 2009.
- [47] K. J. Sampson, V. Iyer, A. R. Marks, and R. S. Kass, "A computational model of Purkinje fibre single cell electrophysiology: implications for the long QT syndrome," *Journal of Physiology*, vol. 588, no. 14, pp. 2643–2655, 2010.
- [48] L. Priebe and D. J. Beuckelmann, "Simulation study of cellular electric properties in heart failure," *Circulation Research*, vol. 82, no. 11, pp. 1206–1223, 1998.
- [49] K. H. W. J. Ten Tusscher, D. Noble, P. J. Noble, and A. V. Panfilov, "A model for human ventricular tissue," *American Journal of Physiology—Heart and Circulatory Physiology*, vol. 286, no. 4, pp. H1573–H1589, 2004.
- [50] T. O'Hara, L. Virág, A. Varró, and Y. Rudy, "Simulation of the undiseased human cardiac ventricular action potential: model formulation and experimental validation," *PLoS Computational Biology*, vol. 7, no. 5, Article ID e1002061, 2011.
- [51] M. Fink, D. Noble, L. Virag, A. Varro, and W. R. Giles, "Contributions of HERG K^+ current to repolarization of the human ventricular action potential," *Progress in Biophysics and Molecular Biology*, vol. 96, no. 1–3, pp. 357–376, 2008.
- [52] R. Plonsey and R. C. Barr, "Mathematical modeling of electrical activity of the heart," *Journal of Electrocardiology*, vol. 20, no. 3, pp. 219–226, 1987.
- [53] Y. B. Chernyak, A. B. Feldman, and R. J. Cohen, "Correspondence between discrete and continuous models of excitable media: trigger waves," *Physical Review E*, vol. 55, no. 3, pp. 3215–3233, 1997.
- [54] L. Tung, *A Bi-Domain Model for describing Ischemic Myocardial D-C Potentials*, Massachusetts Institute of Technology, Cambridge, Mass, USA, 1978.
- [55] K. H. W. J. Ten Tusscher, R. Hren, and A. V. Panfilov, "Organization of ventricular fibrillation in the human heart," *Circulation Research*, vol. 100, no. 12, pp. e87–e101, 2007.
- [56] K. R. Anderson, S. Yen Ho, and R. H. Anderson, "Location and vascular supply of sinus node in human heart," *British Heart Journal*, vol. 41, no. 1, pp. 28–32, 1979.

- [57] T. N. James, "Structure and function of the sinus node, AV node and his bundle of the human heart—part I: structure," *Progress in Cardiovascular Diseases*, vol. 45, no. 3, pp. 235–267, 2002.
- [58] H. Dobrzynski, J. Li, J. Tellez et al., "Computer three-dimensional reconstruction of the sinoatrial node," *Circulation*, vol. 111, no. 7, pp. 846–854, 2005.
- [59] V. V. Fedorov, A. V. Glukhov, R. Chang et al., "Optical mapping of the isolated coronary-perfused human sinus node," *Journal of the American College of Cardiology*, vol. 56, no. 17, pp. 1386–1394, 2010.
- [60] M. Potse, B. Dubé, J. Richer, A. Vinet, and R. M. Gulrajani, "A comparison of monodomain and bidomain reaction-diffusion models for action potential propagation in the human heart," *IEEE Transactions on Biomedical Engineering*, vol. 53, no. 12, pp. 2425–2435, 2006.
- [61] X. Lou et al., "Modified lead oxide-gelatin injection technique for angiography," *Chinese Journal of Clinical Anatomy*, vol. 24, no. 3, p. 4, 2006.
- [62] S. Y. Ho and D. Sánchez-Quintana, "The importance of atrial structure and fibers," *Clinical Anatomy*, vol. 22, no. 1, pp. 52–63, 2009.
- [63] D. Sánchez-Quintana, R. H. Anderson, J. A. Cabrera et al., "The terminal crest: morphological features relevant to electrophysiology," *Heart*, vol. 88, no. 4, pp. 406–411, 2002.
- [64] M. C. Zhang, J. M. Liao, M. Li, and W. D. Zhao, "Reconstruction of the mandibular model using a three-dimensional laser scanner," *Journal of Southern Medical University*, vol. 24, no. 7, pp. 756–757, 2004.
- [65] D. Deng, P. Jiao, G. Shou, and L. Xia, "Registering myocardial fiber orientations with heart geometry using iterative closest points algorithms," in *Medical Imaging, Parallel Processing of Images, and Optimization Techniques*, Proceedings of SPIE, November 2009.
- [66] D. Deng, Y. I. Gong, G. Shou et al., "Simulation of biatrial conduction via different pathways during si-nus rhythm with a detailed human atrial model," *Journal of Zhejiang University Science B*. In press.
- [67] T. N. James and L. Sherf, "Fine structure of the His bundle," *Circulation*, vol. 44, no. 1, pp. 9–28, 1971.
- [68] T. N. James, L. Sherf, and F. Urthaler, "Fine structure of the bundle branches," *British Heart Journal*, vol. 36, no. 1, pp. 1–18, 1974.
- [69] K. H. W. J. Ten Tusscher and A. V. Panfilov, "Cell model for efficient simulation of wave propagation in human ventricular tissue under normal and pathological conditions," *Physics in Medicine and Biology*, vol. 51, no. 23, pp. 6141–6156, 2006.
- [70] J. P. Whiteley, "An efficient numerical technique for the solution of the monodomain and bidomain equations," *IEEE Transactions on Biomedical Engineering*, vol. 53, no. 11, pp. 2139–2147, 2006.
- [71] P. Taggart, P. M. Sutton, T. Opthof et al., "Inhomogeneous transmural conduction during early ischaemia in patients with coronary artery disease," *Journal of Molecular and Cellular Cardiology*, vol. 32, no. 4, pp. 621–630, 2000.
- [72] T. N. James and L. Sherf, "Ultrastructure of the human atrioventricular node," *Circulation*, vol. 37, no. 6, pp. 1049–1070, 1968.
- [73] R. H. Anderson, M. J. Janse, F. J. van Capelle, J. Billette, A. E. Becker, and D. Durrer, "A combined morphological and electrophysiological study of the atrioventricular node of the rabbit heart," *Circulation Research*, vol. 35, no. 6, pp. 909–922, 1974.
- [74] R. H. Anderson and S. Y. Ho, "The architecture of the sinus node, the atrioventricular conduction axis, and the internodal atrial myocardium," *Journal of Cardiovascular Electrophysiology*, vol. 9, no. 11, pp. 1233–1248, 1998.
- [75] D. K. Racker, "The AV junction region of the heart: a comprehensive study correlating gross anatomy and direct three-dimensional analysis—part I: Architecture and Topography," *The Anatomical Record*, vol. 256, no. 1, pp. 49–63, 1999.
- [76] R. H. Anderson, S. Y. Ho, and A. E. Becker, "Anatomy of the human atrioventricular junctions revisited," *The Anatomical Record*, vol. 260, no. 1, pp. 81–91, 2000.
- [77] Y. S. Ko, H. I. Yeh, Y. L. Ko et al., "Three-dimensional reconstruction of the rabbit atrioventricular conduction axis by combining histological, desmin, and connexin mapping data," *Circulation*, vol. 109, no. 9, pp. 1172–1179, 2004.
- [78] J. Li, I. D. Greener, S. Inada et al., "Computer three-dimensional reconstruction of the atrioventricular node," *Circulation Research*, vol. 102, no. 8, pp. 975–985, 2008.
- [79] W. J. Hucker, M. L. McCain, J. I. Laughner, P. A. Iaizzo, and I. R. Efimov, "Connexin 43 expression delineates two discrete pathways in the human atrioventricular junction," *Anatomical Record*, vol. 291, no. 2, pp. 204–215, 2008.
- [80] R. Lemery, G. Guiraudon, and J. P. Veinot, "Anatomic description of Bachmann's Bundle and its relation to the atrial septum," *American Journal of Cardiology*, vol. 91, no. 12, pp. 1482–1485, 2003.
- [81] L. Mitrofanova, V. Ivanov, and P. G. Platonov, "Anatomy of the inferior interatrial route in humans," *Europace*, vol. 7, no. 2, pp. S49–S55, 2005.
- [82] S. I. Sakamoto, T. Nitta, Y. Ishii, Y. Miyagi, H. Ohmori, and K. Shimizu, "Interatrial electrical connections: the precise location and preferential conduction," *Journal of Cardiovascular Electrophysiology*, vol. 16, no. 10, pp. 1077–1086, 2005.
- [83] G. K. Massing and T. N. James, "Anatomical configuration of the His bundle and bundle branches in the human heart," *Circulation*, vol. 53, no. 4, pp. 609–621, 1976.
- [84] L. Miquerol, S. Meysen, M. Mangoni et al., "Architectural and functional asymmetry of the His-Purkinje system of the murine heart," *Cardiovascular Research*, vol. 63, no. 1, pp. 77–86, 2004.
- [85] J. Tranum-Jensen, A. A. Wilde, J. T. Vermeulen, and M. J. Janse, "Morphology of electrophysiologically identified junctions between Purkinje fibers and ventricular muscle in rabbit and pig hearts," *Circulation Research*, vol. 69, no. 2, pp. 429–437, 1991.
- [86] A. Ansari, S. Y. Ho, and R. H. Anderson, "Distribution of the Purkinje fibres in the sheep heart," *Anatomical Record*, vol. 254, no. 1, pp. 92–97, 1999.
- [87] H. Tanaka, T. Hamamoto, and T. Takamatsu, "Toward an integrated understanding of the Purkinje fibers in the heart: the functional and morphological interconnection between the Purkinje fibers and ventricular muscle," *Acta Histochemica et Cytochemica*, vol. 38, no. 4, pp. 257–265, 2005.
- [88] S. Ryu, S. Yamamoto, C. R. Andersen, K. Nakazawa, F. Miyake, and T. N. James, "Intramural Purkinje cell network of sheep ventricles as the terminal pathway of conduction system," *Anatomical Record*, vol. 292, no. 1, pp. 12–22, 2009.
- [89] P. Helm, M. F. Beg, M. I. Miller, and R. L. Winslow, "Measuring and mapping cardiac fiber and laminar architecture using diffusion tensor MR imaging," *Annals of the New York Academy of Sciences*, vol. 1047, pp. 296–307, 2005.

- [90] C. Ramanathan, P. Jia, R. Ghanem, K. Ryu, and Y. Rudy, "Activation and repolarization of the normal human heart under complete physiological conditions," *Proceedings of the National Academy of Sciences of the United States of America*, vol. 103, no. 16, pp. 6309–6314, 2006.
- [91] L. Geerts, P. Bovendeerd, K. Nicolay, and T. Arts, "Characterization of the normal cardiac myofiber field in goat measured with MR-diffusion tensor imaging," *American Journal of Physiology—Heart and Circulatory Physiology*, vol. 283, no. 1, pp. H139–H145, 2002.
- [92] Y. Jiang, K. Pandya, O. Smithies, and E. W. Hsu, "Three-dimensional diffusion tensor microscopy of fixed mouse hearts," *Magnetic Resonance in Medicine*, vol. 52, no. 3, pp. 453–460, 2004.
- [93] K. B. Harrington, F. Rodriguez, A. Cheng et al., "Direct measurement of transmural laminar architecture in the anterolateral wall of the ovine left ventricle: new implications for wall thickening mechanics," *American Journal of Physiology—Heart and Circulatory Physiology*, vol. 288, no. 3, pp. H1324–H1330, 2005.
- [94] R. H. Anderson, M. Smerup, D. Sanchez-Quintana, M. Loukas, and P. P. Lunkenheimer, "The three-dimensional arrangement of the myocytes in the ventricular walls," *Clinical Anatomy*, vol. 22, no. 1, pp. 64–76, 2009.
- [95] P. S. Jouk, Y. Usson, G. Michalowicz, and L. Grossi, "Three-dimensional cartography of the pattern of the myofibres in the second trimester fetal human heart," *Anatomy and Embryology*, vol. 202, no. 2, pp. 103–118, 2000.
- [96] K. Wang, S. Y. Ho, D. G. Gibson, and R. H. Anderson, "Architecture of atrial musculature in humans," *British Heart Journal*, vol. 73, no. 6, pp. 559–565, 1995.
- [97] S. Y. Ho, R. H. Anderson, and D. Sánchez-Quintana, "Atrial structure and fibres: morphologic bases of atrial conduction," *Cardiovascular Research*, vol. 54, no. 2, pp. 325–336, 2002.
- [98] H. Sun and D. S. Khoury, "Electrical conduits within the inferior atrial region exhibit preferential roles in interatrial activation," *Journal of Electrocardiology*, vol. 34, no. 1, pp. 1–14, 2001.
- [99] V. V. Fedorov, A. V. Glukhov, R. Chang et al., "Optical mapping of the isolated coronary-perfused human sinus node," *Journal of the American College of Cardiology*, vol. 56, no. 17, pp. 1386–1394, 2010.
- [100] G. K. Moe, J. B. Preston, and H. Burlington, "Physiologic evidence for a dual A-V transmission system," *Circulation Research*, vol. 4, no. 4, pp. 357–375, 1956.
- [101] T. N. Mazgalev, S. Y. Ho, and R. H. Anderson, "Anatomic-electrophysiological correlations concerning the pathways for atrioventricular conduction," *Circulation*, vol. 103, no. 22, pp. 2660–2667, 2001.
- [102] W. J. Hucker, V. Sharma, V. P. Nikolski, and I. R. Efimov, "Atrioventricular conduction with and without AV nodal delay: two pathways to the bundle of His in the rabbit heart," *American Journal of Physiology—Heart and Circulatory Physiology*, vol. 293, no. 2, pp. H1122–H1130, 2007.
- [103] K. Simelius, J. Nenonen, and M. Horáček, "Modeling cardiac ventricular activation," *International Journal of Bioelectromagnetism*, vol. 3, no. 2, pp. 51–58, 2001.
- [104] E. J. Vigmond and C. Clements, "Construction of a computer model to investigate sawtooth effects in the Purkinje system," *IEEE Transactions on Biomedical Engineering*, vol. 54, no. 3, pp. 389–399, 2007.
- [105] R. Sebastian, V. Zimmerman, D. Romero et al., "Construction of a computational anatomical model of the peripheral cardiac conduction system," *IEEE Transactions on Biomedical Engineering*, vol. 58, no. 12, pp. 3479–3482, 2011.
- [106] R. Bordas, K. Gillow, Q. Lou et al., "Rabbit-specific ventricular model of cardiac electrophysiological function including specialized conduction system," *Progress in Biophysics and Molecular Biology*, vol. 107, no. 1, pp. 90–100, 2011.
- [107] S. Tawara, *Das Reizleitungssystem Des Säugetierherzens. Eine Anatomisch-Histologische Studie Über Das Atrioventrikulär-bündel Und Die Purkinjeschen Fäden*, Verlag von Gustav Fischer, Jena, Germany, 1906.
- [108] M. S. Spach, S. Huang, S. I. Armstrong, and R. V. Canent, "Demonstration of peripheral conduction system in human hearts," *Circulation*, vol. 28, no. 3, pp. 333–338, 1963.
- [109] R. J. Myerburg, H. Gelband, and K. Nilsson, "Physiology of canine intraventricular conduction and endocardial excitation," *Circulation Research*, vol. 30, no. 2, pp. 217–243, 1972.
- [110] A. Atkinson, S. Inada, J. Li et al., "Anatomical and molecular mapping of the left and right ventricular His-Purkinje conduction networks," *The Journal of Molecular and Cellular Cardiology*, vol. 51, no. 5, pp. 689–701, 2011.
- [111] R. Lemery, L. Soucie, B. Martin, A. S. L. Tang, M. Green, and J. Healey, "Human study of biatrial electrical coupling: determinants of endocardial septal activation and conduction over interatrial connections," *Circulation*, vol. 110, no. 15, pp. 2083–2089, 2004.
- [112] A. Hansson, M. Holm, P. Blomström et al., "Right atrial free wall conduction velocity and degree of anisotropy in patients with stable sinus rhythm studied during open heart surgery," *European Heart Journal*, vol. 19, no. 2, pp. 293–300, 1998.
- [113] J. P. Boineau, T. E. Canavan, R. B. Schuessler, M. E. Cain, P. B. Corr, and J. L. Cox, "Demonstration of a widely distributed atrial pacemaker complex in the human heart," *Circulation*, vol. 77, no. 6, pp. 1221–1237, 1988.
- [114] P. C. Dolber and M. S. Spach, "Structure of canine Bachmann's bundle related to propagation of excitation," *American Journal of Physiology—Heart and Circulatory Physiology*, vol. 257, no. 5, part 2, pp. H1446–H1457, 1989.
- [115] P. R. De, S. Y. Ho, J. A. Salerno-Uriarte, M. Tritto, and G. Spadacini, "Electroanatomic analysis of sinus impulse propagation in normal human atria," *Journal of Cardiovascular Electrophysiology*, vol. 13, no. 1, pp. 1–10, 2002.
- [116] J. M. Tapanainen, R. Jurkko, F. Holmqvist et al., "Interatrial right-to-left conduction in patients with paroxysmal atrial fibrillation," *Journal of Interventional Cardiac Electrophysiology*, vol. 25, no. 2, pp. 117–122, 2009.
- [117] Y. G. Li, G. Grönfeld, C. Israel, F. Bogun, and S. H. Hohnloser, "Bundle branch reentrant tachycardia in patients with apparent normal His-Purkinje conduction: the role of functional conduction impairment," *Journal of Cardiovascular Electrophysiology*, vol. 13, no. 12, pp. 1233–1239, 2002.
- [118] D. Romero, R. Sebastian, B. H. Bijnens et al., "Effects of the Purkinje system and cardiac geometry on biventricular pacing: a model study," *Annals of Biomedical Engineering*, vol. 38, no. 4, pp. 1388–1398, 2010.
- [119] P. D. Lambiase, A. Rinaldi, J. Hauck et al., "Non-contact left ventricular endocardial mapping in cardiac resynchronization therapy," *Heart*, vol. 90, no. 1, pp. 44–51, 2004.
- [120] P. M. van Dam, T. F. Oostendorp, A. C. Linnenbank, and A. van Oosterom, "Non-invasive imaging of cardiac activation and recovery," *Annals of Biomedical Engineering*, vol. 37, no. 9, pp. 1739–1756, 2009.